



KAPITAŁ LUDZKI
NARODOWA STRATEGIA SPÓJNOŚCI



Politechnika Wroclawska

UNIA EUROPEJSKA
EUROPEJSKI
FUNDUSZ SPOLECZNY



ROZWÓJ POTENCJAŁU I OFERTY DYDAKTYCZNEJ POLITECHNIKI WROCŁAWSKIEJ

Introduction to Nanoscale Physics and Nanomaterials

A. Podhorodecki, J. Misiewicz



ROZWÓJ POTENCJAŁU I OFERTY DYDAKTYCZNEJ POLITECHNIKI WROCLAWSKIEJ

1. Introduction.....	3	4.8 Matrix related effects.....	87
2. Theoretical background.....	9	(a) Photoluminescence blinking.....	88
2.1 How to calculate energy of electron in solid state.....	12	(b) Spectral diffusion.....	89
(a) Full description.....	12	(c) Interdot interactions.....	92
(b) Born-Oppenheimer approximation...	12	4.9 Mechanical properties of nanomaterials.....	95
(c) Single electron approximation.....	12	5. Nanowires.....	97
(d) Columb interactions.....	16	6. Applications of nanomaterials.....	99
(e) Matrix related effects.....	17	6.1 Bio-nano medicine.....	99
2.1 How to calculate optical functions?.....	19	6.2 Optoelectronics.....	102
(a) Density of states.....	19	7. Characterization techniques.....	103
(b) Transition rate.....	19	7.1 Raman Spectroscopy.....	103
(c) The radiative/nonradiative decay time..	19	(a) Origins of Raman scattering.....	104
(d) The carrier concentration.....	21	(b) Experimental setup.....	106
(e) The absorption coefficient.....	22	(c) Coherent Anti-Stokes Raman Spectroscopy (CARS).....	107
(f) The optical gain.....	22	(d) Raman Microscopy.....	108
2.2 Excitons.....	23	(e) Examples of Raman measurements applications.....	110
3. Nanomaterials synthesis.....	25	7.2 Time-resolved Photoluminescence Spectroscopy.....	114
3.1 MOCVD.....	35	(a) The Stroboscopic Technique (Strobe)...	115
3.2 MBE.....	35	(b) Simple Photon Counting.....	120
3.3 CVD.....	37	(c) Gated Photon Counting.....	121
3.4 Colloidal techniques.....	41	(d) Time-Correlated Single Photon Counting (TCSPC).....	123
4. Optical properties of zero dimensional semiconducting structures.....	46	7.3 Two-dimensional Photoluminescence Excitation Spectroscopy (2D PLE).....	125
4.1 Band gap modifications.....	57	7.4 Scanning Probe Microscopy (SPM).....	131
4.2 Nonlinear effects.....	59	(a) Scanning Tunneling Microscope (STM)	132
4.3 Shape effects.....	61	(b) Atomic Force Microscopy (AFM).....	135
4.4 Lattice vibrations.....	62	(c) Scanning near field optical microscopy (SNOM).....	137
4.5 Surface related effects.....	65	(d) Transmission Electron Microscope (TEM).....	139
4.6 Wave function localization.....	66	(e) X-ray Diffraction (XRD).....	140
4.7 Relaxation processes.....	72		
(a) Auger relaxation.....	73		
(b) Intraband transitions.....	75		
(c) Multi excitons generation (MEG) or Carrier multiplications.....	76		
(d) Gain in single nanocrystals.....	79		



ROZWÓJ POTENCJAŁU I OFERTY DYDAKTYCZNEJ POLITECHNIKI WROCŁAWSKIEJ

1. Introduction ^[1]

Nanotechnology deals with small structures or small-sized materials. The typical dimension spans from subnanometer to several hundred nanometers. A nanometer (nm) is one billionth of a meter, or 10^{-9} m. **Figure 1.1** gives an example of different object typical for certain scale. One nanometer is approximately the length equivalent to 10 hydrogen or 5 silicon atoms aligned in a line. Small features permit more functionality in a given space, but nanotechnology is not only a simple continuation of miniaturization from micron meter scale down to nanometer scale.

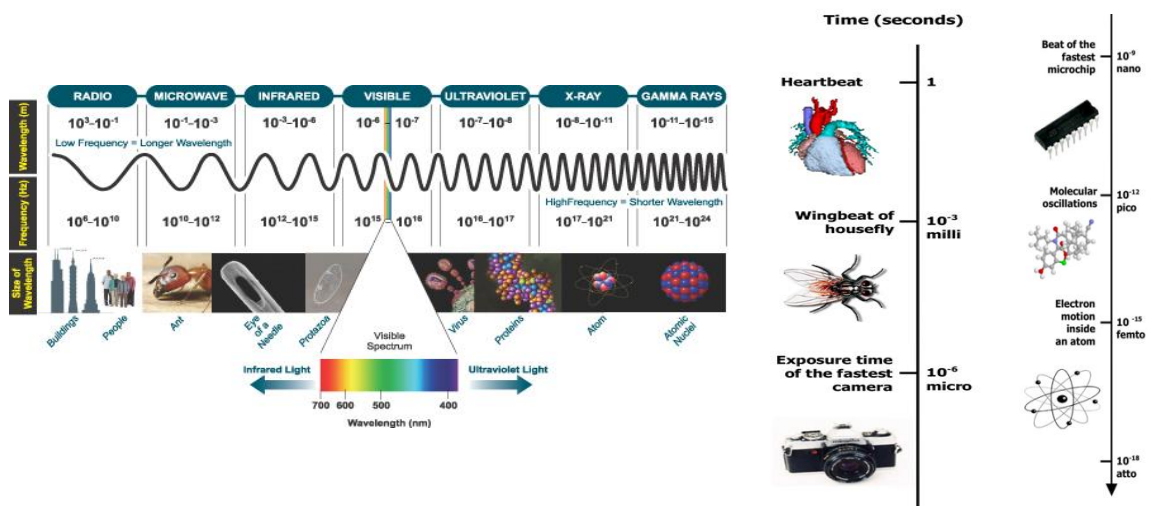


Figure 1.1 (a) Scale regimes with representative for these regimes physical objects, (b) time regimes with representative for these regimes movements.

Materials in the micrometer scale mostly exhibit physical properties the same as that of bulk form; however, materials in the nanometer scale may exhibit physical properties distinctively different from that of bulk form. Materials in this size range exhibit some remarkable specific properties; a transition from atoms or molecules to bulk form takes place in this size range.

¹ Introduction has been written based on introduction taken after: G.Cao, *Nanostructures and Nanomaterials, Synthesis, Properties and applications*, Imperial College Press, London (2004).



ROZWÓJ POTENCJAŁU I OFERTY DYDAKTYCZNEJ POLITECHNIKI WROCLAWSKIEJ

Thus, as we can see recent expectations from new materials are very hard to be fulfilled. Except a cheap prize, a small size following to high integration they should exhibit new, unique physico-chemical properties, be multi-functional, self-sufficient or even *intelligent*. Up to now only the materials from the living world were able to fulfill these expectations what has been shown in **Fig.1.2**.

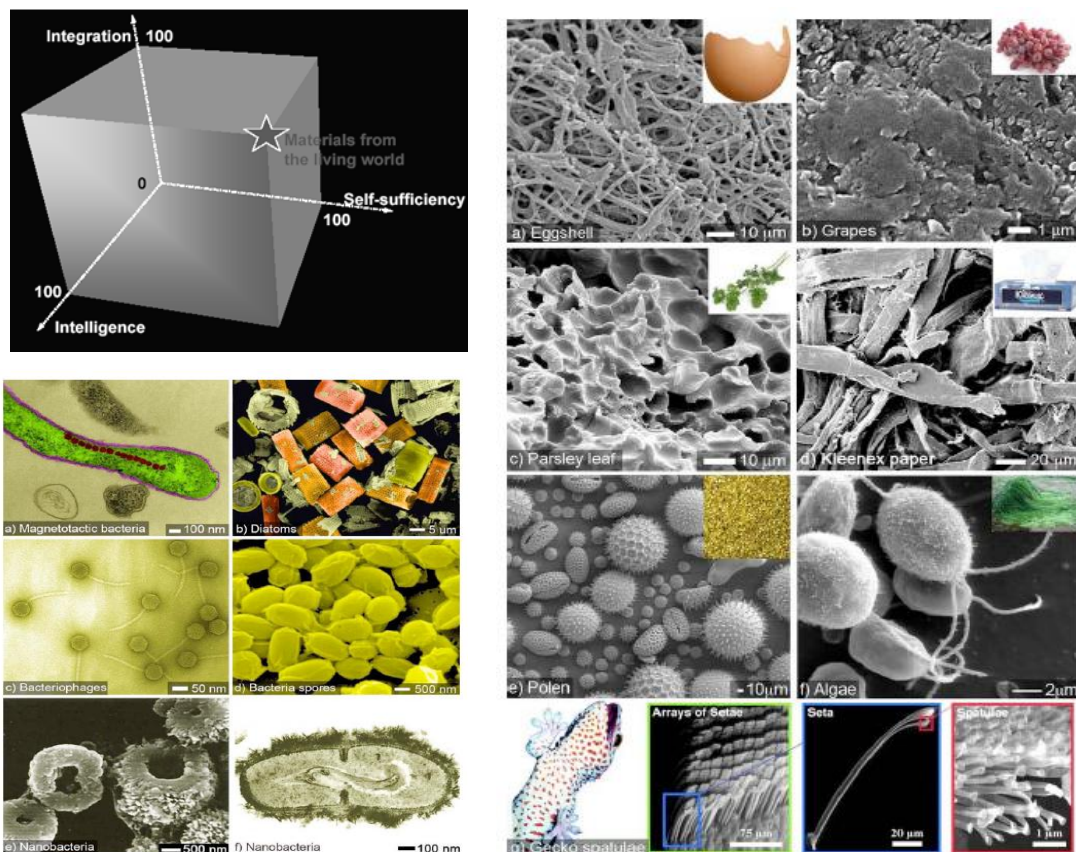


Figure 1.2 (a) Recent expectations from new materials, (b) example of nanomaterials from the living world: SEM images showing the complexity of the world at the micro and nanoscale: Left: Organisms in the nanoscale range or producing solid -state nanoscale debris. (a) TEM of *Aquaspirillum magnetotacticum* - bacterium showing magnetosomes (iron oxide granules). (b) SEM of diatom silica frustules or skeletons. (a and b © Dr. Dennis Kunkel/Visuals Unlimited. Reproduced with permission from Visuals Unlimited [2]. (c) SEM of bacteriophage - a virus that infects bacteria, courtesy of Ross Inman [3]. (d) SEM of *Bacillus anthracis* bacteria spores, that can live for many years, enabling the bacteria to survive in a dormant state until they encounter a suitable host, credit Laura Rose, courtesy of Public Health Image Library [4]. (e) SEM of cultured nanobacteria, (f) Dividing nanobacteria covered with a “hairy” apatite layer, (e and f courtesy of PNAS [5]). Right: (a) the inner surface of a bird’s eggshell, credit: Janice Carr, Sandra L. Westmoreland, courtesy Public Health Image Library [6]; (b) the rough surface of table grape, credit: Janice Carr, courtesy Public Health Image

² www.visualsunlimited.com

³ Ross Inman, Institute for Molecular Virology & Department of Biochemistry, University of Wisconsin- Madison, Wisconsin. USA, <http://www.biochem.wisc.edu/inman/empics/virus.htm>

⁴ Public Health Image Library, <http://phil.cdc.gov/Phil/home.asp>

⁵ Kajander E O and Çiftçioğlu N 1998 Nanobacteria: an alternative mechanism for pathogenic intra- and extracellular calcification and stone formation Proc. Natl. Acad. Sci. **95** 8274-8279

⁶ Public Health Image Library, <http://phil.cdc.gov/Phil/home.asp>



ROZWÓJ POTENCJAŁU I OFERTY DYDAKTYCZNEJ POLITECHNIKI WROCŁAWSKIEJ

Library [7]; (c) the textured surface of a parsley leaf, credit Janice Carr, courtesy Public Health Image Library [8]; (d) Kleenex paper, courtesy of Jim Ekstrom [9]; (e) pollen from a variety of common plants, credit Louisa Howard, Charles Daghljan, courtesy Public Health Image Library [10]; *Biointerphases* vol. 2, issue 4 (2007) pages MR17 - MR172 14 (f) green algae, credit Elizabeth Smith, Louisa Howard, Erin Dymek, Public Health Image Library [11]; (g) Gecko nano-adhesive system, with increasing magnification from left to right: gecko climbing vertical glass, adhesive surface microstructure, individual setae, nanostructure of spatular endings, courtesy of PNAS [12].

For example, crystals in the nanometer scale have a low melting point (the difference can be as large as 1000°C) and reduced lattice constants, since the number of surface atoms or ions becomes a significant fraction of the total number of atoms or ions and the surface energy plays a significant role in the thermal stability. Crystal structures stable at elevated temperatures are stable at much lower temperatures in nanometer sizes, so ferroelectrics and ferromagnetics may lose their ferroelectricity and ferromagnetism when the materials are shrunk to the nanometer scale. Bulk semiconductors become insulators when the characteristic dimension is sufficiently small (in a couple of nanometers). Although bulk gold does not exhibit catalytic properties, Au nanocrystal demonstrates to be an excellent low temperature catalyst. Currently there are a lot of different opinions about what exactly is nanotechnology. For example, some people consider the study of microstructures of materials using electron microscopy and the growth and characterization of thin films as nanotechnology. Other people consider a bottom-up approach in materials synthesis and fabrication, such as self-assembly or biomineralization to form hierarchical structures like abalone shell, is nanotechnology. Drug delivery, e.g. by putting drugs inside carbon nanotubes, is considered as nanotechnology. Micro-electromechanical systems (MEMS) and lab-on-a-chip are considered as nanotechnology. More futuristic or science fiction-like opinions are that nanotechnology means something very ambitious and startlingly new, such as miniature submarines in the bloodstream, smart self-replication nanorobots monitoring our body, space elevators made of nanotubes and the colonization of space. There are many other definitions that people working in nanotechnology use to define the field. These definitions are true to certain specific research fields, but none of them covers the full spectrum of nanotechnology. The many diverse definitions of nanotechnology reflect the fact that

⁷ Public Health Image Library, <http://phil.cdc.gov/Phil/home.asp>

⁸ Public Health Image Library, <http://phil.cdc.gov/Phil/home.asp>

⁹ Public Health Image Library, <http://phil.cdc.gov/Phil/home.asp>

¹⁰ Public Health Image Library, <http://phil.cdc.gov/Phil/home.asp>

¹¹ Public Health Image Library, <http://phil.cdc.gov/Phil/home.asp>

¹² Hansen W R, Autumn K 2005 Evidence for self-cleaning in gecko setae *Proc. Nat. Acad. Sci.* **102** 385-389



ROZWÓJ POTENCJAŁU I OFERTY DYDAKTYCZNEJ POLITECHNIKI WROCŁAWSKIEJ

nanotechnology covers a broad spectrum of research field and requires true interdisciplinary and multidisciplinary efforts.

In general, nanotechnology can be understood as a technology of design, fabrication and applications of nanostructures and nanomaterials. Nanotechnology also includes fundamental understanding of physical properties and phenomena of nanomaterials and nanostructures. Study on fundamental relationships between physical properties and phenomena and material dimensions in the nanometer scale, is also referred to as a nanoscience. In the United States, nanotechnology has been defined as being “concerned with materials and systems whose structures and components exhibit novel and significantly improved physical, chemical and biological properties, phenomena and processes due to their nanoscale size”.

Many technologies have been explored to fabricate nanostructures and nanomaterials such as **top-down** and **bottom-up** (Fig.1.3) approaches, spontaneous and forced processes. Top-down is in general an extension of lithography. The concept and practice of a bottom-up approach in material science and chemistry are not new either. Synthesis of large polymer molecules is a typical bottom-up approach, in which individual building blocks (monomers) are assembled to a large molecule or polymerized into bulk material. Crystal growth is another bottom-up approach, where growth species either atoms, or ions or molecules orderly assemble into desired crystal structure on the growth surface.

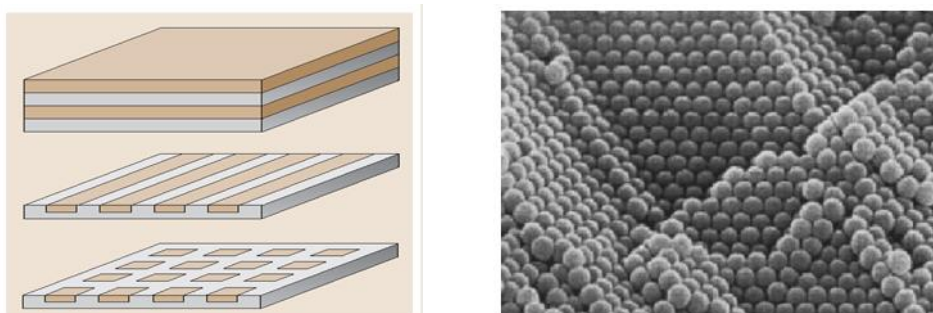


Figure 1.3 Two main concepts of growing structures in nanotechnology (a) top-down and (b) bottom-up techniques.

In order to explore novel physical properties and phenomena and realize potential applications of nanostructures and nanomaterials, the ability to fabricate and process



ROZWÓJ POTENCJAŁU I OFERTY DYDAKTYCZNEJ POLITECHNIKI WROCŁAWSKIEJ

nanomaterials and nanostructures is the first corner stone in nanotechnology. Nanostructured materials are those with at least one dimension falling in nanometer scale, and include nanoparticles (including quantum dots, when exhibiting quantum effects), nanorods and nanowires, thin films, and bulk materials made of nanoscale building blocks or consisting of nanoscale structures (**Fig.1.4a**).

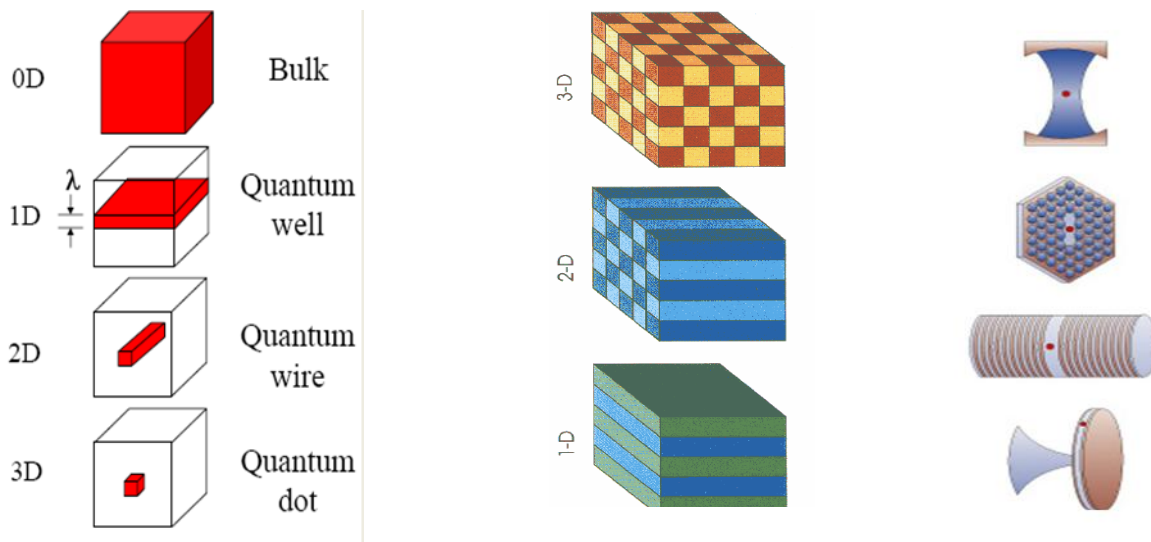


Figure 1.4 (a) different classes of nano (1-100 nm) materials designed for confining electron/hole wavefunctions, (b) different class of nano (100-1000 nm) materials designed for confining electromagnetic wave, (c) nanomaterial combined both (a-b) nanostructures into one.

When at least one dimension of nanomaterial falling in the range of 100-1000 nm, in most of the cases we lost the quantum properties of the matter but we still can have many advantages of such nanomaterial since it can be a photonic crystal, which allows us to play with the properties of incoming or outgoing from the material light (**Fig.1.4 (b)**). Moreover, very recently many efforts in nanotechnology are given to combine both photonic properties of nanomaterials with their quantum confinement related properties. For this purpose nanomaterials (1-100 nm) are placed inside the photonic crystals (**Fig. 1.4 (c)**). **Figure 1.5** illustrates practical realizations of different classes of nanomaterials designed to confine the electron wavefunction in different number of dimensions.



ROZWÓJ POTENCJAŁU I OFERTY DYDAKTYCZNEJ POLITECHNIKI WROCLAWSKIEJ

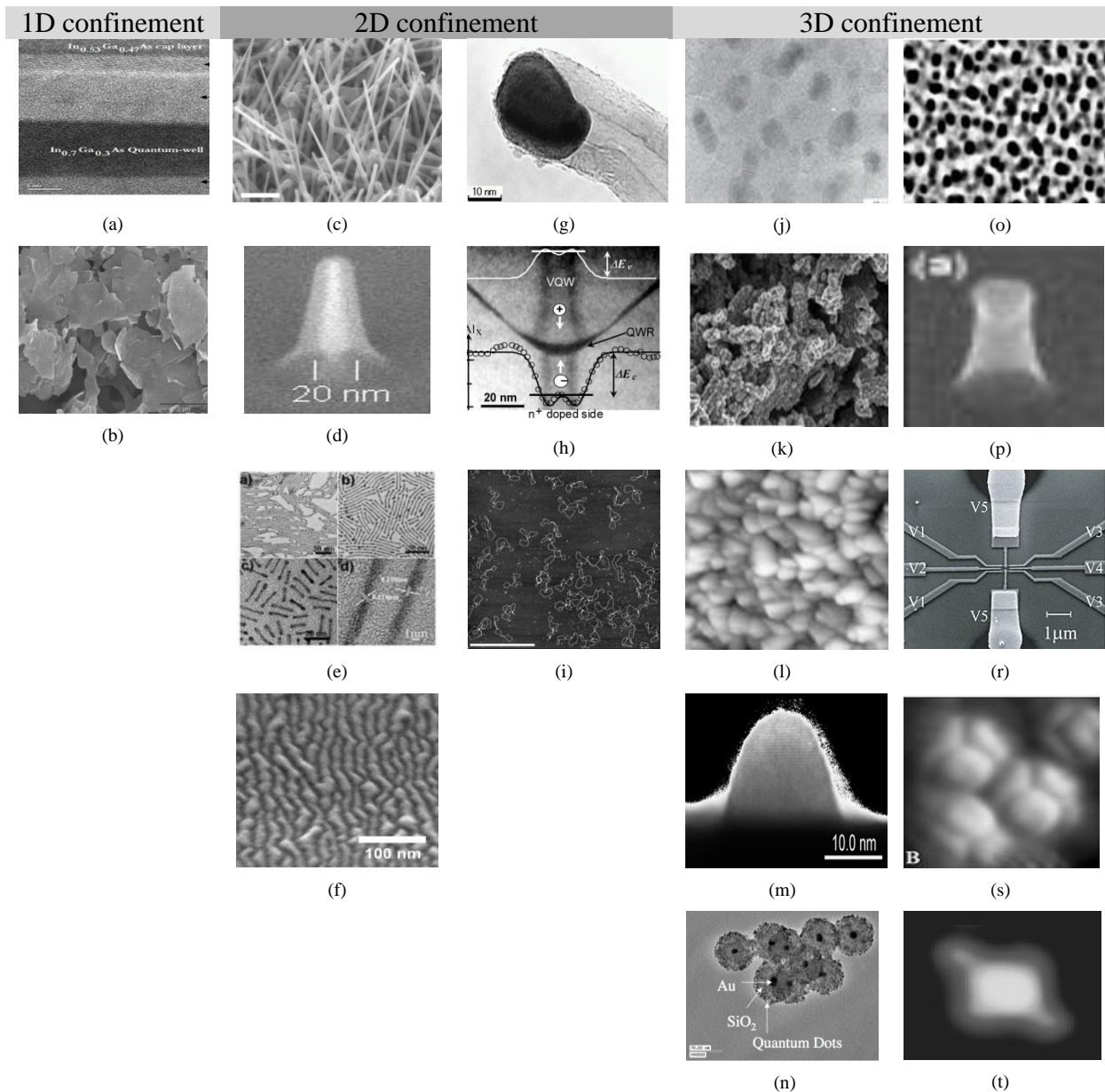


Figure 1.5 (a) InGaAs/InAlAs quantum wells [13], (b) Graphene nanoplatelets [14] (c) InP nanowires [15], (d) silicon pillar [16], (e) iron-platinum nanowires and nanorods [17], (f) InAs/GaAs quantum dashes [18], (g) carbon nanotubes [19], (h) GaAs/AlGaAs V-groove quantum wire [20], (i) AFM image of staphylococcal plasmid pC221 mixed with mobilisation accessory protein MobC [21], (j) GaN nanocrystals [22], (k) GaN nanopowders [23], (l) TiO₂ nanocrystalline films [24], (m) self

¹³Mike Mayberry et al. IEEE Electron Device Letters 28, 685 (2007).

¹⁴PRLog (Press Release) – Jan 09, (2009).

¹⁵Daniel Kane, University of California, San Diego (website, 2008).

¹⁶Credit: The Materials Physics groups, KTH, Sweden (website, 2010)

¹⁷Credit: Chao Wang & Jaemin Kim/Brown University.

¹⁸Credit: G.Sek, Wroclaw University of Technology, Poland.

¹⁹Credit: M.Endo, Shinshu University, Japan.

²⁰Credit: Eli Kapon at the Institute of Quantum Electronics and Photonics, Swiss Federal Institute of Technology in Lausanne (EPFL)

²¹Credit: C. Thomas, School of Biochemistry & Molecular Biology at the University of Leeds (website, 2010)

²² Private data



ROZWÓJ POTENCJAŁU I OFERTY DYDAKTYCZNEJ POLITECHNIKI WROCLAWSKIEJ

assembled quantum dot [²⁵], (n) gold quantum dot [²⁶], (o) nanoporous film [²⁷], (p) nanopilars with silicon QDs [²⁸], (r) electrical quantum dot [²⁹], (s) fullerenes (C-60) [³⁰], (t) STM images of a single terfluorene molecule [³¹].

More, generally materials at nanoscale will start to exhibit new properties when one of their characteristic lengths became comparable with one of their dimensions. There are several parameters which can be defined as **characteristic length** depending, which properties will be changed, namely:

- (a) *Optical properties*: electromagnetic wave, an exciton radius in semiconductors, skin depth in metals
- (b) *Electrical properties*: an electron mean free path, coherence length (superconductors 1-100 nm)
- (c) *Magnetic*: domains of size (exchange length 3-50 nm)
- (d) *Mechanical*: none (multiscale)
- (e) *Chemical*: none (smaller is better)

2. Theoretical background

Frequently one categorizes material properties at the macroscopic scale by terms such as *intensive* and *extensive*. An intensive property is not dependent on the sample size, or mass. For example, if one specifies the temperature of a sample as that of room temperature, the description is complete. One does not need to specify the size of the sample. Other intensive properties include pressure and density. In contrast, an extensive property does depend on the size of the sample. For example, the volume of a sample depends on the size. Two moles of a gas occupies twice the volume as one mole. Therefore, one often specifies volume in terms of the volume per mole, or the specific volume. Other extensive properties include thermodynamics properties like the heat capacity, the enthalpy, the entropy and free energy of the system. Matter at the nanoscale is different. Properties that are intensive at the macroscopic scale may not be intensive at the "nano-" or "subnano-" scale. In fact, such

²⁵ Private data

²⁴ Credit: D.Kaczmarek, Wroclaw University of Technology, Poland

²⁵ T.L. Reinecke, Y. Lyanda-Geller, M. Bayer, and A. Forchel, *Nano Research Letter Review* (2004).

²⁶ Credit: Victor Klimov from Los Alamos' Chemistry Division (website, 2009).

²⁷ Credit: *University of Rochester; BetaBatt, Inc*

²⁸ Nanopilars.

²⁹ Credit: A.Chang, Duke University (from IEEE Spectrum, Can quantum dots can compute? by E.Guizzo, 2004)

³⁰ M. Casarin, D. Forrer, T. Orzali, M. Petukhov, M. Sambri, E. Tondello and A. Vittadini, *J. Phys. Chem. C* 111 (2007)

³¹ L. Grill, M. Dyer, L. Lafferentz, M. Persson, M. V. Peters, S. Hecht, *Nature Nanotechn.* 2, 687 (2007)



ROZWÓJ POTENCJAŁU I OFERTY DYDAKTYCZNEJ POLITECHNIKI WROCŁAWSKIEJ

properties may be hard to define at very small length scales. Consider a small cluster of atoms, e.g., a dozen silicon atoms. Such an ensemble contains so few atoms that it is difficult to define a property such as the temperature³² or the volume. While extensive properties such as the heat capacity or free energy of the system remain so in the sense of changing with the size of the system, such properties may no longer scale linearly with size. For example, the free energy of two dozen atoms of silicon may not be twice the free energy of one dozen atoms of silicon. In this latter example, one can make some simple arguments to explain this behavior. Suppose we consider the scaling of the free energy for a spherical sample of matter whose radius is R . The volume energy term would scale as R^3 ; the surface term as R^2 . As R tends towards the nanoscale, the surface terms can become the dominant term in the free energy. This surface term does not scale linearly with the volume or mass of the sample. This different scaling between volume and surface terms is well known in the **nucleation theory**. A manifestation of this effect is that particles must exceed a certain size before they are stable. One definition of the nanoscale is the size at which deviations from intrinsic intensive and extensive properties at the macroscopic scale occur.

The theory of single atoms it is already reasonably well know issue and there are many numerical techniques which allow us to predict properties of such objects. Very similar level of understanding can be given to bulk material. However, when describing the properties of nanomaterials many problems start to appear. When using for their description formalism used for bulk materials, like effective mass approximation, many effects related to size reduction are missing. On the other hand, when we start to use *ab initio* approach and build our structure atom by atom we start to have serious technical problems since few nanometer size objects generate very complex problem to solve, from the point of view of nowadays computer's possibilities. Moreover, computational studies of semiconducting clusters (like CdSe) related to *ab-initio* studies fall in two broad classes: (1) efforts based on classical

³² For a system in thermal equilibrium at a constant volume, temperature is thermodynamically defined in terms of its energy (E) and entropy (S) as: $T \equiv \partial E / \partial S$. It is possible to extend the definition of temperature even to systems made of few particles, like in a quantum dot. The generalized temperature is obtained by considering time ensembles instead of configuration space ensembles given in Statistical mechanics in the case of thermal and particle exchange between a small system of fermions (N even less than 10) with a single/double occupancy system. The finite quantum grand partition ensemble, obtained under the hypothesis of ergodicity and orthodicity, allows to express the generalized temperature from the ratio of the average time of occupation τ_1 and τ_2 of the single/double occupancy system [*Applied Physics Letters* **96**, 11310, 2010]: $T = k^{-1} \ln 2 (\tau_2 / \tau_1) [E - E_F (1 + 3/2N)]$ where E_F is the Fermi energy which tends to the ordinary temperature when N goes to infinity.



ROZWÓJ POTENCJAŁU I OFERTY DYDAKTYCZNEJ POLITECHNIKI WROCŁAWSKIEJ

molecular dynamics, and first principles techniques without self consistency or geometry optimization, involving a wide range of cluster sizes [³³] and (2) sophisticated self consistent *ab initio* calculations that treat only small or limited cluster sizes [³⁴].

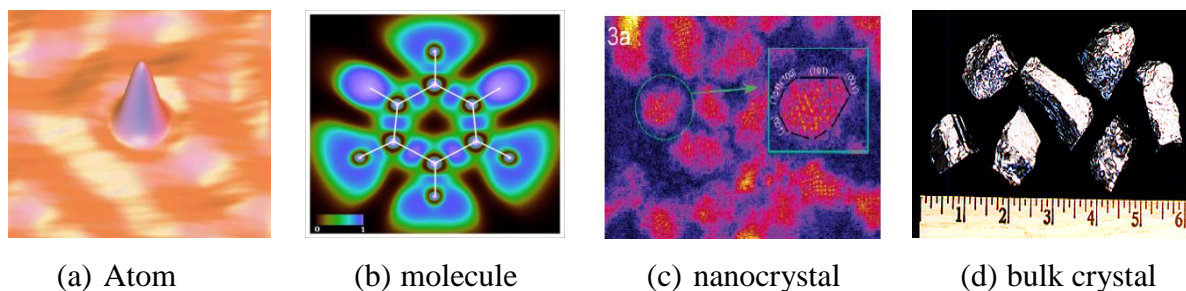


Figure. 2.1 (a) Scanning tunneling microscope (STM) topographic image of a single atom of cobalt (Joseph Stroscio and Robert Celotta, NIST), (b) the electron localization function (ELF) of alloxan (Theoretical Chemistry, UWA), (c) CdSe nanocrystals [³⁵], (d) bulk silicon.

Owing to an inadequate treatment of the electronic or structural degrees of freedom, the former type of calculations may lead to erroneous conclusions concerning the impact of surface relaxations on optical properties. The second class of calculations referred to above provide very accurate information concerning the stability, structure, and optical properties of small semiconductor clusters.

Thus, the issue of theoretical calculation of nanoscale materials properties is still an open and complicated problem. For this reason, in this section, we will only briefly review the concepts of theoretical description of electronic properties of the matter and introduce some basic equations which can be used for predictions of simple experimental data obtained for nanostructures.

³³ P. Sarkar and M. Springborg, Phys. Rev. B **68**, 235409 (2003); E. Rabani, J. Chem. Phys. **115**, 1493 (2001).

³⁴ A. Puzder, A. J. Williamson, F. Gygi, and G. Galli, Phys. Rev. Lett. **92**, 217401 (2004), M. C. Tropicovsky, L. Kronik, and J. R. Chelikowsky, Phys. Rev. B **65**, 033311 (2002); A. Kasuya, R. Sivamohan, Y. A. Barnakov, I. M. Dmitruk, T. Nirasawa, V. R. Romanyuk, V. Kumar, S. V. Mamykin, K. Tohji, B. Jeyadevan, K. Shinoda, T. Kudo, O. Terasaki, Z. Liu, R. V. Belosludov, V. Sundararajan, and Y. Kawazoe, Nat. Mater. **3**, 99 (2004).

³⁵ J.R.McBride et al., Nano Letters **4**, 1279 (2004)



ROZWÓJ POTENCJAŁU I OFERTY DYDAKTYCZNEJ POLITECHNIKI WROCŁAWSKIEJ

2.1 How to calculate energy of electron in solid state?

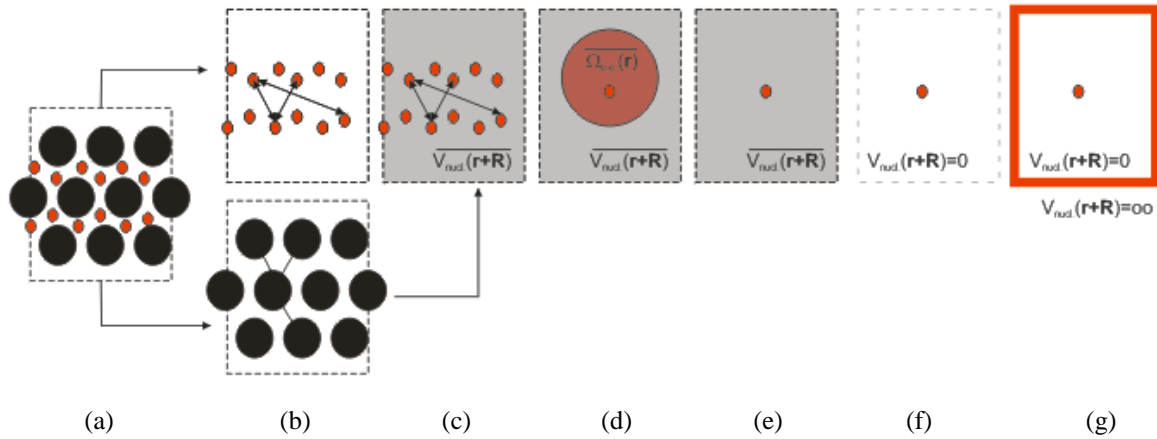


Figure 2.2 Schematical representation of simplification steps used for calculations of energy states of electron in the solid state

(a) Full description

Consider N nucleons of charge Z_n at positions $\{\mathbf{R}_n\}$ for $n=1, \dots, N$ and I electrons at positions $\{\mathbf{r}_i\}$ for $i=1, \dots, M$. The Hamiltonian for this system in its simplest form can be written as:

$$\begin{aligned} \hat{H}_e(\vec{R}_1, \vec{R}_2, \vec{R}_3, \dots; \vec{r}_1, \vec{r}_2, \vec{r}_3, \dots) = & \sum_{n=1}^N \frac{-\hbar^2 \nabla_n^2}{2M_n} + \frac{1}{2} \sum_{n,m=1; n \neq m}^N \frac{Z_n Z_m e^2}{|\vec{R}_n - \vec{R}_m|} + \sum_{i=1}^M \frac{-\hbar^2 \nabla_i^2}{2m_i} + \\ & + \sum_{n=1}^N \sum_{j=1}^M \frac{Z_n e^2}{|\vec{R}_n - \vec{r}_j|} + \frac{1}{2} \sum_{i,j=1; i \neq j}^M \frac{e^2}{|\vec{r}_i - \vec{r}_j|} \end{aligned} \quad (1)$$



ROZWÓJ POTENCJAŁU I OFERTY DYDAKTYCZNEJ POLITECHNIKI WROCŁAWSKIEJ

M_n is the mass of the nucleon, \hbar is Planck's constant divide by 2π , m is the mass of the electron. This expression omits some terms such as those involving relativistic interactions, but captures the essential features for nanoscale matter. Using the Hamiltonian in Eq. 1 the quantum mechanical equation known as the Schrödinger equation for the electronic structure of the system can be written as:

$$\begin{aligned} \mathcal{H}(\vec{R}_1, \vec{R}_2, \vec{R}_3, \dots; \vec{r}_1, \vec{r}_2, \vec{r}_3, \dots) \Psi(\vec{R}_1, \vec{R}_2, \vec{R}_3, \dots; \vec{r}_1, \vec{r}_2, \vec{r}_3, \dots) \\ = E \Psi(\vec{R}_1, \vec{R}_2, \vec{R}_3, \dots; \vec{r}_1, \vec{r}_2, \vec{r}_3, \dots) \end{aligned} \quad (2)$$

where E is the total electronic energy of the system and Ψ is the many body wavefunction. A number of highly successful approximations have been made to solve for the both the ground state and excited state energies. For the most part, these approximations are used to remove as many “irrelevant” degrees of freedom from the system as possible. One common approximation is to separate the nuclear and electronic degrees of freedom. Since the nuclei are considerably more massive than the electrons, it can be assumed that the electrons will respond “instantaneously” to the nuclear coordinates. This approximation is called the **Born-Oppenheimer** or the **adiabatic approximation**. It allows one to treat the nuclear coordinates as classical parameters.

Another common approximation is to construct a specific form for the many body wavefunction. If one can obtain an accurate wave function, then via the variational principle an accurate estimate for the energy will emerge. The most difficult part of this exercise is to use physical intuition to define a trial wave function close to the true wave function. This problem will bring us to a many body wave function known as the Hartree wave function. If one uses this form of the wave function as an approximation to solve the Hamiltonian including the electron-electron interactions, this is known as the **Hartree approximation**. By ignoring the electron-electron terms, the Hartree approximation treats the electrons moving independently in the nuclear potential.



ROZWÓJ POTENCJAŁU I OFERTY DYDAKTYCZNEJ POLITECHNIKI WROCLAWSKIEJ

(b) Born-Oppenheimer approximation

When we applied the Born-Oppenheimer approximation Eq.(1) can be written as two separated hamiltonians given by the following formulas:

$$\hat{H}_e(\vec{r}_1, \vec{r}_2, \vec{r}_3 \dots) = \sum_{i=1}^M \frac{-\hbar^2 \nabla_i^2}{2m_i} + \sum_{n=1}^N \sum_{j=1}^M \frac{Z_n e^2}{|\vec{R}_n - \vec{r}_j|} + \frac{1}{2} \sum_{i,j=1; i \neq j}^N \frac{e^2}{|\vec{r}_i - \vec{r}_j|} \quad (3)$$

and for nucleus

$$\hat{H}_{atoms}(\vec{R}_1, \vec{R}_2, \vec{R}_3 \dots) = \sum_{n=1}^M \frac{-\hbar^2 \nabla_n^2}{2M_n} + \frac{1}{2} \sum_{n,m=1; n \neq m}^M \frac{Z_n Z_m e^2}{|\vec{R}_n - \vec{R}_m|}$$

(4)

In this case the final solution for electron will be given by the wavefunction and energies being a superpositions of wavefunctions and energies obtained from Eq.(3) and Eq. (4).

$$\left| \begin{array}{l} \tilde{\Psi}(\vec{r}_1, \vec{r}_2, \dots, \vec{r}_m; \vec{R}_1, \vec{R}_2, \dots, \vec{R}_n) = \Psi_e(\vec{r}_1, \vec{r}_2, \dots, \vec{r}_m) \cdot \Theta(\vec{R}_1, \vec{R}_2, \dots, \vec{R}_n) \\ E(\vec{k}, \vec{q}) = E_e(\vec{k}) + E_{phn}(\vec{q}) \end{array} \right.$$

(5)

(c) Single electron approximation

Unfortunately, even after such a simplification solving Eq.(3) is still not an easy task thus, further approximations are necessary. One of these approximations is to put electrons only in some effective potential ($U(\mathbf{r} + \mathbf{R})$) and include interactions of one electron with the other electrons by adding some additional term ($\Omega(\mathbf{r})$) (Eq.6).

$$\hat{H}_e(\vec{r}_1, \vec{r}_2, \vec{r}_3 \dots) = \sum_{i=1}^M \frac{-\hbar^2 \nabla_i^2}{2m_i} + \sum_{n=1}^N \sum_{i=1}^M \frac{Z_n e^2}{|\vec{R}_n - \vec{r}_i|} + \sum_{j=1; j \neq i}^N \frac{e^2}{|\vec{r}_i - \vec{r}_j|} = \sum_{i=1}^M \frac{-\hbar^2 \nabla_i^2}{2m_i} + \sum_{j=1}^N U_j(\vec{r}_i + \vec{R}) + \sum_{j=1}^l$$

$$\hat{H}_{ei} = -\frac{\hbar^2}{2m} \nabla_i^2 + \Omega_i(\vec{r}_i) + U_i(\vec{r}_i)$$



ROZWÓJ POTENCJAŁU I OFERTY DYDAKTYCZNEJ POLITECHNIKI WROCŁAWSKIEJ

(6)

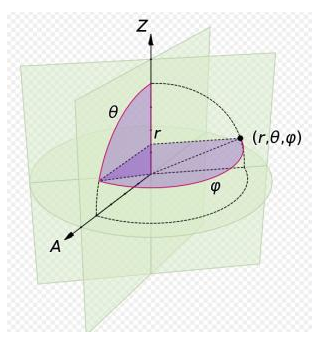
However, in the simplest form of Hamiltonian describing electron in the matter we can assume that the last term in Eq. (6) is not significant one electron represents any electron in the system. At these assumptions we will get then the most common form of Hamiltonian defined by Eq.(7)

$$\hat{H}_{ei} = -\frac{\hbar^2}{2m} \nabla_i^2 + U_i(\vec{r}_i)$$

(7)

The simplest case of solving Eq. (7) is when the potential in which the electron is placed is equal to zero. Defined in this way problem will give the energy and wave functions describing free particle. However, if we will confine the electron in some finite space, for example introducing the infinite potential as a barrier for the particle we will obtain theoretical model estimating the energy levels of electron confined in a low dimensional structure. In this case we can place our particle in the cube or in the sphere surrounded by the infinite potential (see **Fig. 2.3**).

For the spherical potential the Hamiltonian can be defined as follow:



$$-\frac{\hbar^2}{2m} \left[\frac{1}{r^2} \frac{\partial}{\partial r} \left(r^2 \frac{\partial}{\partial r} \right) + \frac{1}{r^2 \sin \theta} \frac{\partial}{\partial \theta} \left(\sin \theta \frac{\partial}{\partial \theta} \right) + \frac{1}{r^2 \sin^2 \theta} \frac{\partial^2}{\partial \phi^2} \right] u + V(r)$$

$$u(r, \theta, \phi) = R(r)Y(\theta, \phi)$$

Figure 2.3 Particle in infinite spherical potential

where the wavefunction can be separated onto following components



ROZWÓJ POTENCJAŁU I OFERTY DYDAKTYCZNEJ POLITECHNIKI WROCLAWSKIEJ

$$Y_{lm}(\theta, \phi) = \varepsilon \left[\frac{(2l+1)(l-|m|)!}{4\pi(l+|m|)!} \right]^{\frac{1}{2}} P_l^m(\cos\theta) \Phi_m(\phi),$$

$$R_{n,l}(r) = \left(\frac{2}{a^3} \right)^{1/2} Y_{l,m}(\theta, \phi) \frac{j_l(k_{n,l}r/a)}{j_{l+1}(k_{n,l})},$$

For the problem defined in this way the final solution for the energy states can be given by the equation

$$E_n = \frac{n^2 \Phi_{l,m}^2}{2mR^2}. \quad (8)$$

which can be simplified for the case where the quantum number $l = 0$ in which case Eq.(8) can be written as:

$$E_n = \frac{n^2 \pi^2 \hbar^2}{2mR^2}. \quad (9)$$

Equations (8-9) allows us to estimate the optical energy (E_{op}) corresponding to experimentally measured emission or absorption bands related with nanostructures with corresponding size.

To obtain this value, confinement energy should be calculated both for the electron and the hole and substituted to the following equation

$$E_{op} = E_g + E_e(R) + E_h(R) = E_g + \frac{n^2 \Phi_{l,m}^2}{2R^2} \left(\frac{1}{m_e} + \frac{1}{m_h} \right)$$

(10)

where E_g is energy band gap of the corresponding bulk material.



ROZWÓJ POTENCJAŁU I OFERTY DYDAKTYCZNEJ POLITECHNIKI WROCLAWSKIEJ

(d) Columb interactions:

Due to strong localization of carriers in zero dimensional structures, Columb interactions between these two, strongly increases and additional term to Eq.(10) should be added. This bring us to most common form of the equation used for estimation of the optical energy observed experimentally

$$E = E_g + E_e(R) + E_h(R) = E_g + \frac{n^2 \Phi_{l,m}^2}{2R^2} \left(\frac{1}{m_e} + \frac{1}{m_h} \right) - \frac{1}{4\pi\epsilon\epsilon_0} \frac{e^2}{R} \quad (11)$$

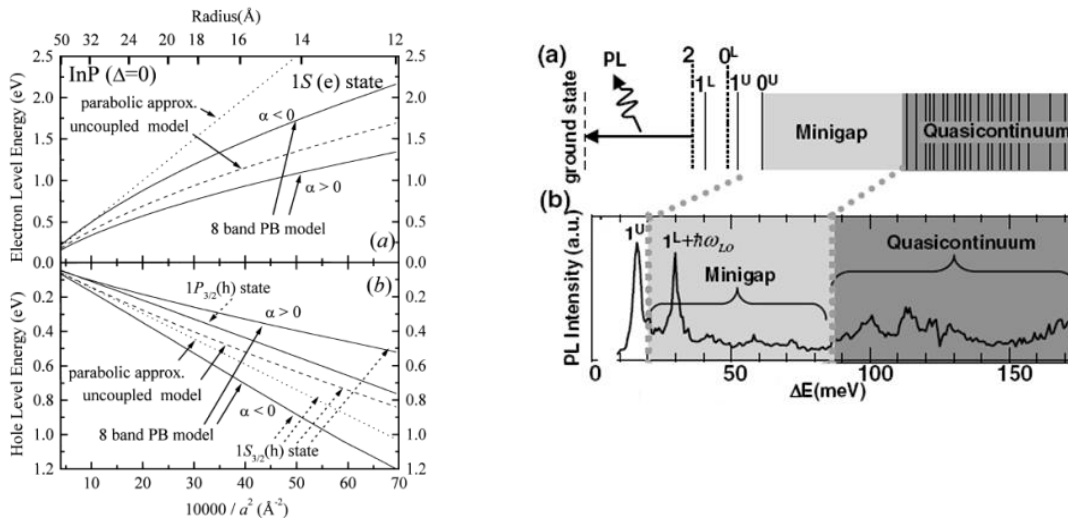


Figure 2.4 (a) Theoretically obtained energy structure for InAs nanocrystals by using different approach [36], (b) experimentally obtained (excitation spectrum) energy structure of a single CdSe nanocrystal [37].

(e) Matrix related effects

In many cases, investigated materials are placed in a dielectric matrix. In this case, we deal with the contrast of the dielectric functions at the quantum dot interface,

³⁶ Al. L. Efros and M. Rosen, The electronic structure of semiconductor nanocrystals, Annu. Rev. Mater. Sci.30, 475 (2000)

³⁷ H.Htoon, Phys.Rev.Lett. 93, 187402 (2004)



ROZWÓJ POTENCJAŁU I OFERTY DYDAKTYCZNEJ POLITECHNIKI WROCLAWSKIEJ

corresponding to formation of dipoles. This influence, very often very strongly, obtained predictions done based on Eq. (11). In this case, Eq.(11) must be modified to Eq. (12) given below:

$$E = E_g + E_e(R) + E_h(R) = E_g + \frac{n^2 \Phi_{l,m}^2}{2R^2} \left(\frac{1}{m_e} + \frac{1}{m_h} \right) - \frac{1}{4\pi\epsilon\epsilon_0} \frac{e^2}{R} + \left\langle \frac{e^2}{R} \sum_n \alpha_n \right\rangle$$

$$\alpha_n = \frac{(\epsilon + 1)(n + 1)}{\epsilon_2(\epsilon n + n + 1)} \quad (12)$$

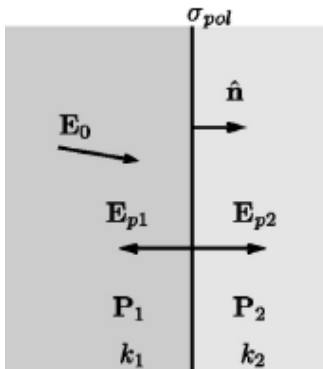


Figure 2.5 Interface between two dielectric media with dielectric constants k_1 and k_2 . \mathbf{E}_0 is an applied electric field that induces polarization \mathbf{P}_1 and \mathbf{P}_2 of the two media. The polarization causes surface charge density σ_{pol} at the surface and electric fields \mathbf{E}_{p1} and \mathbf{E}_{p2} normal to the surface.



ROZWÓJ POTENCJAŁU I OFERTY DYDAKTYCZNEJ POLITECHNIKI WROCLAWSKIEJ

7.5 How to calculate optical functions?

(a) Density of states

When we know the energy structure of our nanomaterial and we are able to predict some their optical properties the next step to better understanding our experimental data is to calculate density of states ($\rho_{nD}(E)$). Starting from the definition: $\rho_{nD}(E) = dN/dE$, and knowing the energy dispersion ($E(\mathbf{k})$), it can be shown that density of states is changing with the material size reduction as follow:

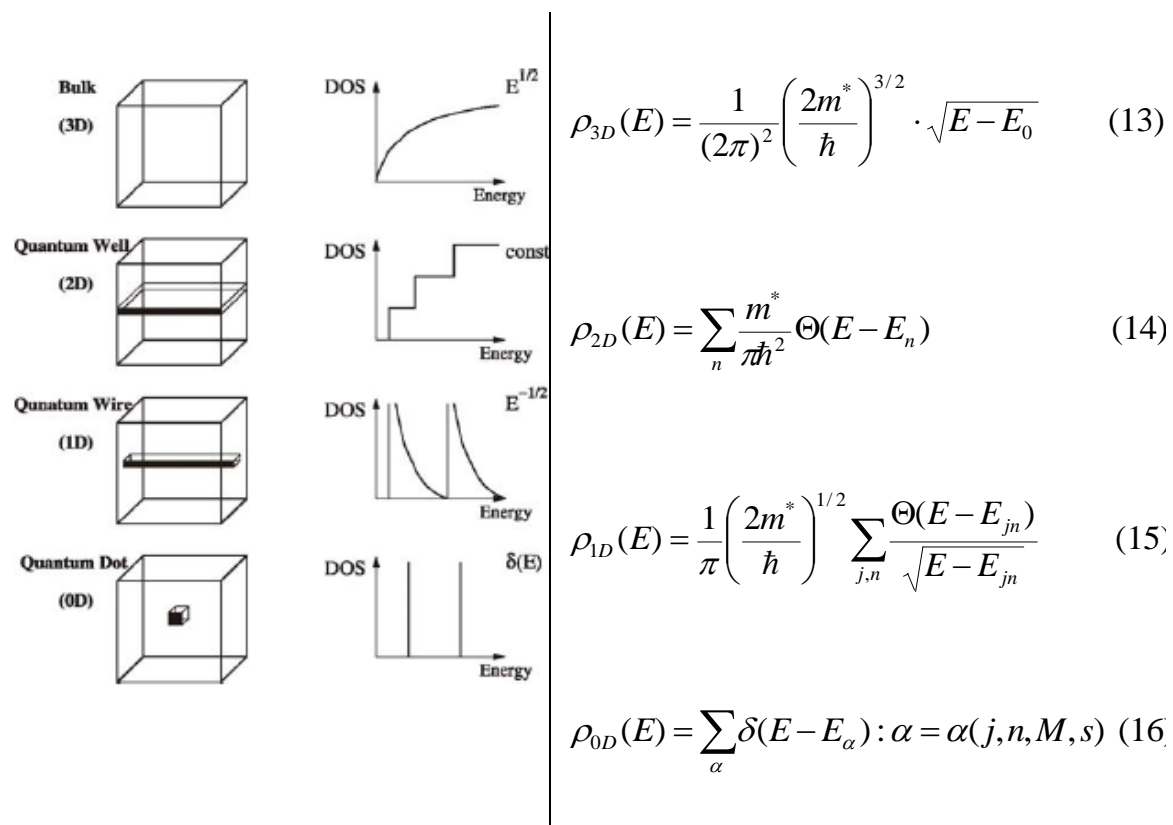


Figure 2.6 Density of states for different dimensionality of nanomaterials

Knowing the energy and density of energy states we can calculate the other important optical functions:



ROZWÓJ POTENCJAŁU I OFERTY DYDAKTYCZNEJ POLITECHNIKI WROCŁAWSKIEJ

(b) Transition rate:

We consider a quantum system described by an Hamiltonian H_{ei0} with known eigenstates $|c^0\rangle$, i.e.

$$H_{ei0}|c^0\rangle = E_a^0|c^0\rangle$$

Now we raise the question, how a small extra term $H_{per}(t)$ (called perturbation) affects the system. In contrast to H_0 , the perturbation can be time-dependent, but it may also be constant, i.e. $H_{per}(t) = H_{per}$. Examples for perturbations are an additional electric field F with $H_{per} = eFz$, or the presence of an electromagnetic wave with frequency ω , coupling to the electron via $H_{per}(t) \propto \cos(\omega t)$. Thus we have the Hamiltonian:

$$H_{ei}(t) = H_{ei0} + H_{per}(t)$$

In contrast to the stationary perturbation theory, where approximations for the eigenstates of

the perturbed Hamiltonian are evaluated, we consider here the time dependence $|\Psi(t)\rangle$ of a system, which is prepared in the state $|\Psi(0)\rangle = |a^0\rangle$ at $t = 0$. Of particular interest is the probability $P_b(t)$ to find the system in another eigenstate $|b^0\rangle$ of H_0 at a later time t , which can be evaluated via

$$P_j(t) = \left| \langle b^0 | \Psi(t) \rangle \right|^2 \quad |\Psi(t=0)\rangle = |a^0\rangle$$

Without the perturbation (i.e. $H_{per} = 0$), the eigenstate $|a^0\rangle$ provides the trivial time



ROZWÓJ POTENCJAŁU I OFERTY DYDAKTYCZNEJ POLITECHNIKI WROCŁAWSKIEJ

dependence $|\Psi(t)\rangle = \exp[-iE_a^0 t/\hbar] \cdot |a^0\rangle$. Thus $P_b(t) = 0$ for $b \neq a$ and $P_a(t) = 1$ and the system stays in state $|a^0\rangle$ forever. However, for a finite perturbation $H_{\text{per}}(t)$, the state $|a^0\rangle$ is no longer an eigenstate of the full Hamiltonian and the time dependent solution of the Schrodinger equation provides admixtures to the different states $|b^0\rangle$. The central result is that for weak perturbations and long times, the transition probability $P_b(t)$ raises linearly in time as $P_b(t) = \Gamma_{a \rightarrow b} \times t$ for $b \neq a$. For a time-independent perturbation potential H_{per} we can calculate transition rate from level i to level j (the **Fermi's golden rule**) as:

$$W_{ij} = \frac{P_{ij}(t)}{T} = \frac{2\pi|M_{ij}|^2}{\hbar} \delta(E_i - E_j) = \frac{2\pi|M_{ij}|^2}{\hbar} \rho_{nD}(E_i = E_j) \quad (2)$$

where M_{ij} is matrix element calculated as $\langle \Psi_i | H_{\text{per}} | \Psi_j \rangle$. Thus transitions are only possible if the initial and final state have the same energy. For a periodic perturbation potential the equation above must be rewritten as:

$$W_{ij} = \frac{2\pi|M_{ij}|^2}{\hbar} \delta(E_i - E_j - \hbar\omega) + \frac{2\pi|M_{ij}^*|^2}{\hbar} \delta(E_i - E_j + \hbar\omega) \quad (21)$$

In this case transitions are only possible if the energy of the final state is $\hbar\omega$ higher/lower than the energy of the initial state. This corresponds to the absorption/emission of the energy

quantum $\hbar\omega$ from/to the oscillating field, respectively. Note that the delta-function appearing in the Fermi's golden rule requires an integral over one of the arguments to be of any meaning. **Thus, the Fermi's golden rule is only applicable if there is either a continuum of final states or a continuum of frequencies ω to integrate over.** Otherwise no linear time dependence $P_b(t) = W_{ii} \cdot t$ is recovered. E.g., for the case of two-level system in a strong monochromatic laser field one observes an oscillatory behavior $P_b(t) \propto \sin^2(-\Omega_R t/2)$, called Rabi oscillation (which is not further discussed here).



ROZWÓJ POTENCJAŁU I OFERTY DYDAKTYCZNEJ POLITECHNIKI WROCLAWSKIEJ

In the simplest case, to get perturbation hamiltonian for light-matter interaction, electron is treated as a quantum object and electromagnetic wave is considered to have classical form we are able to transform hamiltonian defined by Eq.(7) to following form:

$$H_{ei}(\vec{r}) = \frac{1}{2m} \left[\vec{p} + \frac{e}{c} \vec{A}(\vec{r}, t) \right]^2 + U_i(\vec{r}_i)$$

after some simplifications we are able to transform above equation to

$$H_{ei0}(\vec{r}) + \frac{e\vec{A}(\vec{r}, t) \cdot \vec{p}}{mc} = H_{ei0}(\vec{r}) + \frac{e\vec{A}_0(\vec{r}, t)}{mc} e^{i\vec{k}\vec{r}} |\vec{a} \cdot \vec{p}| = H_{ei0}(\vec{r}) + H_{per}(t)$$

finally giving perturbation hamiltonian due to interaction with the electromagnetic wave

(c) The radiative/nonradiative decay time

Using above theoretical approach we can also define the radiative and non-radiative decay rates which are defined as follow:

$$\frac{1}{\tau_R} = W_{ji} = \Gamma_R \quad \left[\frac{1}{s} \right] \quad (2)$$

(d) The carrier concentration

In the next step we can define carrier concentration as:

$$n(E) = \int_{E_c}^{\infty} \rho_{nD}(E) \cdot [f(E_i) - f(E_j)] dE \quad \left[\frac{1}{\text{cm}^n} \right] \quad (3)$$

$$j(E) = n(E) \cdot \mu_e E$$

(e) The absorption coefficient



ROZWÓJ POTENCJAŁU I OFERTY DYDAKTYCZNEJ POLITECHNIKI WROCLAWSKIEJ

The calculation of an absorption coefficient $\alpha(\omega)$ is carried out in several steps. First, the imaginary part of the dielectric function ϵ_2 as a function of photon frequency ω is calculated from interband transitions:

$$\epsilon_2(\omega) = \frac{4\pi^2 e^2}{3m^2 \omega^2} \sum_{ijk} |M_{ij}(\mathbf{k})|^2 \cdot \delta[E_i(\mathbf{k}) - E_j(\mathbf{k}) - \hbar\omega] \quad (26)$$

where e is the electron charge, m is its mass, i and j are the band indices, $E_i(\mathbf{k})$ and $E_j(\mathbf{k})$ are the corresponding band energies, and $M_{ij}(\mathbf{k})$ are the interband momentum matrix elements. Then the real part of dielectric function $\epsilon_1(\omega)$ is calculated from $\epsilon_2(\omega)$ using the Kramer–Kronig relation. $\epsilon_1(\omega)$ and $\epsilon_2(\omega)$ are then related to the index of refraction n_1 and extinction coefficient n_2 by $\epsilon_1(\omega) = n_1(\omega)^2 - n_2(\omega)^2$ and $\epsilon_2(\omega) = 2n_1(\omega)n_2(\omega)$ from which $n_2(\omega)$ can be obtained. Then $\alpha(\omega)$ is simple $2\omega n_2(\omega)/c$, where c is the speed of light. Thus, the final expression for absorption coefficient is the following:

$$\alpha(\omega) = \frac{4\omega \pi^2 e^2}{3n_1(\omega) \cdot c \cdot m^2 \omega^2} \sum_{ijk} |M_{ij}(\mathbf{k})|^2 \cdot \delta[E_i(\mathbf{k}) - E_j(\mathbf{k}) - \hbar\omega] \quad (27)$$

The expression above, describes the internal properties of the material. During the absorption measurement the other effects should be taken into account what give us expression defined below:

$$\alpha_{EXP}(\hbar\omega, t \approx 0) \approx D(\hbar\omega) \cdot V \cdot (\hbar\omega) \cdot \alpha(\omega) \cdot [f(E_i) - f(E_j)] \left[\frac{1}{\text{cm}} \right] \quad ($$

where $D(\hbar\omega)$ describes the density of electromagnetic wave and V excited volume of the material.

(f) The optical gain

The optical gain and loss are of fundamental importance to the study of lasers, since
Projekt współfinansowany ze środków Unii Europejskiej w ramach
Europejskiego Funduszu Społecznego



ROZWÓJ POTENCJAŁU I OFERTY DYDAKTYCZNEJ POLITECHNIKI WROCŁAWSKIEJ

the gain determines many device performance characteristics.

If the number of downward transitions (stimulated emission) per seconds exceeds the number of upward transitions (absorption), there will be a net generation of photons, and **optical gain** (G) [³⁸] can be achieved.

$$G_{ij}(E) = \frac{1}{\Phi} \frac{d\Phi}{dz} = \frac{1}{\hbar\omega} \frac{\pi e^2 \hbar \bar{n}_g}{\varepsilon_0 c m_0^2 \bar{n}^2} |M_{ij}|^2 \cdot \rho_{ij}^d(E) \cdot [f(E_i) - f(E_j)]$$

(22)

Optical gain in the material is attained when we inject a carrier density beyond N_{th} such that the quasi-Fermi levels are separated by energy greater than the band gap.

One should be noted however, that in the literature we often deal with other gain definitions. For example, the **modal gain** (G_M), which is the material gain adjusted to take into account the poor overlap that always exists between the optical mode and the electron envelope function ($G_M = \text{gain} \times \text{confinement factor}$). The other can be the **differential gain** (G_D), which is the rate at which gain increases as we inject more carriers, dG/dN . In **Fig. 2.7** it is shown how the gain is changing when the dimension of the matter is changing.

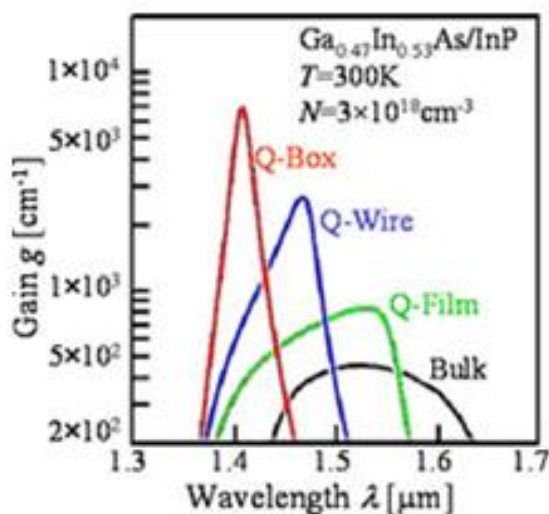


Figure 2.7 Optical gain calculated for GaIn material with different dimensions.

³⁸ Z.M.Li, K.M.Dzurko, A.Delage, S.P.McAlister, IEEE J. Quantum Electronics 28, 792 (1992).



ROZWÓJ POTENCJAŁU I OFERTY DYDAKTYCZNEJ POLITECHNIKI WROCLAWSKIEJ

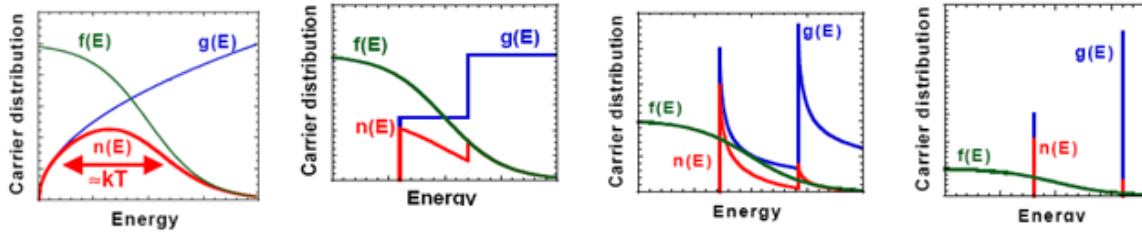


Figure 2.7 Density of states and carrier concentration after modifications by function describing thermal distribution of carriers for structures characterized by different dimensionality.

Very accurately measured values of transparency energy and loss can be yielded by using an indirect technique based on the relationship between spontaneous emission and gain. The optical gain spectra are related to the spontaneous emission spectra from the detailed balance between absorption and emission of photons [39]. That is, the modal gain (G_M) from spontaneous emission is given by:

$$G_M(E) = \frac{h^3 c^2}{8\pi n_f^2 E^2} \left(1 - \exp \frac{E - \Delta F}{kT} \right) R_{sp}(E) \quad (23)$$

in which $R_{sp}(E)$ is the spontaneous emission rate, T is the temperature, E is the optical confinement factor, and ΔF is the transparency energy, which is given by the energy separation of the quasi-Fermi levels of the electrons and holes. In practice, the spontaneous emission power $P_{sp}(\lambda)$ is measured within small resolution intervals $d\lambda$ determined by the spectrometer over the entire spectrum,

$$P_{sp}(\lambda) = K \frac{hc}{\lambda} R_{sp}(\lambda) d\lambda \cdot V \quad (24)$$

so the relation in Eq. 23 must be modified. First, the energy is expressed in terms of the wavelength, then the spontaneous emission rate is substituted by the power through Eq. 24. The result is:

$$G_M(E) = \frac{\lambda^5}{K 8\pi n_f^2 hc^2 V d\lambda} \left(1 - \exp \frac{hc}{\lambda} \frac{\lambda - \Delta F}{kT} \right) P_{sp}(\lambda) \quad (25)$$

³⁹ G. Lasher and F. Stern, Phys. Rev. A 133, 553 (1964).



ROZWÓJ POTENCJAŁU I OFERTY DYDAKTYCZNEJ POLITECHNIKI WROCŁAWSKIEJ

Next the material gain is written in terms of the measured the **net modal gain** (g_M) as:

$$g_M(E) = \Gamma G_M(E) - \alpha_i$$

where Γ is the optical confinement factor and α_i is the intrinsic loss for the optical waveguide mode.

On the theoretical side, conventional optical gain calculations are usually based on the density-matrix theory with a phenomenological damping term which gives the Lorentzian line shape function [⁴⁰].

2.3 Excitons

Excitons can be formed by coulombic interactions between electrical charges or by direct photoexcitation. The exciton luminescence that can follow this charge association underlies organic light emitting diode technologies. Conversely, excitons that are formed readily by photoexcitation can dissociate into free carriers (unbound electrons and holes) and thus play a central role in photovoltaic and solar cell devices. Excitons that remain bound and emit light can be used as laser media. Photoexcitation creates an electron in the conduction band, leaving a ‘hole’ in the valence band. If the interaction between the electron and hole is assumed to be negligible—justified when each wavefunction is spread over an expanse of atoms—then the pair are free carriers. On the other hand, an attractive coulomb interaction between the electron and hole ‘quasi-particles’ binds them into an exciton. A distinguishing feature of excitons is that the spatial extent of an electronic excited state is increased through coherent sharing of the excitation among subunits of the material. That characteristic is determined by electronic coupling among the repeat units that make up the material [^{41, 42, 43, 44, 45}]. By using this criteria we can resolve the localized excitons (the **Frenkel excitons**) and

⁴⁰M. Yamada and Y. Suematsu, J. Appl. Phys. **52**, 2653 (1981).

⁴¹Elliott, R. J. in Polarons and Excitons (eds Kuper, C. G. & Whitfield, G. D.) 269 (Plenum, New York, 1962).

⁴²Knox, R. S. in Collective Excitations in Solids (ed. Bartolo, B. D.) 183 (Plenum, New York, 1981).

⁴³McRae, E. G. & Kasha, M. in Physical Processes in Radiation Biology, 23 (Academic, New York, 1964).

⁴⁴Slater, J. C. & Shockley, W. Optical absorption by the alkali halides. Phys. Rev. **50**, 705 (1936).

⁴⁵Excitons in nanoscale systems, G. D. Scholes, G. Rumbles, Nature Materials **5**, 683 (2006).



ROZWÓJ POTENCJAŁU I OFERTY DYDAKTYCZNEJ POLITECHNIKI WROCLAWSKIEJ

delocalized excitons (the **Wannier excitons**) (**Fig.2.8**). Somewhere between these limited cases are charge-transfer excitons. In bulk material, but also in some nanomaterials, very often we deal with a **free excitons**. These excitons characterize by dispersion of their energy in k-space, what schematically has been shown also in **Fig.2.8** and their can travel through the material over long distances until they became localized or dissociated.

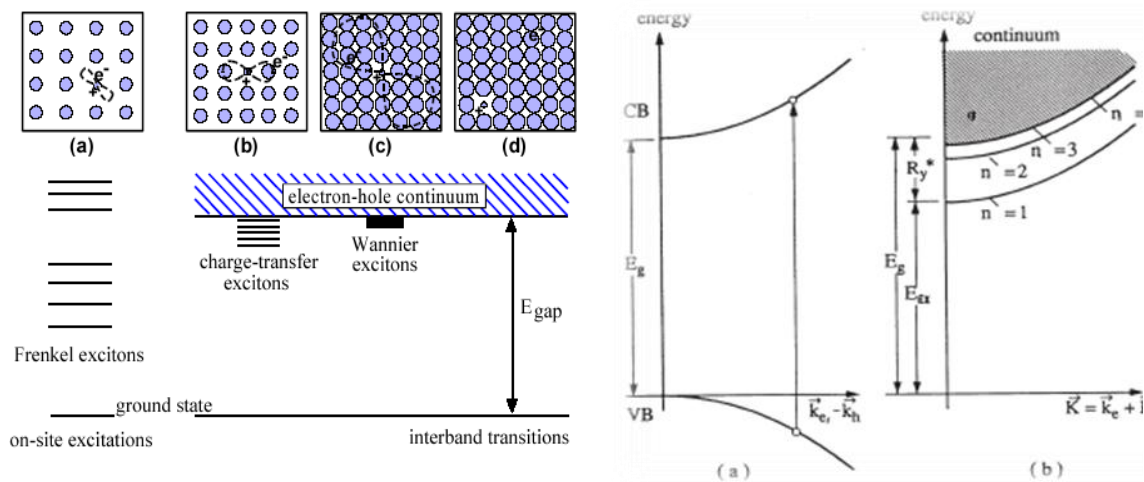


Figure 2.8 Different excitons together with energy dispersion of free excitons in k-space.

Excitons can be characterized by few important parameters namely, the effective excitonic mass (m_{exc}^*), the excitonic Bohr radii (a_{Bexc}) and the exciton binding energy (δE_{EXC}) defined below:

$$m_{exc}^* = \frac{m_e^* m_h^*}{m_e^* + m_h^*} \quad (1)$$

$$a_{exc} = \frac{4\pi\hbar^2 \epsilon \epsilon_0 m_0}{m_{exc}^* m_0 e^2} \quad (2)$$

$$\delta E_{exc} = -\frac{m_{exc}^* e^4}{n^2 2\hbar^2 (4\pi\epsilon \epsilon_0)^2} \quad (3)$$

The new aspect of excitons that is prevalent in, or even defines, nanoscience is that the physical size and shape of the material strongly influences the nature and dynamics of the electronic excitation. Therefore, a deciding property of excitons in nanoscale



ROZWÓJ POTENCJAŁU I OFERTY DYDAKTYCZNEJ POLITECHNIKI WROCLAWSKIEJ

systems is that the exciton size is dictated not by the electron–hole Coulomb interaction, but by the physical dimensions of the material or the arrangement of distinct building blocks. That it is the dominant at interests the chemist because excitons can be engineered in a material according to structure. It is of interest to physicists because the spatial confinement of the exciton accentuates many of its interesting physical properties, exposing them for examination.

Size-tunable spectroscopic properties have been of great interest for over half a century, although recent interest has centered on QDs. The Bohr radius of a semiconductor exciton provides a reference as to the exciton size in the bulk. Size-tuning of properties in QDs is attributed to confinement of the exciton in a nanocrystal significantly smaller than the bulk exciton. The size dependence of exciton transition energies for a range of organic [^{46, 47}] and QD [^{48, 49, 50, 51}] materials is plotted in **Fig. 2.9(a)**.

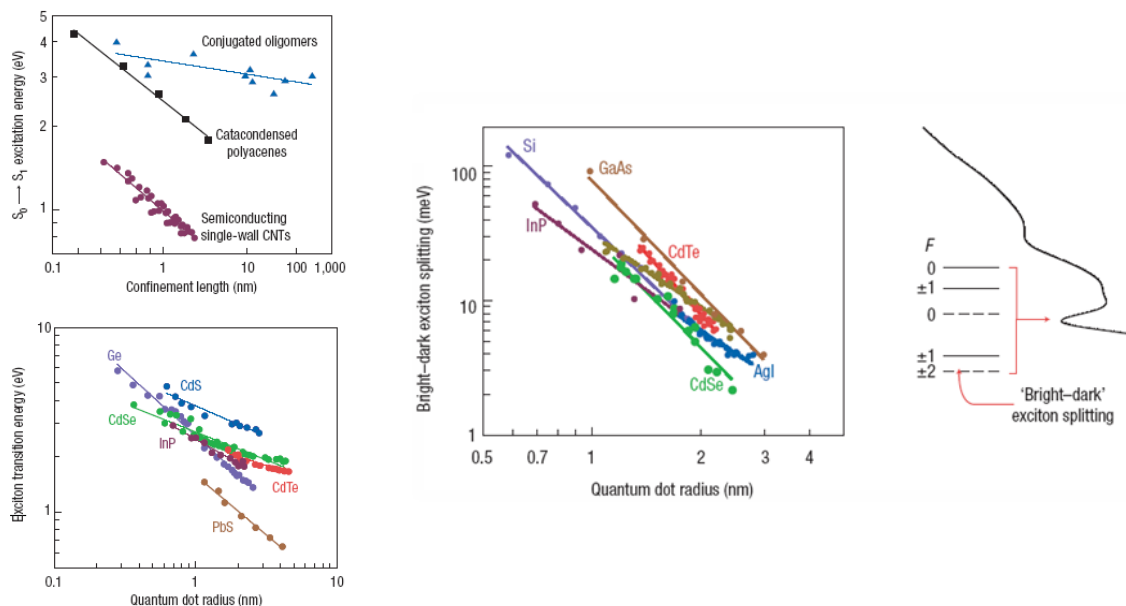


Figure 2.9 Data presenting reported bright–dark exciton splitting for a selection of quantum dots (tight-binding calculations), InP (fluorescence line narrowing, measured at 10 K), GaAs (pseudopotential calculations of rectangular nanocrystals), CdTe (fluorescence line narrowing, 10 K, of colloids in glass), .

⁴⁶ Bachilo, S. M. et al. Structure-assigned optical spectra of single-walled carbon nanotubes. *Science* **298**, 2361 (2002).

⁴⁷ Kleven, H. B. & Platt, J. R. Spectral resemblances of cata-condensed hydrocarbons. *J. Chem. Phys.* **17**, 470 (1949).

⁴⁸ Hines, M. A. & Scholes, G. D. Colloidal PbS nanocrystals with size-tunable near-infrared emission: observation of post-synthesis self-narrowing of the particle size distribution. *Adv. Mater.* **15**, 1844 (2003).

⁴⁹ Micic, O. I. et al. Size-dependent spectroscopy of InP quantum dots. *J. Phys. Chem. B* **101**, 4904 (1997).

⁵⁰ Yu, W. W., Qu, L. H., Guo, W. Z. & Peng, X. G. Experimental determination of the extinction coefficient of CdTe, CdSe, and CdS nanocrystals. *Chem. Mater.* **15**, 2854 (2003).

⁵¹ Neshet, G., Kronik, L. & Chelikowsky, J. R. Ab initio absorption spectra of Ge nanocrystals. *Phys. Rev. B* **71**, 35344 (2005).



ROZWÓJ POTENCJAŁU I OFERTY DYDAKTYCZNEJ POLITECHNIKI WROCŁAWSKIEJ

(fluorescence line narrowing, 2 K), InAs (fluorescence line narrowing, 10 K), and CdSe (fluorescence line narrowing, 10 K). These data are a combination of experimental results and calculations.

Size dependence of the exciton transition energies. Log–log plots of excitation energy versus confinement length (dimension) of the ground and first excited states. For CNTs, the confinement dimension is taken to be the tube diameter. For the other organic materials it is the approximate conjugation length from end to end. (a) Organic materials. Squares show data for the series of aromatic molecules, naphthalene, anthracene, naphthacene, pentacene and hexacene. Triangles indicate data for some oligomers that serve as models for conjugated polymers: methyl-substituted ladder-type poly(p-phenylene) (MeLPPP), poly(2,7-(9,9-bis(2-ethylhexyl)fluorene)) (PF2/6), oligofluorenes and oligothiophenes. Data were typically recorded for samples at 80 K. The filled circles show CNT data recorded at ambient temperature, (b), Size-tuning of excitation energies for various QD materials: Ge, calculated using *ab initio* density functional theory using Δ SCF, CdSe, CdS and CdTe, measured at 250 K, PbS, measured at 293 K, and InP measured at 10 K. [⁵²]

Measurement of the exciton energy does not directly reveal information that allows us to learn generally about excitons by comparing different materials. For example, size-tunable optical properties derive primarily from the bandgap, not the exciton. The bandgap is the energy difference between occupied and unoccupied orbitals. That provides only a starting point for establishing the excitation energy because, first, the electronic excited-state wavefunction is not accurately written as a one-electron excitation between these orbitals.

The **exchange interaction** plays a central role in determining the ordering of electronic spin states in any material. An exchange interaction raises the energy of each singlet state and lowers the energy of the three corresponding triplet spin eigen-states. Such a distinction between singlet and multiplet states is a traditional backbone to atomic and molecular spectroscopy. Similarly, the exchange interaction mixes the single-excitation configurations in a QD, evident as a splitting between the bright and dark exciton states at the band edge [^{53, 54}] (**Fig. 2.9(b)**). As an exciton is spatially compressed by confinement, exchange interactions are increased, as evidenced by larger singlet–triplet splitting. The distinct manifold of states provides an opportunity in spectroscopy to learn about the excited states and electronic structure of nanoscale systems. The challenge, however, for materials such as QDs is that the spectrum is obscured by inhomogeneous line broadening, so specialized techniques are required to probe these states. The basic size-scaling of the dark state/bright state splitting for the range of QDs follows a similar trend to that seen for the organic materials, but the

⁵² *Excitons in nanoscale systems*, G. D. Scholes, G. Rumbles, *Nature Materials* 5, 683 (2006).

⁵³ Efros, A. L. *et al.* Band-edge exciton in quantum dots of semiconductors with a degenerate valence band: dark and bright exciton states. *Phys. Rev. B* 54, 4843–4856 (1996).

⁵⁴ Leung, K., Pokrant, S. & Whaley, K. B. Exciton fine structure in CdSe nanoclusters. *Phys. Rev. B* 57, 12291–12301 (1998).



KAPITAŁ LUDZKI
NARODOWA STRATEGIA SPÓJNOŚCI



Politechnika Wrocławska

UNIA EUROPEJSKA
EUROPEJSKI
FUNDUSZ SPOŁECZNY



ROZWÓJ POTENCJAŁU I OFERTY DYDAKTYCZNEJ POLITECHNIKI WROCŁAWSKIEJ

magnitudes of the splitting are substantially smaller. The main reason for that is that the high dielectric constant of QDs attenuates the long-range electron–electron repulsion compared with these organic materials.

ROZWÓJ POTENCJAŁU I OFERTY DYDAKTYCZNEJ POLITECHNIKI WROCLAWSKIEJ

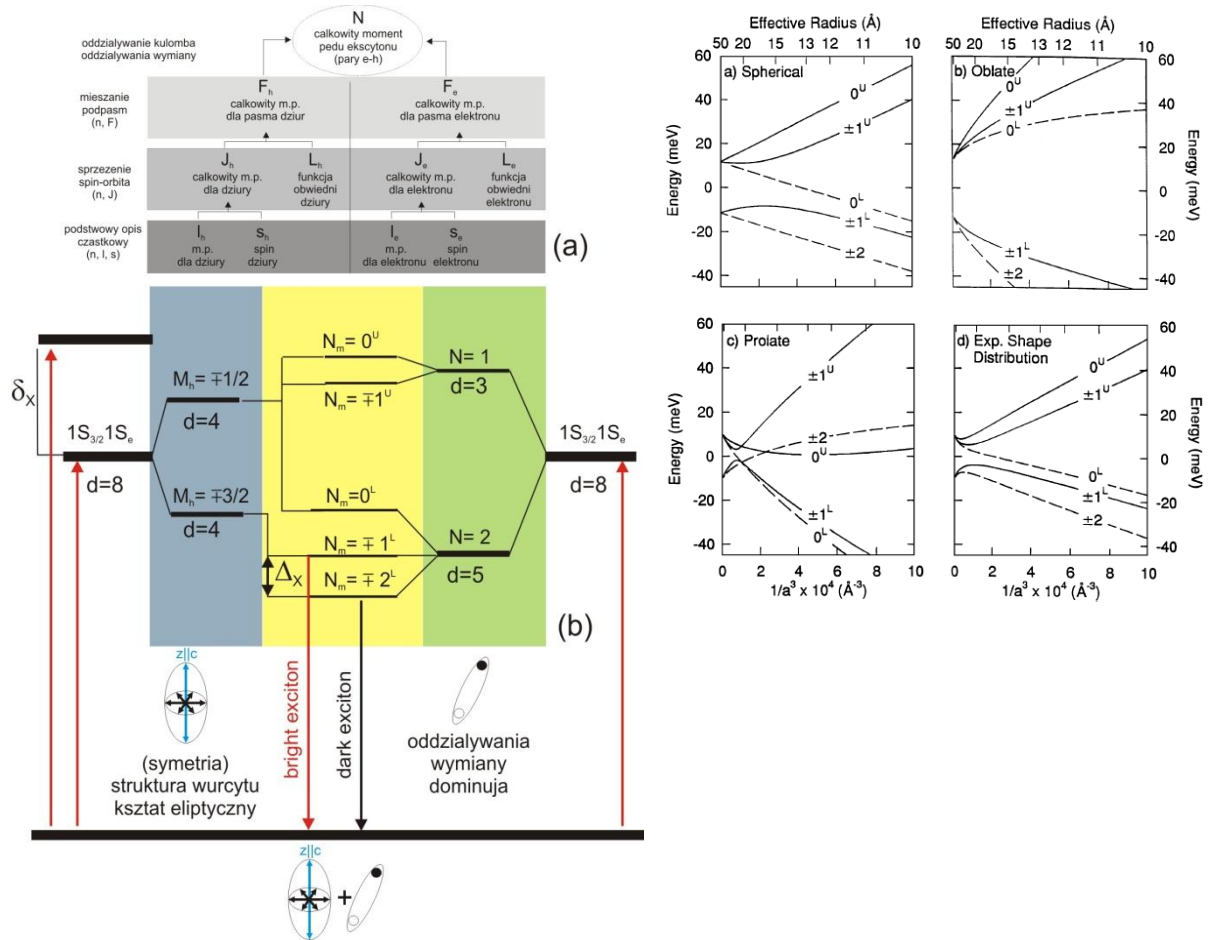


Figure 2.10 Schematic representation of excitonic states splitting due to exchange interactions and symmetry reduction. Schematic representation of singlet/triplet states of excitons. Note that at finite temperature, singlets close to triplets are also populated and life time should be averaged over all excited states with proper thermal population statistics [55]. Excitonic states splitting depending on nanocrystals size and shape of heksagonal CdSe nanocrystals, with different ellipsoid parameter m : (a) spherical nanocrystals ($m=0$); (b) spłaszczone ($m=-0.28$); (c) elongated ($m=0.28$); (d) NCs with sizes estimated from SAXS and TEM. Lines (dashed) describe transitions optically active (not active) [56].

It is striking that the exchange interactions over the range of materials plotted in **Fig.2.9** are similar in magnitude for each QD size. Confinement of the QD exciton is in three dimensions, therefore the exchange is predicted to scale as R^{-3} , where R is the QD radius. That is the case for some of the data plotted here, which include a range of experimental observations and good quality calculations. A scaling of $\sim R^{-3}$ is found for bright–dark splitting of CdSe, CdTe and GaAs QDs. Silicon QDs are calculated to show

⁵⁵ Phys.Rev.Lett.95 247402 (2005).

⁵⁶ Al. L. Efros and M. Rosen, The electronic structure of semiconductor nanocrystals, Annu. Rev. Mater. Sci.30, 475 (2000).



ROZWÓJ POTENCJAŁU I OFERTY DYDAKTYCZNEJ POLITECHNIKI WROCŁAWSKIEJ

R^{-2} , whereas the splitting for AgI, InAs and InP scales as R^{-2} , or slightly more weakly. Future work may expose more details of the spectroscopic signatures of the exciton from beneath the inhomogeneously broadened absorption band. An example was reported recently where the dynamics associated with flipping between two QD fine-structure states was measured [⁵⁷].

The exciton binding energy in a quantum confined system can be taken to be the energy difference between the exciton transition energy (optical gap) and the electronic bandgap. The electronic bandgap can be written as the difference between the ionization potential and electron affinity, assuming no structural relaxation of the material or its surroundings [⁵⁸]. This Coulomb energy, thought of as electron–hole attraction, assumes marked significance in nanoscale materials. In a bulk semiconductor material with high dielectric constant, the exciton binding energy is typically small: 27 meV for CdS, 15 meV for CdSe, 5.1 meV for InP and 4.9 meV for GaAs. Excitons are therefore not a distinctive feature in the spectroscopy of such materials at room temperature, making them ideal for photovoltaic applications. On the other hand, in molecular materials, the electron - hole Coulomb interaction is substantial - a few electronvolts. In nanoscale materials we find a middle ground where exciton binding energies are significant in magnitude - that is, excitons are important - and they are size tunable. For example, exciton self-trapping in organic materials, such as conjugated polymers, leads to a strongly bound (hundreds of millielectronvolts) exciton. Hence the need to dope conjugated polymer solar cells with electron acceptors, such as other polymers [⁵⁹], fullerenes [⁶⁰] or quantum dots [⁶¹], to promote charge separation. In a strongly delocalized exciton, free carriers could be photogenerated directly upon excitation of conjugated polymers. The extent to which that occurs is still a matter for debate. The exciton binding energy in QDs of radii $R \approx 1\text{--}2$ nm is in the range 200–50 meV, scaling approximately as $1/R$, according to the size dependence of the electron–hole Coulomb

⁵⁷ Huxter, V. M., Kovalevskij, V. & Scholes, G. D. Dynamics within the exciton fine structure of colloidal CdSe quantum dots. *J. Phys. Chem. B* 109, 20060–20063 (2005).

⁵⁸ Yaron, D., Moore, E. E., Shuai, Z. & Brédas, J. L. Comparison of density matrix renormalization group calculations with electron–hole models of exciton binding in conjugated polymers. *J. Chem. Phys.* 108, 7451 (1998).

⁵⁹ Halls, J. J. M. et al. Efficient photodiodes from interpenetrating polymer networks. *Nature* 376, 498 (1995)

⁶⁰ Sariciftci, N. S., Smilowitz, L., Heeger, A. J. & Wudl, F. Photoinduced electron transfer from a conducting polymer to buckminsterfullerene. *Science* 258, 1474 (1992).

⁶¹ Huynh, W. U., Dittmer, J. J. & Alivisatos, A. P. Hybrid nanorod–polymer solar cells. *Science* 295, 2425 (2002).



ROZWÓJ POTENCJAŁU I OFERTY DYDAKTYCZNEJ POLITECHNIKI WROCŁAWSKIEJ

interaction [62]. A key difference between these inorganic materials and organic materials is dielectric constant. Dielectric constant is central in determining the exciton binding energy because it shields electron–electron repulsions, or equivalently electron–hole interactions. Interestingly, it has been reported that dielectric constant diminishes with size for QDs, further increasing the size effect of the exciton binding energy [63].

The purely ‘electronic’ models for describing excitons are modified by the coupling between the exciton and the bath of nuclear motions. That coupling is manifest in spectroscopy as line broadening, Stokes shift and vibronic structure in absorption and photoluminescence spectra [64, 65]. The aim of this section is to categorize the important elements of line broadening in nanomaterials, highlight their size dependences and provide some specific examples that give an overall picture of the diverse consequences of disorder and exciton–bath coupling. Any model for the eigenstates and energies of excitons contains the energy at each repeat unit (molecule, unit cell, atom), known as the site energy, and information on how those repeat units are coupled. In the most general model, each site can accommodate an excitation, an electron or a hole. Clearly both the composition of the eigenstates and the corresponding energies will be affected by energetic disorder in the site energies or couplings. Such disorder is caused by random fluctuations in the positions of atoms [66]. The timescale of those fluctuations is important in delimiting the effects as static (on the timescale of the measurement) or fluctuating. The former gives rise to inhomogeneous line broadening, the latter to homogeneous line broadening [67]. Static disorder is seen as a temperature-independent gaussian line shape in absorption or photoluminescence, whereas homogeneous line broadening can play an important role in trapping an exciton on a fast timescale [68] (femtoseconds to picoseconds). The interaction between excitons and nuclear motions can introduce time-dependent confinement effects, known as exciton self-trapping, where the exciton becomes trapped in a lattice deformation [69]. Those nuclear motions

⁶² Fanceschetti, A. & Zunger, A. Direct pseudopotential calculation of exciton coulomb and exchange energies in semiconductor quantum dots. *Phys. Rev. Lett.* 78, 915 (1997).

⁶³ Fanceschetti, A. & Zunger, A. Direct pseudopotential calculation of exciton coulomb and exchange energies in semiconductor quantum dots. *Phys. Rev. Lett.* 78, 915 (1997).

⁶⁴ Lax, M. The Franck–Condon principle and its application to crystals. *J. Chem. Phys.* 20, 1752 (1952).

⁶⁵ Sumi, H. Exciton–lattice interaction and the line shape of exciton absorption in molecular crystals. *J. Chem. Phys.* 67, 2943 (1977).

⁶⁶ Sumi, H. Exciton–lattice interaction and the line shape of exciton absorption in molecular crystals. *J. Chem. Phys.* 67, 2943 (1977).

⁶⁷ Fleming, G. R., Passino, S. A. & Nagasawa, Y. The interaction of solutes with their environments. *Phil. Trans. R. Soc. London A* 356, 389 (1998).

⁶⁸ Nakajima, S. The Physics of Elementary Excitations (Springer, New York, 1980).

⁶⁹ Nakajima, S. The Physics of Elementary Excitations (Springer, New York, 1980).



ROZWÓJ POTENCJAŁU I OFERTY DYDAKTYCZNEJ POLITECHNIKI WROCŁAWSKIEJ

are contributed by intramolecular vibrations and the environment. Exciton self-trapping occurs through a local collective structural change, connected to random nuclear fluctuations by the fluctuation-dissipation theorem. The resultant exciton is also called a polaron-exciton. Hence the size and electronic make-up of an organic exciton can change markedly on short timescales after photoexcitation (tens of femtoseconds) [70]. That is understood as the tendency of molecules to change their equilibrium geometry in the excited state compared with the ground state, which is observed, together with salvation [71], as spectral diffusion. The associated reorganization energy is equal to half the Stokes shift. A very small change in the equilibrium coordinates of many vibrational modes can inspire surprisingly rapid localization of the exciton. In other words, exciton self-trapping is induced by the amplitude of fluctuations as well as their characteristic timescales. The precise excited state dynamics are dictated by competition between the delocalizing effect of electronic coupling and the localizing influence of electron-phonon coupling. QD excitons couple relatively weakly to nuclear motions and the homogeneous line broadening is consequently narrow compared with organic materials, suggesting possible applications of QDs as single-photon sources and ‘qubits’ for quantum computation. That is perhaps because QDs, and indeed also CNTs, are considerably more rigid and ordered than the flexible structures of organic materials. There are two characteristic types of vibrations in a QD [72]. The higher-frequency mode is that of the longitudinal optical (LO) phonon, which has a frequency that is typically very similar to the frequency known for the corresponding bulk material. For CdSe the LO-phonon mode frequency is 207 cm^{-1} . The radial breathing modes of CNTs [73] are conceptually similar kinds of vibrations. The frequencies of radial breathing modes, however, scale with the CNT diameter d (in nm), according to the empirical relation [74] $\omega = (214.4/d) + 18.7 \text{ cm}^{-1}$. Coupling of the exciton to vibrations with frequencies greater than thermal energies leads to phonon sidebands in frequency-resolved spectroscopies and quantum beats (oscillations) in ultrafast time domain experiments.

⁷⁰ Franco, I. & Tretiak, S. Electron-vibrational dynamics of photoexcited polyfluorenes. *J. Am. Chem. Soc.* 126, 12130 (2004).

⁷¹ Fleming, G. R., Passino, S. A. & Nagasawa, Y. The interaction of solutes with their environments. *Phil. Trans. R. Soc. London A* 356, 389 (1998).

⁷² Takagahara, T. Electron-phonon interactions and excitonic dephasing in semiconductor nanocrystals. *Phys. Rev. Lett.* 71, 3577 (1993).

⁷³ Plentz, F., Ribeiro, H. B., Jorio, A., Strano, M. S. & Pimenta, M. A. Direct experimental evidence of exciton-phonon bound states in carbon nanotubes. *Phys. Rev. Lett.* 95, 247401 (2005).

⁷⁴ Telg, H., Maultzsch, J., Reich, S., Hennrich, F. & Thomsen, C. Chirality distribution and transition energies of carbon nanotubes. *Phys. Rev. Lett.* 93, 177401 (2004).



ROZWÓJ POTENCJAŁU I OFERTY DYDAKTYCZNEJ POLITECHNIKI WROCŁAWSKIEJ

The principal vibrations that contribute to QD line shape are acoustic phonons. In the bulk these are analogous to sound waves travelling through the crystal. Owing to the small size of QDs, the acoustic phonon modes are quantized torsional and spheroidal modes - the motions of an elastic sphere that leave its volume constant. The frequencies of these phonon modes lie in the range 5 to 40 cm^{-1} , depending on the QD size. The exciton - phonon coupling scales as $1/R^2$, where R is the QD radius [75]. Models for phonons in bulk crystals assume the displacements of the modes are small. That makes sense for an infinite-sized crystal, in which coupling between many oscillators limits the amplitude of motion. On the other hand, for nanoscale materials such as QDs, exciton-phonon coupling may be better described by considering aspects of theories developed for molecules.

Translational dynamics of excitons are obviously not important in QDs. However, radiationless relaxation processes from higher excited states in QDs to the lowest exciton state have been widely investigated [76]. The electron and hole levels in small QDs, typical of colloidal QDs, are widely spaced compared with the LO-phonon frequency. It was therefore expected that relaxation of the electron and hole, and hence exciton, would be impeded: the phonon bottleneck effect. In fact, it has been found that the relaxation is very fast in CdSe [77]. For CdSe the valence band consists of more closely spaced levels than the conduction band (see **Fig. 2.4(b)**). Bearing this in mind, the fast exciton relaxation has been explained on the basis of an Auger-like process whereby the highly excited electron interacts with the hole through an electronic (coulombic) interaction that enables the electron to relax to its lowest level by scattering the hole deeper into the valence band [78]. Because the valence band has a high density of states, phonon-mediated relaxation of the hole is possible. However, that rationale does not satisfactorily explain the fast exciton relaxation observed in IV-VI QDs, for which the electron and hole states are thought to be approximately equally spaced. Guyot-Sionnest *et al.* have further suggested that surface ligands may play a role in

⁷⁵ Takagahara, T. Electron-phonon interactions and excitonic dephasing in semiconductor nanocrystals. *Phys. Rev. Lett.* 71, 3577 (1993).

⁷⁶ Burda, C., Chen, X. B., Narayanan, R. & El-Sayed, M. A. Chemistry and properties of nanocrystals of different shapes. *Chem. Rev.* 105, 1025 (2005).

⁷⁷ Klimov, V. I., McBranch, D. W., Leatherdale, C. A. & Bawendi, M. G. Electron and hole relaxation pathways in semiconductor quantum dots. *Phys. Rev. B* 60, 13740-13749 (1999).

⁷⁸ Klimov, V. I., McBranch, D. W., Leatherdale, C. A. & Bawendi, M. G. Electron and hole relaxation pathways in semiconductor quantum dots. *Phys. Rev. B* 60, 13740-13749 (1999).



ROZWÓJ POTENCJAŁU I OFERTY DYDAKTYCZNEJ POLITECHNIKI WROCLAWSKIEJ

assisting exciton relaxation [79]. Whether independent consideration of the electron and hole relaxations is a good approximation may also be questioned given the significant Coulomb and exchange energies that bind the exciton. As opposed to most organic materials, QDs can support multiple exciton populations, biexcitons, triexcitons and so on, for times significant compared with the exciton lifetime, what has been shown schematically in Fig.2.11.

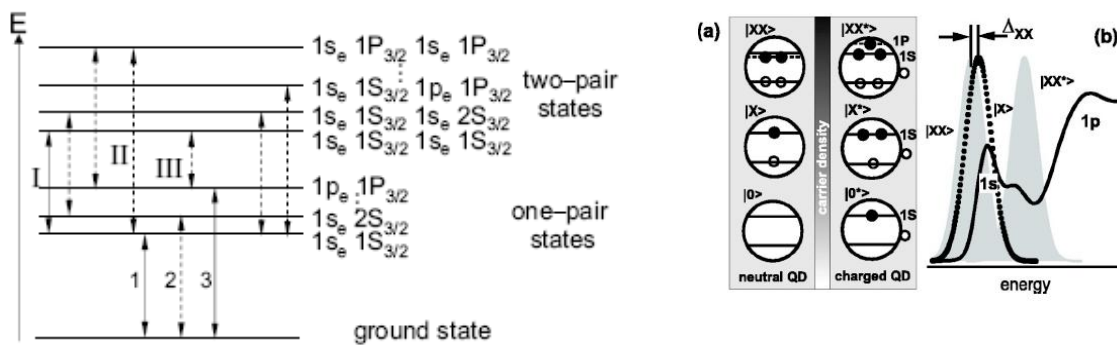


Figure 2.11 Schematic representation of Bi-excitons formation in nanocrystals, (b) filling of nanocrystals carriers when the excitation flux increases leading to bi, tri-excitons generation. Typical emission spectrum CdSe nanocrystals, where X-exciton, XX-neutral bi-exciton, XX* - charged bi-exciton [80].

Biexcitons in CdSe QDs have recombination times of the order of tens of picoseconds, depending on the QD size [81]. Nozik proposed that the unique properties of multiexcitons in QDs could be harnessed to increase the energy conversion efficiency of solar cells [82]. Recently that prediction was confirmed for PbS and PbSe QDs by the striking observations of band-edge exciton yields of >300% when the pump energy is tuned to greater than three times the bandgap [83, 84].

We see that nanoscale materials provide a fascinating intermediate ground between molecular and bulk materials. Interesting spectroscopic properties of excitons, which are often minuscule in bulk materials, are greatly accentuated in nanometresized materials and molecules. For example, the electron-hole exchange interaction is of the order of

⁷⁹ Guyot-Sionnest, P., Wehrenberg, B. & Yu, D. Intraband relaxation in CdSe nanocrystals and the strong influence of the surface ligands. *J. Chem. Phys.* **123**, 74709 (2005).

⁸⁰ M. Achermann, J. A. Hollingsworth, and V. I. Klimov, *Phys. Rev. B* **68**, 245302 (2003).

⁸¹ Klimov, V. I., Mikhailovsky, A. A., McBranch, D. W., Leatherdale, C. A. & Bawendi, M. G. Quantization of multiparticle Auger rates in semiconductor quantum dots. *Science* **287**, 1011–1013 (2000).

⁸² Nozik, A. J. Quantum dot solar cells. *Physica E* **14**, 115–120 (2002).

⁸³ Schaller, R. D. & Klimov, V. I. High efficiency carrier multiplication in PbSe nanocrystals: Implications for solar energy conversion. *Phys. Rev. Lett.* **92**, 186601 (2004).

⁸⁴ Ellingson, R. J. et al. Highly efficient multiple exciton generation in colloidal PbSe and PbS quantum dots. *Nanoletters* **5**, 865–871 (2005).



ROZWÓJ POTENCJAŁU I OFERTY DYDAKTYCZNEJ POLITECHNIKI WROCLAWSKIEJ

millielectronvolts in bulk semiconductor materials, but is increased 1,000-fold in QDs [85, 86, 87, 88, 89]. That is still several hundred times smaller than exchange interactions in organic materials that are <10 nm in size (Fig.2.10). However, once an exciton in an organic material is as large as that in a CNT, the exchange interaction is reduced to tens of meV.

3. Nanomaterials synthesis

Before each synthesis of any nanomaterial the main question should be answered: what band gap should have our material and what will be its lattice parameter. The answer to this question will determine properties of our materials and its quality.

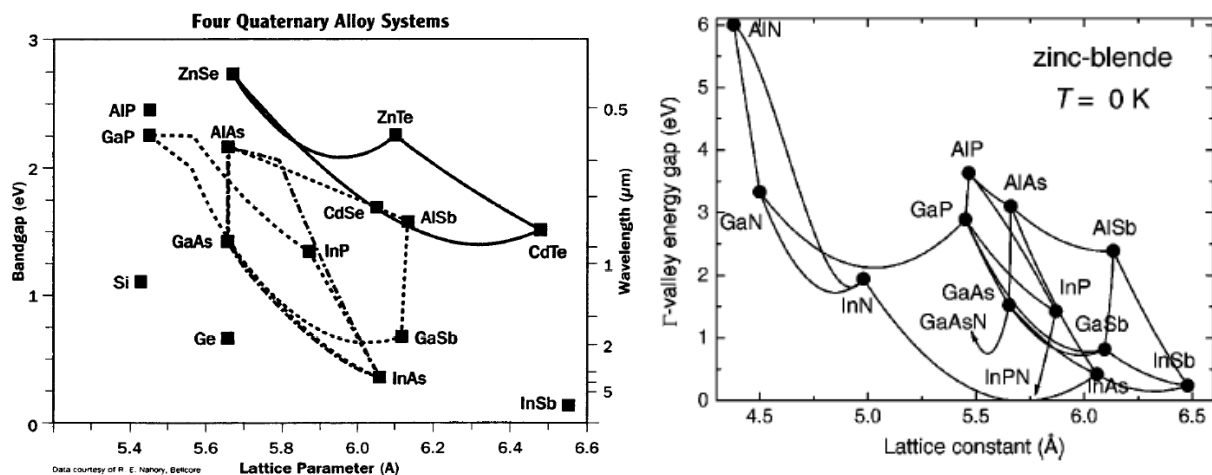


Figure 3.1 Band gap energies for binary compounds and corresponding to this alloys lattice parameters [90].

⁸⁵ Efros, A. L. et al. Band-edge exciton in quantum dots of semiconductors with a degenerate valence band: dark and bright exciton states. *Phys. Rev. B* **54**, 4843–4856 (1996).

⁸⁶ Fanceschetti, A. & Zunger, A. Direct pseudopotential calculation of exciton coulomb and exchange energies in semiconductor quantum dots. *Phys. Rev. Lett.* **78**, 915–918 (1997).

⁸⁷ Fu, H. X. & Zunger, A. InP quantum dots: electronic structure, surface effects, and the redshifted emission. *Phys. Rev. B* **56**, 1496–1508 (1997).

⁸⁸ Banin, U., Lee, J. C., Guzeliyan, A. A., Kadavanich, A. V. & Alivisatos, A. P. Exchange interaction in InAs nanocrystal quantum dots. *Superlattices Microstruct.* **22**, 559–567 (1997).

⁸⁹ Gogolin, O., Mshvelidze, G., Tshitshvili, E., Djanelidze, R. & Klingshim, C. Exchange interaction in argentine iodide nanocrystals. *J. Lumin.* **102**, 414–416 (2003).

⁹⁰ I. Vurgaftman and J. R. Meyer, L. R. Ram-Mohan, Band parameters for III–V compound semiconductors and their alloys, *J. Appl. Phys.* **89**, 5815 (2001)



ROZWÓJ POTENCJAŁU I OFERTY DYDAKTYCZNEJ POLITECHNIKI WROCLAWSKIEJ

Figure 3.1 shows collected data for different materials which will help us to understand many problems appearing in the nanomaterials synthesis discussed in the next paragraphs.

3.1 MOCVD

The evolution of metalorganic chemical vapor deposition, MOCVD, as a growth technology for multilayer heterostructures has provided access to improved and new device concepts and facilitated the large scale fabrication of multilayer device structures. In general MOCVD (also referred to as MOVPE, metalorganic vapor phase epitaxy, in order to stress the epitaxial character in the growth process, or OMVPE) is the growth of compound semiconductor layers by metalorganic and hydride precursors in the gas phase.

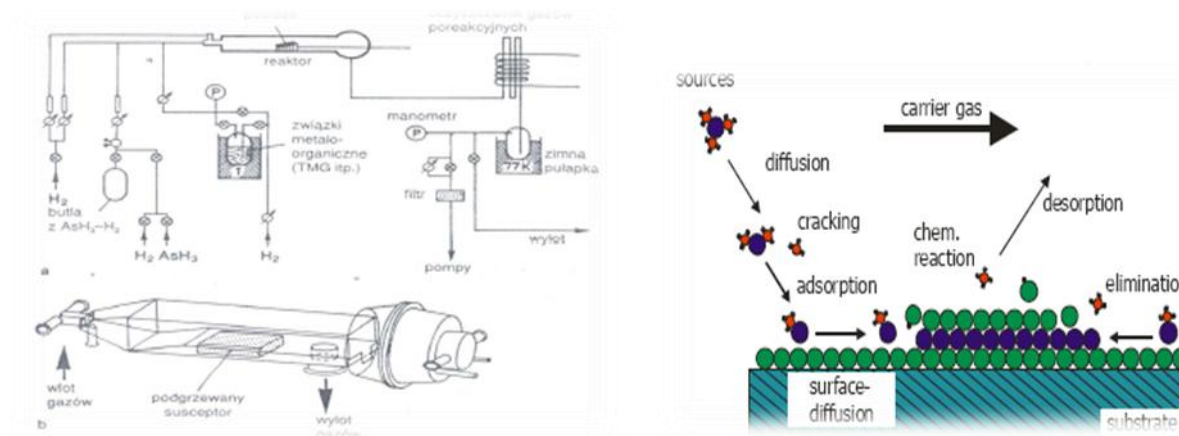


Figure 3.2 Schematic representation of chamber used for MOVCD growth together with scheme showing different steps during He MOCVD growth process.

First experiments were reported by Didchenko, Alix and Toeniskoetter in 1960, when they investigated the formation of InP by trimethylindium and phosphine at about 270 to 300°C [91]. Independent of these first growth studies with metalorganic compounds and hydrides, Harrison and Tompkins prepared GaAs and InSb in 1962[92] and Manasevit grew single crystal GaAs films on insulating substrates in 1968 [93].

Theoretical models describing the MOCVD growth process are helpful for finding an appropriate design of the reactor cells and also for optimizing the epitaxial parameters and

⁹¹ Didchenko, R., Alix, J. E., Toeniskoetter, R. H., J. Inorg. Nucl. Chem., 14, 35 (1960)

⁹² Harrison, B. C., Tompkins, E. H., Inorg. Chem., 1, 951 (1962)

⁹³ Manasevit, H. M., Appl. Phys. Lett., 12, 156 (1968)



ROZWÓJ POTENCJAŁU I OFERTY DYDAKTYCZNEJ POLITECHNIKI WROCŁAWSKIEJ

schematically have been shown in **Fig.3.2**. Generally, for gas phase deposition of epitaxial layers, a thermodynamic driving force has to be present in order to achieve supersaturation of the gas phase. The growth precursors are introduced into the reaction zone, and their concentration and reaction rate must be high enough in order to ensure sufficient decomposition so that this local supersaturation is produced. This shows that the stability of the precursors for example is an important parameter determining the thermodynamic driving force. In a very simple model, the MOCVD growth process can be described in four steps: (i) mass transport of the reactants to the growth surface, (ii) reaction at or near the surface, (iii) incorporation of the new material, and (iv) removal of the reaction by-products. Of course, the slowest step in this sequence will be the growth rate limiting step. The model simulated growth rates and impurity incorporation as a function of epitaxial parameters; for example, the computations showed that the temperature of the reactor walls plays an important role in controlling uniformity. Good agreement between model predictions and experimental data was found. Two alternative routes should be mentioned plasma enhanced MOCVD (PE-MOCVD) and atomic layer epitaxy (ALE). The former technique is very promising for a growth process where relatively stable precursors are used. In ALE growth of compound layers, the same precursors as in conventional MOCVD can be applied; growth is achieved by the separate and alternate exposure of the substrate to the reactants containing the group III and group V elements of the compound. This leads to an ideal two-dimensional growth process offering excellent control of the growth process at the monolayer level by a self-limiting growth mechanism.

3.2 MBE

Molecular beam epitaxy (MBE) is an ultrahigh vacuum (UHV) atomic layer by atomic-layer crystal growth technique based on reaction of molecular or atomic beams with a heated crystalline substrate (**Fig. 3.3**). MBE is capable of producing extremely high purity and highly crystalline thin films with precise control over composition, doping, and interfaces in the fraction of nanometer range in the growth direction with precise lateral uniformity.



ROZWÓJ POTENCJAŁU I OFERTY DYDAKTYCZNEJ POLITECHNIKI WROCLAWSKIEJ

[⁹⁴, ⁹⁵, ⁹⁶, ⁹⁷, ⁹⁸]. MBE is widely employed to grow semiconductor, metal, insulator, and ceramic thin films.

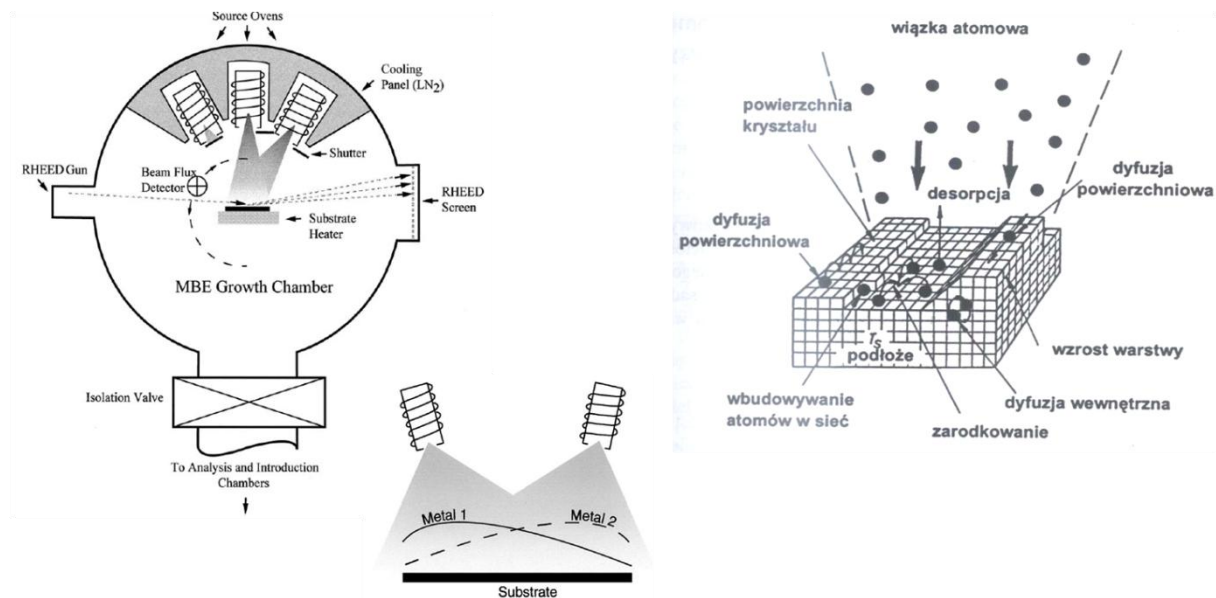


Figure 3.3 MBE chamber together with different processes appearing during an MBE growth.

The remarkable degree of freedom in materials composition and doping profiles in the sub-nanometer range afforded by MBE directly translates into freedom to tailor bandgaps, electron and hole wavefunctions, effective masses, carrier density of states, and optical transition energies and optical density of states. Because of the fundamental properties of such microscopic and mesoscopic structures, especially prevalence of quantum effects due to confinement of electrons, holes and photons, new physics and novel device concepts have emerged. Examples of such quantum structures abound, including quantum wells, compositional or doping superlattices, graded composition or chirped superlattices, two-dimensional electron or hole gas, delta doping, and strained layer superlattices. These flexibilities in tailoring the microscopic properties of layered materials is referred to as bandgap engineering, band structure engineering, wave function engineering or density of states engineering by various authors. An example of the degree of freedom afforded by MBE growth is incorporation of predetermined coherent strains, (compressional and/or tensile),

⁹⁴ Cho, A. Y., and Arthur, J. R., Progress in Solid State Chemistry, (G. Somorjai and J. McCaldin, eds.), 10(3):157, Pergamon Press, New York (1975)

⁹⁵ Chang, L. L., and Ludeke, R., Epitaxial Growth, (J. W. Mathews, ed.), Part A, Ch. 2.2, pp. 37, Academic Press, New York (1975)

⁹⁶ Ploog, K., Crystal Growth, Properties, and Applications, (H. C. Freyhardt, ed.), 3, 73, Springer-Verlag, Berlin (1980)

⁹⁷ Foxon, C. T., and Joyce, B. A., Current Topics in Materials Science, (FL Kaldis, ed.), 7, 1, New York (1981)

⁹⁸ Cho, A. Y., Molecular Beam Epitaxy, Am. Inst. Physics, New York (1994)



ROZWÓJ POTENCJAŁU I OFERTY DYDAKTYCZNEJ POLITECHNIKI WROCŁAWSKIEJ

which also leads to the modification of bandgap, effective mass, and the density of states especially in the valence bands. This is achieved by growth of alternating layers with different lattice constants which are thin enough so as to leave the strains unrelaxed. The term *molecular beam* describes a unidirectional kinematic flow of atoms or molecules with no collisions among them as opposed to a viscous fluid-like flow. The term epitaxy is composed of the Greek words *epi* meaning akin or upon, and *taxis* meaning arrangement or order. Epitaxy refers to ordered growth of one crystalline layer on another crystalline layer, with the same (or related) crystal arrangement. Consequently, a critical issue in MBE is the surface condition of the starting crystal (the substrate) and the subsequent layers as they are being grown. Molecular beam epitaxy is a form of vacuum evaporation technique, however it distinguishes itself from other evaporation crystal growth methods by its precise control of beam fluxes using collimated beams and rapid flux switching, more precise control of growth conditions, and the UHV environment which ensures high purity. Most importantly, it allows real time in-situ monitoring and control during the substrate preparation and film growth to ensure best conditions for stoichiometry and epitaxy.

There were two major factors in the initial development of the molecular beam epitaxy. First was the application of in-situ real time surface analysis to the understanding and optimization of processes involved in the substrate preparation and epitaxial growth. Second was the conscious and sustained focus on applying and refining the MBE growth system and technique for successful realization of epitaxial heterostructures for various electronic and optoelectronic devices, which put a much more stringent requirement on the quality of the films beyond the question of stoichiometry and epitaxy.

A list of important features of MBE growth follows:

1. Epitaxial growth proceeds monolayer by monolayer in a two dimensional manner at relatively low growth rates, typically 0.1 to 1.5 ML/s. Step-growth or 2-D nucleation and island growth prevails over 3-D nucleation growth. Surface smoothing takes advantage of surface migration and incorporation at step edges. The sides of any nucleated island serve as new step edges for the incorporation of newly arriving elements, leading to two dimensional growth.



ROZWÓJ POTENCJAŁU I OFERTY DYDAKTYCZNEJ POLITECHNIKI WROCŁAWSKIEJ

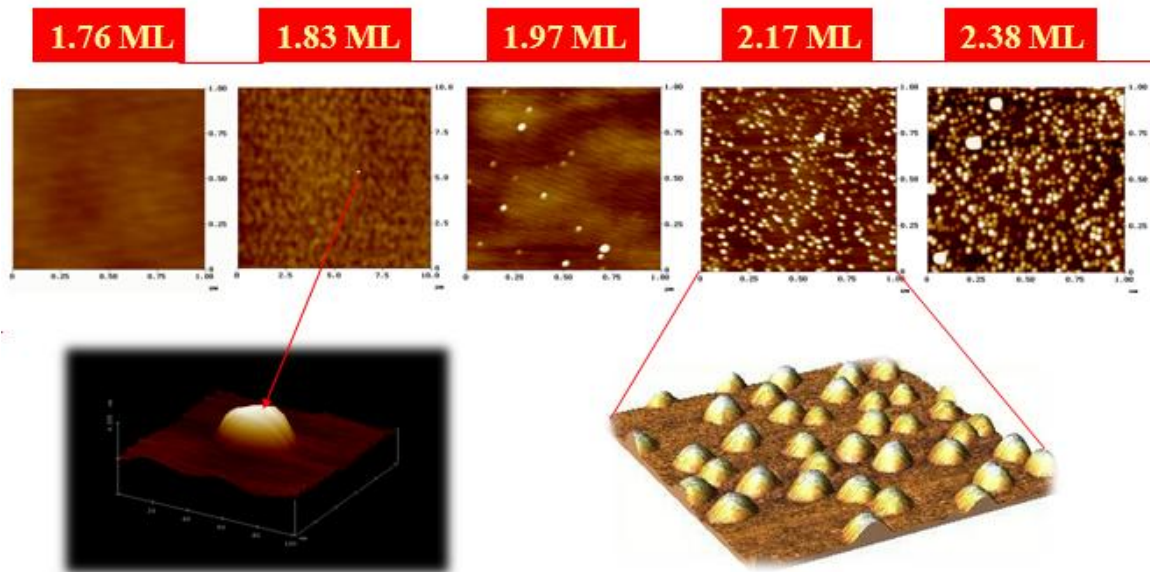


Figure 3.4 Example of MOMBE growth of InAs/InP Quantum Dots. QD Density vs. InAs nominal thickness [99].

2. Growth rate, composition, and doping concentration is determined mainly by arrival rate of different species in collimated beams and can be precisely controlled during the growth allowing precisely controlled, abrupt or graded composition and doping profile in the growth direction.

3. Use of growth interruption and relatively low temperature growth allows planar doping with extremely high sheet doping concentrations ($\text{Si} = 10^{13} \text{cm}^{-2}$ in GaAs).

4. Multilayer structures with smooth, abrupt, near-ideal interfaces can be grown because:

- a. The constituent atoms arrive at the surface as atomic or molecular beams without collision with other atoms or molecules, as opposed to viscous or diffusive flow. Growth proceeds by reaction of these species with the surface. Those that do not get incorporated leave the surface without interacting with the arriving beams and do not linger over the surface. Therefore, no stagnant layer is involved.
- b. Shutters can be opened and closed much faster (CO.1 set) than the time it takes to grow one monolayer (typically 1 set). Normal substrate temperature is low enough that

⁹⁹ Credit: Tal Raz, Technion-Israel Institute of Technology, Israel (2003).



ROZWÓJ POTENCJAŁU I OFERTY DYDAKTYCZNEJ POLITECHNIKI WROCŁAWSKIEJ

layer interdiffusion can be negligible (e.g., for GaAs, typical growth temperature is between 550-620°C).

d. Growth mechanism is based on kinetic processes and is two dimensional.

e. RHEED intensity oscillation monitoring during the growth, together with shutter sequencing, flux adjustment, and substrate temperature adjustment can be applied to ensure exact monolayer material deposition and incorporation. The above can also be used to ensure optimal surface migration and incorporation for surface smoothing on one monolayer scale (phase-locked epitaxy, migration enhanced epitaxy, atomic layer epitaxy).

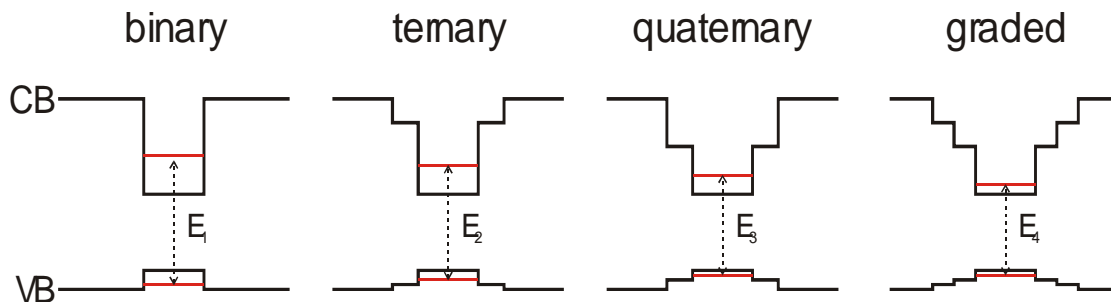


Figure 3.5 Examples of different designs of quantum wells designed to obtain different emission wavelengths

5. For MBE growth of III-V compounds using elemental atomic or molecular beams, epitaxial growth can be achieved over a wide range of substrate temperatures. The growth rate and composition are independent of substrate temperature over a wide range and are determined solely by group III element fluxes (sticking coefficient near unity), provided sufficient group V flux is present. The incorporation of the group V element is self-regulatory and ensures stoichiometry since the excess desorbs. For high substrate temperatures and for mixed group V compounds, this picture is somewhat modified.

As the success of MBE over the years became established, a number of variations on the original theme were employed to extend its applicability to new materials, or to simplify new aspects of the technique. The most basic and most common form of MBE uses elemental beams delivered from heated solid or liquid sources. This is variously referred to as conventional MBE, elemental MBE, condensed phase MBE, or simply MBE. Gas source



ROZWÓJ POTENCJAŁU I OFERTY DYDAKTYCZNEJ POLITECHNIKI WROCŁAWSKIEJ

MBE (GSMBE) is a generic name used when one or more of the beams are derived from a gas source. The simplest of GSMBE's is hydride MBE, where As and P are derived from cracked ASH, and PH, at the source end and are delivered to the substrate as elemental dimeric or monomeric beams. In this sense, hydride MBE is very similar to conventional MBE except that the background pressure is higher. In metalorganic MBE (MOMBE) or Chemical Beam Epitaxy (CBE), the metallic elements are delivered to the substrate as volatile organometallic compounds, relying on the substrate thermal energy for decomposition and release of the metallic element. A variety of approaches are possible in this method, namely using metalorganits for some of the beams (e.g., for Ga and In), hydrides for others (e.g., ASH), and elemental for yet others (e.g., Be for p-doping), or all fluxes can be from gas sources. The use of the word chemical in this conjunction is to emphasize that the constituents are delivered to the substrate in chemical beams and depend on surface chemical reactions to release the element before incorporation. It is important to emphasize that although the background pressure can be orders of magnitude higher in Gas Source MBE vs. conventional MBE, nevertheless, the material is delivered as collisionless kinematic beams, as opposed to the viscous flow in MOCVD.

3.3 CVD

Chemical vapour deposition (CVD) techniques based on using the reactions of chemicals in the gas phase to form the deposited thin film. The energy needed for the chemical reactions to occur is usually supplied by maintaining the substrate at elevated temperatures (LPCVD – low pressure) or plasma (PECVD) or optical excitation. The **CVD** refers to an entire class of thin film deposition techniques, in which selected precursor gases (dependent on the desired film) are supplied to a substrate whereupon they are made to chemically react with each other. Certain of the reaction products chemisorb on the surface to form the desired film while the remainder desorb and are removed from the system. With properly engineered reaction chemistry, the film stoichiometry and bond structure can be precisely and repeatably controlled with a minimum incorporation of impurity elements. The various methods by which the energy is supplied to drive the necessary chemical reactions define the specific types of CVD. Thermal CVD, wherein the reaction is enabled by substrate and gas heating, is inherently simple but is often not practical for the deposition of dielectric films (such as SiO₂)



ROZWÓJ POTENCJAŁU I OFERTY DYDAKTYCZNEJ POLITECHNIKI WROCŁAWSKIEJ

required in back-end CMOS or optoelectronic integrated circuit fabrication. A major effort in process engineering has historically been devoted to the development of low temperature thin film deposition systems – particularly those for depositing SiO₂ – which can duplicate the excellent quality and film uniformity of thermal CVD (such as the thermal oxidation of Si). Plasmas provide a means of achieving both objectives because they can simultaneously contain high energy particles but maintain a low overall temperature. The extremely high energy electrons in a plasma can be used to supply the thermal energy necessary to drive the reaction, while low temperatures can be maintained in the deposition chamber and at the substrate. The use of a plasma to “enhance” the rate of chemical reaction of the precursor gases in CVD is referred to as plasma enhanced CVD (PECVD). There are various types of PECVD, each defined by a different method for generating the plasma. The most common is radio frequency (RF) PECVD (or often simply designated ‘direct PECVD’) which has an inherently simple implementation in the form of parallel electrodes between which a standard capacitive plasma is generated. The geometry of such an electrode system, however, necessitates that the substrate and therefore the film is submerged directly in the glow discharge of the plasma. The bombardment of the films by ions and other energetic particles present in the glow discharge can lead to both radiation and sputtering related damage to the film and incorporation of unintended products. Furthermore, the fact that all of the precursor gases are flowed through the plasma means that one has little control over the reaction pathways that lead to film deposition. A partial solution to these issues is to design a ‘remote’ deposition system, in which the substrates are located a distance from the plasma, and in which precursors can be introduced at different locations in the reactor chamber. This usually necessitates a new technique for generating the plasma such as electron cyclotron resonance (ECR). In fact, ECR-PECVD (electron cyclotron resonance plasma enhanced chemical vapour deposition) has become popular in the deposition of numerous different dielectric optical coatings having demanding quality and uniformity requirements. The ECR can be used to generate a stable plasma since the resonant effect quickly (and stochastically) generates electrons with sufficient energy to ionize neutral gas atoms/molecules through inelastic collisions, liberating further electrons which then undergo the ECR themselves – creating an avalanche effect.



ROZWÓJ POTENCJAŁU I OFERTY DYDAKTYCZNEJ POLITECHNIKI WROCLAWSKIEJ

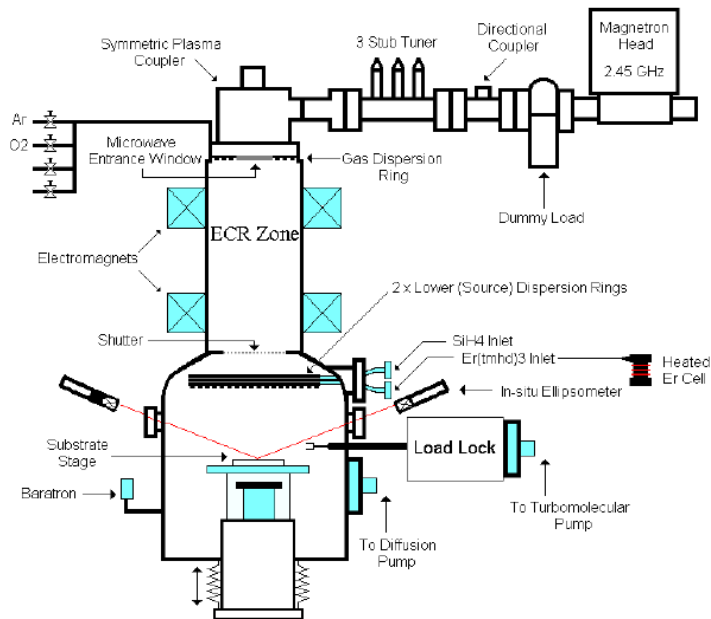


Figure 3.6 Schematic representation of PECVD system.

Advantages of ECR-PECVD

There are several characteristic features of the ECR plasmas. These include, but are not limited to, the following:

- Generation of a dense plasma (electron density of 10^{10} to 10^{12} cm⁻³).
- generation of a highly ionized plasma (10^{10} to 10^{11} ions/cm³).
- The ions leaving the ECR zone exhibit minimal energy dispersion.
- Highly activated plasma (high density of charged species) is easily obtained at low gas pressures.
- Charged species escape the plasma through a moderately diverging magnetic field; the substrate/plasma potential difference accelerates the ions, which impinge on the substrate with energies as low as 20-30 eV. Within the magnetic bottle, the most energetic particles are reflected back into the ECR zone (the [average] ion temperature is likely a few eV in the ECR region). This avoids damaging of the substrate by those energetic ions, which in direct PECVD systems can be as high as 1 keV. In the ECR plasmas these more energetic particles dissipate this excess energy through ionizing collisions thereby increasing the ion density of the plasma.
- High quality thin films can be deposited at low temperature (also a characteristic of PECVD in general).



ROZWÓJ POTENCJAŁU I OFERTY DYDAKTYCZNEJ POLITECHNIKI WROCŁAWSKIEJ

Technological parameters used in PECVD technique

	Stoichiometry	T _{substr.}	p _H	p _{Ar}	P [W]	Plasma density		Ta [°C]	Atmos. (O/Ar)	t [min]
NCs size							Post growth			
NCs phase										
NCs density										
Number of defects										
Hydrogen contamination										
Surface/interface quality										

Before we start do discuss other chemical techniques we will discuss shortly some important effects which often appear during the synthesis in nano scale. The most important, and unwanted effect, is size/shape distribution of obtained nanomaterials. Schematically the importance of this effect has been shown in **Fig. 3.7**.



ROZWÓJ POTENCJAŁU I OFERTY DYDAKTYCZNEJ POLITECHNIKI WROCLAWSKIEJ

A. Size Histograms B. Aspect Ratio Histograms

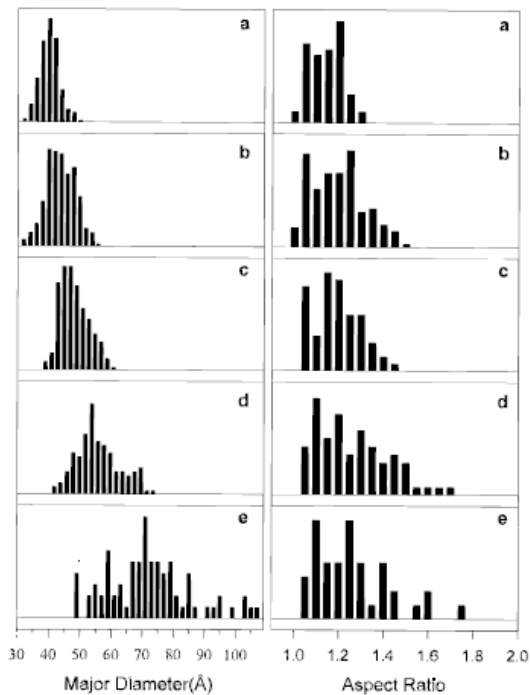


Figure 3.7 (A) Histograms of grain sizes, (B) histograms of width to length ratio obtained for 150 nanocrystals CdSe from 8 set of samples [¹⁰⁰].

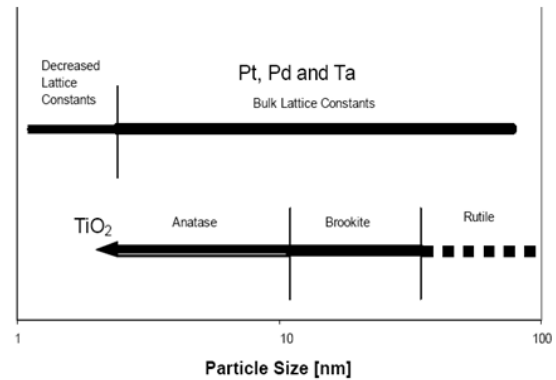


Figure 3.8 Crystal phase evolution with reduction in TiO₂ grain sizes [¹⁰¹].

If the size distribution is present and is significant it will influence somehow properties of investigated nanomaterials which are size dependent like: band gap, decay time, oscillator strength of optical transitions etc.

The other very important feature characterizing nanomaterials is their huge surface-to-volume ratio, reflected in high number of surface atoms as compared to volume atoms what can be seen from **Fig.3.9**.

¹⁰⁰ B. O. Dabbousi, J. Rodriguez-Viejo, F. V. Mikulec, J. R. Heine, H. Mattoussi, R. Ober, K. F. Jensen, and M. G. Bawendi, *J. Phys. Chem. B* 101, 9463 (1997)

¹⁰¹ Z.L.Wang et al. -*Adv. Mat.* 10 (1998)



ROZWÓJ POTENCJAŁU I OFERTY DYDAKTYCZNEJ POLITECHNIKI WROCLAWSKIEJ

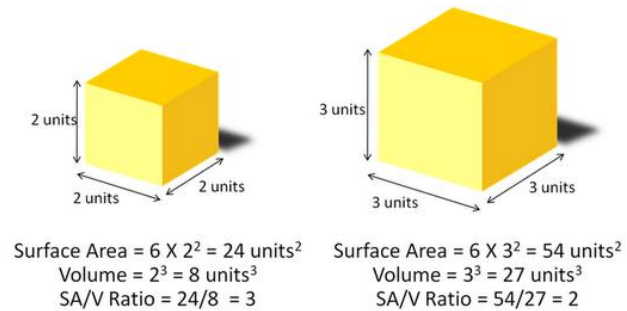
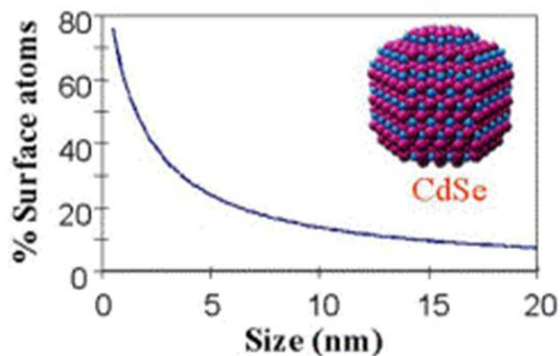


Figure 3.9 The number of surface atoms in quantum dot when their size is changed. Figure 3.10 The method of surface to volume ratio.

The main consequence of this effect is high surface activity and their influence on properties of the nano materials as a whole. The other modification which will have strong consequences on synthesis of nanomaterials is reduction of melting point and appearance of the phase transition depending on the nanomaterials size (see **Fig.3.8**) and modifications in lattice constants. More generally, depending on the nanomaterials size we can see many different crystallographic stages of the growth process what can be seen from **Fig. 3.10**.

3.4 Coloidal techniques

In principle growth process in this technique can be well described by theory of La Mer and Dinegar [¹⁰²,¹⁰³] and schematically has been shown in **Fig. 3.11 (a)**. This process include discrete transition phase of nucleation, fast growth of monomers from the liquid chaise and slow growth of nanocrystals in *Oswald ripening* process. This process dominates in the phase where already some smaller seeds already exist. Theory of this growth process has been also developed by *Lifshits and Slyozova* [¹⁰⁴], and main conclusion from this theory is the equation describing how the grains size changes with some technological parameters

¹⁰² V. K. La Mer, R. H. Dinegar, J. Am. Chem. Soc. 123, 4847 (1950).

¹⁰³ C. B. Murray, C.R. Kagan, M. G. Bawendi, Annu. Rev. Mater. Sci. 30, 545 (2000).

¹⁰⁴ I.M.Lifshits, V.V. Slyzov, JEPT, 35, 331 (1959).



ROZWÓJ POTENCJAŁU I OFERTY DYDAKTYCZNEJ POLITECHNIKI WROCŁAWSKIEJ

$$\langle d \rangle = \left(\frac{4}{9} \alpha D_0 \exp\left(\frac{-E_D}{kT}\right) \right)^{\frac{1}{3}} \quad (3.1)$$

where D is diffusion constant, E_D and α are parameters dependent on surface energy. The nucleation process is induced by injection of precursors into the *coordinating solvent*. Schematically the growth process has been shown in **Fig. 3.11**.

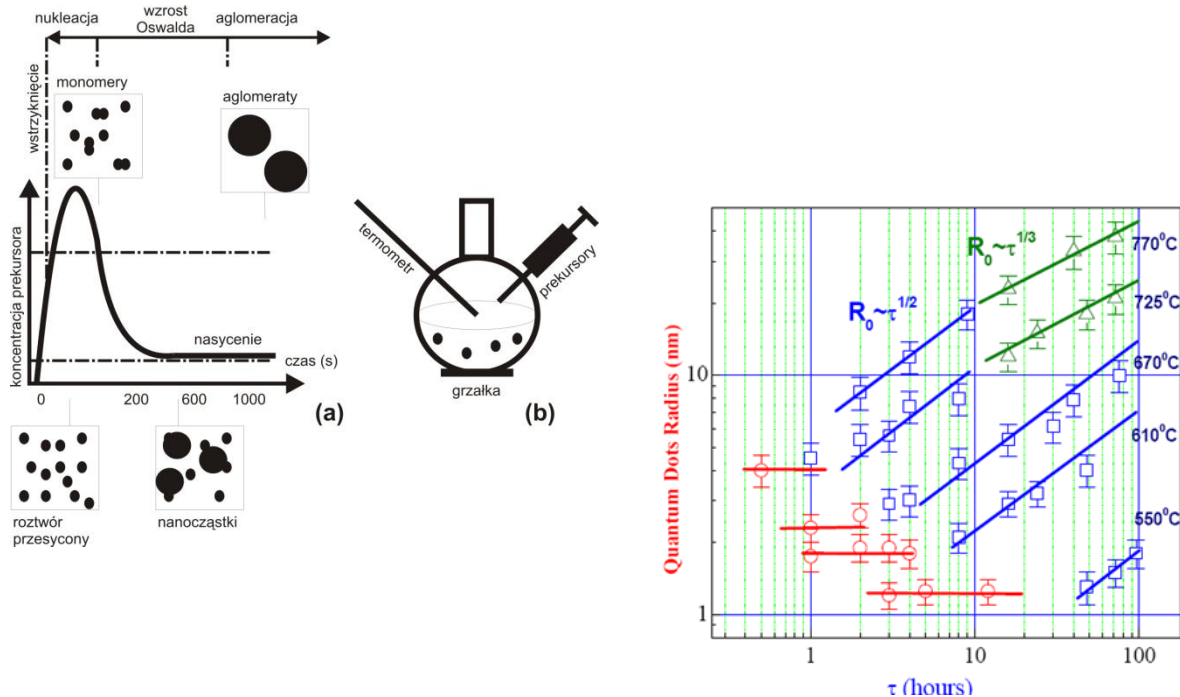


Figure 3.11 Schematic description of growth process In colloidal techniques, (a) graph showing how the grains size depends on temperature and time of the growth process [105].

In consequence we got thermal decomposition of precursor reagents and supersaturation of monomers which starts to form the nano clusters. Above processes can be controlled by time and temperature of the growth process or by introducing some additional ligands into the solution. These ligands can block growth of the material in some directions and in this way

¹⁰⁵ V.Golubukov, A.Ekimov, A.Onushenko, V.Tzehomskii, Sov.Phys.Chem.of Glass 6, 511 (1980)



ROZWÓJ POTENCJAŁU I OFERTY DYDAKTYCZNEJ POLITECHNIKI WROCLAWSKIEJ

modifies the shape and size or crystallographic structure of nanomaterials [¹⁰⁶]. When the nanocrystals will reach the expected size the quick reduction in temperature block their growth. At this stage we can inject the other precursors and cover our nanocrystals by additional shell. The shell has two main reasons- prevents quick oxidation and destruction of our nanocrystals and pasivate all surface states (i.e. dangling bonds) strongly improving optical properties of our nanocrystals. This allows us to obtain nanocrystals with size distribution less than 5% and quantum efficiency higher than 50%. The main common materials combination for this purpose are CdSe, CdS covered by ZnS [^{107, 108, 109}], CdS [¹¹⁰] or TOPO what gives QE as high as 70%. During the shell growth some other effects can be observed. For example instead of continuous shell formation some discrete island can be formed (quantum dots on quantum dot) depending on lattice parameters mismatch between core and surface reflected in strain at the interface. The optimal condition of the core-shell nanocrystals has been fund for CdSe/ZnS system where lattice parameters mismatch is 12% [¹¹¹]. In the case of 2D structures this 12% would induce strong strain and in consequence many defects formation. Here, due to spherical symmetry all strain at the interface is relaxed, what has been found from HRTEM investigations HRTEM [¹¹²].

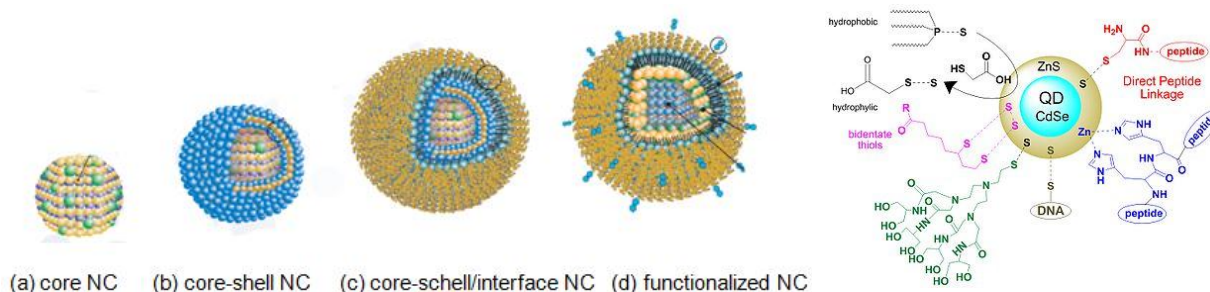


Figure 3.12 Evolution of nanocrystals formation used in as biological optical markers.

¹⁰⁶ S. M. Lee, Y. Jun, S.N.Cho, J. Cheon, J.Am.Chem.Soc, 124, 11, 224 (2002).

¹⁰⁷ V.I.Klimov, A.A.Mikhailovsky, D.W.McBrench, C.A.Leatherdale, M..G.Bawendi, Science 287, 1011 (2000).

¹⁰⁸ M. A. Hines, P. Guyot-Sionnest, J. Phys. Chem. 100, 468 ().

¹⁰⁹ B. O. Dabbousi, J. Rodriguez-Viejo, F.V. Mikulec, J. R. Hiene, M. Mattoussi, R. Ober, K. F. Jensen, M. G. Bawendi, J. Phys. Chem. B 101, 9463 (1997).

¹¹⁰ X. Peng, M. C. Schlamp, A. V. Kadavenich, A. P. Alivisatos, J. Am. Chem. Soc. 119, 7019 (1997).

¹¹¹ Semiconductor and Metal Nanocrystals, Synthesis and Electronics and Optical Properties, V.I.Klimov, Marcel Dekker, Inc. New York, (2004).

¹¹² B. O. Dabbousi, J. Rodriguez-Viejo, F.V. Mikulec, J. R. Hiene, M. Mattoussi, R. Ober, K. F. Jensen, M. G. Bawendi, J. Phys. Chem. B 101, 9463 (1997).



ROZWÓJ POTENCJAŁU I OFERTY DYDAKTYCZNEJ POLITECHNIKI WROCLAWSKIEJ

To get nanocrystals by using colloidal growth which can be used in some special application the growth process is much more complicated. The **Fig. 3.12** shows the growth steps necessary to obtain nanocrystals which can be used as optical markers in biology. In the first step, we have to define material and nanocrystals size to get adequate to our application emission wavelength. In the second step we have to cover our core by shell to reduce all defect states and to prevent our core from interaction with the environment. In the third step we have cover our core-shell nanocrystals by additional layer which help us to get high solubility of our nanocrystals in water. In the final step we have to introduce the biological interface onto our nanocrystals, other words we have functionalized our structures. **Figure 3.13** shows different possibilities of covering the nanocrystals core with some physical consequences and their reasons.

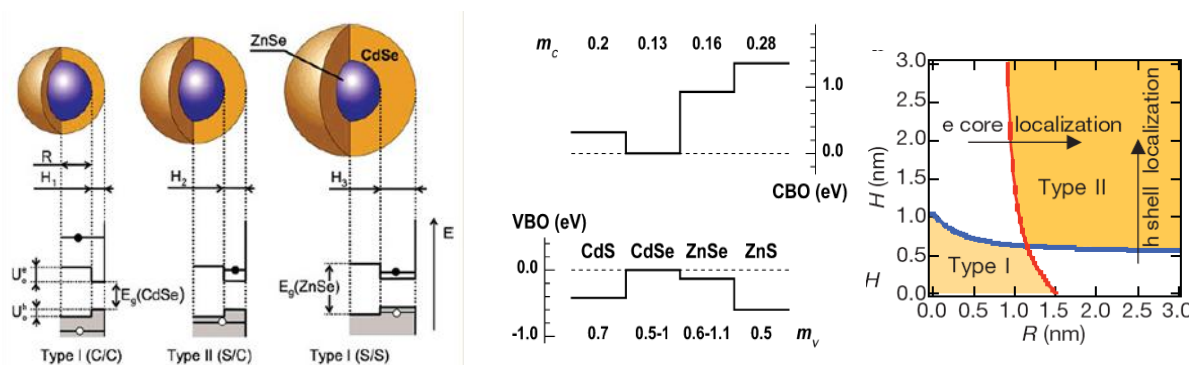


Figure 3.13 Examples of different concepts in covering the core by the shell together with parameters of materials used typically as a shell. The energy/wavelength of the lowest transition of the hetero-NC plotted as a function of core radius and shell thickness. Two red lines mark the energies corresponding to the transitions between different localization regimes. [¹¹³, ¹¹⁴, ¹¹⁵].

Core/shell NC heterostructures can show either type I or type II carrier localization, depending on the energy offsets between the core and the shell materials, effective masses, and the relation between the core diameter and the shell thickness. The type I regime corresponds to the situation in which both an electron and a hole are predominantly located in the same part of the heterostructure (in the core or in the shell), while in the type II regime, electrons and holes are spatially separated and occupy different parts of the hetero-NC.

¹¹³ Sergei A. Ivanov, Jagjit Nanda, Andrei Piryatinski, Marc Achermann, Laurent P. Balet, Ilia V. Bezel, Polina O. Anikeeva, Sergei Tretiak, and Victor I. Klimov, Light Amplification Using Inverted Core/Shell Nanocrystals: Towards Lasing in the Single-Exciton Regime, *J. Phys. Chem. B* 108,10625 (2004)

¹¹⁴ J.Bleuse et al. *Physica E* 21, 331 (2004)

¹¹⁵ Shinae, J. *Nanotechnology*. 2006, 17, 3892



ROZWÓJ POTENCJAŁU I OFERTY DYDAKTYCZNEJ POLITECHNIKI WROCŁAWSKIEJ

ZnSe and CdSe are characterized by type I energy offsets in the bulk form (U_{0e}) 0.86 eV and U_{0h}) 0.14 eV, see **Fig. 3.13**) that should nominally favor localization of both carriers in CdSe core. However, a core/shell ZnSe/CdSe nanostructure can exhibit either type I or type II behavior, depending upon the ZnSe core radius, R , and the CdSe shell thickness, H . In particular, for a fixed core radius, one can continuously tune the localization regime from type I to type II and then back to type I by varying H . **Figure 3.13** shows the calculated dependence of the lowest transition energy, E_{11} , and the corresponding wavelength, λ_{11} , on the core radius and shell thickness. Two red lines mark the energies corresponding to the critical shell widths $H_c(e)$ and $H_c(h)$ that separate different localization regimes. In the case of type I(C/C) localization, the energy of the lowest transition is strongly dependent upon both R and H (i.e., on the size of the entire hetero-NC), while for the type II(S/C) and type I(S/ S) localization, E_{11} is primarily determined by the width of the shell. The changes in the localization regime, however, do not significantly alter the scaling of the Coulomb interactions that remain approximately inversely proportional to the size of the entire NC, further suggesting that Auger recombination times will scale in proportion to the total volume of the hetero-NCs (independent of the localization regime), as in the case of traditional monocomponent nanoparticles. These observations indicate that inverted ZnSe/CdSe structures with a large core radius and a thin shell can significantly reduce Auger recombination rates but still maintain the strong confinement that is required for producing emission in the green to blue range of the spectrum.

The transition between localized and delocalized states can be observed experimentally as the unusually large shift between the PL band and the first well-pronounced absorption feature. This absorption feature is likely due to a spatially direct transition, which, however, is not the lowest in energy. The actual lowest transition is weak because of its spatially indirect character and therefore, is not well pronounced in the absorption spectra. To further improve the quality of the surface the gradient core-shell quantum dots can be grown. The simplest example of such structure is core-shell-shell QDs shown in **Fig. 3.14**. This design should allow considerable reducing of the strain inside nanocrystals.

ROZWÓJ POTENCJAŁU I OFERTY DYDAKTYCZNEJ POLITECHNIKI WROCLAWSKIEJ

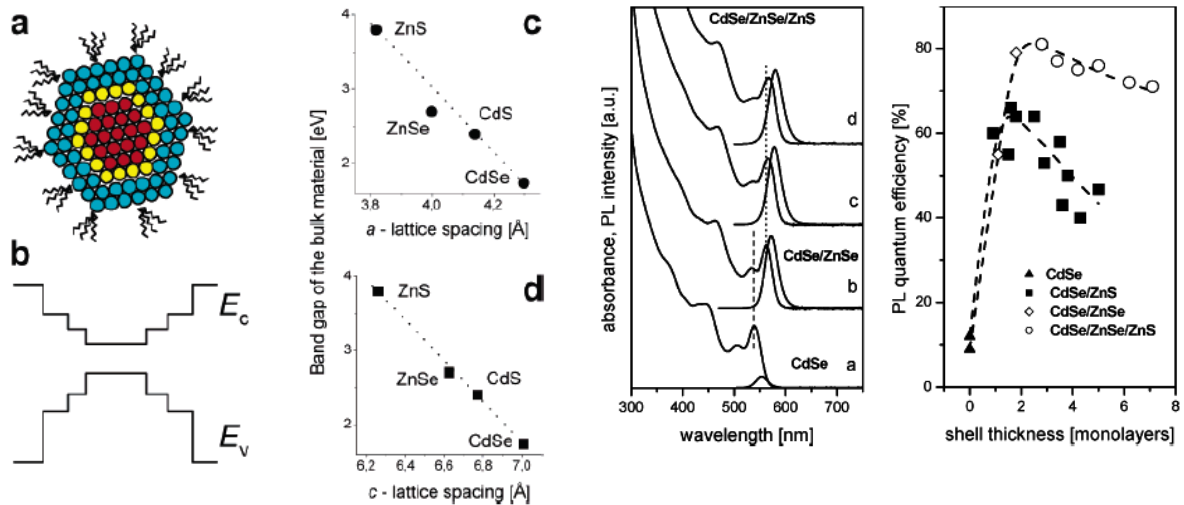


Figure 3.14 Core-shell-shell nanocrystal: (a) schematic outline and (b) the energy level diagram; (c, d) relationship between band gap energy and lattice parameter of bulk wurzite phase CdSe, ZnSe, CdS and ZnS [¹¹⁶].

Left: absorption and PL spectra of (a) CdSe cores, (b) CdSe/ ZnSe core-shells (thickness of ZnSe shell ~2 monolayers), (c, d) CdSe/ ZnSe/ZnS nanocrystals with the thickness of ZnS shell ~2 monolayers (c) and ~4 monolayers (d). Right: room-temperature PL quantum yields of CdSe, CdSe/ZnSe, and CdSe/ZnSe/ZnS nanocrystals dissolved in chloroform. For comparison, the dependence of PL quantum yield on the shell thickness for various samples of CdSe/ZnS nanocrystals is shown.

To grow the shell, the molecular precursors (further referred to as “monomers”) are slowly added into a colloidal solution of core nanocrystals. The kinetics of shell growth can be limited either by diffusion of monomers toward the nanocrystal surface or by the rate of decomposition of monomers on the nanocrystal surface. Theoretical considerations predict that diffusion-limited growth should always result in narrowing of the particle size distribution [¹¹⁷]. Such narrowing or “focusing” of the size distribution induced by addition of monomers was observed experimentally in the synthesis of single phase nanocrystals (CdSe [¹¹⁸], CdTe [¹¹⁹])

The lattice mismatch between the core and the shell creates a barrier for nucleation of the shell material. Moreover, the interfacial strain at the core-shell interface gives an additional contribution to the chemical potential of the whole nanocrystal. Note that this

¹¹⁶ Dmitri V. Talapin, Ivo Mekis, Stephan Go1tzinger, Andreas Kornowski, Oliver Benson, and Horst Weller, CdSe/CdS/ZnS and CdSe/ZnSe/ZnS Core-Shell-Shell Nanocrystals, *J. Phys. Chem. B* 108, 18826 (2004).

¹¹⁷ Talapin, D. V.; Rogach, A. L.; Haase, M.; Weller, H. *J. Phys. Chem. B* 2001, 105, 12278; Rogach, A. L.; Talapin, D. V.; Shevchenko, E. V.; Kornowski, A.; Haase, M.; Weller, H. *Adv. Funct. Mater.* 2002, 12, 653.

¹¹⁸ Peng, X.; Wickham, J.; Alivisatos, A. P. *J. Am. Chem. Soc.* 1998, 120, 5343.

¹¹⁹ Talapin, D. V.; Rogach, A. L.; Shevchenko, E. V.; Kornowski, A.; Haase, M.; Weller, H. *J. Am. Chem. Soc.* 2002, 124, 5782.



ROZWÓJ POTENCJAŁU I OFERTY DYDAKTYCZNEJ POLITECHNIKI WROCŁAWSKIEJ

strain-induced contribution depends on the presence of defects and dislocations inside the shell, which may vary from particle to particle. These arguments may explain why the presence of a highly strained interface inside a nanocrystal causes poor control over kinetics of shell growth which, in turn, result in broadening of the particle size distribution. Reducing the interfacial strain by engineering the lattice spacing (e.g., introducing the middle shell) seems to be the general way to achieving narrow in situ size distributions of heterogeneous nanocrystals. In addition to reducing the interfacial strain between the core and the outer shell, the middle shell in the Core-Shell-Shell nanocrystal can also determine the particle shape. Recently, the group of Talapin have demonstrated the possibility of synthesizing colloidal heterostructure nanorods consisting of spherical CdSe core and CdS rodlike shells grown preferentially on the {00-1} facet of the CdSe core [¹²⁰]. The electronic structure of CdSe/CdS nanorods provides a very different level of confinement for electrons and holes. The hole is strongly confined to the CdSe core and maintains 0-D character, whereas the electron gains 1-D character due to delocalization into the 1-D rodlike shell. This quantum confinement regime results in linear polarization of PL along the nanorod.

Growing the shell of ZnS around CdSe/ZnSe nanocrystals results in a small (~15 meV) red shift of absorption and PL spectra. The PL quantum efficiency of CdSe/ZnSe/ZnS nanocrystals is nearly as high as that of CdSe/ZnSe. In the case of CdSe/ZnSe/ZnS nanocrystals the effect of a decreasing PL efficiency with increasing shell thickness is much less pronounced.

Figure 3.14 shows how can we avoid nanocrystals agglomeration and obtain their high solubility by covering their surface by some additional layer.

¹²⁰ Talapin, D. V.; Koeppel, R.; Götzinger, S.; Kornowski, A.; Lupton, J. M.; Rogach, A. L.; Benson, O.; Feldmann, J.; Weller H. *Nano Lett.* **2003**, *3*, 1677.



ROZWÓJ POTENCJAŁU I OFERTY DYDAKTYCZNEJ POLITECHNIKI WROCLAWSKIEJ

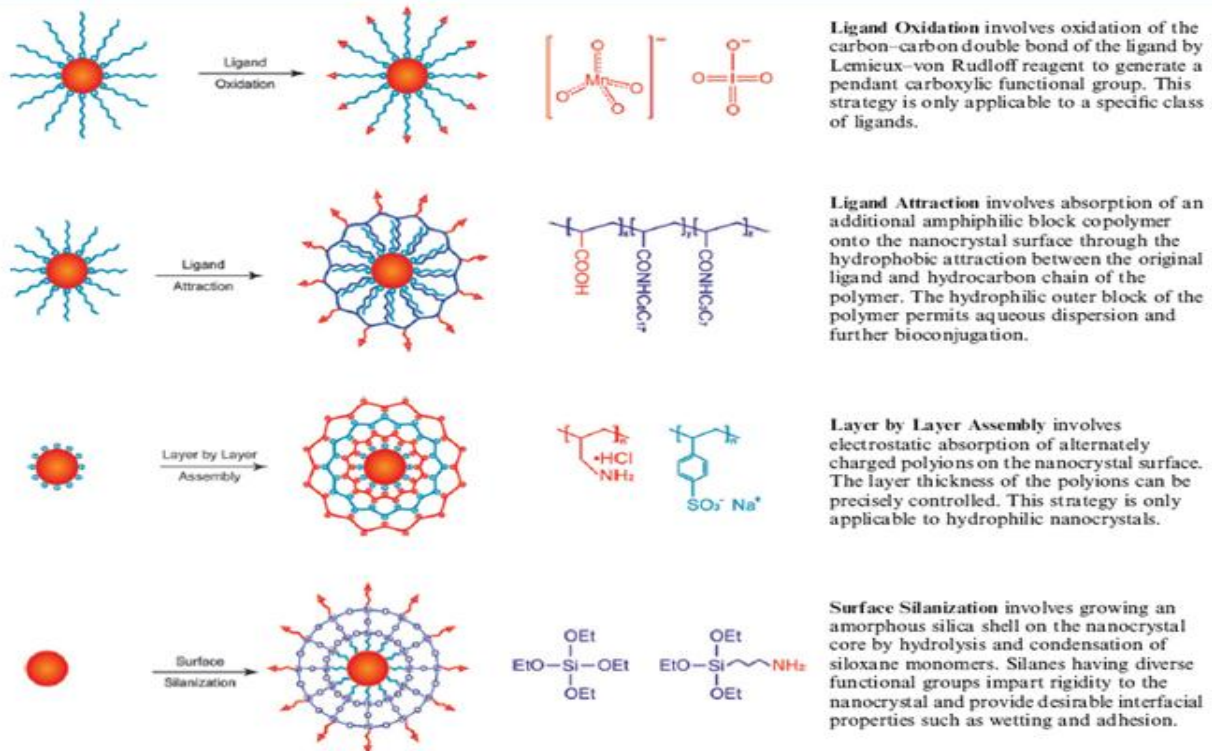


Figure 3.14 Different concepts of covering nanocrystals by additional layer responsible for their better solubility in water.

ROZWÓJ POTENCJAŁU I OFERTY DYDAKTYCZNEJ POLITECHNIKI WROCLAWSKIEJ

QDs as synthesized ^{1,24,27}		Soluble in: toluene hexanes chloroform	QD-Cap linking functionality: Hydrophobic	Excess 'cap' or ligand	Soluble in: basic buffer	Hydrophilic
Representative surface-capping strategies	Mechanism of interaction	Examples				
a Monothiolated caps $n = 1$: mercaptoacetic acid $n = 2, 10, 15$: benzyl 		Mercaptoacetic acid ²⁸ Alkylthiol terminated DNA ⁴¹ Thioalkylated oligo-ethylene glycol ²¹				
b Bidentate thiols 		Dihydrolypic acid derivatives ^{24, 42}				
c Silane shell or box dendimer 		Mercaptoalkyl silane ^{24, 43} Amine box dendimers ²¹				
d Hydrophobic interactions 		Phosphatidylethanol amine Phosphatidylcholine micelles ²¹ Modified acrylic acid polymers ^{24, 44, 45} Poly(maleic anhydride) alt-1-tetradecene ²⁵				
e Functionalized oligomeric phosphines 		Oligomeric phosphines ²⁷				
f Amphiphilic triblock copolymer 		Site for EDC-based antibody conjugation Amphiphilic triblock copolymer ⁴⁶				
g Amphiphilic saccharides 		Internal alkanes interdigitate with TOPO Amphiphilic saccharides ²¹				
h Direct attachment of protein/peptides to QD surface 		Biotin-G-Cys-E-Cys-G-G-Cys-E-Cys-G-Cha-C-C-Cha-Cmid Phycochelatin- α -peptides ¹⁹ Histidine-rich aptopes ²⁴ Polyhistidine metal-affinity coordination ^{21, 44}				

Capping ligands serve another critical role in insulating/passivating/protecting the QD surface from deterioration in biological media. Synthesis of new caps create an ever-increasing library available for obtaining aqueous QD dispersions; however, many were created for specialized uses and thus have limited general applicability. A representative list of caps and the QD dispersal strategies they use is provided in Table 1. These strategies can be grouped into three major routes. The first uses 'cap exchange' and involves the substitution of the native TOP/TOPO with bifunctional ligands, each presenting a surface anchoring moiety to bind to the inorganic QD surface (for example, thiol) and an opposing hydrophilic end group (for example, hydroxyl, carboxyl) to achieve water-compatibility. These include an array of thiol and phosphine mono and multidentate ligands (Table 1a,b). The second strategy involves formation of polymerized silica shells functionalized with polar groups, which insulate the hydrophilic QD (Table 1c)^{3,40}. The third method preserves the native TOP/TOPO on the



ROZWÓJ POTENCJAŁU I OFERTY DYDAKTYCZNEJ POLITECHNIKI WROCŁAWSKIEJ

QDs and uses variants of amphiphilic ‘diblock’ and ‘triblock’ copolymers and phospholipids to tightly interleave/interdigitate the alkylphosphine ligands through hydrophobic attraction, whereas the hydrophilic outer block permits aqueous dispersion and further derivitization (Table 1d,f,g)33–36,44–46.

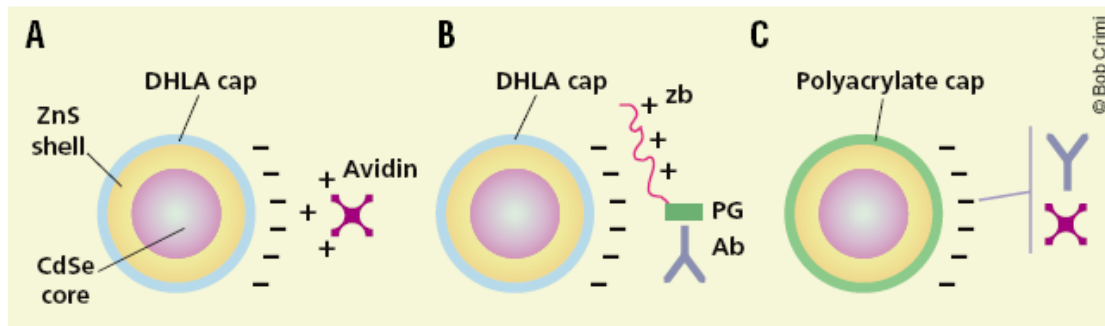


Figure 1. Three strategies for bioconjugation to quantum dot probes. The quantum dot consists of a CdSe core passivated by a ZnS shell. The surface cap is negatively charged, with carboxylate groups from either DHLA or an amphiphilic polymer (40% octylamine modified polyacrylic acid). Proteins are conjugated to the DHLA–quantum dots electrostatically either (A) directly or (B) via a bridge consisting of a positively charged leucine zipper peptide (zb) fused to recombinant protein G (PG). The latter binds to a primary antibody (Ab) with specificity for the intended target. In (C), antibodies, streptavidin, or other proteins are coupled covalently to the polyacrylate cap with conventional carbodiimide chemistry. (A, B) from Jaiswal *et al.*⁵; (C) from Wu *et al.*⁶

Below are some other examples of nanocrystals synthesis by using wet-chemistry.



Figure.3.15 Different techniques used for NCs synthesis.



ROZWÓJ POTENCJAŁU I OFERTY DYDAKTYCZNEJ POLITECHNIKI WROCŁAWSKIEJ

Below are some examples of nanomaterials synthesis by using different techniques:

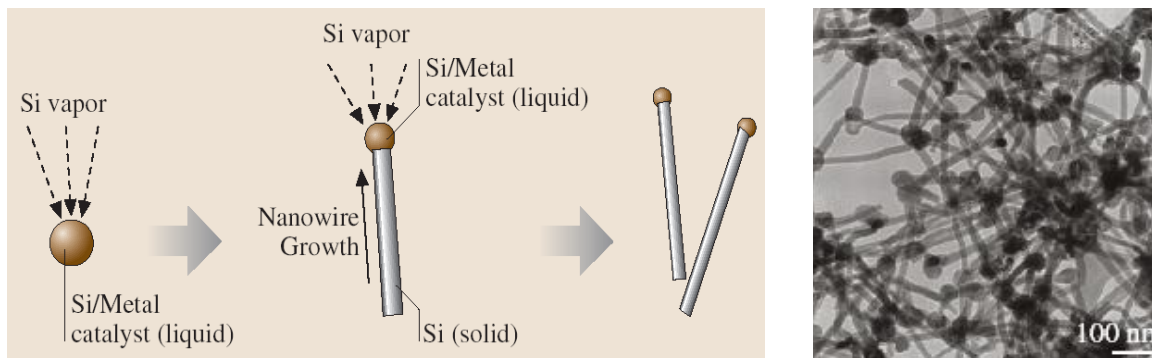


Figure 3.16 Nanowires obtained by **Vapour Liquid Solid (VLS)** method. Growth mechanism involves the absorption of source material from the gas phase into a liquid droplet of catalyst [¹²¹].

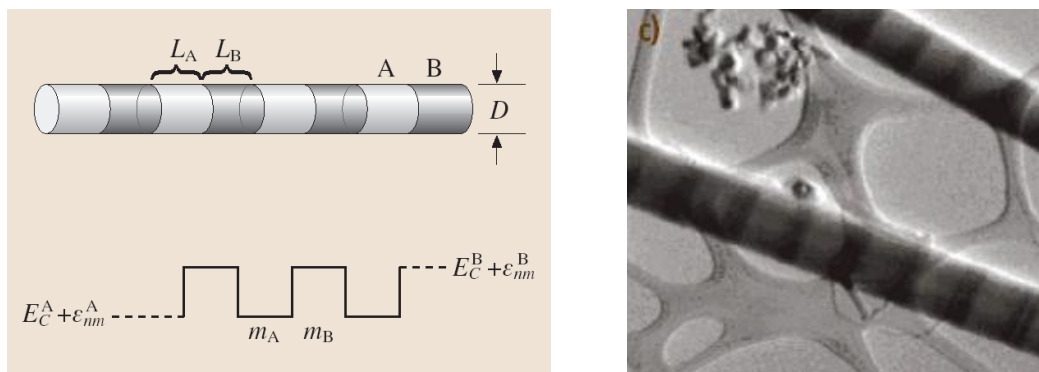


Figure 3.17 Example of using VLS technique to obtaining Si/SiGe super lattice nanowires [¹²²].

¹²¹ Springer Handbook of Nanotechnology, Edited by: Bhushan, Bharat © 2004 Springer – Verlag.

¹²² Springer Handbook of Nanotechnology, Edited by: Bhushan, Bharat © 2004 Springer – Verlag.

ROZWÓJ POTENCJAŁU I OFERTY DYDAKTYCZNEJ POLITECHNIKI WROCLAWSKIEJ

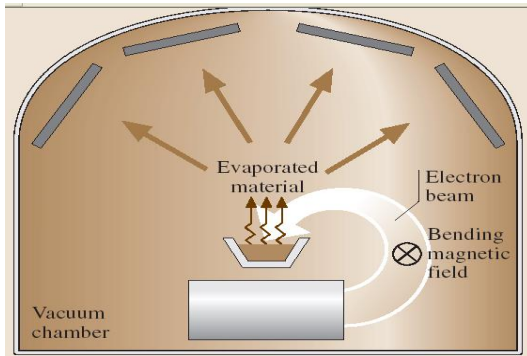


Figure 3.18 In the **evaporation technique** (metal depositions) the source is placed in a small container with tapered walls, called a crucible, and heated up to a temperature at which the evaporation occurs [123].

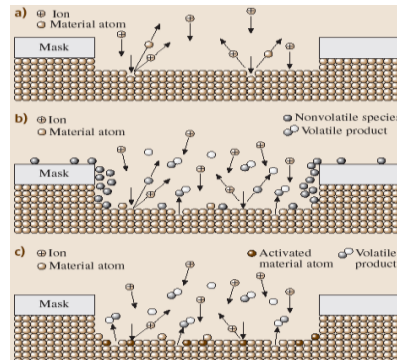


Figure 3.19 **Etching** (Selectivity and Directionality): Wet etching: (a) isotropic and (b) anisotropic. Dry etching (plasma based)

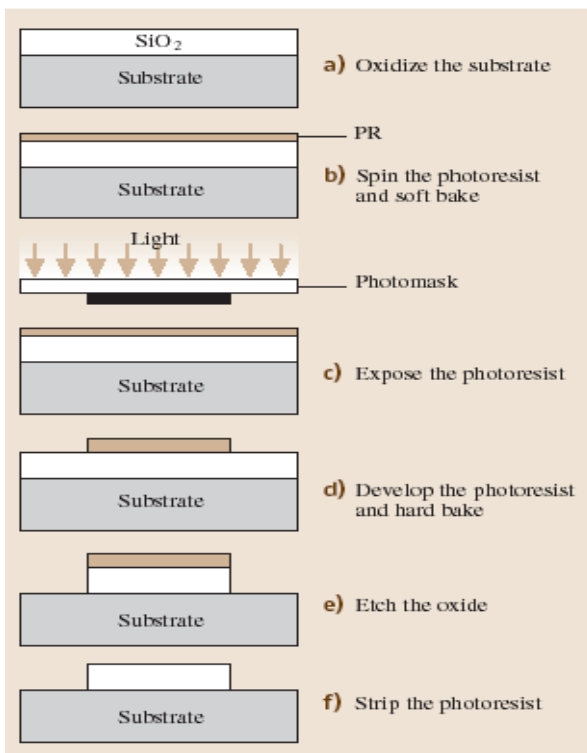


Figure 3.20 **Lithography** is the technique used to transfer a computer generated pattern onto a substrate (silicon, glass, GaAs etc.). This pattern is subsequently used to etch an underlying thin film (oxide, nitride, etc.).





ROZWÓJ POTENCJAŁU I OFERTY DYDAKTYCZNEJ POLITECHNIKI WROCŁAWSKIEJ

4. Optical properties of zero dimensional semiconducting structures

Fascinating properties of quantum dots have been used already in ancient times in paintings, ceramics etc. where people used scattering properties of golden, silver and many other metallic quantum dots. For example **Fig. 4.1(a)** shows some ceramic from *Manises* (XV century) while **Fig. 4.1 (b)** shows TEM image of this ceramic with well recognizable quantum dots inside. However, even if metallic quantum dots are the first used by human the semiconducting quantum dots revolutionary the nowadays technology. The first paper which deals with electron confinement in three dimensions appears in early 60' [¹²⁴] and then in 80' by Brus [¹²⁵], Ekimova [¹²⁶], Efrosa [¹²⁷], Brusa [¹²⁸], Weller [¹²⁹] and Hengelin [¹³⁰].

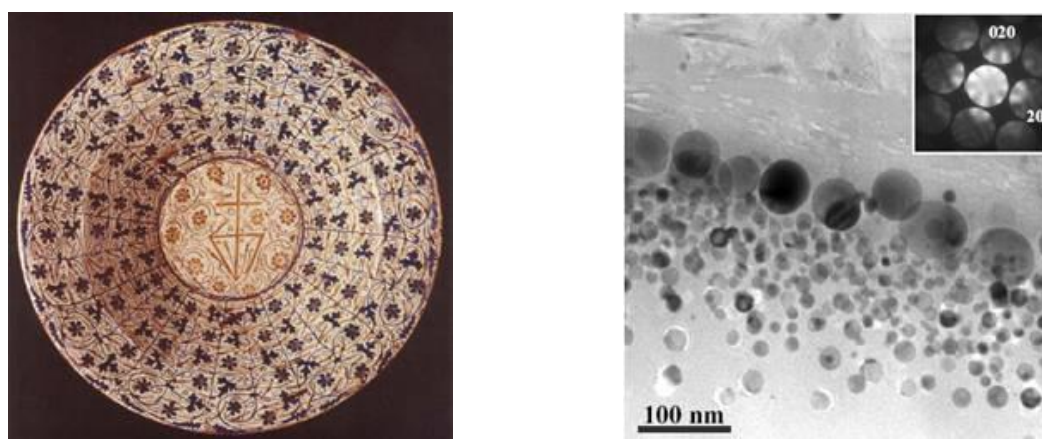


Figure 4.1 (a) Ceramic from Manises (XV century), museum in Barcelona, Spain, (b) TEM image of ceramic from Manises [¹³¹].

¹²⁴ Frölich (1937) and Kubo (1962)

¹²⁵ R. Rossetti and L. Brus, Electron-Hole Recombination Emission as a Probe of Surface Chemistry in Aqueous CdS Colloids, J.Phys. Chem., 86 23 4470-4472, (1982); A. I. Ekimov and A. A. Onushchenko,

Quantum size effect in three-dimensional microscopic semiconductor crystals, Journal of Experimental and Theoretical Physics Letters 34 6 346-349, (1982); Al. L. Efros and A. L. Efros, Interband absorption of light in a semiconductor sphere, Soviet Physics: Semiconductors 16 7 772-775, (1982)

¹²⁶ A.I.Ekimov, A.A.Onushenko, V.A.Tzekhomskii, Sov. Phys. Semicond. 6, 511 (1980).

¹²⁷ Al. L. Efros, A.L. Efros, Sov. Phys. Semicond. 16, 772 (1982).

¹²⁸ L.E.Brus, J. Phys.Chem. 79, 5566 (1983).

¹²⁹ H. Weler, H. Koch, U. Gutierrez, M.Henglein, Phys. Chem. 88, 594 (1984).

¹³⁰ A.Hengelin, Ber Bunsenges, Phys.Chem.88, 301 (1982).

¹³¹ Josefina Perez-Arategui, Angel Larrea, Trends in Analytical Chemistry 22, 327 (2003).



ROZWÓJ POTENCJAŁU I OFERTY DYDAKTYCZNEJ POLITECHNIKI WROCŁAWSKIEJ

This issue has been strongly developed when in 1982 Y. Arakawa has proposed this kind of nanomaterial as an excellent candidate for laser material [¹³²]. However, it has been quickly found that the only technique which can be able to deliver quantum dots with high enough quality is MBE. However, very soon two other important papers have shown high potential of use chemically obtained quantum dots. Namely, as part of 3D crystals [¹³³] and optical marker in nano-biomedicine [¹³⁴]. Since that time, technology, understanding and applications of chemically grown nanocrystals have been strongly developed [¹³⁵, ¹³⁶].

In principle the quantum dots can be divided into 8 groups: (i) nanocrystalline powders, (ii) nanocrystalline films, (iii) nanocrystalline seeds, (iv) self assembly quantum dots, (v) porous materials, (vi) electrically formed quantum dots, (vii) quantum dots obtained by lithography, and (viii) C-60 or other molecularly obtained zero dimensional objects which all have been shown in **Fig 1.4**. The first three kinds of quantum dots (QDs) we will be also called as nanocrystals (NCs). In the case of nanocrystals we can also make other classification. The more general name can be nanoclusters. In this case, when the nanoclusters exhibit well defined crystallographic structure we will call them nanocrystals but when there won't be any indication of local atomic ordering we will call our materials nanocluster or amorphous nanocluster.

Historically, the first well investigated nanocrystals were nanocrystals from group II-VI i.e. CdS, CdSe, and latter same nanocrystals covered by some additional shell like ZnS, ZnSe or organic layer. From the point of view of application the development of nanocrystals can be divided onto few areas:

- (a) **optoelectronics**: optical amplifiers [¹³⁷], single photon sources, LEDs and lasers [¹³⁸, ¹³⁹, ¹⁴⁰, ¹⁴¹], sensitizers, holography [¹⁴²], photovoltaic [¹⁴³], photo-catalysis

¹³² Y. Arakawa and H. Sakaki (laser), Appl. Phys. Lett., vol. 40, pp. 939-941(1982).

¹³³ C. B. Murray, C. R. Kagan, M. G. Bawendi, Self Organization of CdSe Nanocrystallites into Three-Dimensional QD Superlattices Science 270 5240 1335-1338, (1995)

¹³⁴ P. Alivisatos, et al. Organization of 'nanocrystal molecules' using DNA Nature 382 6592 609-611, (1996) J. G. C. Veinot, M. Ginzburg, and W. J. Pietro Surface Functionalization of Cadmium Sulfide Quantum-Confined Nanoclusters, Chemistry of Materials 9 10 2117-2122, (1997); M. Bruchez Jr., M. Moronne, P. Gin, S. Weiss, and A. P. Alivisatos Semiconductor Nanocrystals as Fluorescent Biological Labels, Science 281 2013-2015, (1997)

¹³⁵ L.E. Brus, Appl. Phys. Lett. 53, 465 (1991).

¹³⁶ A.P. Alivisatos, Science 271, 933 (1996).

¹³⁷ Sergei A. Ivanov, Jagjit Nanda, Andrei Piryatinski, Marc Achermann, Laurent P. Balet, Ilia V. Bezel, Polina O. Anikeeva, Sergei Tretiak, and Victor I. Klimov, Light Amplification Using Inverted Core/Shell Nanocrystals: Towards Lasing in the Single-Exciton Regime, J. Phys. Chem. B 2004, 108, 10625-10630

¹³⁸ Y. Vandyshv, V. Dneprovskii, V. Klimov, D. Okorokov, JEPT Lett. 54, 442 (1991).



ROZWÓJ POTENCJAŁU I OFERTY DYDAKTYCZNEJ POLITECHNIKI WROCŁAWSKIEJ

- (b) **bio-nano medicine:** ex-vivo live cell imaging, in-vivo targeting, fixed cell imaging, biosensors [¹⁴⁴],
- (c) **nanoelectronics:** nanomemories,
- (d) **macrocrystals synthesis** [¹⁴⁵].

Moreover, very recently we can observe strong development in synthesis of silicon nanocrystals with use in photovoltaics and light sources which can be used for optical computer and telecommunication. Furthermore, nanocrystals are also used as nano-laboratory when many fundamental physical processes can be examined and verified [¹⁴⁶, ¹⁴⁷, ¹⁴⁸].

In the next sections we will describe the main physical effects which can be observed in optical properties of zero dimensional nanomaterials.

4.1 Band gap modifications

As it has been already mentioned in the previous sections when the size of semiconductor is reduced down to nanometre range, at some critical size its band gap starts strongly increases and energy levels become discrete. This is due to strong *quantum confinement* of carriers (electron/holes) in material. This effect has been shown schematically in **Fig. 4.2 (a)**. Moreover, as it can be seen from **Fig. 4.2 (b)** this effect can be used to modeling the materials which can be characterized by different emission wavelengths.

¹³⁹ V.I.Klimov, A.A.Mikhailovsky, Su.Xu, A.Malko, J.A.Hollingsworth, C.A.Leatherdale, H.J.Eisler, M.G.Bawendi, Science 290, 314 (2000).

¹⁴⁰ B.O.Dabbousi, M. Bawendi, O.Onitsuka, M.F.Rubner, Appl. Phys. Lett. 66, 1316 (1995).

¹⁴¹ V.Colvin, M.Schlamp, A.Alivisatos, Nature 370, 354 (1994).

¹⁴² B. Kraabel, A. Malko, J.A.Hollingsworth, V.I.Klimov, Appl.Phys.Lett.78, 1814 (2001).

¹⁴³ A.Hagfeld, M.Graetzel, Chem. Rev. 95, 49 (1995).

¹⁴⁴ W.C.W.Chan, S. Nie, Science 281, 2016 (1998).

¹⁴⁵ Elena V. Shevchenko, Dmitri V. Talapin, Christopher B. Murray, and Stephen O'Brien, J. Am. Chem. Soc. 128, 3620-3637 (2006).

¹⁴⁶ C.C.Chen, A.B.Herhold, C.S.Johnson, A.P.Alivisatos, Science 276, 398 (1997).

¹⁴⁷ J.N.Wickham, A.B.Herhold, A.P.Alivisatos, Phys.Rev.Lett. 84, 923 (2000).

¹⁴⁸ K. Jacobs, D.Zaziski, E.C.Scher, A.B.Herhold, A.P.Alivisatos, Science 293, 1803 (2001).

ROZWÓJ POTENCJAŁU I OFERTY DYDAKTYCZNEJ POLITECHNIKI WROCLAWSKIEJ

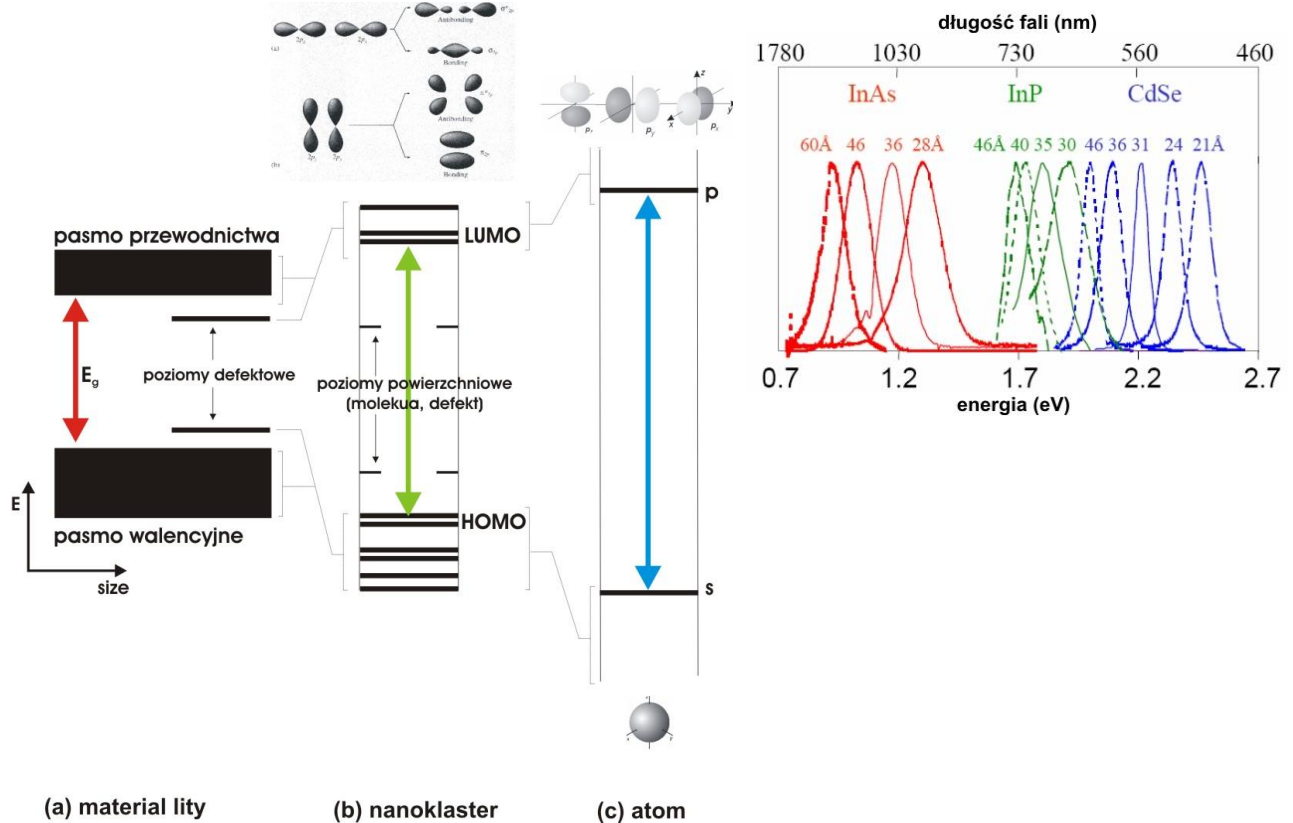


Figure 4.2 (a) Schematic modifications in energy structure during the transition from bulk material to atom, (b) examples of emission control by changing NCs size and composition [149].

Unfortunately, the characteristics that make quantum dots interesting also make them inherently difficult to study. Variations in size and shape within ensemble samples can result in extensive inhomogeneous spectral broadening. The result is a loss of spectral information in ensemble samples. For instance, theory predicts that quantum dots should have a spectrum of discrete, atomic-like energy states. However, while the discrete nature of the excited states in CdSe nanocrystals has been verified, transition line widths appear significantly broader than expected (see Fig. 4. 2). This is true even when size-selective optical techniques are used to extract homogeneous line widths. In addition, incoherent dynamic and orientational effects may exist, which can be completely hidden when averaged over an ensemble.

¹⁴⁹ M. Bruchez, M. Moronne, P.Gin, S.Weiss, A.P.Alivisatos, Science 281, 2013 (1998).



ROZWÓJ POTENCJAŁU I OFERTY DYDAKTYCZNEJ POLITECHNIKI WROCŁAWSKIEJ

4.2 Nonlinear effects

The response of the materials to the application of static or time varying electric field is the key ingredient in the design and investigation of NLO materials. Response properties of molecular system in general involves energy derivatives namely polarizabilities and hyperpolarizabilities. The electric dipole moment can be expanded into different orders of external fields. It is represented as

$$\begin{aligned} \mu_a = & \mu_a(E^b = E^c = E^d \dots = 0) + \sum_b \alpha_{ab} E^b \\ & + 1/2 ! \sum_{bc} \beta_{abc} E^b E^c + 1/3 ! \sum_{bcd} \gamma_{abcd} E^b E^c E^d, \end{aligned}$$

where $E_a(r, t)$, $E_b(r, t)$, . . . , are the external electric fields consisting of a monochromatic and a static part and the Cartesian directions a, b, \dots equal to x, y , or z . In the expansion, the first term corresponds to permanent dipole moment of the sample. α_{ab} , β_{abc} , and γ_{abcd} represent the elements of linear polarizability tensor, first order hyperpolarizability tensor and second order hyperpolarizability tensor, respectively. Time dependence of dipole moment leads to various frequency dependent polarizability and hyperpolarizability tensors. The first order hyperpolarizability tensor is described in terms of three frequency dependent components namely second harmonic generation (SHG), electrooptical Pockels effect (EOPE), optical rectification (OR) and the static first order hyperpolarizability. In the same way, in addition to the static analog the frequency dependent components of second order hyperpolarizability tensor are third harmonic generation (THG), electrooptical Kerr effect (EOKE), dc-induced second harmonic generation (dc-SHG) and intensity dependent refractive index (IDRI) or degenerate four-wave mixing (DFWM).

Due to discrete energy levels in nanocrystals, the preferred process is excitation of one excitons per one NCs. However, at high excitation flux the higher energy states filling can be observed which can be observed as strong increases in nonlinear properties of nanocrystals.



ROZWÓJ POTENCJAŁU I OFERTY DYDAKTYCZNEJ POLITECHNIKI WROCŁAWSKIEJ

At the same time with the further increase in excitation flux we observe so-called *saturation phenomenon*. The origin of this effect can be related to many body interactions in single NCs [¹⁵⁰, ¹⁵¹] which interaction in general depend on the NC size. In this way we can control the nonlinear properties of the NCs by controlling their size. Such strong nanolinear effects are difficult to observe in bulk materials due to small separation between energy levels and efficient thermal carriers relaxation.

4.3 Shape effects

The important property of nanocrystals except the possibility of their size control is also ability to control their shape. The shape became in this way another parameter which can be used to control optical properties of nanocrystals. Except, the changes in band gap and excited states positions the main consequence of changing the nanocrystals shape from spherical to elongated in one direction are changes in polarization properties of such nanostructures.

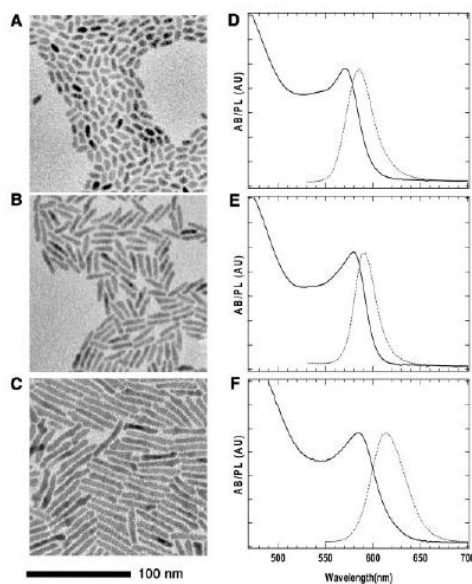


Figure 4.3 TEM images and (D through F) UV-Vis absorption (solid lines) and

Some recent theoretical calculations [¹⁵²] predicts a sharp transition from plane-polarized emission to highly linearly polarized emission when the nanocrystals change from spherical to rodlike, even for an aspect ratio of not much greater than unity (see Fig.4.3(b)).

Furthermore, theoretical calculations also suggest that the global Stokes shift [the energy difference between the first ultraviolet-visible (UV-Vis) absorption peak and the luminescence peak of the nanocrystals] should at first decrease and then increase as a function of the aspect ratio. These two

¹⁵⁰ V.Klimov, Handbook on Nanostructured Materials and Nanotechnology edited by H.Nalwa, (Academic Press, San Diego, 1999).

¹⁵¹ Semiconductor Nanocrystals, From Basic Principles to Applications, Ed. A.L.Efros, D.J.Lockwood, L. Tsybeskov, Kluwer Academic/Plenum Publishers, New York (2003).

¹⁵² Jiangtao Hu, Liang-shi Li, Weidong Yang, Liberato Manna, Lin-wang Wang, A. Paul Alivisatos, Linearly Polarized Emission from Colloidal Semiconductor Quantum Rods, Science 292, 2060 (2001)

ROZWÓJ POTENCJAŁU I OFERTY DYDAKTYCZNEJ POLITECHNIKI WROCLAWSKIEJ

photoluminescence (dotted lines) spectra of three rod samples. Quantum rods with diameters of ~ 4.2 nm and lengths of 11 [(A) and (D)], 20 [(B) and (E)], and 40 nm [(C) and (F)]. [¹⁵³]

predictions of the empirical pseudopotential calculations are also qualitatively reproduced in eight-band effective-mass-approximation calculations.

Some other example of such modification in polarization properties are presented in **Fig. 4.4** and **4.5**.

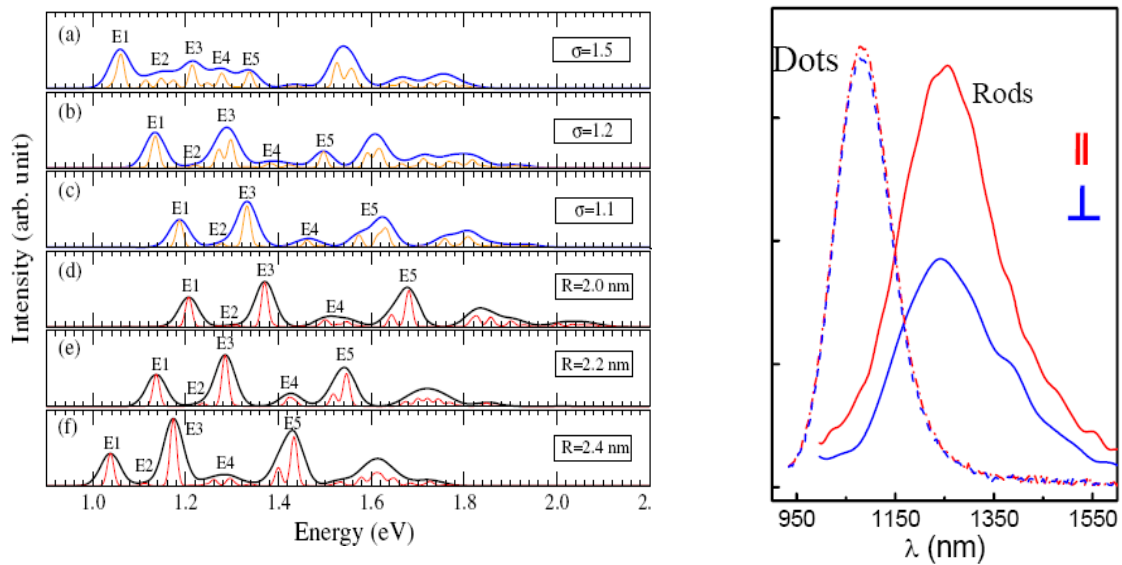
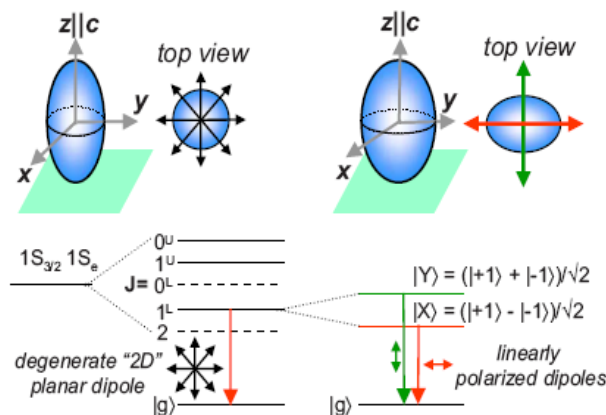


Figure 4.4 Optical absorption spectra calculated for InAs NCs with $R = 20$ Å and $\sigma = 1.5$ (a), 1.2 (b), 1.1 (c) and 1.0 (d) and dots ($\sigma = 1$) with $R = 21.7$ (e) and 24.1 Å (f), using a broadening of 30 meV (black and blue thick lines) and 10 meV (red and orange thin lines). [¹⁵⁴], (b) emission spectra recorded for spherical and elongated InAs NCs.



¹⁵³ Jiangtao Hu, Liang-shi Li, Weidong Yang, Liberato Manna, Lin-wang Wang, A. Paul Alivisatos, Linearly Polarized Emission from Colloidal Semiconductor Quantum Rods, Science 292, 2060 (2001)

¹⁵⁴ T Puangmali, Marco Califano and P Harrison, The effect of small elongations on the electronic and optical signatures in InAs nanocrystal quantum dots, J.Phys.Condens.Matter 21, 144212 (2009)



ROZWÓJ POTENCJAŁU I OFERTY DYDAKTYCZNEJ POLITECHNIKI WROCŁAWSKIEJ

Figure 4.5 Different polarization axis and their modifications with the shape distortion [¹⁵⁵].

Emission polarization can be studied in single nanocrystals by measuring changes in the detected emission intensity as a linear polarizer (analyzer) is rotated in the detection pathway. In the single molecules studied to date, a unidirectional transition dipole exists, creating a single “bright axis” along which the emitted light is coupled. The strength of emission as a function of polarization is proportional to $|\mu\mathbf{E}|^2$, where μ is the transition dipole vector and \mathbf{E} is the polarization of the emitted light. The intensity of the detected signal is then proportional to $\cos^2(\Theta)\cos^2(\phi)$ where Θ is the angle between the emission polarization and the projection of μ onto the sample plane (the plane normal to the detection axis), and ϕ is the tilt angle between μ and the sample plane (out-of plane angle). When a polarizer is rotated in the emission pathway, the detected intensity oscillates between $I_{\min} = 0$ and $I_{\max} = |\mu|^2\cos^2(\phi)$.

The varying degrees of polarization shown in **Fig.4.6** are actually the result of the nature of the emission transition dipole. Due to the prolate shape and unidirectional wurtzite crystal structure, theoretical calculations have predicted two potential transition dipole orientations for the band edge states of CdSe nanocrystals [¹⁵⁶]. The first is similar to what was described above for single molecules, with a unidirectional “bright axis” oriented parallel to the wurtzite c-axis. Transitions involving these states should have a polarization dependence similar to what is seen for single DiI molecules, with a high degree of polarization observed for every nanocrystal. The other potential orientation is a doubly degenerate two-dimensional transition dipole oriented isotropically in the xy plane of the nanocrystal. In this case, what remains is a unidirectional “dark axis” along which no light is emitted. This “dark axis” is oriented parallel to the c-axis. Transitions involving states with a “dark axis” should show very different polarization dependence than “bright axis” states.

¹⁵⁵ S.A. Empedocles, Phys. Rev. Lett. 77, 3873 (1996)

¹⁵⁶ A. L. Efros, Phys. Rev. B 1992, 46, 7448



ROZWÓJ POTENCJAŁU I OFERTY DYDAKTYCZNEJ POLITECHNIKI WROCŁAWSKIEJ

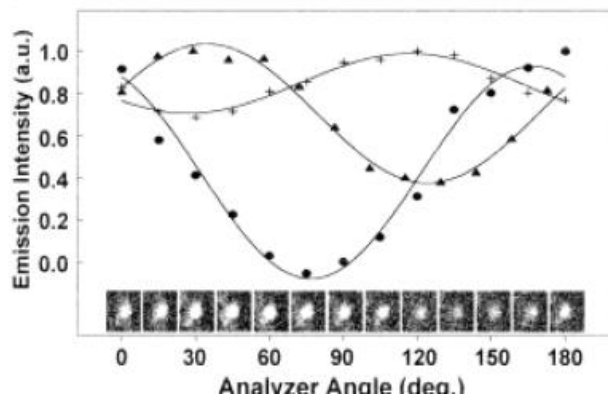


Figure 4.6 Single nanocrystal polarization spectroscopy. Normalized emission intensity of three single 0.52 nm overcoated nanocrystals as a function of analyzer angle. The solid lines correspond to the fit to a sine-squared function of analyzer angle with a 180° period. Data in Figure 5 is the average of six complete 180° rotations. All data was taken with a 5 s integration time, 60 W/cm² excitation intensity and 0° excitation polarization [].

The data in **Fig. 4.6** suggests that emission in CdSe nanocrystals results from a “dark axis” state. This is not surprising since the two lowest optically active states in CdSe nanocrystals are predicted to have “dark axis” transition dipoles. Since the lowest excited state is formally spin forbidden, emission is likely to proceed through some form of mixing or phonon mediated transition involving one of these near-lying optically active states.

There are two additional effects that contribute to the predicted polarization dependence of both “bright” and “dark” axis transitions and therefore affect the shape of the expected probability distribution. First, we have only considered the radiation pattern from an isolated dipole in free space. However, the pattern of radiation from a dipole in a thin film on a dielectric interface has been found, both theoretically and experimentally to be significantly different to that of a free dipole. Second, we have so far assumed an infinitely small collection angle in our detection optics.

In addition, changes in the orientation of the transition dipole over time could indicate either rotation of the nanocrystal within the sample or significant changes in the electronic structure.

4.4 Lattice vibrations

As it can be seen from **Fig. 4.7** reduction in nanocrystals size leads to strong modification in their crystallographic structure. These modifications will be reflected in



ROZWÓJ POTENCJAŁU I OFERTY DYDAKTYCZNEJ POLITECHNIKI WROCLAWSKIEJ

available for the excited carriers vibrational modes. Moreover, as it can be seen from **Fig.4.7** in the case of spherical NCs new, so-called surface vibrational modes appears.

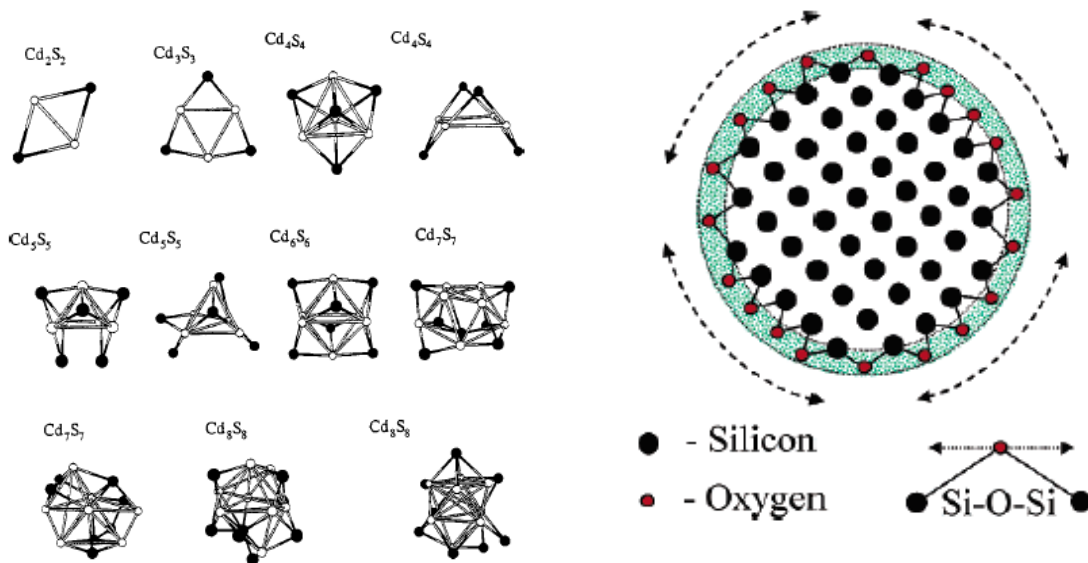


Figure 4.7 Evolution of CdS NCs crystallographic structure when the number of atoms increases. The right picture shown different vibration modes in Si nanocrystals placed in the SiO₂ matrix.

4.5 Surface related effects

Due to high surface-to-volume ratio (S/V) [¹⁵⁷] the surface of NCs plays an important and very often determining role in optical properties of NCs. *Wise* [¹⁵⁸] estimated that for CdSe NCs with the size of excitons Bohr radius approximately 30% all atoms are atoms at the surface. The main reason of such importance of surface in nanocrystals is existence at the surface number of defect states or other in nature surface states which will strongly modifies the relaxation and recombination processes since the excited wave function very quickly is

¹⁵⁷ L.J.Brus, P. Szajowski, W. Wilson, T. Harris, T. Schuppler, P. Citrin, J. Am. Chem. Soc. 117, 2915, (1995).

¹⁵⁸ F.W.Wise, Accounts of Chem. Res. 33 (11), 773 (2000).



ROZWÓJ POTENCJAŁU I OFERTY DYDAKTYCZNEJ POLITECHNIKI WROCŁAWSKIEJ

localized at the surface. Taking into account the surface in theoretical investigations is very difficult task. For this reason most of recent calculations have been done for fully passivated nanocrystals. Also for this reason the only reasonable agreement between experiment and theory up to now has been obtained for core shell NCs where approximation of fully passivated NCs is reasonable. In reality surface atoms of NCs interact strongly with their local environment leading to following effects: (a) different than ideal configuration of atoms at the surface (strain) [surface reconstruction is needed as it has been shown in **Fig. 4.8 (a)**], (b) existence strongly localized states at the surface (**Fig.4.8 (b)**). This means that even for the NCs with the same size we deal with different surface configurations leading to different optical properties (see nano1, nano2 in **Fig. 4.8 (b)**). All these effects are much less significant in the case of amorphous nanoclusters.



ROZWÓJ POTENCJAŁU I OFERTY DYDAKTYCZNEJ POLITECHNIKI WROCLAWSKIEJ

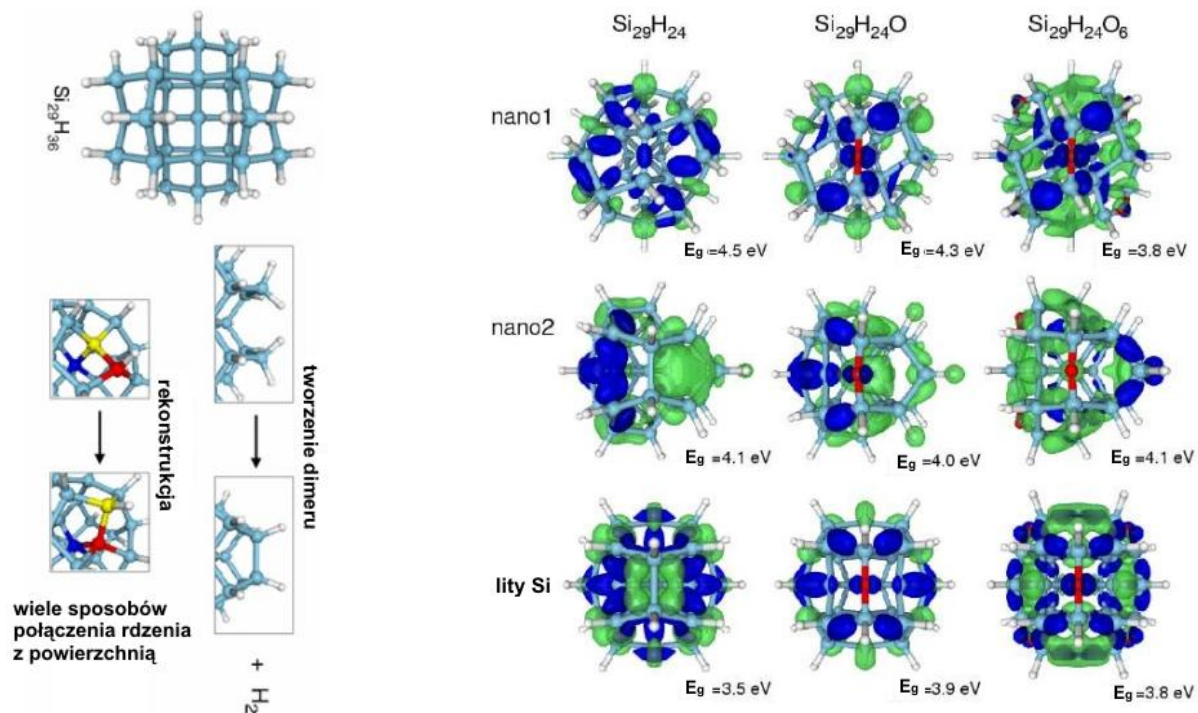


Figure 4.8 (a) Different variants of surface reconstruction for Si_{29} . Fully spherical and passivated by hydrogen Si NCs ($\text{Si}_{29}\text{H}_{36}$) (b) influence of oxygen adsorption on HOMO (blue) and LUMO (green). Band gap values obtained based on QMC technique. Legend: $\text{Si}_{29}\text{H}_{24}$ (bulk), $\text{Si}_{29}\text{H}_{24}$ (nano1), $\text{Si}_{29}\text{H}_{24}$ (nano2) [¹⁵⁹].

One of solutions to include the surface in theoretical calculations is *Density Functional Theory* (DFT) and *Quantum Monte Carlo* (QMC). Recent calculations show that presence of hydrogen or oxygen at the NCs surface has strong influence on the energy structure of NCs and excitons lifetime [¹⁶⁰]. The presence of oxygen cause the reduction in energy band gap (**Fig. 4.8 (b)**). **Figure 4.8 (b)** shows izosurfaces of HOMO and LUMO orbitals for silicon NCs obtained from 35 atoms a passivated by different atoms, i.e. hydrogen oxygen fluor.

¹⁵⁹ A. Puzder, A. J. Williamson, J.C. Grossman, G. Galli, Surface control of optical Properties of silicon nanoclusters, *J. Chem. Phys.* **117**, 6721 (2002), A. Puzder, A. J. Williamson, J.C. Grossman and G. Galli, Surface Chemistry of silicon nanoclusters, *Phys. Rev. Lett.* **88**, 097401 (2002)

¹⁶⁰ N. Daldosso, M. Luppi, S. Ossicini, E. Degoli, R. Magri, G. Dalba, P. Fornasini, R. Grisenti, F. Rocca, L. Pavesi, S. Boninelli, F. Priolo, C. Spinella, F. Iacona, *Phys. Rev. B.* **68**, 085327 (2003).

ROZWÓJ POTENCJAŁU I OFERTY DYDAKTYCZNEJ POLITECHNIKI WROCŁAWSKIEJ

Figure 4.9 [161] shows experimentally and theoretically obtained results for NCs passivated by oxygen and hydrogen.

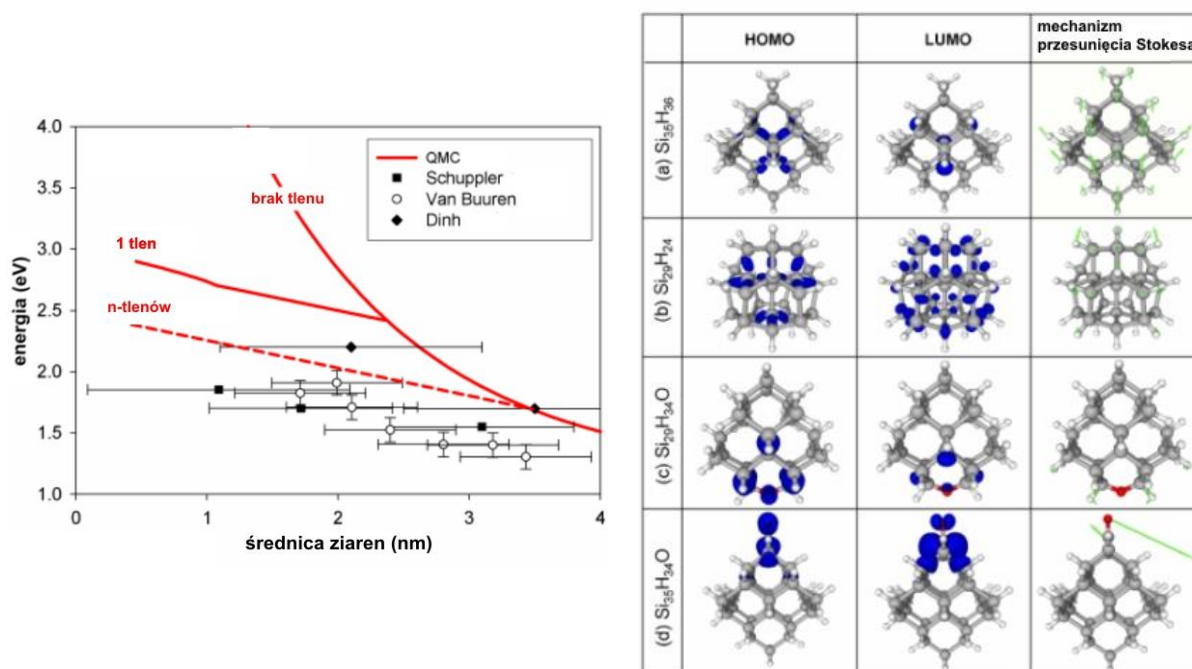


Figure 4.9 Comparison of experimental results for band gap measurements (Schuppler [162], Van Buuren [163], Dinh [164]) with theoretical ones for Si NCs passivated with different degree by oxygen. Right: Silicon nanoclusters with different surface properties with size of ~ 1 nm [165].

Theoretical calculations have show that even absorption properties of NCs their emission properties can be very different and strongly depends on surface properties. **Figure 4.9** shows theoretical calculations done for NCs with 1 nm size. **Figure 4.9 (a)** shows NCs passivated only by hydrogen atoms and without surface reconstruction. In this case both HOMO and LUMO orbitals are localized inside the NCs. **Figure 4.9 (b)** shows that HOMO and LUMO orbitals are localized at the surface when surface is after reconstruction. **Figure 4.9 (c)** shows influence of introducing only one oxygen atom in Si-O-Si position at the reconstructed surface. Similar effect has been observed for F atom. In this case bigger part of

¹⁶¹ A. Puzder, A.J. Williamson, F. Reboredo, G. Galli, Structural Stability and Optical Properties of Nanomaterials with Reconstructed Surfaces, *Physical Review Letters* **91**, 157405 (2003)

¹⁶² S. Schuppler, S. L. Friedman, M. A. Marcus, D. L. Adler, Y. H. Xie, F. M. Ross, *Phys. Rev. B* **52**, 4910 (1995).

¹⁶³ T. van Buuren, L. N. Dinh, L. L. Chase, W. J. Siekhaus, L. J. Terminello, *Phys. Rev. Lett.* **80**, 3803-3806 (1998).

¹⁶⁴ L. N. Dinh, L. L. Chase, M. Balooch, W. J. Siekhaus, F. Wooten, *Phys. Rev. B* **54**, 5029-5037 (1996).

¹⁶⁵ A. Puzder, A. J. Williamson, J.C. Grossman, G. Galli, *Optical Emission of Silicon nanoclusters*, *J. Amer. Chem. Soc.* **125**, 2786 (2003).



ROZWÓJ POTENCJAŁU I OFERTY DYDAKTYCZNEJ POLITECHNIKI WROCLAWSKIEJ

orbitals is localized inside the NCs core. In the case of placing the oxygen atoms in Si=O position onto not reconstructed surface, HOMO-LUMO orbitals are totally localized onto Si=O bond. Moreover, **Fig.4.9** shows influence of excitons formation on vibrational properties of NCs, where length of arrows corresponds to distance of atoms from their equilibrium positions. And respectively, averaged square deviation for tatory H-passivated NCs $\text{Si}_{35}\text{H}_{36}$, is equal to $\sim 0.3 \text{ \AA}$ when the NCs size is equal to 1nm and strongly is reduced to values Lower than 0.1 \AA for bigger NCs up to 2 nm. For NCs with additional oxygen at the surface $\text{Si}_{35}\text{H}_{34}\text{O}$ (**Fig. 4.9 (d)**) deviation is a bit higher. However, in this case, deformations focus around the oxygen atom. In this case the Stokes shift strongly depends on NCs size because the HOMO and LUMO orbitals are localized on the Si=O bond.

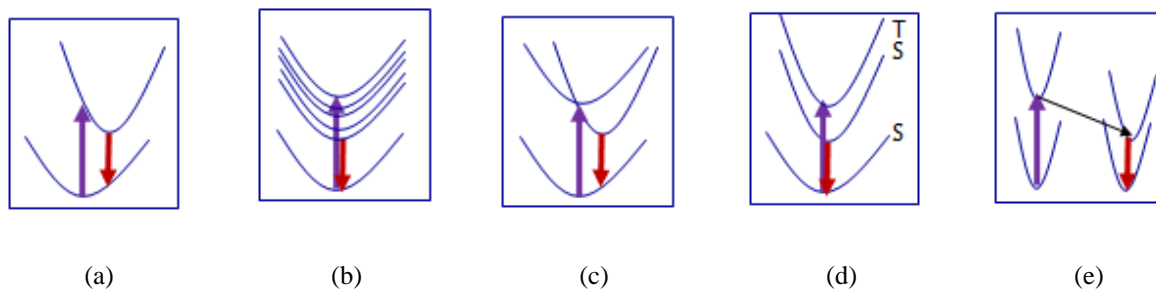


Figure 4.10 Different mechanisms responsible for observed experimentally Stokes Shift (a) strong Franck-Condon coupling: lattice relaxation, (b) weak Franck-Condon coupling: lattice relaxation, (c) excitons localization, (d) Coulomb interactions, (e) excitons migration.

In this place, it is worth to mention about the other mechanisms responsible for Stokes Shift (Δ_s) formation in nanostructures. In the most common version the Stokes Shift is defined as difference between the main absorption peak and the main emission peak energy positions ($\Delta_s = E_0 - E_{PL}$). The value of Stokes shift $\Delta_s \neq 0$ mean that emission is coming from the levels lower than the levels to which carriers have been excited.

The first effect responsible for the Stokes shift can be due to formation of dark and bright excitons in NCs. This situation is shown in **Fig. 4.10 (d)**. In this case the values of Stokes shift are in the range from several meV up to 20-30 meV for very small NCs. Other effect, responsible for observed Stokes shift is coupling of excited carriers with lattice vibrations (**Fig. 4.10 (a-b)**). In the case of strong coupling the NCs structure is strongly



ROZWÓJ POTENCJAŁU I OFERTY DYDAKTYCZNEJ POLITECHNIKI WROCLAWSKIEJ

modified after the excitation and recombination is placed in new metastable structure. In this case the values of Stokes shift are much higher and can be as high as 1-2 eV. The most common mechanism responsible for Stokes shift is excited carriers relaxation from excited states to defect/surface states from which carriers recombine radiatively (**Fig. 4.10 (c)**). Finally, the Stokes shift can be generated by excitons migration from the smallest one to the biggest one from which excitons recombine radiatively. This mechanism however, will be dominating only when we will deal with very high density of NCs which allows excitons to migrate nonradiatively in dipole-dipole process.

As it has been already discussed previously, to reduce the effect of surface, the surface is covered by additional layer called shell. The example of such solution with consequences to wavefunctions of excited carriers has been shown in **Fig.4.11**

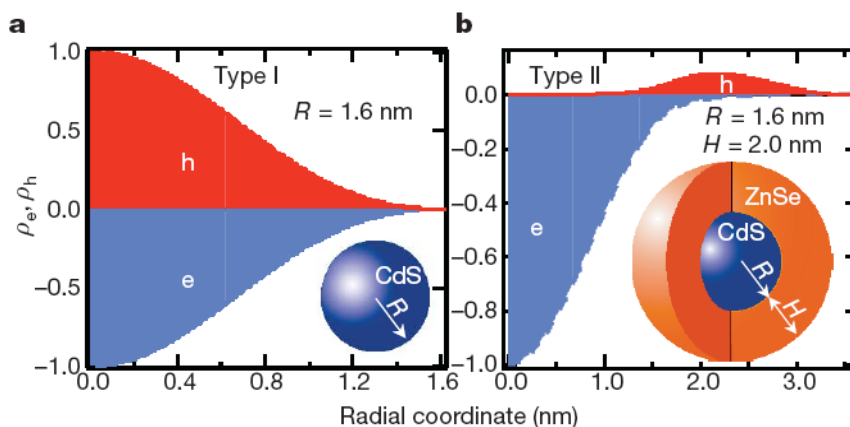


Figure 4.11 Wavefunctions localization for core CdS NCs and ones passivated by ZnSe layer [¹⁶⁶].

This layer, together with the variety of passivating agents, is deemed essential for cladding these NCs to achieve high photoluminescence PL efficiency (i.e., as high as 50%). If, however, various asperities (such as vacancies, incomplete coverage, and dangling bonds) are present at the outermost surface layer, NC PL efficiency is severely reduced [¹⁶⁷, ¹⁶⁸].

¹⁶⁶ Victor I. Klimov, Sergei A. Ivanov, Jagjit Nanda, Marc Achermann, Ilya Bezel, John A. McGuire & Andrei Piryatinski, Single-exciton optical gain in semiconductor nanocrystals, *Nature* 447, 441(2007)

¹⁶⁷ C. B. Murray, C. R. Kagan, and M. G. Bawendi, *Annu. Rev. Mater. Sci.* **30**, 545 (2000).

¹⁶⁸ A. P. Alivisatos, *J. Phys. Chem.* **100**, 13226 (1996).

ROZWÓJ POTENCJAŁU I OFERTY DYDAKTYCZNEJ POLITECHNIKI WROCLAWSKIEJ

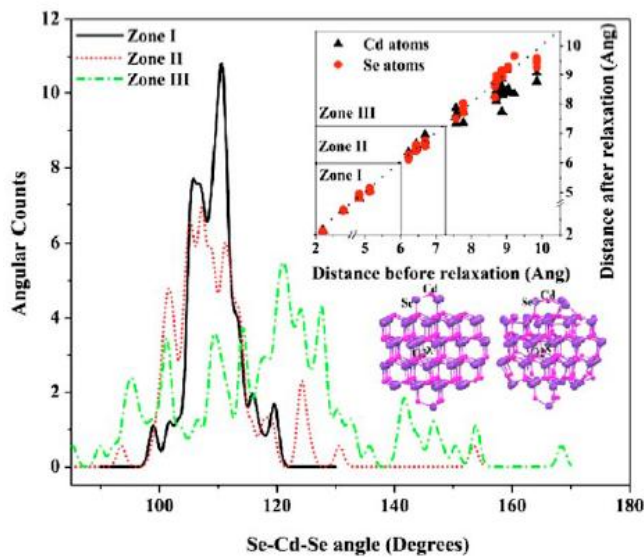


Figure 4.12 Angular and radial (top inset) relaxations for the 144 atom CdSe cluster whose structures before (bottom left inset) and after (bottom right inset) geometry optimization are also shown. Points that fall on the dotted line in the top inset correspond to atoms that have not relaxed radially. [¹⁶⁹]

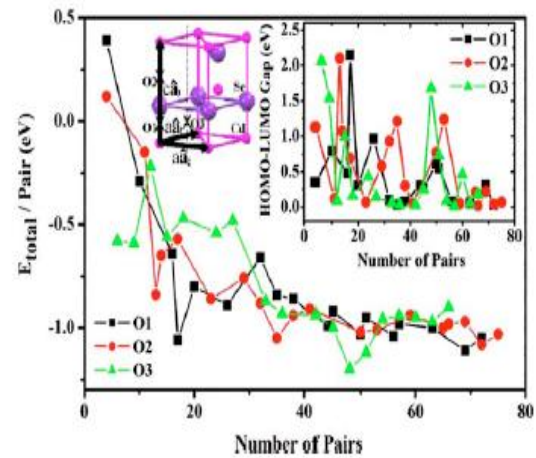


Figure 4.13 Calculated total energies per pair of the fully relaxed CdSe nanoclusters and the HOMO-LUMO gaps (right inset) as a function of the nanocluster size (number of CdSe pairs) for three different choices, O1, O2, and O3, of origin (left inset). Note the correlation between high stability and large HOMO-LUMO gaps, especially for smaller clusters containing 60 or less pairs.

Figure 4.12 (inset) illustrates the calculated (radial) structural relaxations of CdSe cluster (0.7 nm) from its initial starting geometry [which was based on an ideal wurtzite structure]. The dotted line represents the situation with no radial relaxations. In zone I, extending from the origin to 6 Å, atoms undergo negligible radial relaxations; this zone is thus the “core region” which is well screened from the surface atoms. In zone II, Cd and Se atoms show small but perceptible relaxations. In zone III, which consists mainly of surface atoms, Cd atoms prefer to move radially inward while some Se atoms move radially outward. **Figure 4.12** also shows the angular distribution of Se–Cd–Se bond angles of the same 144 atom cluster. In the core region (zone I), most of the Se–Cd–Se angles are within a few percent of the tetrahedral (109.5°) angle, indicating predominantly sp^3 bonding. The corresponding angles in zones II and III show progressively more dispersion, indicating that sp^3 -like bonds between Cd and its four neighboring Se atoms are not the dominant ones (especially in zone III, where angles in the neighborhood of 120° dominate, characteristic of sp^2 bonding). The total energies and

¹⁶⁹ M. Yu and G. W. Fernando, R. Li and F. Papadimitrakopoulos, N. Shi and R. Ramprasad, First principles study of CdSe quantum dots: Stability, surface unsaturations, and experimental validation, Appl.Phys.Lett. 88, 231910 (2006)



ROZWÓJ POTENCJAŁU I OFERTY DYDAKTYCZNEJ POLITECHNIKI WROCŁAWSKIEJ

HOMO-LUMO gaps calculated for clusters up to 75 CdSe pairs (150 atoms) are shown in **Fig. 4. 13** (inset). Several interesting trends can be observed. Firstly, the total energy per CdSe pair, E_{pair} , converges steadily with increasing cluster size. However, E_{pair} shows local minima, reminiscent of the so-called “magic sizes,” [170] with clusters composed of 13, 17, 26, 35, 48, 69, and 72 pairs displaying the maximum relative stability. Some of these clusters have already been identified by Kasuya *et al.* as having high stability based on their time-of-flight experiments [171]. Secondly, the stability is strongly a function of the choice of origins, especially for the small clusters. Thirdly, while the HOMO-LUMO (or optical) gaps generally decrease for increasing cluster sizes, occasional large gaps can be seen that correlate with a low E_{pair} (or high stability); i.e., the magic size clusters show relatively large, and locally largest, gaps. Inspection of the physical structure of the clusters indicates that the non-magic-size clusters have surface atoms with a high degree of unsaturation (two or more dangling bonds). These surface atoms give rise to electronic states, resulting in an apparent reduction in the HOMO-LUMO gap. It thus appears that, in contrast to previous beliefs, structural relaxation alone cannot open up the HOMO-LUMO gaps, especially in non-magic-size clusters. This expectation is further confirmed by explicit analysis of the DOS and its decomposition in terms of the contributions from various atomic basis functions (the partial density of states or PDOS).

Thus, the nature of the surface atoms in a given cluster crucially determines both the stability of the cluster and its optical gap. When the nanoclusters were allowed to relax from their bulk wurtzite positions, Cd atoms at the surface are observed to move inwards preferentially compared with Se atoms. A coordination number of 3 for all surface atoms resulted in closed-shell structures with high stability and maximum optical gap. One or more suboptimally coordinated surface atoms resulted in clusters with lower stability and smaller to negligible optical gaps.

4.6 Wave function localization

¹⁷⁰ L. E. Brus, *J. Phys. Chem.* **90**, 2555 (1986); Z. A. Peng and X. Peng, *J. Am. Chem. Soc.* **124**, 3343 (2002); V. N. Soloviev, A. Eichhöfer, D. Fenske, and U. Banin, *J. Am. Chem. Soc.* **122**, 2673 (2000).

¹⁷¹ A. Kasuya, R. Sivamohan, Y. A. Barnakov, I. M. Dmitruk, T. Nirasawa, V. R. Romanyuk, V. Kumar, S. V. Mamykin, K. Tohji, B. Jeyadevan, K. Shinoda, T. Kudo, O. Terasaki, Z. Liu, R. V. Belosludov, V. Sundararajan, and Y. Kawazoe, *Nat. Mater.* **3**, 99 (2004).



ROZWÓJ POTENCJAŁU I OFERTY DYDAKTYCZNEJ POLITECHNIKI WROCLAWSKIEJ

Optical recombination in silicon is a second-order process as it requires the involvement of an additional phonon to fulfill linear momentum conservation (see **Fig.4.14**). Except the fact that spatial confinement shift both absorbing and luminescing states to higher energies and affect the density of electronic states due to the rising of minimum kinetic energy, additionally the geometrical confinement results in delocalization of carriers in k -space thus allowing zero phonon optical transitions and significantly enhancing the oscillator strength of the zero phonon transitions in small Si nanocrystals [¹⁷²]. Moreover, due to the better overlap of electron and hole envelope wavefunctions one can expect a strong enhancement of the e-h exchange interaction inducing a splitting of the exciton levels [¹⁷³]. Finally, the local concentration of e-h pairs in nanocrystals due to the spatial confinement is very high and this can lead to a variety of nonlinear phenomena and irreversible consequences, one of which is Auger-autoionization of nanocrystals [¹⁷⁴].

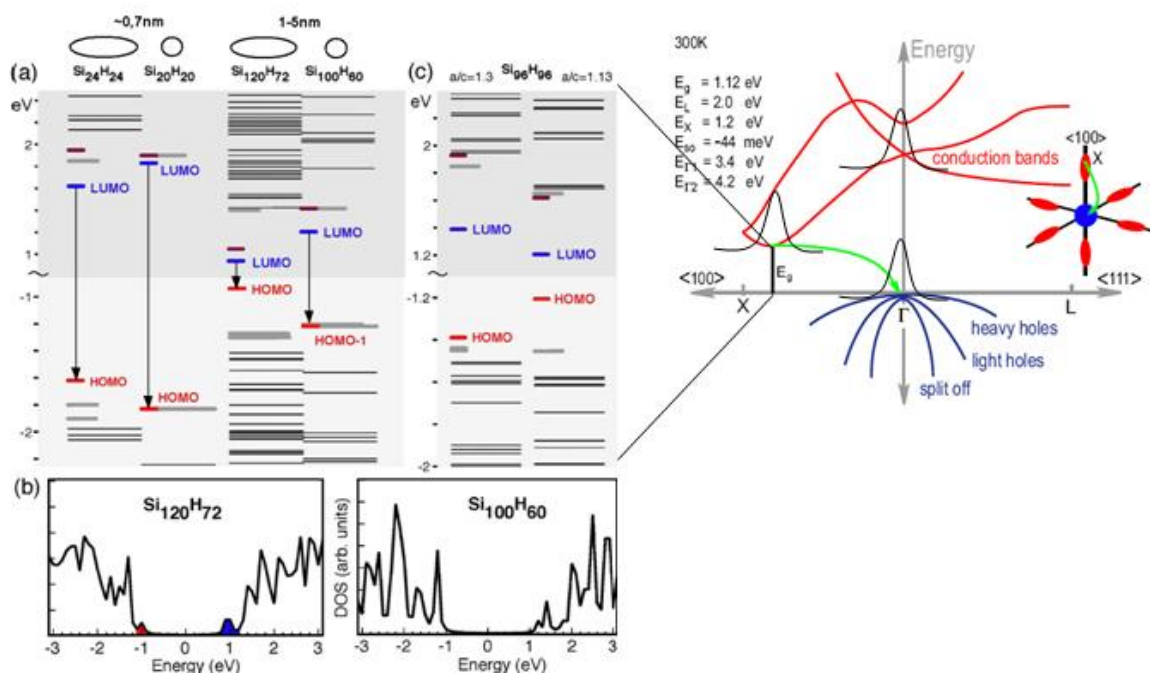


Figure 4.14 Energy band structure for bulk silicon (right side) and energy structure together with density of states calculated for silicon nanocrystals [¹⁷⁵].

¹⁷² M.S. Hybertsen, Phys. Rev. Lett. 72, 1514 (1994).

¹⁷³ A.I.L. Efros, M. Rosen, M. Kuno, M. Nirmal, D.J. Norris, and M. Bawendi, Phys. Rev. B 54, 4843 (1996).

¹⁷⁴ V.A. Kharchenko and M. Rosen, J. Lumin. 70, 158 (1996).

¹⁷⁵ S.G.Hao, Phys.Rev B 76, 081305R (2007).



ROZWÓJ POTENCJAŁU I OFERTY DYDAKTYCZNEJ POLITECHNIKI WROCLAWSKIEJ

4.7 Relaxation processes

On excitation with an ultrashort pulse, a semiconductor undergoes several stages of relaxation before returning to equilibrium. The energy is transferred first to the electrons and then to the lattice. The interaction includes several regimes of carrier excitation and relaxation. We can distinguish the following four regimes: (1) carrier excitation, (2) thermalization, (3) carrier removal and (4) thermal and structural effects. These regimes and the timescales for the corresponding processes are shown in **Fig.4.15**.

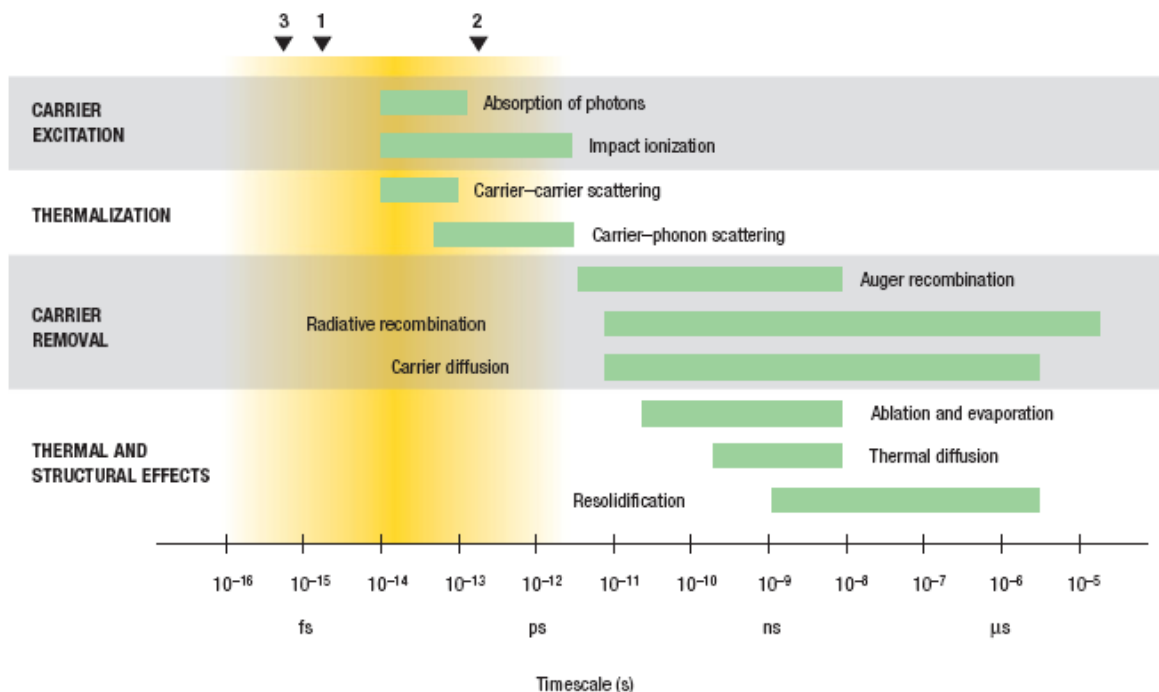


Figure 4.15 Timescales of various electron and lattice processes in laser-excited solids (after ref. [176]). Each green bar represents an approximate range of characteristic times over a range of carrier densities from 10^{17} to 10^{22} cm^{-3} . The triangles at the top show the current state-of-the-art in the generation of short pulses of electromagnetic radiation: 1 5 fs (visible), 2 120 fs (X-ray), 3 0.5 fs (far ultraviolet).

After the excitation, electrons and holes are redistributed throughout the conduction and valence bands by carrier-carrier and carrier-phonon scattering. Carrier-carrier scattering (**Fig. 4.16d**) is a two-body process (an electrostatic interaction between two carriers), which does not change the total energy in the excited carrier system or the number of carriers.

¹⁷⁶ Callan, J. P. in *Ultrafast Dynamics And Phase Changes In Solids Excited By Femtosecond Laser Pulses* 59–104 Thesis, Harvard Univ., Cambridge, (2000).



ROZWÓJ POTENCJAŁU I OFERTY DYDAKTYCZNEJ POLITECHNIKI WROCLAWSKIEJ

Carrier–carrier scattering can cause dephasing in less than 10 fs, but it takes hundreds of femtoseconds for the carrier distribution to approach a Fermi–Dirac distribution. In a carrier–phonon scattering process, free carriers lose or gain energy and momentum by emission or absorption of a phonon. The carriers remain either in the same conduction or valence band valley (intravalley scattering, **Fig. 4.16e**) or transfer to a different valley (intervalley scattering, **Fig. 4.16f**). Although carrier–phonon scattering (or carriers cooling (CC)) does not change the number of carriers, their energy decreases due to spontaneous phonon emission, which transfers energy to the lattice. In metals and semiconductors, the carrier–carrier and carrier–phonon scattering occur concurrently during the first few hundred femtoseconds after excitation. Because the emitted phonons carry little energy, it takes many scattering processes, and therefore several picoseconds, before the carriers and the lattice reach thermal equilibrium.

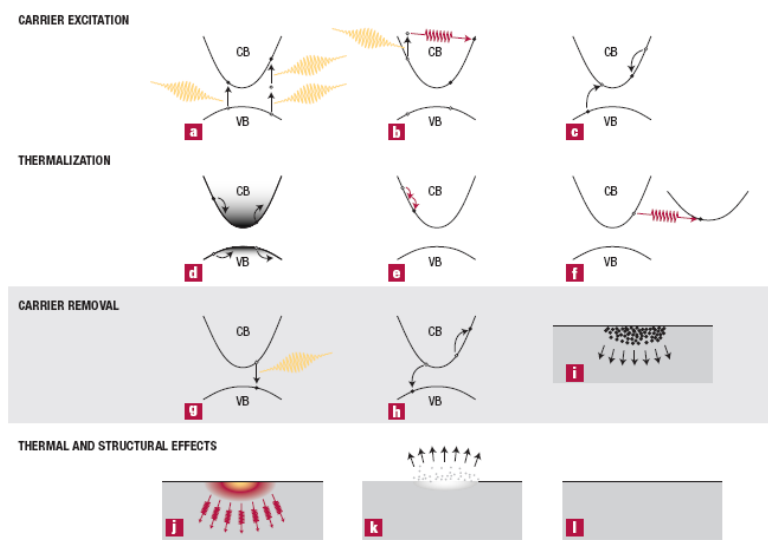


Figure 4.16 Electron and lattice excitation and relaxation processes in a laser-excited direct gap semiconductor. CB is the conduction band and VB the valence band. (a) Multiphoton absorption, (b) Free-carrier absorption, (c) Impact ionization, (d) Carrier distribution before scattering, (e) Carrier–carrier scattering, (f) Carrier–phonon scattering, (g) Radiative recombination, (h) Auger recombination, (i) Diffusion of excited carriers, (j) Thermal Diffusion, (k) Ablation, (l) Resolidification or condensation [¹⁷⁷].

Except the thermal carriers cooling (EC or HC) processes excited carriers can loss their energy in the following processes: (a) Auger recombination (AR), (b) intraband recombination (IR), (c) multiexciton generation (MEG), (d) interband recombination. All these processes differs for nanomaterials as compared with bulk material and will be discussed in more detail in the next sections.

¹⁷⁷ S. K. Sundaram, E. Mazur, Inducing and probing non-thermal transitions in semiconductors using femtosecond laser pulses, *Nature Materials* 1, 217 (2002).



ROZWÓJ POTENCJAŁU I OFERTY DYDAKTYCZNEJ POLITECHNIKI WROCLAWSKIEJ

(a) Auger relaxation

In CdSe NCs, optical gain occurs if the average number of electron-hole (e-h) pairs (excitons) per nanoparticle, N , is greater than 1. This requirement indicates that optical gain in these NCs relies on *multiexciton* states (biexciton, triexcitons, etc.), and therefore, its dynamical and spectral properties are strongly affected by exciton-exciton (x-x) interactions [¹⁷⁸, ¹⁷⁹]. In particular, these interactions open a highly efficient *nonradiative* decay channel (picoseconds time scale) associated with an Auger-type process, in which the e-h recombination energy is transferred to a third particle (an electron or a hole). Because of rapid shortening of Auger lifetime, with decreasing NC radius, R , it becomes progressively more difficult to achieve the optical gain and ASE regimes for shorter wavelengths that require the use of NCs of small sizes. For example, although CdSe NCs exhibit strong optical-gain performance in the red to yellow spectral ranges, they do not show efficient ASE in the range of green to blue colors.

(b) Intraband transitions

In contrast, the relaxation of carriers between the quantum states within a band, either the valence or conduction band, *intraband* relaxation, is systematically in the picoseconds or subpicosecond regime [¹⁸⁰] 10^6 times faster than the estimated radiative lifetimes. This rapid intraband relaxation rate is relevant to several applications. It is actually necessary for interband lasing, as it allows rapid population of the lowest states from which light is emitted.

¹⁷⁸ Klimov, V. I.; Mikhailovsky, A. A.; Xu, S.; Malko, A.; Hollingsworth, J. A.; Leatherdale, C. A.; Eisler, H.-J.; Bawendi, M. G. *Science* **2000**, *290*, 314-317; Klimov, V. I. Charge Carrier Dynamics and Optical Gain in Nanocrystal Quantum Dots: From Fundamental Photophysics to Quantum-Dot Lasing. In *Semiconductor and metal nanocrystals: synthesis and electronic and optical properties*; Klimov, V. I., Ed.; Marcel Dekker: New York, 2003, Chapter 5; Mikhailovsky, A. A.; Malko, A. V.; Hollingsworth, J. A.; Bawendi, M. G.; Klimov, V. I. *Appl. Phys. Lett.*, *80*, 2380 (2002).

¹⁷⁹ Klimov, V. I.; Mikhailovsky, A. A.; McBranch, D. W.; Leatherdale, C. A.; Bawendi, M. G. *Science* **287**, 1011 (2000); Htoon, H.; Hollingsworth, J. A.; Dickerson, R.; Klimov, V. I. *Phys. Rev. Lett.* *91*, 227401 (2003).

¹⁸⁰ V. I. Klimov, D. W. McBranch, C. A. Leatherdale, and M. G. Bawendi, *Phys. Rev. B* **60**, 13740 (1999); B. L. Wehrenberg, C. J. Wang, and P. Guyot-Sionnest, *J. Phys. Chem. B* **106**, 10634 (2002).



ROZWÓJ POTENCJAŁU I OFERTY DYDAKTYCZNEJ POLITECHNIKI WROCŁAWSKIEJ

On the other hand, the intraband transitions could be used for mid-infrared light sources and detectors if the relaxation rates were significantly slower.

Intraband relaxation in quantum dots should be quite distinct from energy relaxation in the bulk. In bulk semiconductors, there is a continuum of electronic states and the energetic carriers lose their energy by emitting optical phonons, with energy relaxation rates of the order of 0.5 eV/ ps. However, in quantum dots, the discrete energy levels modify the relaxation rate and mechanism. For quantum dots of weak confinement energies, < 0.1 eV in most materials, the electronic states are separated by only one or two optical-phonon energies. The electronic states are therefore strongly coupled via the optical phonons and may be better described as polarons [¹⁸¹]. The relaxation rate is then dominated by the phonon lifetime themselves which is of the order of tens of picoseconds. In strongly confined quantum dots, the electronic states are separated by several multiples of $\hbar\omega_{LO}$, 0.03 eV for CdSe, and coupling to the optical phonons cannot compensate for the large energy mismatch. This is the regime of the *phonon bottleneck*, where phonons should not account for the energy relaxation [¹⁸²]. This should lead to very long relaxation times. However, very fast intraband relaxation is the general observation. To explain the fast relaxation, a mechanism has been proposed where the electrons relax via their strong Coulomb interaction with the holes [¹⁸³]. The strong overlap of the holes and electrons further enhances this effect in the quantum dots. For III-V and II-VI materials, the high mass of the hole and the threefold band degeneracy of the valence band still lead to weak confinement of the hole state, and hole energy relaxation can therefore proceed via phonon-mediated processes. In agreement with this mechanism, colloidal CdSe quantum dots that are photoexcited in the *P* excitonic state exhibit an ultrafast relaxation to the *S* exciton in the subpicosecond regime. An energy relaxation rate of ~ 1 eV/ps has been observed, increasing for smaller dots. Theoretical relaxation times with this mechanism range from ~ 100 ps (Ref. [¹⁸⁴]) to a few picoseconds 10 and even tens of femtoseconds [¹⁸⁵], and encompass all measurements to date. With this mechanism, the fast relaxation should be avoidable if the quantum dot has only electrons or if both holes and electrons have similarly sparse density of states.

¹⁸¹ O. Verzele, G. Bastard, and R. Ferreira, Phys. Rev. B **66**, 081308 (2002).

¹⁸² H. Benisty, C. M. Sotomayor-Torres, and C. Weisbuch, Phys. Rev. B **44**, 10945 (1991).

¹⁸³ I. Vurgaftman and J. Singh, Appl. Phys. Lett. **64**, 232 (1994); A. L. Efros, V. A. Kharchenko, and M. Rosen, Solid State Commun. **93**, 281 (1995).

¹⁸⁴ I. Vurgaftman and J. Singh, Appl. Phys. Lett. **64**, 232 (1994).

¹⁸⁵ M. Califano, A. Zunger, and A. Franceschetti, Nano Lett. **4**, 525 (2004).



ROZWÓJ POTENCJAŁU I OFERTY DYDAKTYCZNEJ POLITECHNIKI WROCŁAWSKIEJ

Experiments have been performed on colloidal quantum dots where the surface has been modified to provide a trapping site for the hole after photoexcitation of the electron-hole pair. Thus, thiophenol and pyridine, which act as hole traps, could slow down the $1Pe-1Se$ relaxation to about 2–3 ps [¹⁸⁶], which is qualitatively consistent with the electron-hole Auger mechanism. However, one should expect a much larger decrease of the coupling as the hole moves from a delocalized hole state to a surface-trapped state, and it is therefore surprising that the lifetimes were not longer than a few picoseconds. Finally, reduced colloidal nanocrystals have been investigated to specifically test the role of the hole. Using a strongly reducing agent such as sodium biphenyl, electrons were injected in the $1Se$ state of the nanocrystals [¹⁸⁷]. Pumpprobe experiments carried out on the $1Se-1Pe$ infrared transition have led to similar intraband relaxation rate as when the electrons were photoexcited. *N*-type ZnO and CdSe colloidal nanocrystals showed resolution-limited relaxation lifetimes of ~5 ps even down to 6 K [¹⁸⁸]. *N*-type InP also showed fast relaxation of the order of 3–8 ps [¹⁸⁹], similar to that of photoexcited nanocrystals. These results on *n*-type nanocrystals indicate most clearly that, in the absence of a free hole, another efficient mechanism must lead to the fast intraband relaxation.

Having ruled out that the trapped hole or the optical phonons are responsible for the picosecond intraband relaxation, surface electronic or vibrational excitations remain likely candidates. The surface of colloidal quantum dots is a mostly uncharacterized system, with multiple bonding geometries of surface atoms, typically a cocktail of surface ligands, and physisorbed impurities attracted to the polar core. Thus, surface modification strongly affects the intraband relaxation, leading to much longer intraband relaxation times.

¹⁸⁶ P. Guyot-Sionnest, M. Shim, C. Matraga, and M. A. Hines, Phys. Rev. B **60**, R2181 (1999); V. I. Klimov, A. A. Mikhailovsky, D. W. McBranch, C. A. Laetherdale, and M. G. Bawendi, Phys. Rev. B **61**, R13349 (2000).

¹⁸⁷ M. Shim and P. Guyot-Sionnest, Nature (London) **407**, 981 (2001).

¹⁸⁸ M. Shim and P. Guyot-Sionnest, Phys. Rev. B **64**, 245342 (2001)

¹⁸⁹ J. L. Blackburn, R. J. Ellingson, O. I. Micic, and A. J. Nozik, J. Phys. Chem. B **107**, 102 (2003).



ROZWÓJ POTENCJAŁU I OFERTY DYDAKTYCZNEJ POLITECHNIKI WROCLAWSKIEJ

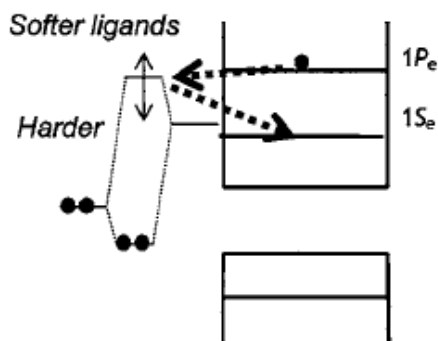


Figure 4.17 Schematic of the potential role of surface Cd atoms in assisting the intraband relaxation and the role of surface ligands. As the softer ligands form a more covalent bond, the antibonding ligand-surface Cd orbital is moved higher in energy, beyond the $1Pe$ state [¹⁹⁰].

The ligands coordinate essentially to the surface Cd^{2+} ions. Their interaction with Cd^{2+} can be discussed in the context of the hard-soft acid-base theory used in inorganic chemistry. Cd^{2+} is a soft acid consistent with its large and polarizable ionic core. Therefore, slow relaxation correlates with softer ligands and decreased polarity of the metal ligand bond. A likely candidate for electronic relaxation is charge transfer from the $1Pe$ state to a surface state such as the empty s orbital of the exposed surface Cd^{2+} atoms. For all ligands, the surface Cd^{2+} orbitals should be mostly above the $1Se$ level, otherwise rapid electron trapping would occur. However, if this orbital is between the $1Pe$ and $1Se$ states, it can shuttle the electrons between the $1Pe$ state and the $1Se$ state. This “defect-assisted” mechanism for intraband relaxation was discussed by Schroeter *et al.* in the context of the surface-grown quantum dots [¹⁹¹]. The mechanism shown schematically in **Fig. 4.17** is consistent with the observed trend that the softer ligands lead to a slower relaxation. Softer ligands form a more covalent bond with the Cd^{2+} orbital. This leads to a filled bonding orbital, of mostly ligand character, below the conduction band and an empty antibonding orbital, mostly Cd^{2+} , that may be pushed higher than the $1Pe$ state.

The relaxation rate may also correlate with the infrared activity of the ligand shell, where the high-frequency vibrations associated with the ligands can serve as sinks to the intraband excitation. This is a peculiarity of the colloidal quantum dots compared to the surface-grown quantum dots, which are embedded in an all-inorganic matrix. All the ligands share similar CH vibrational modes, and therefore, these high-frequency stretching vibrations

¹⁹⁰ Philippe Guyot-Sionnest, Brian Wehrenberg, and Dong Yu, Intraband relaxation in CdSe nanocrystals and the strong influence of the surface ligands, *The Journal of Chemical Physics* 123, 074709 (2005)

¹⁹¹ D. F. Schroeter, D. J. Griffiths, and P. C. Sercel, *Phys. Rev. B* 54, 1486 (1996).



ROZWÓJ POTENCJAŁU I OFERTY DYDAKTYCZNEJ POLITECHNIKI WROCŁAWSKIEJ

($\sim 3000\text{ cm}^{-1}$) and bending vibrations ($\sim 1400\text{ cm}^{-1}$) could not be responsible for the differing relaxation rates.

The coupling of the $1Se-1Pe$ electronic transition to the surface molecular vibrations can be direct via the wavefunction overlap. Another mechanism for energy transfer to vibrations is by near-field infrared absorption.

Concerning the mechanism for relaxation, the influence of the trapped hole has been observed to be negligible. This is in contrast to the case of excitonic relaxation, where hot holes may still be the explanation for the subpicosecond relaxation. The alternative intraband relaxation mechanisms that have been proposed in this work involve energy transfer to electronic states mediated by the interfacial polarity or energy transfer to high-frequency vibrations of the ligands. In particular, estimates of the energy-transfer rate to surface molecular vibration are rather consistent with the observations. It is expected that this mechanism should play a very significant role, and future work should investigate samples imbedded in a shell and a matrix free of high-frequency vibrations.

(b) Multi excitons generation (MEG) or Cartier multiplications

One interesting effect often discussed in the framework of properties of nanomaterials is so called multi-exciton generation (MEG) or other words carrier multiplication (CM). This effect is also observed for bulk materials but it is expected to observe its strong enhancement in the case of quantum dots. There is a strong interest in using this effect for obtaining more than 100% efficient solar cells. Efficient MEG was first reported in PbSe and PbS nanocrystals [¹⁹²] and was later observed in CdSe nanocrystals [¹⁹³], InAs [¹⁹⁴], Si [¹⁹⁵, ¹⁹⁶] and PbTe [¹⁹⁷]. MEG process has been schematically shown in **Fig. 4.18**.

¹⁹²R. D. Schaller and V. I. Klimov, Phys. Rev. Lett. **92**, 186601 (2004), A. J. Nozik, Annu. Rev. Phys. Chem. **52**, 193 (2001). R. J. Ellingson, M. C. Beard, J. C. Johnson, P. Yu, O. I. Micic, A. J. Nozik, A. Shabaev, and A. L. Efros, Nano Lett. **5**, 865 (2005).

¹⁹³R. D. Schaller, V. M. Agranovitch, and V. I. Klimov, Nat. Mater. **1**, 189 (2005).

¹⁹⁴J. J. H. Pijpers, E. Hendry, M. T. W. Milder, R. Fanciulli, J. Savolainen, J. L. Herek, D. Vanmaekelbergh, S. Ruhman, D. Mocatta, D. Oron, A. Aharoni, U. Banin, and M. Bonn, J. Phys. Chem. C **111**, 4146 (2007).

¹⁹⁵M. C. Beard, K. P. Knutsen, P. Yu, J. M. Luther, Q. Song, W. K. Metzger, R. J. Ellingson, and A. J. Nozik, Nano Lett. **7**, 2506 (2007)

¹⁹⁶Timmerman, D.; Izeddin, I.; Stallinga, P.; Yassievich, I. N.; Gregorkiewicz, T. Spaceseperated quantum cutting with silicon nanocrystals for photovoltaic applications. *Nat. Photonics* **2**, 105 (2008).

¹⁹⁷J. E. Murphy *et al.*, J. Am. Chem. Soc. **128**, 3241 (2006).

ROZWÓJ POTENCJAŁU I OFERTY DYDAKTYCZNEJ POLITECHNIKI WROCLAWSKIEJ

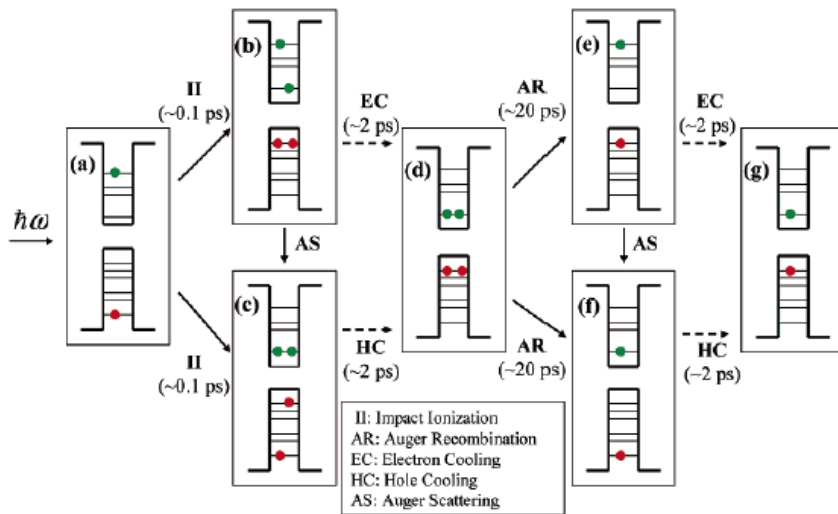


Figure 4.18 Different steps of MEG process together with taking into account all competitive for MEG processes. Times have been given for PbSe QDs. [198]

Two main processes compete with the MEG process, thermal cooling (EC or HC) and Auger recombination (AR). The final efficiency of the MEG process will depend on the ratio between all these processes and in more directly depend on the characteristic for this process decay times. The typical relations between all these decay times have been shown in Fig. 4.19.

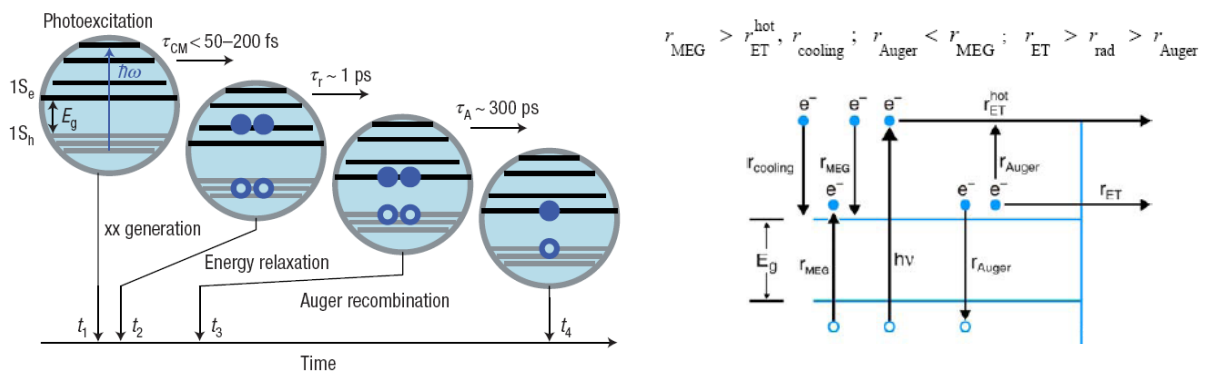


Figure 4.19 Typically observed decay times corresponding to different relaxation process in QDs with their relation to each other.

On the theoretical side, three interesting proposals were put forward to explain MEG processes:

¹⁹⁸ Meirav Ben-Lulu, David Mocatta, Mischa Bonn, Uri Banin and Sanford Ruhman, Nano Letters 8, 41207 (2008).



ROZWÓJ POTENCJAŁU I OFERTY DYDAKTYCZNEJ POLITECHNIKI WROCŁAWSKIEJ

(i) **the impact ionization** (II) theory of Zunger et al. [¹⁹⁹] based on detailed pseudopotential and configurational interactions (CI) calculations, suggests that the Coulomb interaction between the exciton and multiexciton **states** is responsible for the efficient MEG. Their work was followed by a theoretical screening of candidate materials and by a detailed analysis specific to PbSe nanocrystals. A full nonequilibrium description of the MEG process, emphasizing the important role of the density of states of the one-exciton states was given.

However, II was dismissed as a possible explanation of carrier multiplication in PbSe quantum dots on the basis that it would be too slow to account for the observed high carrier multiplication efficiency. Instead, rather exotic explanations, involving resonance between single-exciton and multi-exciton states [²⁰⁰] or second-order coupling with virtual excitons [²⁰¹] were tentatively offered.

(ii) The Klimov group developed the alternative scenario of “**virtual exciton generation**” [²⁰²]. In this picture the generation of the initial high-energy exciton takes place simultaneously and coherently with the generation of additional excitons.

(iii) Finally, Efros et al. suggested a third explanation. In their **coherent exciton states** (CES) picture the incident photon generates a single exciton, which then coherently evolves into a multiexciton state, enabled by the degeneracy of these states.

Noticeably, all these theoretical frameworks build on a detailed knowledge of single particle excitations; nevertheless most studies have so far focused on low lying excitations, with very few studies exploring high-energy excitation spectra. In addition, none of the existing calculations has used *ab initio* techniques and has investigated the role played by surface states.

¹⁹⁹A. Franceschetti, J. M. An, and A. Zunger, *Nano Lett.* **6**, 10 2191 (2006).

²⁰⁰ Ellingson, R. J.; Beard, M. C.; Johnson, J. C.; Yu, P.; Micic, O. I.; Nozik, A. J.; Shabaev, A.; Efros, Al. L. *Nano Lett.* **2005**, *5*, 865.

²⁰¹ Schaller, R. D.; Agranovich, V. M.; Klimov, V. I. *Nat. Phys.* **2005**, *1*, 189.

²⁰²R. D. Schaller, V. M. Agranovich, and V. I. Klimov, *Nat. Phys.* **1**, 189 (2005).



ROZWÓJ POTENCJAŁU I OFERTY DYDAKTYCZNEJ POLITECHNIKI WROCŁAWSKIEJ

The experimental observation of carrier multiplication in quantum dots has raised several interesting questions:

- (i) *Asymmetry between carrier multiplication and Auger recombination rates:*
Carrier multiplication was shown to have a much shorter lifetime than the nonradiative decay of a biexciton into a single-exciton (Auger recombination, AR).
- (ii) *Carrier multiplication threshold:* Significantly different values of the energy threshold for carrier multiplication, that is, the minimum photon energy necessary to achieve multi-exciton generation, have been reported in the literature.

Based on accurate atomistic pseudopotential methods to address these controversial findings it has been found already [²⁰³] that (i) the observed asymmetry between the II and AR transition rates is due to the very different densities of final states for these processes, (ii) well passivated semiconductor nanocrystals, and particularly semiconductor core/shell systems, can reach emission quantum efficiencies (QE) of their single excitons states near unity, with radiative lifetimes of tens to hundreds of nanoseconds. In contrast, multiple excitons decay much more rapidly to long-lived monoexciton states via Auger recombination, which is essentially the inverse of carrier multiplication. Quantum confinement enhances the rate of this process, resulting in relaxation from multi- to monoexcitons within a few tens of picoseconds. This separation of timescales allows estimation of the initial multiple vs. single exciton occupation numbers by monitoring excited-state decay kinetics, either by recording the absorption bleach kinetics at the band edge, or by directly time-resolving photoluminescence.

Theories promoted for explaining CM in QDs suggest that its efficiency depends on high spatial overlap of mono- and multiexciton states high above the band gap. This could be affected by the presence of a significant shell layer that is energetically permeable to high energy monoexcitons but less so to biexcitonic states of equal total energy.

²⁰³ Meirav Ben-Lulu, David Mocatta, Mischa Bonn, Uri Banin and Sanford Ruhman, Nano Letters 8, 41207 (2008).

ROZWÓJ POTENCJAŁU I OFERTY DYDAKTYCZNEJ POLITECHNIKI WROCLAWSKIEJ
(d) Gain in single nanocrystal [²⁰⁴]

Optical gain corresponds to a light–matter interaction regime for which generation of photons by stimulated emission dominates over photon absorption. As in other lasing media, optical gain in nanocrystals requires population inversion—that is, the situation in which the number of electrons in the excited state is greater than that in the ground state. The lowest-energy emitting transition in nanocrystals of II–VI semiconductors studied here can be described in terms of a two-level system that has two electrons in its ground state. Excitation of a single electron (single exciton) across the energy gap (E_g) in this system does not produce optical gain but rather results in optical transparency, for which stimulated emission by a conduction-band electron is exactly compensated by absorption due to the electron remaining in the valence band (Fig. 4.20a).

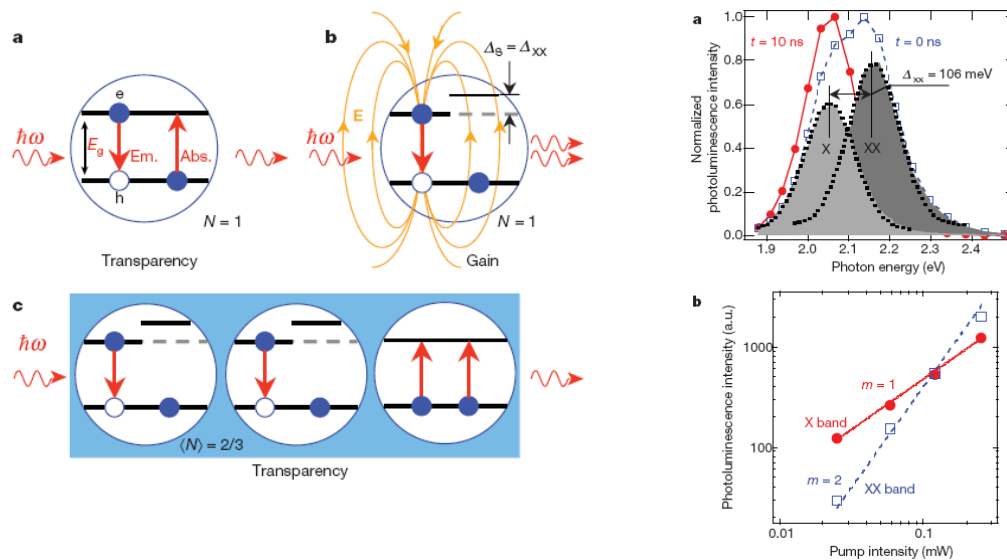


Figure 4.20 The concept of single-exciton nanocrystal lasing. a, In the absence of X–X interactions, excitation of a single electron–hole pair (single exciton) per nanocrystal (NC) on average does not produce optical gain but results in optical transparency—that is, the regime for which stimulated emission (Em.) is exactly compensated by absorption (Abs.). e. Electron; h, hole. b, The balance between stimulated emission and absorption is broken if one accounts for X–X interactions that spectrally displace the absorbing transition with respect to the emission band. The latter effect can be interpreted in terms of the transition Stark shift ($\Delta_S = \Delta_{XX}$) induced by a local electric field (E) associated with a single-exciton state. If the transition shift is greater than the ensemble line width, optical gain can occur in the single-exciton regime. c, In the case of large Δ_S ($\Delta_S \gg \Gamma$), stimulated emission in singly excited NCs (n_x is their fraction in the NC ensemble) competes only with absorption in unexcited NCs (fraction $(1-n_x)$; here, we neglect multiexcitons). The stimulated-emission cross-section of a singly excited NC is one half of the absorption cross-section of the lowest-energy NC transition. Based on these

²⁰⁴ This section has been written based on following paper: Victor I. Klimov, Sergei A. Ivanov, Jagjit Nanda, Marc Achermann, Ilya Bezel, John A. McGuire & Andrei Piryatinski, Single-exciton optical gain in semiconductor nanocrystals, Nature 447, 441(2007)



ROZWÓJ POTENCJAŁU I OFERTY DYDAKTYCZNEJ POLITECHNIKI WROCŁAWSKIEJ

considerations, the optical-gain threshold can be found from the condition $n_x/2=(1-n_x)$, which indicates that the single exciton gain onset corresponds to the situation where two-thirds of the NCs are excited with single excitons.

Experimental demonstration of giant X–X repulsion in type-II CdS/ZnSe NCs. a, Short- (open squares) and long- (solid circles) time room-temperature photoluminescence spectra of CdS/ZnSe NCs. Deconvolution of the t_{50} spectrum into two bands shown by grey areas (dotted lines are gaussian fits) reveals the short-lived XX feature due to emission from biexcitons that is located to high energies from the singleexciton X band. The spacing between these two bands indicates giant X–X repulsion characterized by $\Delta_{XX} = 106$ meV. b, Photoluminescence pump intensity dependences indicate that the growth of X and XX features with excitation power shows log–log slopes of $m=1$ and 2, respectively. These slopes are consistent with single-exciton and the biexciton mechanisms for the X and XX emission bands, respectively.

Stimulated emission dominates over absorption only if the second electron is also excited across the energy gap, indicating that optical gain requires doubly excited nanocrystals, that is, biexcitons. These considerations imply that population inversion in a nanocrystal ensemble can only be achieved if $\langle N \rangle$ is greater than 1. The condition for optical gain however changes if one accounts for a local electric field associated with an excited electron–hole pair. This field can alter the absorption energy of the electron remaining in the valence band by the carrier-induced Stark effect (**Fig. 4.20b**). If the magnitude of the Stark shift (Δ_S) is comparable to or greater than the transition line width (Γ), it can completely eliminate absorption losses at the emission wavelength in excited nanocrystals, which should allow optical gain using single-exciton states. Specifically, the threshold for population inversion in the presence of the transient transition shift is determined by the condition $\langle N \rangle = 2 / (3 - \exp(-\Delta_S^2 / \Gamma^2))$. If $\Delta_S = \Gamma$, it reduces to $\langle N \rangle \sim 1$, which corresponds to the usual case of multiexciton optical gain. However, if $\Delta_S \ll \Gamma$, $\langle N \rangle = 2/3$ (**Fig. 4.20c**), which implies that optical gain does not require multiexcitons.

The carrier-induced Stark effect can be described in terms of the Coulomb interaction of the initially generated exciton with the exciton created in the second excitation act. In this description, the transient Stark shift is determined by the X–X Coulomb interaction energy ($\Delta_{XX} = \Delta_S$) defined as $\Delta_{XX} = E_{XX} - 2E_X$, where E_X and E_{XX} are single- and biexciton energies, respectively. The X–X interaction strength is also often characterized in terms of the biexciton binding energy (δE_{XX}), which relates to Δ_{XX} by $\delta E_{XX} = -\Delta_{XX}$. The energy Δ_{XX} depends on the local electrical charge density $\rho_X(\mathbf{r})$ associated with a single-exciton state and, hence, on the sum of the hole (ρ_h) and the electron (ρ_e) charge densities: $\rho_X(\mathbf{r}) = \rho_e(\mathbf{r}) + \rho_h(\mathbf{r})$ (\mathbf{r} is the spatial coordinate). Because of almost identical spatial distributions of electron (Ψ_e) and hole (Ψ_h) wavefunctions, $\rho_X(\mathbf{r})$ is nearly zero in homogeneous nanocrystals ($\rho_X(\mathbf{r}) \sim e(|\Psi_e(\mathbf{r})|^2 - |\Psi_h(\mathbf{r})|^2) \approx 0$, e is the electron charge) (**Fig. 4.20a**), which leads to relatively small X–X



ROZWÓJ POTENCJAŁU I OFERTY DYDAKTYCZNEJ POLITECHNIKI WROCŁAWSKIEJ

interaction energies of ,10 to , 30 meV [²⁰⁵]. These values are smaller than typical transition line widths in existing nanocrystal samples (ensemble broadening of 100 meV or greater) and, therefore, do not allow significant suppression of absorption at the emission wavelength. The separation of electrons and holes between the core and the shell in type-II nanocrystals (**Fig. 4.20b**) can lead to sizable local charge densities and, hence, large Coulomb interaction energies.

In type-I nanocrystals, Coulomb interactions tend to spatially arrange charges in such a way that the biexciton energy E_{XX} is less than twice the single-exciton energy E_X . This situation corresponds to a negative value of Δ_{XX} (positive biexciton binding energy), which can be interpreted in terms of an effective X–X attraction. In type-II nanocrystals, the spatial distribution of charges is controlled not by Coulomb interactions but by large energy gradients at the core/shell interface, which leads to concentration of the same-sign charges in the same part of the heteronanocrystal (both electrons in the core; both holes in the shell) and spatial separation of charges of the opposite sign across the hetero-interface. This type of spatial arrangement increases the repulsive component of the Coulomb interaction and decreases its attractive component, which produces net X–X repulsion (negative biexciton binding energy), as indicated by the positive sign of the calculated values of Δ_{XX} .

The sign of Δ_{XX} has an important effect on the optical-gain properties of nanocrystals because it determines the direction of the shift of the absorbing transitions with respect to the emission line. If Δ_{XX} is negative (X–X attraction), the transitions move downward in energy, which may have a detrimental effect on lasing performance because of increasing absorption due to the manifold of strong transitions located immediately above the emitting band. On the other hand, strong X–X repulsion, which can be produced in type-II nanocrystals, should benefit lasing because it moves strongly absorbing transitions away from the emission line.

In order to experimentally measure the X–X interaction energy in type-II core/shell nanocrystals, we compare the position of the biexciton photoluminescence band with respect to the single-exciton line. Radiative recombination of the biexciton produces a photon ($\hbar\omega_{XX}$) and an exciton and hence, $\hbar\omega_{XX} = E_{XX} - E_X = E_X + \Delta_{XX}$. On the basis of this expression, the shift of the biexciton line with respect to the single-exciton band ($\hbar\omega_X = E_X$) provides a direct

²⁰⁵ Kang, K. I. et al. Confinement-enhanced biexciton binding energy in semiconductor quantum dots. Phys. Rev. B 48, 15449–15452 (1993); Achermann, M., Hollingsworth, J. A. & Klimov, V. I. Multiexcitons confined within a subexcitonic volume: Spectroscopic and dynamical signatures of neutral and charged biexcitons in ultrasmall semiconductor nanocrystals. Phys. Rev. B 68, 245302(2003).



ROZWÓJ POTENCJAŁU I OFERTY DYDAKTYCZNEJ POLITECHNIKI WROCLAWSKIEJ

measure of the X–X interaction energy: $\Delta_{XX} = \hbar\omega_{XX} - \hbar\omega_{XX}$. The challenge in experimentally detecting photoluminescence from nanocrystal multiexcitons is associated with their short (picoseconds to hundreds of picoseconds) lifetimes, which are limited by non-radiative Auger recombination. Because these times are significantly shorter than the radiative time constants, signals from multiexcitons are not well pronounced in steady-state photoluminescence spectra. This has been shown in **Fig.4.21**. The measured pump-intensity dependences indicate that the growth of band X is linear in pump fluence (filled circles in **Fig. 4.21b**), as expected for single-exciton emission. On the other hand, the high-energy band XX shows a quadratic growth (open squares in **Fig. 4.21b**), which is typical for emission from biexcitons. The fast decay of this feature is also consistent with its multiexciton origin, and is due to efficient Auger recombination. The fact that the biexciton emission occurs at higher energies than the single-exciton photoluminescence indicates the repulsive character of the X–X interaction.

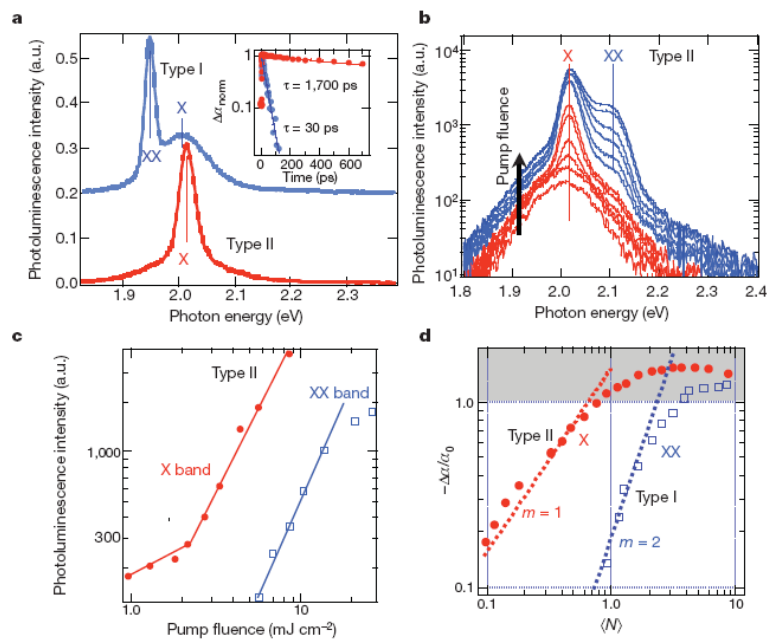


Figure 4.21 Optical amplification in type-I and type-II NCs. a, Room temperature ASE spectra of type-I CdSe NCs (blue line; offset vertically for clarity) and type-II CdS/ZnSe NCs (red line; sample is similar to the one shown in Fig. 4) prepared in the form of close-packed drop-cast films and excited by 100-fs pulses at 3 eV. Inset, transient-absorption dynamics measured for these NCs (colour-matched symbols) at the position of the ASE band for the pump intensity that corresponds to the optical-gain onset. b, The pump-intensity-dependent photoluminescence spectra of the type-II sample show the development of a narrow ASE peak near the centre of the single-exciton emission band. The second ASE band, which develops at higher fluences, is located near the XX photoluminescence feature. c, Both ASE features show superlinear pump dependence above the threshold pump intensities of $\sim 2 \text{ mJ cm}^{-2}$ (band X) and $\sim 6 \text{ mJ cm}^{-2}$ (band XX). d, The dependence of normalized absorption bleaching at the position of the ASE band in type-I (squares) and type-II (circles) NCs (measured ~ 3 ps after excitation) as a function of $\langle N \rangle$ in comparison with linear (red straight line) and quadratic (blue straight line) growth. The area shown in grey corresponds to optical gain ($2Da/a0.1$).



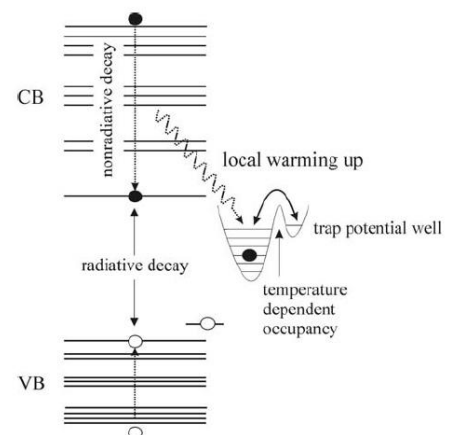
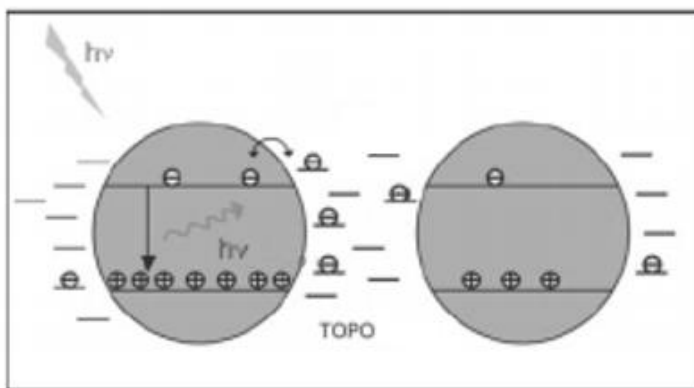
ROZWÓJ POTENCJAŁU I OFERTY DYDAKTYCZNEJ POLITECHNIKI WROCLAWSKIEJ

Discussed above results obtained by V. Klimov group represents the first practical demonstration of nanocrystal structures that produce optical amplification due to stimulated emission of single-exciton states, which eliminates complications associated with ultrafast multiexciton Auger recombination. This new approach makes use of dynamic splitting of the degeneracy of the lowest-energy emitting transition by giant X–X interactions that develop in type-II heterostructures following spatial separation of electrons and holes

4.8 Matrix related effects

In many cases, because of further applications, NCs must be introduced into the matrix or they must be grown already inside the matrix. In the first case, we have much better control of properties of NCs but in this case it is very difficult to introduce the NCs in homogeneous way into the matrix. In the second approach, it is reasonably easy to get good homogeneity of the sample on macro scale however to control the properties of NCs is very difficult task.

In both cases, the matrix strongly influence on the optical properties of NCs. There are few important effects being the consequence of introducing of NCs into the matrix or more precisely excited carrier ionization. This ionization will induce some additional charge at the NCs surface what has been schematically shown in **Fig. 4.22**.





ROZWÓJ POTENCJAŁU I OFERTY DYDAKTYCZNEJ POLITECHNIKI WROCŁAWSKIEJ

Figure 4.22 Effect of nanocrystals ionization and charging the nanocrystals-matrix interface.

Moreover, the matrix introduces some other effects like NCs-NCs interactions and excitons migration or tunneling from the NCs.

(a) Photoluminescence blinking

The first important effect experimentally observed which is a consequence of introducing NCs inside the matrix is photoluminescence bleaching (Fig. 4.23).

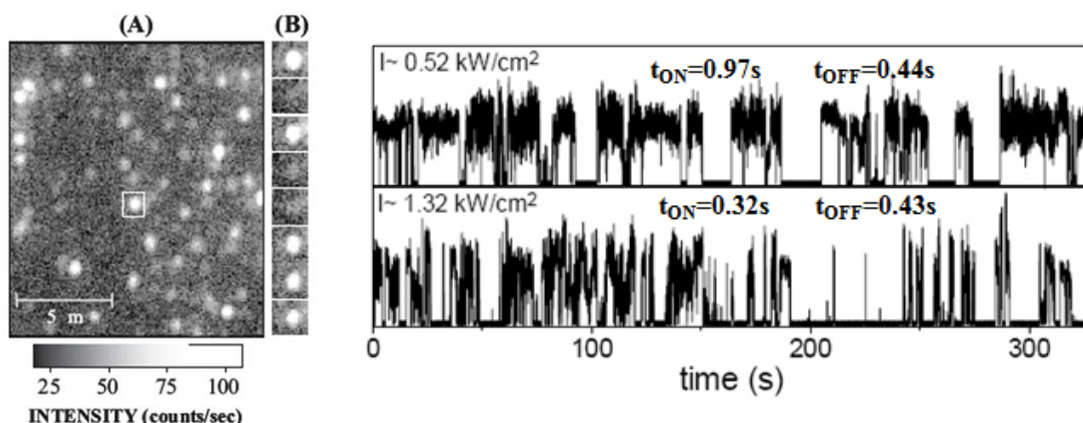


Figure 4.23 A) Image of single 0.45 nm nanocrystals taken with a 0.5 s integration time and an excitation intensity of 60 W/cm². B) Consecutive 0.5 s images of the nanocrystal indicated by the white dotted box in (A). The images show binary fluorescence blinking over time [²⁰⁶], Photoluminescence intensity recorded for single nanocrystals in function of time for two excitation fluxes [²⁰⁷].

This is microscopic effect related to single NCs which however can be also observed as a macroscopic one. **Figure 4.23** shows experimentally measured the PL intensity in function of time. It can be seen that emission intensity fluctuates in non deterministic way. Observed

²⁰⁶ A. Empedocles, Robert Neuhauser, Kentaro Shimizu, and Mounji G. Bawendi, Photoluminescence from Single Semiconductor Nanostructures, Adv. Mater. 11, 1243 (1999)

²⁰⁷ M. Nirmal, Nature 383, 802 (1996), Adv.Matt.11 (2005)



ROZWÓJ POTENCJAŁU I OFERTY DYDAKTYCZNEJ POLITECHNIKI WROCŁAWSKIEJ

effect is due to NCs ionization (NCs not optically active) and carriers recovery (NCs optically active).

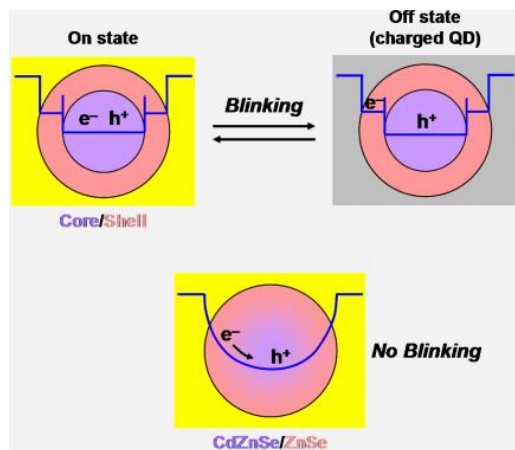


Figure 4.24 The concept of obtained non blinking nanocrystals.

Very recently [²⁰⁸], in a common effort between the University of Rochester, Cornell University, Kodak Eastman and the Naval Research Laboratory in the USA, researchers were able to synthesize a QD that emits a constant stream of light. Blinking is caused by an electron that, upon photoexcitation, escapes the core and becomes trapped in the shell, forming a charged QD. At that point, non-radiative relaxation is favored and, for an instant, emission ceases (see figure). Unlike in a typical QD, in the one reported by Prof. Krauss and collaborators the core (CdZnSe) and the shell (ZnSe) fade into each other, so there is no abrupt boundary between the two regions. The potential energy surface declines steadily towards the center of the QD (blue lines in the figure). In this way, the non-radiative mechanism becomes highly unfavorable, even when a charged QD is formed. Irradiation remains steady for hours. Although important challenges must be addressed for full applicability (for instance, the emitted light is not monochromatic), the non-blinking CdZnSe/ZnSe represents a milestone in photoluminescent nanocrystal research.

(b) Spectral diffusion

²⁰⁸ "Non-Blinking Semiconductor Nanocrystals", X. Wang, X. Ren, K. Kahen, M. A. Hahn, M. Rajeswaran, S. Maccagnano-Zacher, J. Silcox, G. E. Cragg, Al. L. Efros, T. D. Krauss, *Nature*, **2009**, 459, 686-689



ROZWÓJ POTENCJAŁU I OFERTY DYDAKTYCZNEJ POLITECHNIKI WROCLAWSKIEJ

The second important effect related to introducing NCs inside the matrix is spectral diffusion. This is also microscopic effect but rather not observed in macroscale. The main consequence of this effect is fluctuations of carriers (charge) at the NCs surface. This will cause the modulated Stark effect and in consequence the modulations of NCs band gap.

Figure 4.25 shows experimentally obtained results for single NCs.

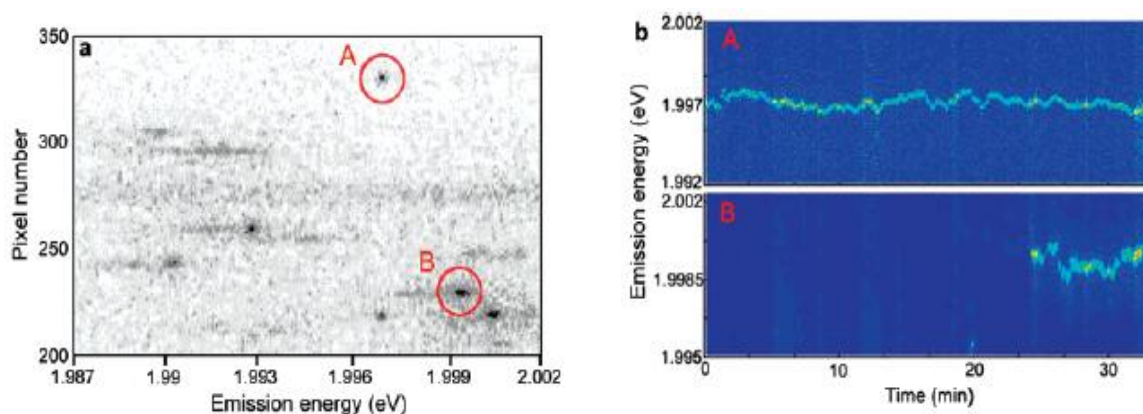


Figure 4.25 Experimentally recorded spectra diffusion for single nanocrystal [²⁰⁹].

Examination of many single nanocrystal spectra reveals a wide range of linewidths and non-Lorentzian lineshapes. In addition, the lineshape of individual nanocrystals is found to be extremely sensitive to experimental parameters such as excitation intensity. This is true even though excitation occurs far from the emitting state (>200 meV) so that traditional power or saturation broadening should be insignificant. There is also a strong lineshape dependence on integration time. In single molecule spectroscopy, lineshapes are thought to arise from rapid shifting of the emission energy (spectral diffusion) on a timescale that is fast relative to the acquisition time of the experiment. These spectral shifts result from changes in the local environment, which interact with single molecules through short range strain fields [²¹⁰]. In these cases, the lineshape of single molecule spectra is determined by the dynamics of the local environment and not the intrinsic physics of the molecule.

There are two main implications of the data in **Fig. 4.25**. First, it is clear that the line

²⁰⁹ Fernee, J.Phys.Cem.C

²¹⁰ J. Koedijk, R. Wannemacher, R. Silbey, S. Volker, J. Phys. Chem. 1996, 100, 19 945.



ROZWÓJ POTENCJAŁU I OFERTY DYDAKTYCZNEJ POLITECHNIKI WROCLAWSKIEJ

shape of a single nanocrystal contains information about changes in the surrounding environment and not the intrinsic physics of the nanocrystal. Second, changes in the lineshape of a single nanocrystal spectrum resulting from different experimental conditions are likely to be the result of changes in spectral diffusion.

While the small spectral shifts described above occur on a very fast timescale, a second type of spectral shifting is also observed. These shifts result in much larger changes in the emission energy and occur on a timescale from seconds to many minutes, even under high excitation intensities. **Figure 4.26** shows consecutive low-resolution spectra of a single nanocrystal that reversibly shifts in energy more than 80 meV over 16 min. The large decrease in emission intensity as the spectrum shifts to the red may be the result of the absorbing states shifting out of resonance with the exciting laser. The most interesting feature of **Figure 4.26** is that as the spectrum shifts to lower energies, there is a significant increase in coupling to LO phonons, which is measured as the ratio of the integrated intensity of the zero and one phonon peaks.

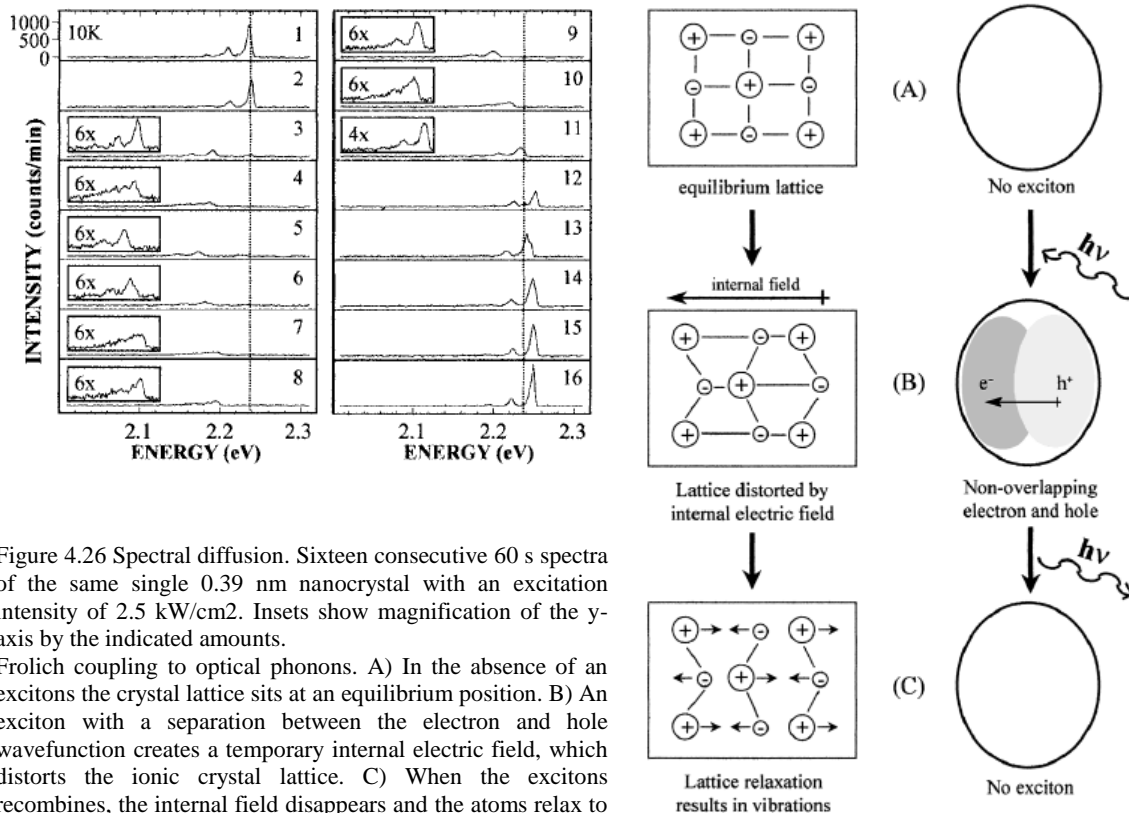


Figure 4.26 Spectral diffusion. Sixteen consecutive 60 s spectra of the same single 0.39 nm nanocrystal with an excitation intensity of 2.5 kW/cm². Insets show magnification of the y-axis by the indicated amounts. Frolich coupling to optical phonons. A) In the absence of an excitons the crystal lattice sits at an equilibrium position. B) An exciton with a separation between the electron and hole wavefunction creates a temporary internal electric field, which distorts the ionic crystal lattice. C) When the excitons recombines, the internal field disappears and the atoms relax to their equilibrium positions, creating lattice vibrations



ROZWÓJ POTENCJAŁU I OFERTY DYDAKTYCZNEJ POLITECHNIKI WROCŁAWSKIEJ

Phonon coupling is a very sensitive measure of the overlap between the electron and hole wavefunctions within the nanocrystal core (**Fig. 4.26**). A separation between the electron and hole results in a temporary electric field within the nanocrystal. This field tends to distort the ionic CdSe crystal lattice by pulling the positively charged Cd²⁺ ions toward the electron and the negatively charged Se^{2±} ions toward the hole (**Fig. 4.26B**). When the exciton recombines, the temporary field is removed and the distorted crystal lattice relaxes to its equilibrium state resulting in vibrations (**Fig. 4.26C**). The result is enhanced coupling of the emitted photon to optical phonons. This interaction is called Frölich coupling and the degree of coupling is related to the amount of separation between the electron and hole wavefunctions. The changes in phonon coupling observed in **Figure 4.26** suggests that these large spectral diffusion shifts are accompanied by a change in the overlap of the electron and hole wavefunctions. One possible source of such a change is a local electric field, which could pull the electron and hole wavefunctions toward opposite sides of the nanocrystal. In fact, the spectral characteristics seen in **Figure 4.26** are very similar to what is observed in low-temperature ensemble Stark experiments [²¹¹]. In the presence of an applied electric field, ensemble emission spectra are seen to shift to lower energies with a corresponding increase in phonon coupling. The observed similarities suggest that perhaps changing local electric fields around individual nanocrystals may play a role in spectral diffusion.

(c) Interdot interactions

Several types of site–site coupling have been observed in superlattices composed of both metallic and semiconductor dots. Collier *et al.* [²¹²] have reported quantum coupling due to electron tunneling when they tuned the interdot spacing between organically passivated silver dots in two dimensional arrays from 12 to 5 Å and observed a metal/insulator transition for an interparticle distance of ~5 Å. For semiconductor nanoparticles, Kagan *et al.* observed coupling between CdSe nanoparticles in close-packed three dimensional (3D) arrays, which was attributed to classical dipole–dipole coupling described by Forster [²¹³, ²¹⁴]. There appears to be little evidence of direct coupling of carriers between semiconductor nanoparticles, such

²¹¹ A. Sacra, Ph. D. Thesis, Massachusetts Institute of Technology 1996

²¹² C. P. Collier, R. J. Saykally, J. J. Shiang, S. E. Henrichs, and J. R. Heath, *Science* **277**, 1978 (1997).

²¹³ C. R. Kagan, C. B. Murray, M. Nirmal, and M. G. Bawendi, *Phys. Rev. Lett.* **76**, 1517 (1996).

²¹⁴ C. R. Kagan, C. B. Murray, and M. G. Bawendi, *Phys. Rev. B* **54**, 8633(1996).



ROZWÓJ POTENCJAŁU I OFERTY DYDAKTYCZNEJ POLITECHNIKI WROCŁAWSKIEJ

as by tunneling, at ambient pressure. The photoconductivity experiments by Leatherdale *et al.*^[215] suggest that the probability of charge separation in photoexcited CdSe quantum dot solids is small.

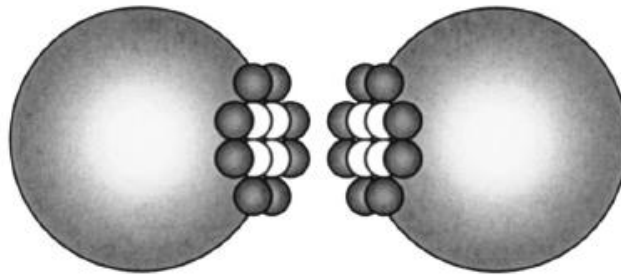


Figure 4.27 Schematic of those pyridine sites on neighboring dots that can be involved in contact between the dots, including the four (2x2) inner sites (white) and eight surrounding ones (gray) on each dot described in the model (Not drawn to scale).

Interdot coupling of electrons and/or holes will lower the quantum confinement energy of each, which can be seen in photoluminescence and absorption (transmission) experiments if the coupling is sufficiently fast. Near a threshold pressure, interdot coupling may occur only in localized regions in an array, while at higher pressure it can occur throughout the sample. This decrease in band gap can be distinguished from the increase in band gap energy with pressure for these semiconductors by comparing the pressure dependence of the array with that of isolated dots in solution. One consequence of interdot radiative transfer is that excitation energy is transferred from smaller to larger nearby dots (with smaller confinement energy) and that it can be transferred to defect sites and be quenched before luminescence.

Moreover there are some reports ^[216] on the extension of the possible radiationless transition processes to include a novel case of long-range electronic-to-vibrational energy transfer (EVET). Some experimental and theoretical results indicate for dipole-dipole long-range, resonance, radiationless interconversion of core band-gap electronic excitation of semiconductor nanocrystal quantum dots (QDs) to C–H vibrational overtones of various matrices, which competes with the emission process. The proposed mechanism becomes possible due to the large transition dipole moment of the QD, which couples to the smaller transition dipole of the (3n) overtone of the C–H vibrational stretch, sufficient to induce

²¹⁵ C. A. Leatherdale, C. R. Kagan, N. Y. Morgan, S. A. Emedocles, M. A. Kastner, and M. G. Bawendi, *Phys. Rev. B* **62**, 2669 (2000).

²¹⁶ Assaf Aharoni, Dan Oron, and Uri Banin, Eran Rabani and Joshua Jortner, Long-Range Electronic-to-Vibrational Energy Transfer from Nanocrystals to Their Surrounding Matrix Environment, *Phys.Rev.Lett.* **100**, 057404 (2008)

ROZWÓJ POTENCJAŁU I OFERTY DYDAKTYCZNEJ POLITECHNIKI WROCLAWSKIEJ

nonradiative transitions on time scales of the order of submicroseconds.

Shape control of nanocrystals allows a further increase in the absorption cross-section by the addition of wide-gap shell material with minimal perturbation of the nanocrystal ground state from which emission occurs [217]. We recently showed that a combination of spherical CdSe cores with elongated CdS shell structures (transmission electron micrographs shown in **Fig. 4.28 (a,b)**) provides particles with large molar extinction coefficients orders of magnitude greater than those of typical dyes [218]. In particular, asymmetric shell growth allows efficient manipulation of the degree of wavefunction confinement, which leads to an exceptionally large tunable quantum-confined Stark effect[219] (QCSE).

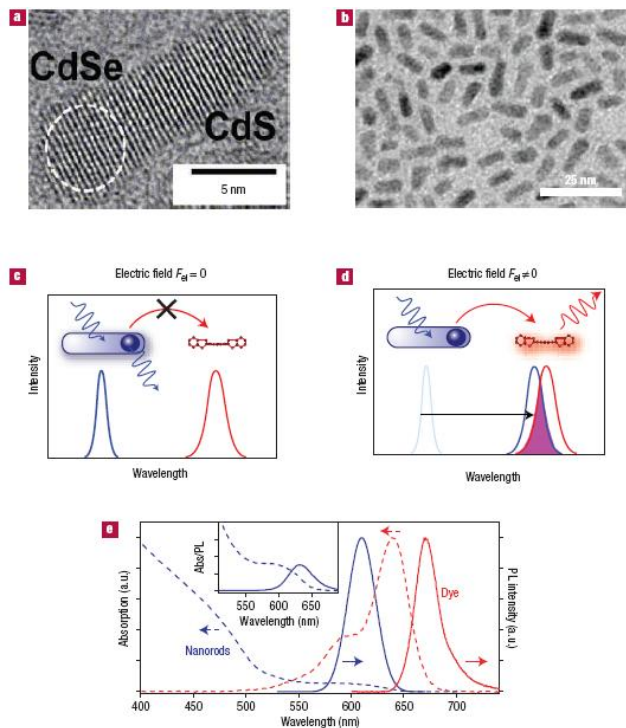


Figure 4.28 Electrically tunable energy transfer from a single semiconductor nanorod to a dye molecule. a,b, High-resolution (a) and overview (b) transmission electron micrographs showing the structure of the CdSe/CdS nanocrystals used. c, For a specific set of a single nanocrystal and a single dye molecule no energy transfer occurs because of the lack of spectral overlap between nanocrystal emission and dye absorption. d, After application of an electric field, the nanocrystal's PL is red-shifted, resulting in resonance of the nanocrystal and dye transitions. This leads to energy transfer to the dye and subsequent emission. e, Absorption (dashed lines) and PL (solid lines) spectra of nanocrystals (blue lines) and dye (red lines). Absorption spectra were taken from chloroform solution at room temperature, whereas emission spectra were taken from polystyrene/dye blends at 50 K. Note the considerable spectral overlap of nanocrystal emission with dye absorption. The inset shows the solution absorption and PL of the nanocrystal excitonic feature [220].

The principle of electrical control of energy transfer from a single nanocrystal towards a single-dye acceptor is shown in **Fig. 4.28 (c,d)**. At low temperatures, when the electronic transitions narrow, energy can only be transferred between a single nanocrystal and a single dye molecule given sufficient spectral overlap of the individual transitions, which are not readily accessible from the ensemble data broadened by energetic disorder. Whereas the dye

217 Müller, J. *et al.* Wave function engineering in elongated semiconductor nanocrystals with heterogeneous carrier confinement. *Nano Lett.* **5**, 2044–2049 (2005).

218 Talapin, D. V. *et al.* Highly emissive colloidal CdSe/CdS heterostructures of mixed dimensionality. *Nano Lett.* **3**, 1677–1681 (2003).

219 Müller, J. *et al.* Wave function engineering in elongated semiconductor nanocrystals with heterogeneous carrier confinement. *Nano Lett.* **5**, 2044–2049 (2005).

220 K. Becker, J. Lupton, J. Lleri, A. L. Rogach, D. V. Talpin, H. Weller, J. Feldmann, Electrical control of Förster energy transfer, *Nature Materials* **5**, 777 (2006)



ROZWÓJ POTENCJAŁU I OFERTY DYDAKTYCZNEJ POLITECHNIKI WROCŁAWSKIEJ

transition is virtually unaffected by electric fields, the nanocrystal emission can be tuned over a wide range by exploiting the QCSE. This is due to the fact that the electron wavefunction can penetrate the shell and delocalize from the hole, an effect that can be enhanced by tilting the bands in an external potential. The elongated nanocrystals exhibit a typical QCSE^[221] almost an order of magnitude stronger than that of spherical particles ^[222]. This allows us to tune the microscopic resonance condition between the nanocrystal and dye and therefore the efficiency of energy transfer.

The dye emission exhibits a linewidth of ~ 7 nm around 670 ± 12 nm, whereas the single-nanocrystal PL can be tuned spectrally over a range of up to 25 nm ^[223] with a spectral width of below 1 nm. As energy transfer occurs from the nanocrystal to a vibrational level of the excited state of the molecule, the emission linewidth of the dye provides an upper limit for the spectral tunability of the nanocrystal necessary to electrically tailor the resonance condition. This spectral shift can be used to tune the spectral overlap with the absorption of an adjacent dye molecule and therefore the FRET coupling strength.

²²¹ Muller, J. et al. Wave function engineering in elongated semiconductor nanocrystals with heterogeneous carrier confinement. *Nano Lett.* **5**, 2044 (2005).

²²² Empedocles, S. A. & Bawendi, M. G. Quantum-confined Stark effect in single CdSe nanocrystallite quantum dots. *Science* **278**, 2114 (1997).

²²³ Muller, J. et al. Wave function engineering in elongated semiconductor nanocrystals with heterogeneous carrier confinement. *Nano Lett.* **5**, 2044 (2005).



ROZWÓJ POTENCJAŁU I OFERTY DYDAKTYCZNEJ POLITECHNIKI WROCŁAWSKIEJ

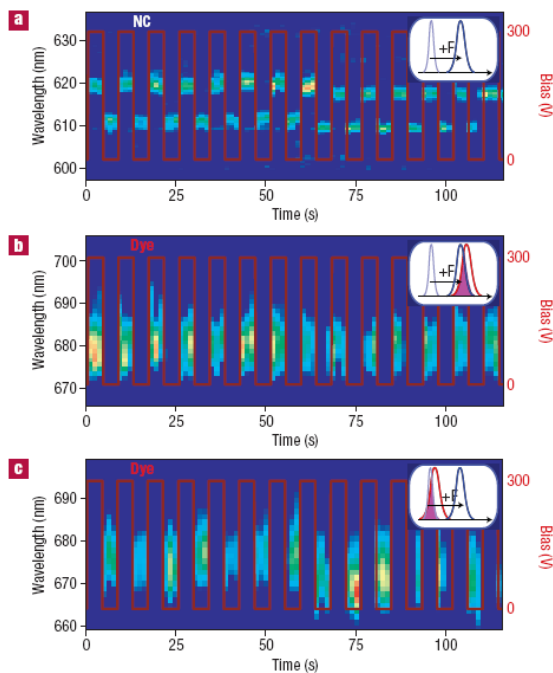


Figure 4.29 Electrical tuning of resonant energy transfer from nanocrystals to single dye molecules using the QCSE at 50 K. **a**, Dependence of the PL spectrum of a single nanocrystal on electric field in the absence of dye molecules. **b,c**, Modulation of the fluorescence of two different nanocrystal–dye couples by cyclic application of a bias. Depending on the spectral position of the nanocrystal, FRET occurs either with (**b**) or without (**c**) an electric field, so that the dye emission switches on and off with a change in field. Note that the nanocrystal concentration in **b** and **c** is 100-fold that in **a** to increase the probability of creating a switchable nanocrystal–dye couple [224].

This spectral shift can be used to tune the spectral overlap with the absorption of an adjacent dye molecule and therefore the FRET coupling strength. This spectral shift can be used to tune the spectral overlap with the absorption of an adjacent dye molecule and therefore the FRET coupling strength.

4.9 Mechanical properties of nanomaterials

In 1926, Jacov Frenkel estimated [225] the ideal (maximum attainable) shear strength of a perfect crystal to be about a tenth of its shear modulus (initial rigidity). But at that time, tests performed on real materials yielded strengths two to three orders of magnitude lower. This discrepancy was attributed to dislocations, which are boundaries of planar fault regions in the crystal structure where atoms slip out of position when the material is strained. However, as the characteristic scale (such as the crystal grain size or the smallest dimension of a thin film) shrinks below 100 nm, dislocations are ‘fatally attracted’ to internal interfaces (such as crystal grain boundaries) and surfaces of the specimen. Consequently, it becomes much more difficult to sustain a permanent population of mobile dislocations — which are

²²⁴ K. Becker, J. Lupton, J. Lleri, A. L. Rogach, D. V. Talpin, H. Weller, J. Feldmann, Electrical control of Forster energy transfer, *Nature Materials* 5, 777 (2006)

²²⁵ Frenkel, J. Z. *Phys.* 37, 572 (1926).



ROZWÓJ POTENCJAŁU I OFERTY DYDAKTYCZNEJ POLITECHNIKI WROCLAWSKIEJ

the vehicles of plastic deformation during straining — inside the material [²²⁶]. In these cases, deformation can be achieved only if new dislocations are nucleated afresh, usually from the same internal interfaces and surfaces that also absorb and annihilate them [²²⁷]. The continual need to nucleate new dislocations in these tiny crystals results in a significant increase in the material's strength.

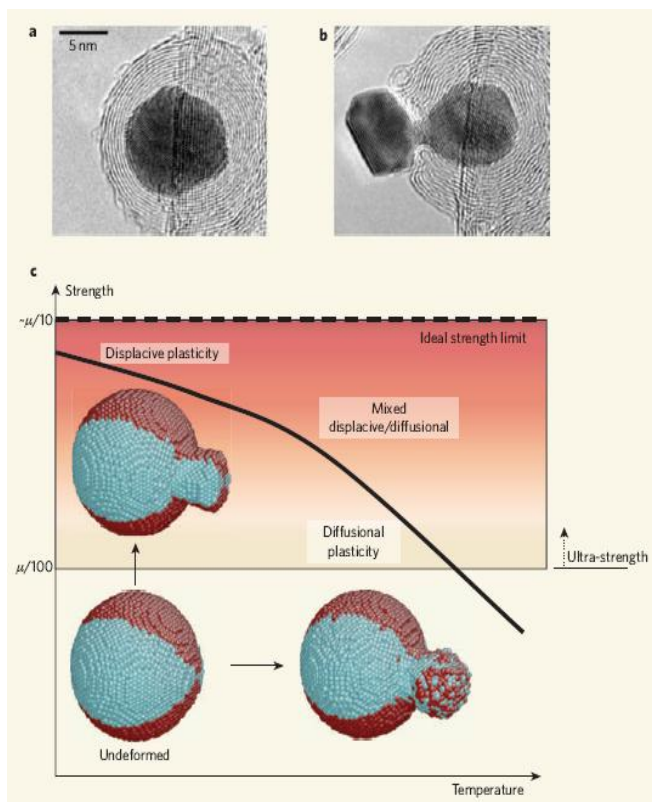


Figure 4.30 Crystal plasticity. Sun *et al.* [²²⁸] performed *in situ* transmission electron microscopy observations of the extrusion of single gold nanocrystals from graphitic capsules under electron irradiation at 300 °C. a, Before irradiation. b, After irradiation for 540 seconds. c, Deformation mechanisms. The black curve shows the typical dependence of the strengths of crystalline materials — expressed as a fraction of their shear modulus, μ — on temperature. As the temperature increases, one of three competing mechanisms operates: displacive, mixed or diffusional plasticity. Superimposed are illustrative simulations, which we carried out, of the plasticity of copper nanospheres at a temperature of 300 K (sphere at the top) and 900 K (sphere on the right), in which deformation is thought to be controlled by displacive and diffusional plasticity, respectively. The copper atoms are shown in two colours (red and cyan) to make it easier to track their motions from the undeformed crystal state (bottom left sphere) to the deformed state. At 900 K, the random mixing of red- and cyan-coloured atoms in the extrusion-neck region (where the stress gradient is largest) indicates that extensive surface diffusion is taking place. (a, b, Courtesy American Physical Society.)

One of three competing mechanisms, all dependent on temperature and mechanical strain rate, induces plastic deformation: displacive, diffusional or mixed plasticity. Displacive plasticity is produced by the collective shearing of atoms, that is, the glide of dislocations. Diffusional plasticity is governed by many, almost random, individual atom or vacancy hops. In conventional coarse-grained metals, typically below about $T_M/3$, where T_M is the absolute temperature at melting, deformation is dominated by displacive mechanisms, whereas above about $2T_M/3$ diffusional mechanisms control the process. A mixture of these two mechanisms

²²⁶ Greer, J. R. & Nix, W. D. Phys. Rev. B 73, 245410 (2006); Shan, Z. W., Mishra, R. K., Syed Asif, S. A., Warren, O. L. & Minor, A. M. Nature Mater. 7, 115 (2008).

²²⁷ Zhu, T., Li, J., Samanta, A., Kim, H. G. & Suresh, S. Proc. Natl Acad. Sci. USA 104, 3031–3036 (2007); Zhu, T., Li, J., Samanta, A., Leach, A. & Gall, K. Phys. Rev. Lett. 100, 025502 (2008)

²²⁸ Sun, L., Krashenninikov, A. V., Ahlgren, T., Nordlund, K. & Banhart, F. Phys. Rev. Lett. 101, 156101 (2008).



ROZWÓJ POTENCJAŁU I OFERTY DYDAKTYCZNEJ POLITECHNIKI WROCLAWSKIEJ

occurs at in-between temperatures; in such cases the inelastic strain is still mainly produced by dislocation glide but its rate is controlled by diffusion (**Fig. 4. 30c**).

5. Nanowires

Recently there is strong interest in investigations and applications of carbon-based nanomaterials like fullerenes (C-60), graphen or carbon nanotubes. Among the carbon nanotubes we can find two main class of this material: a single-wall nanotubes (SWNT) and a multi-wall nanotubes (MWNT) what has been shown in **Fig. 5.1**.

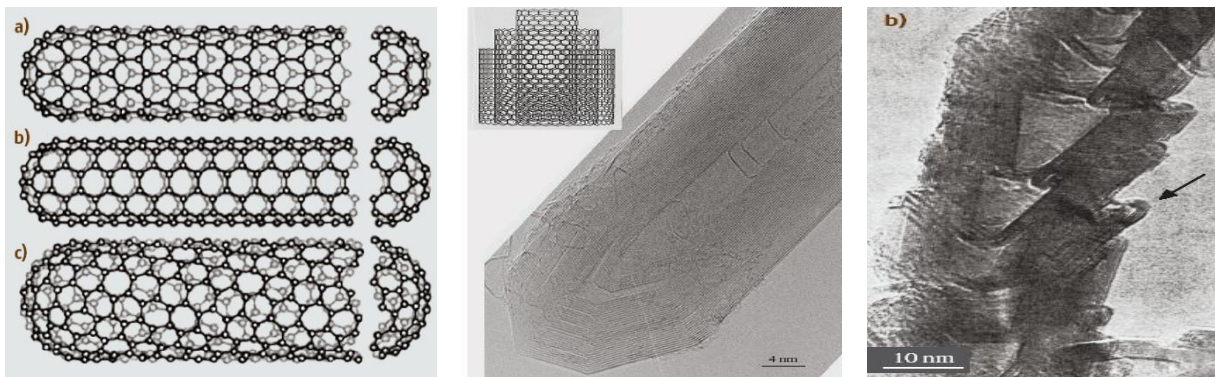
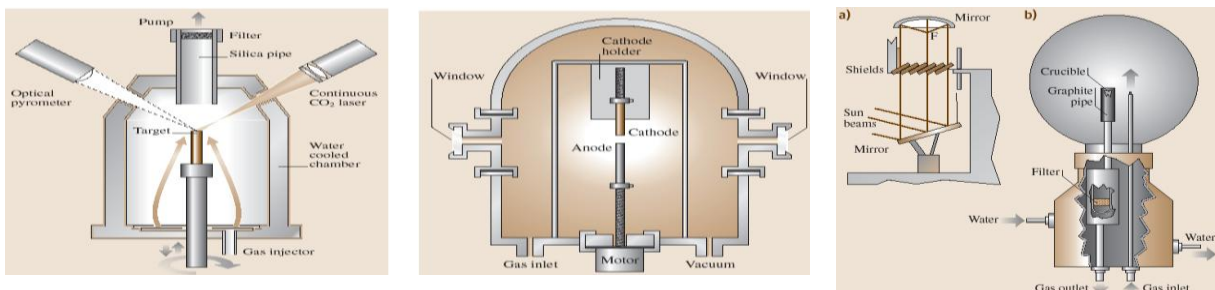


Figure 5.1 (a) SWNT (single-wall nanotubes) Optimal diameter 2.5nm(0.4nm) Chiral and achiral, (b) MWNT (multi-wall nanotubes) Concentric type (c-MWNT), (c) bamboo multi-wall nanotubes [229].

Figure 5.2 schematically shows different growing processes of such nanotubes.



²²⁹ Handbook of Nanotechnology, Bhushan, Bharat (Ed.), Springer 3rd ed. (2010).



ROZWÓJ POTENCJAŁU I OFERTY DYDAKTYCZNEJ POLITECHNIKI WROCŁAWSKIEJ

Figure 5.2 Different techniques of growing carbon nanotubes: (a) Laser ablation (pulsed or continual mode), (b) Electric arc, (c) Catalysis enhanced thermal cracing of gaseous carbon source (hydrocarbons, CO): Involves the catalitic decomposition of carbon containig source on small metallic particle or clusters [²³⁰].

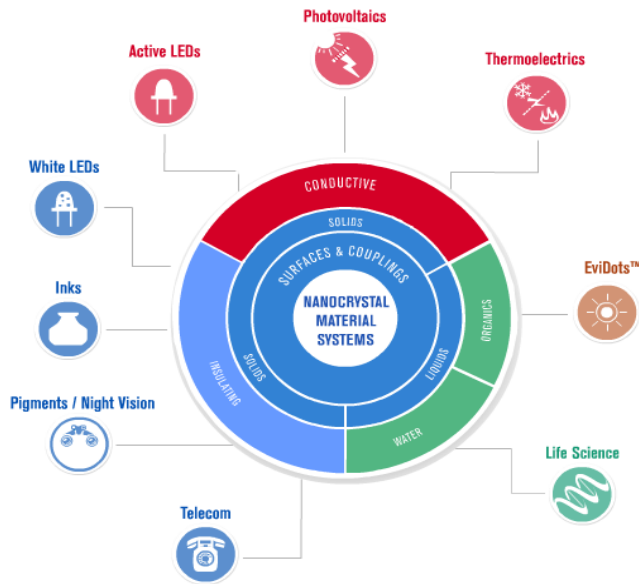
Nanotubes can be characterized by very interesting properties i.e. **mechanical properties**: different length of C-C bonds (diamond(sp³)=0.154nm : SWNT (sp²)=0.142nm), elasticity modulus better than 1000 GPa, very high flexibility, **chemical properties**: large surface come mainly from the caps of nanotube, filling by capillarity of crystallites, gas adsorption, grafting of molecules at the surface, **field emission properties**: excellent field emitter; high aspect ratio and small tip radius of curvature are ideal for field emission, cold emission of electrons under an electric field, tip effect, **electronic properties**: versatility: metallic or semiconductor depending on helicity: ‘tunable’ bandgap electronic properties can be tailored through application of external magnetic field, application of mechanical deformation...quantum effect due to the dimensionality reduction, conduction with no energy dissipation in certain cases, electrical conductivity six orders of magnitude higher than copper, very high current carrying capacity.

²³⁰ Handbook of Nanotechnology, Bhushan, Bharat (Ed.), Springer 3rd ed. (2010).



ROZWÓJ POTENCJAŁU I OFERTY DYDAKTYCZNEJ POLITECHNIKI WROCLAWSKIEJ

6. Applications of nanomaterials



In Fig. 6.1 there are some examples of nanomaterials used in different applications areas. In the next paragraph some examples of using nanomaterials (mostly quantum dots) will be given in more details.

Figure 6.1 Examples of application areas covered by quantum dots.

6.1 Bio-nano-medicine

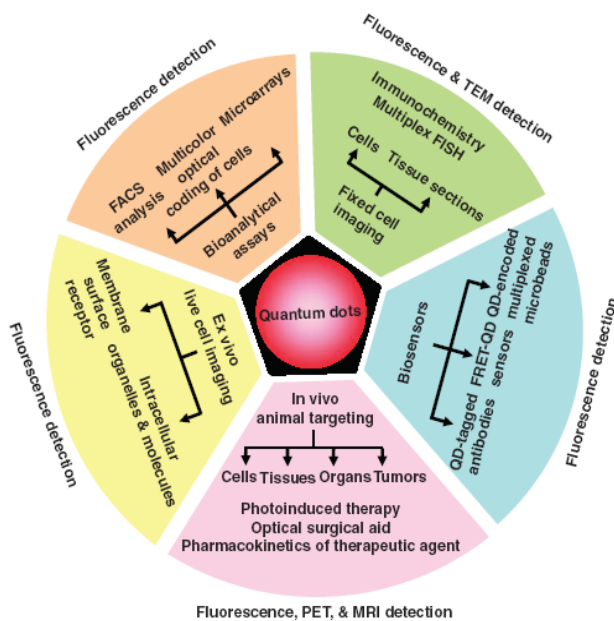


Figure 6.2 Application of quantum dots as multimodal contrast agents in bioimaging

Nanocrystals are recently very often used in bio-imaging. This is due to their much better, from some point of views, properties than i.e. proteins and molecular markers. The main advantages of such markers are (a) the size effect enable to tune the emission and absorption properties of each markers in wide range of wavelengths, (b) they are chemically stable- quantum dots last much longer than fluorescent



ROZWÓJ POTENCJAŁU I OFERTY DYDAKTYCZNEJ POLITECHNIKI WROCLAWSKIEJ

dyes with $< \sim 30$ minutes life,

(c) the emission from the quantum dots is nearly 100 times more stable than fluorescent dye molecules {e.g., rhodamine 6G (R6G)} against photobleaching. Experimental examples of many advantages of QDs as a optical markers have been shown in **Fig. 6.3**.

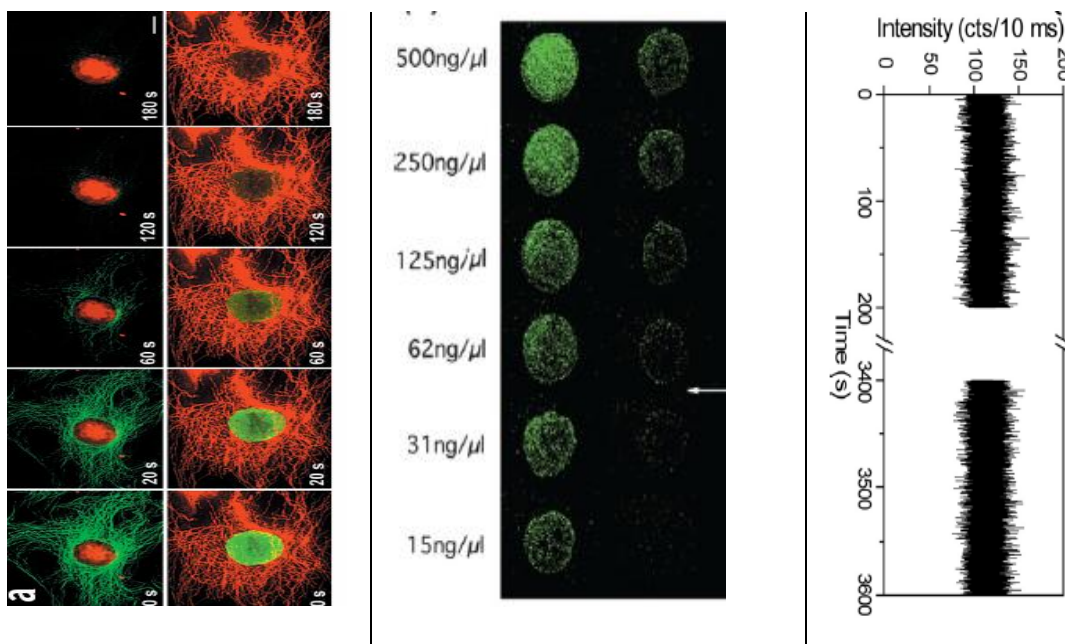


Figure 6.3 Comparison of optical properties of QDs vs. commonly used markers (a) Red=NC's; Green=Alexa 488 [²³¹], (b) Left = UC-NC's; Right = Cy 5 [²³²], (c) stability in time of emission recorded for single QD [²³³]

The very important parameter of nanocrystals used in biological systems is their size. **Figure 6.4** shows what sizes are typical for biological objects for better understanding of advantages and disadvantages of using nanocrystals in biology.

²³¹ Nature Methods 3, 647 (2006).

²³² Chem. Soc. Rev. 38, 976 (2009)

²³³ PNAS 106, 10917 (2009).



ROZWÓJ POTENCJAŁU I OFERTY DYDAKTYCZNEJ POLITECHNIKI WROCŁAWSKIEJ

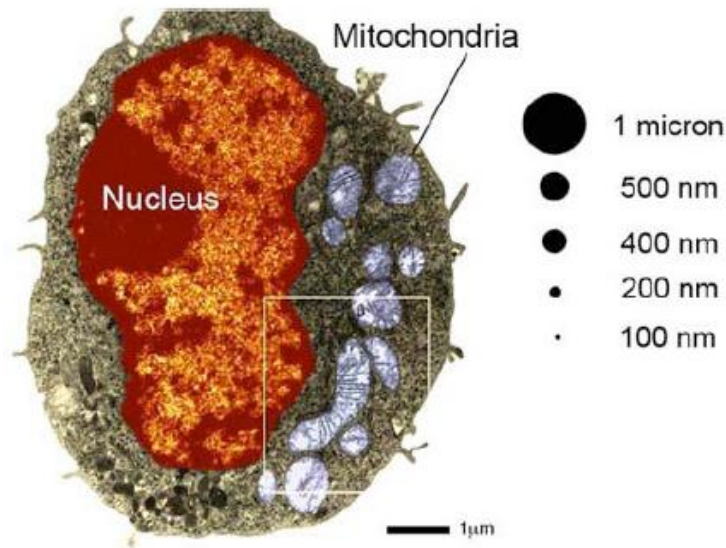


Figure 6.4 Comparison of rat macrophage cells size to nanoparticles size (at scale). Human macrophages are up to two times larger than rat macrophages. TEM image reproduced with permission from Environmental Health Perspectives [234].

Figure 6.4 shows other approaches when QDs are used for bio-application like bio sensing.

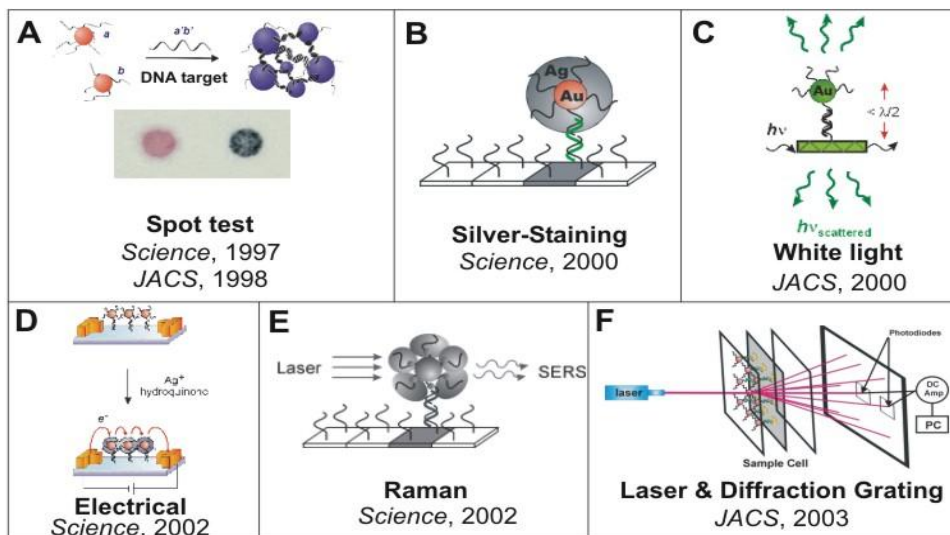


Figure 6.4 Different concepts of using QDs for bio-sensing.

²³⁴ Li N, Sioutas C, Cho A, Schmitz D, Misra C, Sempf J, Wang M, Oberley T, Froines J, Nel A 2003, Ultrafine Particulate Pollutants Induce Oxidative Stress and Mitochondrial Damage *Environ. Health Persp.* **111** 455-460

ROZWÓJ POTENCJAŁU I OFERTY DYDAKTYCZNEJ POLITECHNIKI WROCLAWSKIEJ

6.2 Optoelectronic applications

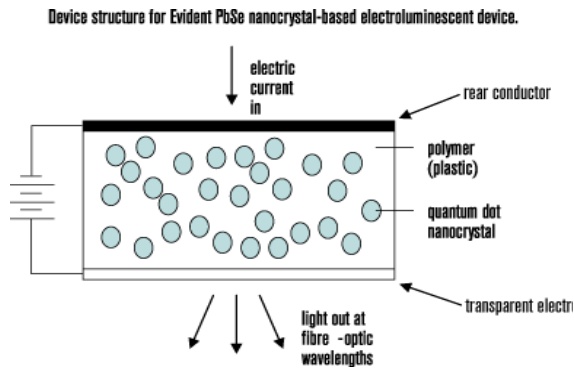


Figure 6.5 LED device based on QDs

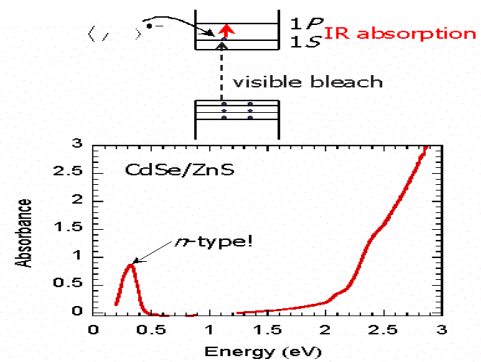


Figure 6.6 Infrared wavelengths detector based on QDs application [235]

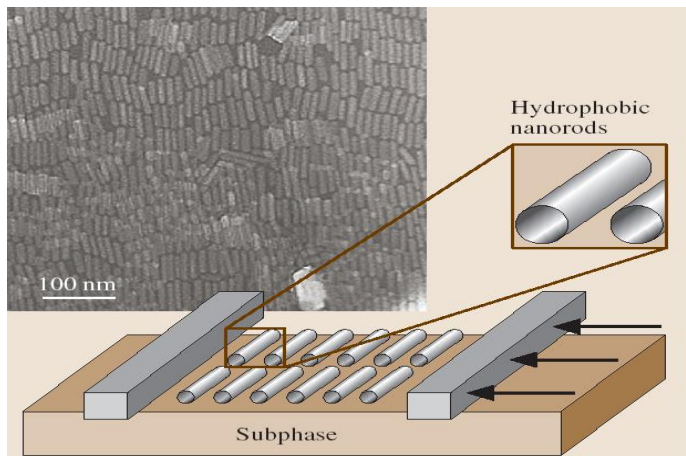


Figure 6.7 Hydrophobic layer based on nanowires application.

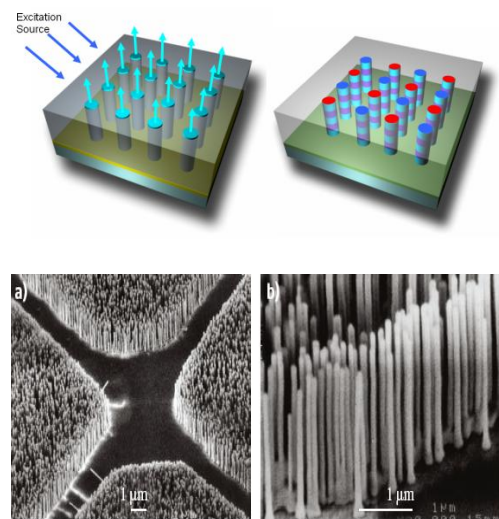


Figure 6.8 Field emitters based on using nanowires.

²³⁵ M. Shim, P. Guyot-Sionnest, Nature 407, 981 (2000)



ROZWÓJ POTENCJAŁU I OFERTY DYDAKTYCZNEJ POLITECHNIKI WROCŁAWSKIEJ

7. Characterization techniques

In this section, the main experimental techniques will be presented and briefly discussed.

7.1 Raman Spectroscopy

Raman spectroscopy is an important experimental technique based on inelastic scattering of monochromatic light, usually from a laser source. Inelastic scattering means that the frequency ν_0 of photons in monochromatic light changes after interaction with a sample. When monochromatic radiation is incident upon a sample then this light will interact with the sample in some fashion. Some of the interacting photons are transmitted, some are absorbed, but a majority of photons are scattered. Most of the scattered light is elastically scattered which means that frequency of the photons does not change. This kind of scattering is called Rayleigh scattering and is the same process described by Lord Rayleigh and which accounts for the blue color of the sky. However, the smaller portion of the scattered photons have frequency shifted up or down in comparison with original laser light frequency (so called Raman shift, frequently expressed as $\nu = 1/\lambda_{\text{original}} - 1/\lambda_{\text{scattered}}$). This phenomena is called the Raman effect. This inelastic scattered light makes up the Raman spectrum. Approximately only about 10^{-7} of the scattered light is Raman and therefore very precise instruments are needed to distinguish it from the predominant Rayleigh scattering. Instruments such as notch filters, tunable filters, laser stop apertures, double and triple spectrometric systems are used to reduce Rayleigh scattering and obtain high-quality Raman spectra. Raman shifted photons of light provides information i.e. about vibrational, rotational and other low frequency transitions in molecules. The amount of shift observed is characteristic for a particular kind of structure. It provide information about phonons in solids as well as vibrational, rotational and other low frequency transitions in molecules. In this way, Raman spectra may be used to examine chemical and structural properties of solid, liquid and gaseous samples. In Raman spectroscopy no probe physically touches the material the laser light is the only thing to disturb the sample, this means that the material is not disturbed by the probe physically touching it and in some cases is the only way to accurately study a material.



ROZWÓJ POTENCJAŁU I OFERTY DYDAKTYCZNEJ POLITECHNIKI WROCŁAWSKIEJ

(a) Origins of Raman scattering

The Raman effect is based on molecular deformations in electric field E determined by molecular polarizability α . The laser beam can be considered as an oscillating electromagnetic wave with electrical vector \mathbf{E} . Upon interaction with the sample it induces electric dipole moment $\mathbf{P} = \alpha\mathbf{E}$ which deforms molecules. Because of periodical deformation, molecules start vibrating with characteristic frequency ν_n . In this way, after scattering process, the original light frequency ν_0 may be down-shifted ($\nu_0 - \nu_n$) or up-shifted ($\nu_0 + \nu_n$). The first process is called Stokes Raman scattering and the second Anti-Stokes Raman scattering. By far the stronger of the two processes is the Stokes scattering.

In the quantum picture, the molecular vibrations ν_n are quantized. The scattering process is viewed as the creation and annihilation of vibrational excitations (or "phonons") by photons. This interpretation leads naturally to the fact that photons can always create more vibrational quanta in a system, so that the probability of Stokes scattering is not temperature-dependent. However, the probability of annihilation of a vibrational quantum depends on the probability of finding the system in an excited vibrational state. The ratio of the intensities of Stokes and anti-Stokes bands thus reflects i.e. the Boltzmann factor $\exp(-h\nu/kT)$.

The following diagram illustrates the transitions involved in light scattering; here, $h\nu$ is the photon energy and n is the number of vibrational quanta present in the system. This latter can be related to phonon modes, rotational and vibrational states etc. There are assumed to be several vibrational levels within the electronic ground state.



ROZWÓJ POTENCJAŁU I OFERTY DYDAKTYCZNEJ POLITECHNIKI WROCLAWSKIEJ

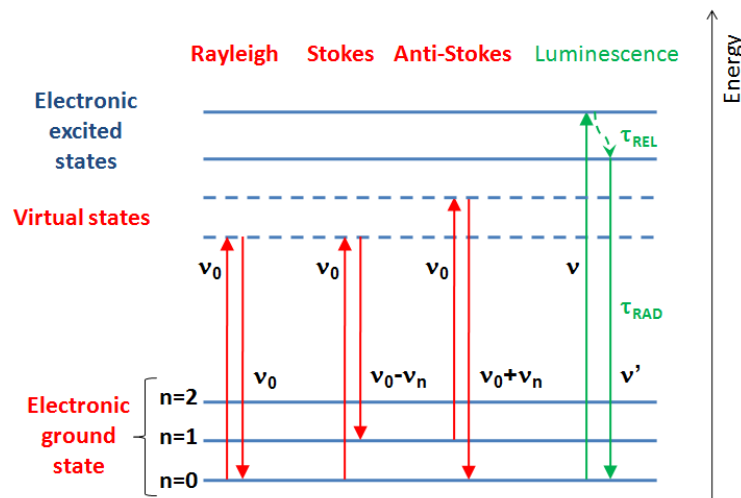


Figure 1. Diagram illustrating transitions involved in light scattering (Rayleigh, Stokes Raman and Anti-Stokes Raman scattering) and luminescence processes. The incident photon frequency is ν_0 for scattering processes.

There is one thing common for all scattering processes: excitation by the incoming light involves transition from electronic ground state to an virtual state. A virtual transition can occur for a photon whose energy is below the ground-to-first excited-state gap. A strong light source can produce a distorted (perturbed) excited state due to the change in the potential caused by the external electromagnetic field, represented as a virtual superposition of the free molecular states. Nevertheless, for transitions involving virtual states a few possibilities exist:

- The Rayleigh scattering. In this case transition occurs between a virtual state and electronic ground state without changing the vibrational quantum number n . Therefore this is the elastic scattering case where frequency of scattered photons remains unchanged.
- The Stokes Raman scattering. This process consists of a dipole transition from the ground state with vibrational quantum number $n=0$ to the virtual state and then return transition from the virtual state to the ground state with higher vibrational quantum number $n=1$. This means that the frequency of scattered photons is lowered and equal to $\nu_0 - \nu_n$.
- The Anti-Stokes scattering. In this process transition to the virtual state occurs from ground state with vibrational quantum number $n=1$ and then carriers return to the ground state with $n=0$. This means that the frequency of the scattered photons increased being equal to $\nu_0 + \nu_n$.



ROZWÓJ POTENCJAŁU I OFERTY DYDAKTYCZNEJ POLITECHNIKI WROCŁAWSKIEJ

It should be emphasized here, that the Raman effect differs essentially from the process of luminescence. For the latter, the incident photon is absorbed and the system is transferred to an excited state from which it may relax nonradiatively to various lower states after a certain time τ_{REL} and then relax radiatively to the ground state after τ_{RAD} . It is therefore a lasting process that occurs only for resonant excitation frequency. The lifetimes of luminescence may be very long. As opposite to this, the Raman effect involves virtual transitions and may take place for any frequency of the incident light (non-resonant process). What is more, the Raman scattering takes place during the excitation and is therefore an instant process. We may also conclude that fluorescence peak is anchored at a specific excitation frequency, whereas a Raman peak maintains a constant separation from the excitation frequency. It is however possible to involve real electronic state in Raman scattering instead of virtual one. This kind of resonant Raman process can increase many orders the cross-section for Raman scattering. This effect is often exploited experimentally to obtain stronger signals or even to investigate the electronic energy levels of the system.

(b) Experimental setup

A system used for Raman spectroscopy usually consists of four major components:

1. Excitation source (Laser).
2. Optics to illuminate sample and collect sample response.
3. Spectrometer (wavelength selector).
4. Detector (Photodiode array, CCD or PMT).

During measurement a sample is illuminated with a laser beam in the ultraviolet (UV), visible (Vis) or near infrared (NIR) range. Scattered light is then collected with optical system of lenses and sent spectrometer to obtain Raman spectrum of a sample.



ROZWÓJ POTENCJAŁU I OFERTY DYDAKTYCZNEJ POLITECHNIKI WROCLAWSKIEJ

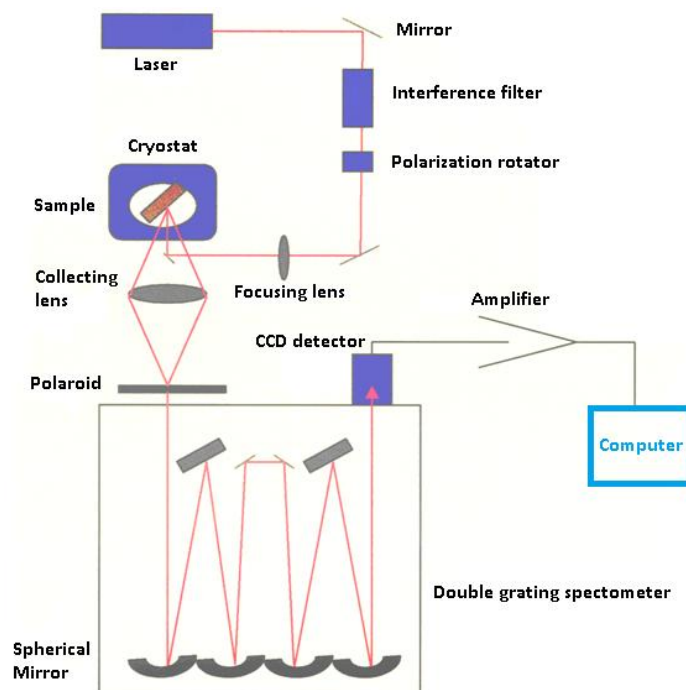


Figure 2. Typical Raman system with double grating spectrometer and CCD camera used for signal detection.

Since spontaneous Raman scattering is very weak the main difficulty of Raman spectroscopy is separating it from the intense Rayleigh scattering. More precisely, the major problem here is not the Rayleigh scattering itself, but the fact that the intensity of stray light from the Rayleigh scattering may greatly exceed the intensity of the useful Raman signal in the close proximity to the laser wavelength. In many cases the problem is resolved by simply cutting off the spectral range close to the laser line where the stray light has the most prominent effect. People use commercially available interference (notch) filters which cut-off spectral range of $\pm 80\text{-}120\text{ cm}^{-1}$ from the laser line. This method is efficient in stray light elimination but it does not allow detection of low-frequency Raman modes in the range below 100 cm^{-1} . Stray light is generated in the spectrometer mainly upon light dispersion on gratings and strongly depends on grating quality. Raman spectrometers typically use holographic gratings which normally have much less manufacturing defects in their structure than the ruled ones. Stray light produced by holographic gratings is about an order of magnitude less intense than from ruled gratings of the same groove density. Using multiple dispersion stages is another way of stray light reduction. Double and triple spectrometers allow taking Raman



ROZWÓJ POTENCJAŁU I OFERTY DYDAKTYCZNEJ POLITECHNIKI WROCŁAWSKIEJ

spectra without use of notch filters. In such systems Raman-active modes with frequencies as low as $3\text{-}5\text{ cm}^{-1}$ can be efficiently detected.

In earlier times people primarily used single-point detectors such as photon-counting Photomultiplier Tubes (PMT). However, a single Raman spectrum obtained with a PMT detector in wavenumber scanning mode was taking substantial period of time, slowing down any research or industrial activity based on Raman analytical technique. Nowadays, more and more often researchers use multi-channel detectors like Photodiode Arrays (PDA) or, more commonly, a Charge-Coupled Devices (CCD) to detect the Raman scattered light. Sensitivity and performance of modern CCD detectors are rapidly improving. In many cases CCD is becoming the detector of choice for Raman spectroscopy.

(c) Coherent Anti-Stokes Raman Spectroscopy (CARS)

There are many ways to enhance weak Raman signal intensity. One of them called Coherent Anti-Stokes Raman Spectroscopy is type of “non-linear” Raman spectroscopy. In this technique, instead of one laser beam, two very strong collinear lasers illuminate a sample. Usually, frequency of the first laser remains constant during experiment. However, the frequency of the second laser may be tuned so that the frequency difference between the two beams equals exactly the frequency of some Raman-active mode of interest. This particular mode will be the only extremely strong mode in the Raman signal. In this way, only one strong Raman peak of interest may be obtained. In CARS measurement a monochromator is not really required. Instead of this a wideband interference filter and a detector behind the filter may be used.

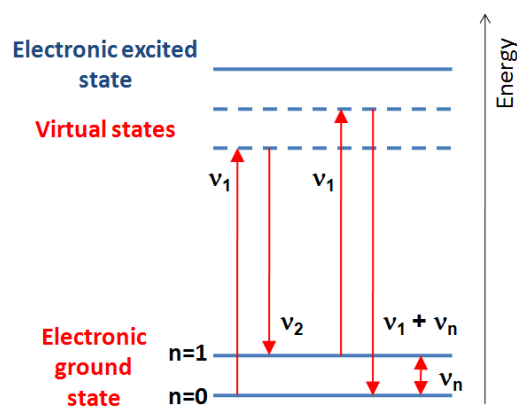


Figure 3. Transitions scheme for CARS. Two laser frequencies are used (ν_1 and ν_2).



ROZWÓJ POTENCJAŁU I OFERTY DYDAKTYCZNEJ POLITECHNIKI WROCŁAWSKIEJ

To understand CARS in more details the transitions involved in light scattering have been illustrated in the figure above. Two laser with frequencies ν_1 and ν_2 ($\nu_1 > \nu_2$) interact coherently, and due to wave mixing [²³⁶], produce strong scattered light of frequency $2\nu_1 - \nu_2$. If the frequency difference between two lasers $\nu_1 - \nu_2$ is equal to the frequency ν_n of a Raman-active mode then a strong light of frequency $\nu_1 + \nu_n$ is emitted. In other words, to obtain strong Raman signal the second laser frequency should be tuned in a way that $\nu_2 = \nu_1 - \nu_n$. Then the frequency of strong scattered light will be $2\nu_1 - \nu_2 = 2\nu_1 - (\nu_1 - \nu_n) = \nu_1 + \nu_n$, which is higher than the excitation frequency ν_1 and therefore considered to be Anti-Stokes frequency. Coherent Anti-Stokes Raman Spectroscopy derives its name from the fact that it uses two Coherent laser beams and the resulting signal has Anti-Stokes frequency.

(d) Raman Microscopy

The Raman microscope is by far one of the best instrumentation enhancements one can make. The new generation of Raman microscopes may offer a powerful non-destructive and non-contact method of sample analysis. In this kind of system sample regions as small as one micron can be examined. This is completely different than in macro-sampling mode where the obtained Raman spectrum provides average information over a large area.

In Raman Microscope the traditional Raman spectroscopy is combined with optical microscopy to investigate microscopic samples present as, for example, inclusions within other materials. This technique has found many industrial applications, for instance, in the diagnosis of problems in the production of plastics, where catalyst particles embedded in the polymer can be identified.

²³⁶ Mingjun Chi, J-P. Hignard, P. M. Petersen, "A general theory of two-wave mixing in nonlinear media", J. Opt. Soc. Am. B 26, 1578 (2009)

ROZWÓJ POTENCJAŁU I OFERTY DYDAKTYCZNEJ POLITECHNIKI WROCLAWSKIEJ

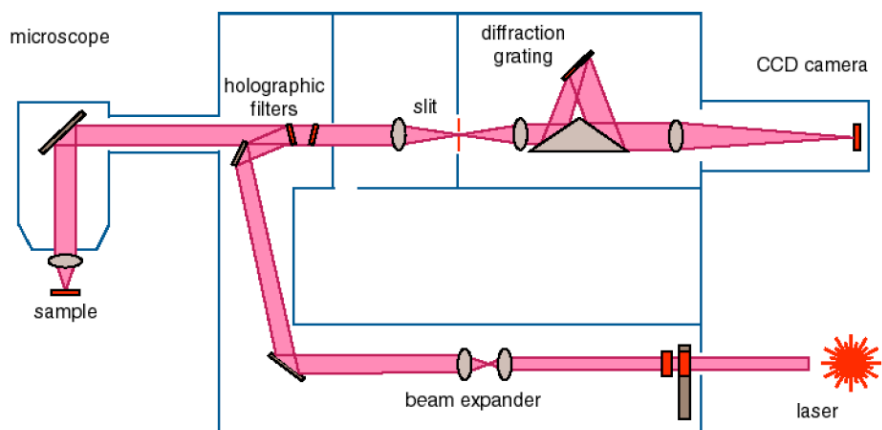


Figure 4. Example of Micro-Raman Spectrometer (picture after Renishaw).

A microscope may be used in conjunction with a Raman spectrometer in two basic ways. Firstly, one may select a region of a sample by inspecting its white-light image; the Raman spectrum of that region may then be recorded. Alternatively, one may record a two-dimensional "map" of the intensity of some Raman band of the material as a function of position. Reference [237] contains a very useful introductory chapter on this subject.

The laser beam is generally introduced into the microscope via a side-arm with a spatial filter to improve the beam profile; a beam splitter then reflects some of the laser beam down to the sample through the objective lens. The scattered light is collected through the same objective lens and some of it passes through the beam splitter. A movable prism or mirror can be inserted into the microscope column to reflect the beam out to a spectrometer; the prism can also be withdrawn so that the light passes up to a video camera in order to allow one to identify the desired region of the sample. Spatial resolutions of around 10^{-6} m can be achieved, depending on the particular optical system used.

Note that by use of a confocal system with appropriate spatial filtering, it is possible to obtain a very restricted depth of field, so that spectra may even be obtained from different depths in transparent samples. Moreover, it is possible to obtain 1 μm resolution inside the sample (confocal resolution) using 514.5 nm laser excitation and 100X objective. In this way, sample properties may be investigated deep inside, penetrating sample layer after. The depth

²³⁷ "Practical Raman Spectroscopy", D. J. Gardiner and P. R. Graves (eds.) (Springer-Verlag 1989)



ROZWÓJ POTENCJAŁU I OFERTY DYDAKTYCZNEJ POLITECHNIKI WROCŁAWSKIEJ

of penetration depends on wavelength of excitation, objective magnification and sample quality.

(e) Examples of Raman measurements applications

As has been described, Raman spectroscopy can be used to obtain information about the vibrational spectrum of a material. This can lead to a better understanding of the chemical composition of the sample, as in many organic compounds, where different chemical bonds have very characteristic vibrational frequencies. It may also be possible to deduce the structure of a material; for example, in molecular systems, the juxtaposition of different chemical species leads to small modifications of the usual vibrational frequencies, so that longer-scale structure may be investigated. In crystalline solids, the selection rules for scattering from the lattice vibrations (phonons) indicate the symmetry of the crystal unit cell and can thus reveal (for example) phase changes. Finally, via resonance Raman spectra, one can sometimes correlate a particular vibrational mode with a particular electronic transition energy and thus learn more about the electronic structure of the material. Below, we give a few examples of Raman spectroscopy applications.

Figure 5 shows a Raman spectra obtained for II-VI semiconductors doped with 3d elements [²³⁸]. The spectrum of ZnSe sample (dotted lines) contains the well known phonon modes: TO, LO, 2LO and 2TA(X). After doping the spectrum undergoes a number of changes (broadening, change of the peaks intensity) due to presence of Cr and Ni elements. Some of these changes can be interpreted as induced by increasing lattice strains that appear after dopant introduction.

²³⁸ V. I. Sokolov et. al. Phys. Sol. State 47, 1567 (2005)



ROZWÓJ POTENCJAŁU I OFERTY DYDAKTYCZNEJ POLITECHNIKI WROCŁAWSKIEJ

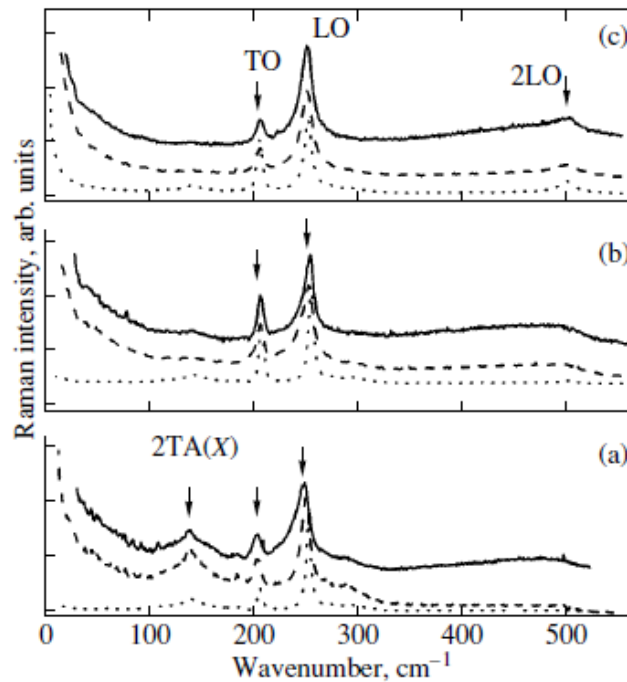


Figure 5. The room-temperature Raman spectra of ZnSe (dotted lines), Zn_{1-y}Cr_ySe (dashed lines) and Zn_{1-x}Ni_xSe (solid lines). The laser excitation wavelength is (a) 632.8, (b) 514 and (c) 488 nm. Optical as well as acoustic phonon modes characteristic for ZnSe semiconductor may be identified.

While many techniques can inform on the nature of the elements of a material sample, Raman spectroscopy can also give the evidence of chemical bonds between atoms, either the sample is in the gaseous, liquid or solid state. The Raman spectrum of a Si_{0.74}Ge_{0.26} alloy (Fig. 6), shows not only bands characteristic of Si-Si bond at 466 cm⁻¹ and Ge-Ge bond at 272 cm⁻¹ but also Ge-Si bond at 388 cm⁻¹. In addition, the frequency and the relative intensity of these bands compared to those of pure Si (521 cm⁻¹) and Ge (300 cm⁻¹) also indicate the aggregate composition and geometry of the alloy.



ROZWÓJ POTENCJAŁU I OFERTY DYDAKTYCZNEJ POLITECHNIKI WROCŁAWSKIEJ

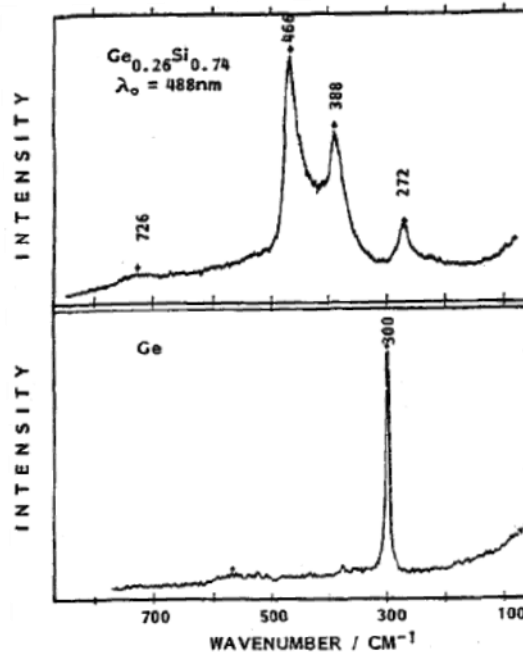


Figure 6. Raman spectrum of Ge-Si alloy [²³⁹].

Although vibrational spectroscopy is only an indirect method for the structural determination, this technique presents some advantage in comparison to other direct diffraction methods, in the studies of amorphous or disordered materials. For silicon, it is not only easy to distinguish crystalline silicon from amorphous silicon (Fig. 7) but one is able to follow several degrees of amorphicity by measuring the frequency, varying from 461 cm^{-1} in totally amorphous, to 521 cm^{-1} in bulk crystalline silicon. Of course, the band width at half intensity or the band shape can also help to understand the dynamic aspect of the silicon motion inside of the disordered network. This technique is particularly helpful in the characterization of a silicon annealed by a laser.

²³⁹ P. V. Huong, J. Phys. IV France, 1, C6 (1991)

ROZWÓJ POTENCJAŁU I OFERTY DYDAKTYCZNEJ POLITECHNIKI WROCŁAWSKIEJ

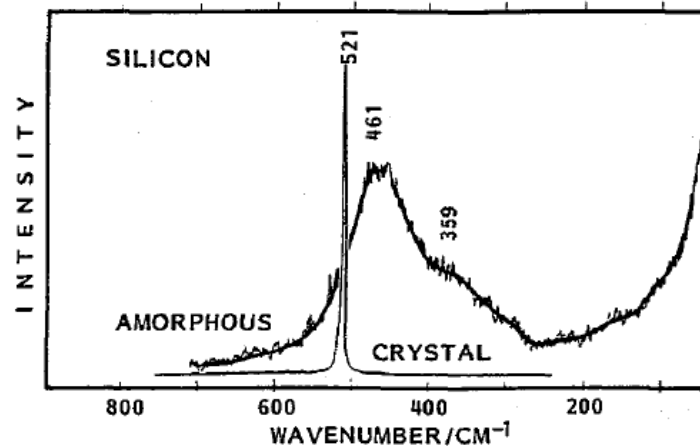


Figure 7. Raman spectrum of amorphous silicon [4].

Raman spectroscopy may be also used for investigations of low dimensional semiconductor nanostructures. In this case, electronic and phonon quantum confinement have been the subject of extensive studies in the past decades. The electronic quantum size effect is mostly detected as a shift of the interband absorption or luminescence peak to higher energies. This is normally observed in quantum wells, quantum wires or in quantum dots. However, it turns out that also vibrational properties changes when the size of the structure is reduced and size-induced phonon confinement effects may be observed.

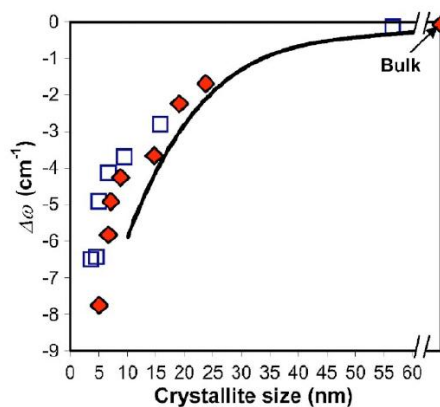


Figure 8. Crystallite-size-dependent Raman frequency shift of the A_{1g} mode relative to bulk frequency. The empty squares represent nano-crystalline rutile SnO₂, solid diamonds represents rutile TiO₂, and the solid curve is a phonon confinement model prediction for rutile SnO₂. The picture was taken from [240].

²⁴⁰ Varghese Swamy and Barry C. Muddle "Size-dependent modifications of the Raman spectrum of rutile TiO₂", Appl. Phys. Lett. 89,163118 (2006).



ROZWÓJ POTENCJAŁU I OFERTY DYDAKTYCZNEJ POLITECHNIKI WROCŁAWSKIEJ

Confining a phonon of wave vector k_0 in a nano-structure of size L requires the superposition of many bulk phonons covering the range $\Delta k \sim 1/L$. This result is essentially a manifestation of the uncertainty principle: i.e. $1 \sim \Delta k L$. This range of Δk of "activated" phonons should lead to a broadening and shifting of the nano-wire phonon Raman band relative to the band symmetry in the bulk. For 0-dimensional nano-structures there are many systematic experimental investigation of size dependent Raman shifts. In Fig. 8 an example of such a study on TiO_2 and SnO_2 low dimensional crystallites is shown. Some more examples of confinement effects on Raman spectra can be found in reference [241].

The main difference between Raman scattering from bulk systems and lower dimensional systems is that the latter have electronic states and vibrational properties different from the bulk. While these differences do not cause any principal limitations, the small number of atoms present in the lower dimensional systems turns out to be the main experimental obstacle. As a result the scattering intensities are low and the experiment needs to be carefully designed.

7.2 Time-resolved Photoluminescence Spectroscopy

Suppose a sample with one sort of emitters (quantum dots, nanocrystals) is excited with an infinitesimally sharp pulse of light. This results in an initial population of the excited state emitters N_0 . The emitter that is in the excited state may then emit a photon and return to the ground state. In this way the population of excited emitters changes in time. In the simplest case this relaxation process may be described by differential equation of the following form:

$$\frac{dN(t)}{dt} = -k \cdot N(t)$$

where $N(t)$ is the number of excited emitters at the moment t and k is a constant decay rate (number of decay processes per time). The solution of the above equation is:

$$N(t) = N_0 \exp(-kt)$$

²⁴¹ S. K. Gupta, P. K. Jha, "Modified phonon confinement model for size dependent Raman shift and linewidth of silicon nanocrystals", Solid State Communications 149, 1989 (2009)



ROZWÓJ POTENCJAŁU I OFERTY DYDAKTYCZNEJ POLITECHNIKI WROCŁAWSKIEJ

We may now define a photoluminescence intensity as negative time derivative of the $N(t)$ function which means that number of emitted photons is determined by how fast the number of excited emitters decreases in time:

$$g(t) = -\frac{dN(t)}{dt} = A \cdot \exp(-kt)$$

where A is a constant. The function $g(t)$ is called response function of the sample and describes how photoluminescence intensity changes in time. Moreover, a photoluminescence lifetime $\tau=1/k$ may be defined as a time after which initial intensity A decreases e times so that $g(\tau)=A/e$. An example how the decay curve may look like have been shown in the picture below.

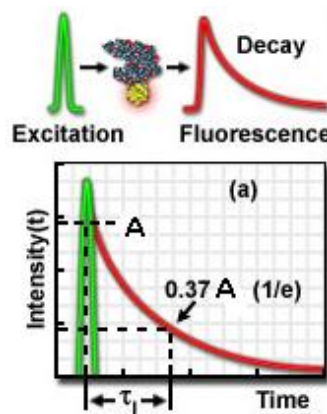


Figure 9. Time domain photoluminescence decay measurement. The decay curve as well as excitation pulse are shown.

It should be noted here, that in real situations the decays are frequently much more complex than single-exponential. Nevertheless, measurement of the time-resolved luminescence properties of a given emitting structure is an integral part of the determination of the photo-physical parameters of the species. These properties are useful in spectroscopy, kinetics, energy transfer, analytical applications and in characterization of chemical, biological and physical systems which emit light. For photoluminescence decay measurement an examined structure has to be excited with a appropriately short light pulse. Many different pulsed light sources may be utilized: LED, a laser diode, gas laser, xenon lamp. The photoluminescence intensity is measured at different time delays after the pulse. As a result, a photoluminescence decay curve is collected. The major difference between different techniques is in the detection.



ROZWÓJ POTENCJAŁU I OFERTY DYDAKTYCZNEJ POLITECHNIKI WROCLAWSKIEJ

(a) The Stroboscopic Technique (Strobe)

The most important feature of the Strobe technique is that during measurement the detector (which is a specially-configured photomultiplier tube - PMT) is active only for a very short period of time after the excitation pulse is released. The detector records the intensity of the photoluminescence at the moment it is active. The window of time during which the PMT is active is controlled by a delay gate generator. The standard delay gate generator may step the delay in constant time increments. In this way, the delay consequently increases with each excitation pulse (in other words, it sweeps the delay). As a result, a decay curve is produced.

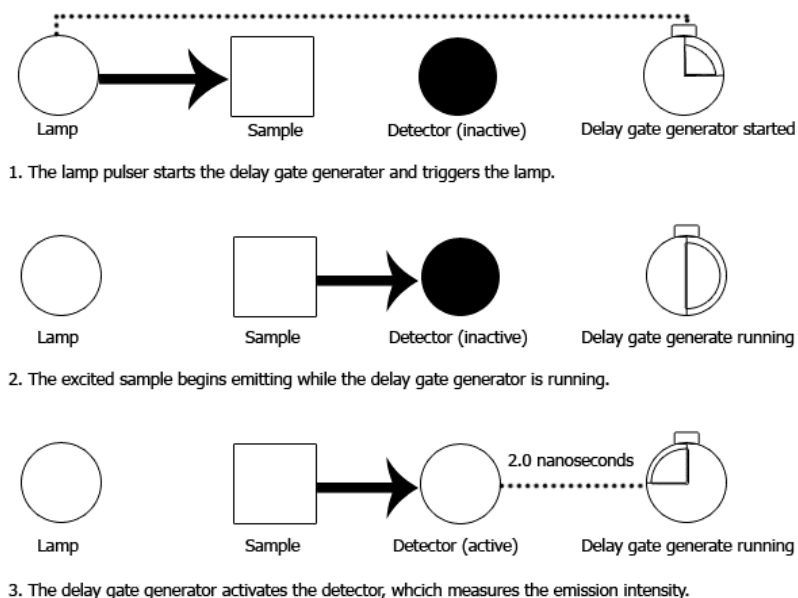


Figure 9. The Strobe technique principles (after Photon Technology International).

Above you can find a graphic representation of the Strobe technique principles. In the first step, the excitation source release a short light pulse. Simultaneously, delay gate generator is activated. In the second step, sample is excited by the light pulse and starts emitting. Delay gate generator is still running but the detector is inactive. In the last step, the delay gate generator activates the detector to measure the emission intensity. The detector remains active only for a very short period of time (so called *integration time*). In general, the shorter detector activity period the better time-resolution of the measurement. However,



ROZWÓJ POTENCJAŁU I OFERTY DYDAKTYCZNEJ POLITECHNIKI WROCŁAWSKIEJ

decreasing integration time leads to the signal intensity drop and this should be always taken into account while choosing experimental conditions. The three steps described above are then repeated. With each cycle, the delay gate generator increases the delay by a multiple of some constant time interval and the data is collected again. After many cycles the decay curve is built as shown in Fig. 10.

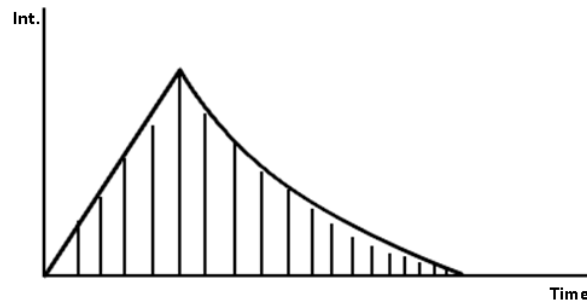


Figure 10. The photoluminescence decay curve after 18 cycles. The constant time interval between each experimental point is controlled by delay gate generator.

To increase experiment accuracy, the entire sweep can be repeated, and the individual intensities averaged. This is helpful when the overall signal is low and noisy. However, as you can see, a full decay curve is attainable after just one sweep which makes this technique very fast. This is because it measures fluorescence intensity directly and, unlike photon counting techniques, is not limited by photon counting statistic and can therefore take advantage of high intensity fluorescence.

A block diagram of led-based stroboscopic system is shown in Fig. 11. A master clock (oscillator) generates pulses at a fixed 25 kHz frequency. The pulses are routed simultaneously to the LED pulser and a digital delay gate generator (DGG) unit. The pulser triggers the LED; the LED flashes and excites the sample, which subsequently emits fluorescence. At the same time the pulse synchronized with the LED pulse triggers the DGG, which outputs a delayed TTL pulse.

The DDG is under computer control and the value of the TTL pulse delay is determined in the acquisition software. The delayed pulse triggers an avalanche circuit, which provides a high voltage pulse (ca. 500 V) for the detection circuitry. This pulse creates the gain and the temporal discrimination gate for the photomultiplier.

ROZWÓJ POTENCJAŁU I OFERTY DYDAKTYCZNEJ POLITECHNIKI WROCŁAWSKIEJ

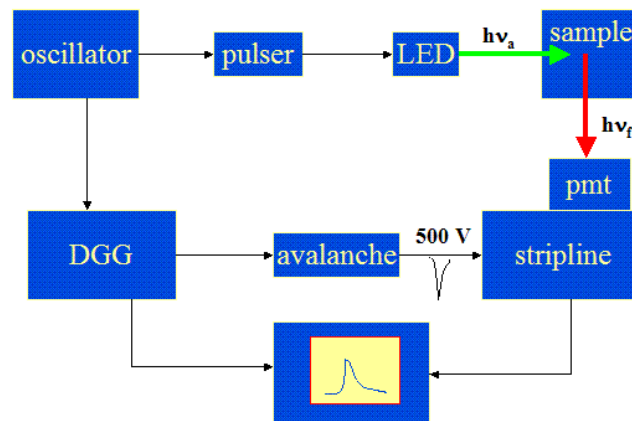


Figure 11. Block diagram of LED-based stroboscopic setup (after Photon Technology International).

An important feature is that the strobe technique does not use a conventional voltage divider network for providing inter-dynode voltages in the photomultiplier (PMT). Instead, the PMT dynodes are interconnected by a stripline circuit. The pulse from the avalanche is injected in the stripline at the time delay specified by the DGG. The pulse travels along the dynode chain amplifying the primary photoelectrons generated at the specific time delay. In this way high amplification and time gating are simultaneously achieved in the PMT strobe circuit.

In case when lifetime of photoluminescence decay is comparable to excitation pulse duration the measured decay curve $PL(t)$ is in fact convolution of two functions: instrument response function IRF and photoluminescence response of the sample $g(t)$. This means that the excitation pulse distorts the intrinsic luminescence response from the sample. This is a common problem for all the time-domain measurements techniques.



ROZWÓJ POTENCJAŁU I OFERTY DYDAKTYCZNEJ POLITECHNIKI WROCŁAWSKIEJ

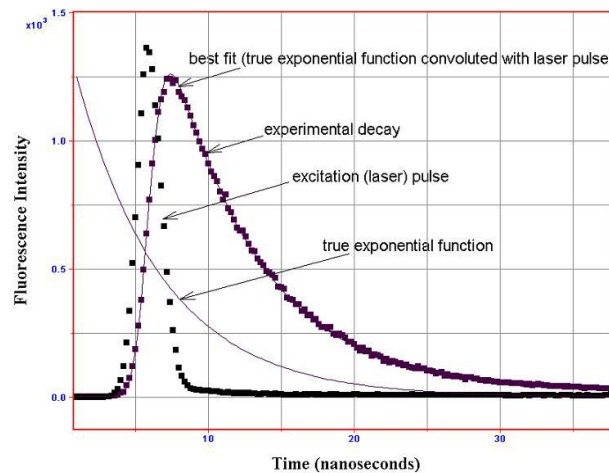


Figure 12. Example of experimental data: the measured decay and excitation pulse are shown. After deconvolution procedure it was found that sample response is an exponential function.

To calculate the real sample response $g(t)$ that have physical meaning a deconvolution procedure should be applied. This can be done, for instance, using the convolution integral [242]:

$$PL(t) = A_0 \int_0^t IRF(\tau)g(t-\tau)d\tau$$

In a typical experiment, IRF function may be measured. This can be done using a scatterer solution and measuring the scattered excitation light decay (detection wavelength should be set equal to excitation wavelength). Analysis is then performed according to the above equation: the IRF is taken from experiment and a model function is applied for $g(t)$ (e.g. a single exponential decay or a double exponential decay or some other function). In the next step the calculated $PL(t)$ is compared with the experimental decay (the parameters used in the $g(t)$ model can be modified in this point). This may be done by an iterative numerical procedure until the best agreement with the experimental decay curve is achieved. Resulting from the best fit $g(t)$ is the real sample response function. It should be however noted here, that choice of the $g(t)$ function is often a very difficult task and fit quality does not prove that the model is unique. Therefore very careful analysis should be performed to find the right function.

In Fig. 12 the sample response function $g(t)=I_0\exp(-t/\tau)$ was chosen to model measured $PL(t)$ decay. All the $g(t)$ parameters (the amplitude I_0 , the lifetime τ) were then

²⁴² D. F. Eaton Pure and Appl. Chem. "Recommended methods for fluorescence decay analysis" 62, 1631 (1990). Some more technical information about analysis of luminescence decays may be found in the above publication.



ROZWÓJ POTENCJAŁU I OFERTY DYDAKTYCZNEJ POLITECHNIKI WROCŁAWSKIEJ

calculated by means of least squares fit to the experimental data. Obtained in this way function have now physical meaning (described at the beginning of this chapter) and is not distorted by IRF excitation pulse.

It is interesting to see how convolution integral behaves when the $g(t)$ function has very fast decay time that is much faster than time-resolution of the used setup. In this case the delta function may be used to model $g(t)$ and convolution integral take the form:

$$\int_0^t IRF(\tau)\delta(t-\tau)d\tau = IRF(t)$$

This result means that it is very difficult to distinguish between different scattering processes (that are very fast and can be described by delta-like function) and fast photoluminescence processes with lifetime beyond setup resolution. Both processes are however visible in the experiment and have the form of IRF function.

(b) Simple Photon Counting

Another kind of technique that allows to measure photoluminescence decay is photon counting method. The simplest photon counter consists of a detector (usually PMT), followed by a discriminator and a counter (see Fig. 13). The discriminator is a part of the setup that receives single-photon pulses from the detector. To obtain pulses of sufficient amplitude at the discriminator input a preamplifier can, but need not, be used in front of the discriminator.

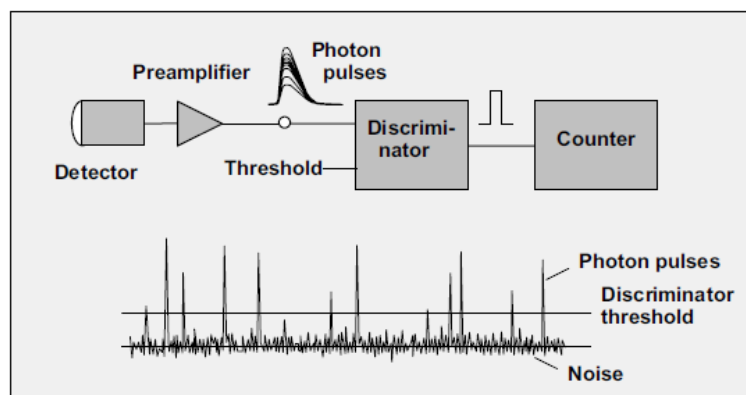


Figure 13. The simplest photon counting setup [²⁴³].

²⁴³ W. Becker „Advanced time-correlated single photon counting techniques”, Springer.



ROZWÓJ POTENCJAŁU I OFERTY DYDAKTYCZNEJ POLITECHNIKI WROCŁAWSKIEJ

The single-photon pulses have a more or less random amplitude. There is a noise background consisting of low amplitude pulses from the detector, noise from the environment, and electronic noise from the amplifier. The discriminator therefore has an adjustable threshold, which is set to discriminate the single-photon pulses against the background noise. The discriminator threshold is set well above the noise level, but below the peak amplitude of the photon pulses delivered by the detector. When a single-photon pulse exceeds the selected threshold, the discriminator delivers a pulse of a defined duration and a defined logic level. The discriminator output pulses are counted by the subsequent counter. The photons are acquired for a given time period, after which the result is read from the counter in equidistant time intervals. Although the simple circuit shown in Fig. 13 lacks any appreciable time resolution, it has most of the positive features of photon counting: background suppression, suppression of detector gain noise, and a sensitivity independent of detector gain variations over a wide range. Photon counters of this type are often built as compact modules that include a detector, its power supply, a discriminator, a counter, and an RS 232 interface.

(c) Gated Photon Counting

In real measurements the technique described above is often modified. A logic gate between the discriminator and the counter is added and single-photon pulses can be counted within narrow time intervals. The principle is shown in Fig. 14.

ROZWÓJ POTENCJAŁU I OFERTY DYDAKTYCZNEJ POLITECHNIKI WROCLAWSKIEJ

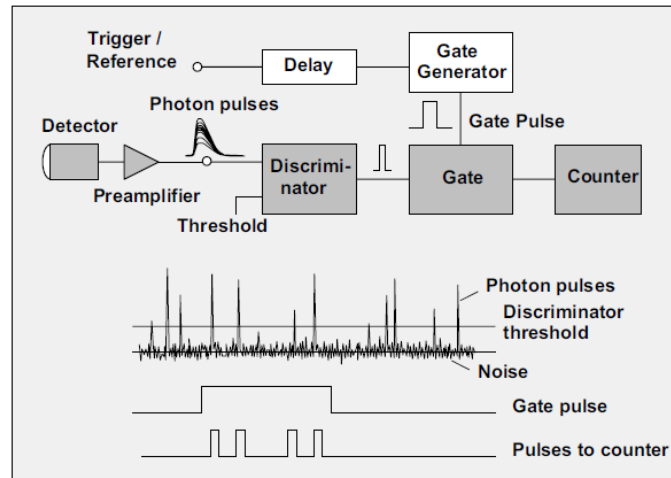


Figure 14. The gated photon counting block diagram.

The discriminator role is to separate the single-photon pulses from the background noise. The discriminator output pulses are sent through a logic gate, and only pulses within the gate pulse are counted. The gate pulses are triggered externally, e.g. by a photodiode receiving the pulses of the excitation laser. Often a gate pulse generator and a delay generator are used to control the gate pulse duration and delay. By controlling the time-delay of the gate pulse a decay curves are constructed. A large number of measurement cycles is run, and the waveform of the input signal is sampled by scanning the delay of the gate pulse. The PL decay is obtained in form of histogram.

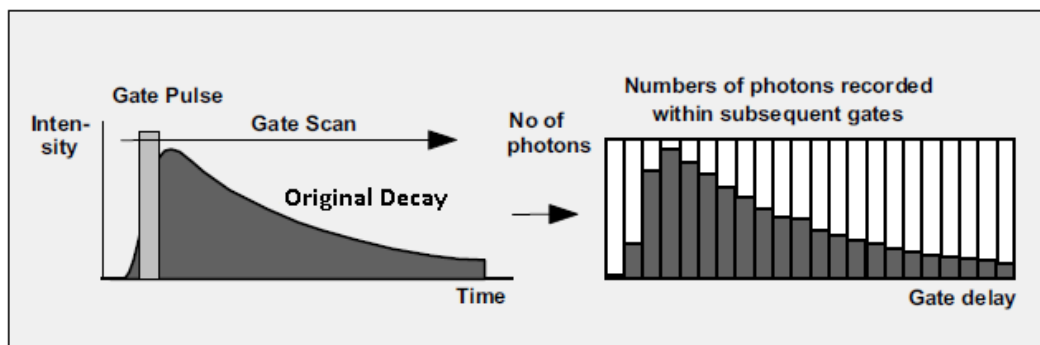


Figure 15. Recording the PL decay by gated photon counting method. The PL decay curve is obtained in form of histogram of photon events in particular delay gate moment.

In practice, the counter counts only detector pulses whose leading edges are within the gate pulse as shown in Fig. 16. This shows a remarkable feature of gated photon counting: the time resolution can be better than the width of the single-photon response of the detector. This



ROZWÓJ POTENCJAŁU I OFERTY DYDAKTYCZNEJ POLITECHNIKI WROCLAWSKIEJ

feature is inherent to all photon counting techniques and is found in extreme form in time-correlated single photon counting. Some typical timing situations are shown in Fig. 2.3, right.

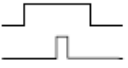
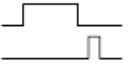
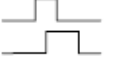
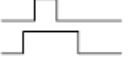
Temporal Relation	Count	Temporal Relation	Count
	yes		no
	yes		no
	yes		no

Figure 16. Possible photon events and counter reaction. The counter counts only detector pulses whose leading edges are within the gate pulse. This allows to obtain a better time-resolution than the width of the single-photon response of the detector.

The gate scan technique is the photon-counting equivalent to the stroboscopic technique. The major difference is that the stroboscopic technique is used to record analog signals. Also, compared to the strobe technique, gated photon counting (in principle) yields a better time resolution and a better signal-to-noise ratio. However, since scanning a narrow gate over the signal rejects the majority of the detected photons, the gate scan technique has a very poor efficiency. This can be improved using multiscaler techniques. This technique counts the photon pulses of a high-speed detector directly, using several parallel gated counters. The gates are controlled via separate gate delays and by separate gate pulse generators. If the measured decay curve is completely covered by consecutive gate intervals, all detected photons are counted. The counting efficiency thus approaches one. The counters can be made very fast and, in principle, the count rates are only limited by the detector. With the commonly used PMTs, peak count rates around 100 MHz and average count rates of several tens of MHz can be achieved.

(d) Time-Correlated Single Photon Counting (TCSPC)

Time-Correlated Single Photon Counting is based on the detection of single photons of a periodical (i.e. modulated) light signal, the measurement of the detection times of the



ROZWÓJ POTENCJAŁU I OFERTY DYDAKTYCZNEJ POLITECHNIKI WROCLAWSKIEJ

individual photons and the reconstruction of the luminescence decay from the individual time measurements (histogram of photon detection times). The method makes use of the fact that for low level, high repetition rate signals the light intensity is usually so low that the probability of detecting one photon in one signal period is much less than one. In fact, depending on the desired accuracy, the light intensity for TCSPC measurement must be no higher than that necessary to detect 0.1 to 0.01 photons per signal period. Multi-photon events will affect the histogram statistics and will yield to erroneous measurement results (this is known in literature as “pulse pile-up problem”). The principle of TCSPC technique is shown in the figure below.

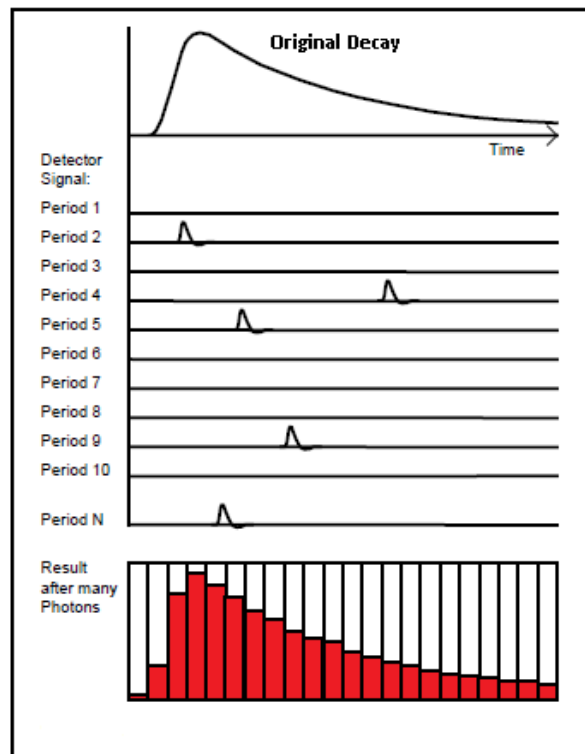


Figure 17. Principles of TCSPC. Detection times of individual photons are recorded. The histogram represents reconstructed PL decay. No-photon periods are also shown. “Period” is a time between two excitation pulses. For TCSPC measurement, probability of photon detection per one period must be much lower than 1.

The detector signal consists of a train of randomly distributed pulses due to the detection of the individual photons. There are many signal periods without photons, other signal periods contain one photon pulse. Periods with more than one photons are very rare. When a photon is detected, the time of the corresponding detector pulse is measured. The events are collected in memory by adding a ‘1’ in a memory location with an address



ROZWÓJ POTENCJAŁU I OFERTY DYDAKTYCZNEJ POLITECHNIKI WROCŁAWSKIEJ

proportional to the detection time. After many photons the histogram of the detection times, i.e. the luminescence decay, builds up in the memory. Although this principle looks complicated at the first glimpse, it is very efficient and accurate for the following reasons: The accuracy of the time measurement is not limited by the width of the detector pulse. Thus, the time resolution is much better than with the same detector used in front of an oscilloscope or another linear signal acquisition device.

It should also be pointed out that the TCSPC technique does not use any time-gating. Therefore all detected photons contribute to the result of the measurement. The counting efficiency, i.e. the ratio of the numbers of recorded and detected photons, is close to one. In conjunction with the large number of time channels, TCSPC can achieve a near-ideal „Figure of Merit“, i.e. an uncertainty of luminescence lifetime measurements close to the statistical limit.

The time of the individual single-photon events may be measured with high accuracy. Thus, the bandwidth of a photon counting experiment is limited only by the transit time spread (TTS) of the pulses in the detector. It is however not limited by the width of the single-photon pulses (the single electron response, SER). The TTS is usually an order of magnitude narrower than the shape of the SER. Therefore, for a particular detector (i.e. PMT), TCSPC obtains a significantly higher time-resolution than any analog recording technique.

The effective resolution of a TCSPC experiment is characterized by its instrument response function (IRF). The IRF contains the pulse shape of the light source used, the temporal dispersion in the optical system, the transit time spread in the detector, and the timing jitter in the recording electronics. With ultra-short laser pulses, the IRF width at half-maximum for TCSPC is typically 25 to 60 ps for microchannel-plate (MCP) PMTs, and 150 to 250 ps for conventional short-time PMTs. The IRF width of inexpensive standard PMTs is normally between 300 ps to 1 ns, but has been tweaked down to less than 120 ps. Standard avalanche photodiodes operating above the breakdown voltage and commercially available single-photon APD modules deliver IRF widths in the range of 40 to 400. Special APDs have achieved IRF widths down to 20 ps.

The width of the time channels of the recorded photon distribution can be made as small as 1 ps. The small time-bin width in conjunction with the high number of time channels available makes it possible to sample the signal shape adequately according to the Nyquist theorem. Therefore standard deconvolution techniques can be used to determine fluorescence



ROZWÓJ POTENCJAŁU I OFERTY DYDAKTYCZNEJ POLITECHNIKI WROCŁAWSKIEJ

lifetimes much shorter than the IRF width and to resolve the components of multi-exponential decay functions.

7.3 Two-dimensional Photoluminescence Excitation Spectroscopy (2D PLE)

In many cases absorption spectrum became very difficult of impossible to determine. In most of these cases, the reason is non-transparent for the light passing through the material substrate on which the investigated sample is deposited. Alternative method, which allows us to investigate the energy structure of the material (and especially excited states) is photoluminescence excitation spectroscopy (PLE). The most general expression describing the probability of detecting a photon emitted by the investigated emitter after the laser excitation (P_{PL}) can be written as [244]:

$$P_{PL}(E_{EXC}, \Theta_{EXC}; E_{PL}, \Theta_{PL}) = I_{EXC}(E_{EXC}, \Theta_{EXC}) \cdot T_{EXC}(E_{EXC}, \Theta_{EXC}) \cdot P_{abs}(E_{EXC}, \Theta_{EXC}) \cdot P_{rel}(E_{EXC}, \Theta_{EXC}; E_L, \Theta_L) \cdot P_{em}(E_L, \Theta_L) \cdot T_{em}(E_L, \Theta_L) \quad (1)$$

where E_{EXC} and Θ_{EXC} describe an energy and incident angle of incoming photons (coming from the laser beam), respectively, while the E_{PL} and Θ_{PL} describe the energy and outgoing angle of photons emitted by the emitter. The expression $I_{EXC}(E_{EXC}, \Theta_{EXC}) \cdot T_{EXC}(E_{EXC}, \Theta_{EXC})$ describe the energy delivered into the system, P_{abs} describe the probability of absorption at excitation energy E_{EXC} , P_{rel} describe combined probability of relaxation of electron and hole to the lowest energy levels E_{PL} from the excited levels E_{EXC} , and P_{em} describe the probability of radiative recombination after carriers relaxation to levels E_{PL} . Finally, the expression $T_{em}(E_{PL}, \Theta_{PL})$ describes probability, that emitted photon will be transmitted outside the emitter.

²⁴⁴ G. Bastard, Wave mechanics Applied to Semiconductor Heterostructures (Le edition le physique, 1997), P. Y. Yu, M. Cardona, Fundamentals of semiconductors: Physics and materials properties (Springer-Verlag, Berlin 1996) p. 357



ROZWÓJ POTENCJAŁU I OFERTY DYDAKTYCZNEJ POLITECHNIKI WROCŁAWSKIEJ

In general, all parts of (Eq.1) do not depend on Θ_{EXC} , because mostly all experiment is done at the same setup configuration. Additionally, assuming that we deal with an isotropic material (optical properties are the same in all directions) we can also assume that all parts in (Eq.1) do not depend on Θ_{PL} . Moreover, assuming that emission depends on excitation flux in linear way, we can also assume that (Eq.1) do not depends on I_{EXC} . Additionally, we can also assume that P_{em} is constant. At all these assumption we can reduce the (Eq.1) to the much more simple form:

$$P_{PL}(E_{EXC}; E_{PL}=\text{const}) = P_{PLE}(E_{EXC}) \propto P_{abs}(E_{EXC}) \cdot P_{rel}(E_{EXC}; E_{PL}) \quad (2)$$

This equation shows that by detecting the emission signal at energy E_{PL} for different excitation wavelengths E_{EXC} we became able to describe the probability of photon absorption at energy E_{EXC} . Nevertheless, from Eq.(2) it can be seen that obtained in this way absorption probability is still a complex function and include also the probability of carrier relaxation and exact correlation between the obtained signal P_{PLE} and P_{abs} is, in general, still not possible. Thus, additional knowledge about the carrier relaxation is needed, i.e. what is the mechanism and efficiency of electron-phonon interaction, how fast the carriers relax etc. Fortunately, when the experiment is carry on at low temperatures (4K) we can assume that the carriers relaxation is very fast (fs-ps) and carriers just after the excitation are in the E_{PL} levels. In this case, we can assume that $P_{rel} = 1$ what brings us to the equation in which the probability of absorption P_{abs} can be well described by the emission intensity P_{PLE} :

$$P_{PL}(E_{EXC}; E_{PL}=\text{const}) = P_{PLE}(E_{EXC}) \propto P_{abs}(E_{EXC}) \quad (3)$$



ROZWÓJ POTENCJAŁU I OFERTY DYDAKTYCZNEJ POLITECHNIKI WROCŁAWSKIEJ

However, in the case of some emission centers characterized by the distribution of their energy levels, i.e. quantum dots, where the separation between the energy levels depends on quantum dot's size, in fact, at certain energy we analyze the response from whole ensemble of different centers characterized by different absorption properties which overlap in detected point E_{PL} . Taking into account this fact, we can transform Eq.(3) to more realistic one defined as ^[245]:

$$P_{PL}(E_{EXC}) \propto P_{PLE} \int dR \left(g(R, E_{EXC}) F(R) \frac{\Gamma_{PL}}{(E_1(R) - E_{PL} - \Delta(R))^2 + \Gamma_{PL}^2} \right) \quad (4)$$

Γ_{PL} is homogeneous emission line broadening, $\Delta(R)$ define distribution function of quantum dots (QDs), R is QDs size while

$$g(R, E_{EXC}) \propto \sum_n \frac{B_n}{(E_n(R) - E_{EXC})^2 + \Gamma^2} \quad (5)$$

describe excitation probability of QDs with size R and at energy \gg then the QDs bandgap. Obtained in this way function fitted to obtained PLE signal will be describing partial density of states for QDs with exact size R . The only reasonable way to discuss properties of such systems is instead of measuring $I_{PL}(E_{PL})$ for different E_{EXC} , integrate each obtained PL spectrum $I_{PL}(E)$ for each E_{EXC} ^[246].

In this case, the formula describing such procedure will be given as follow:

²⁴⁵ C.F. Klingshirn, Semiconductors Optics, Springer, Berlin, p.403 (1997).

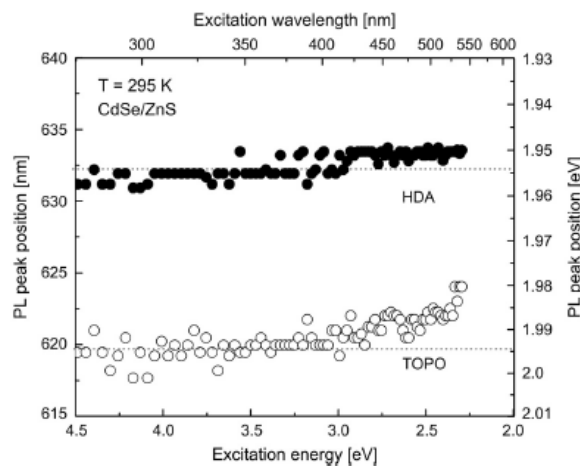
²⁴⁶ S. A. Filonovich, Y. P. Rakovich, M. I. Vasilevskiy, M. V. Artunyevev, D. V. Talapin, A. L. Rogach, A. G. Rolo, M. J. M. Gomes, Chemical Monthly 133, 909 (2002).



ROZWÓJ POTENCJAŁU I OFERTY DYDAKTYCZNEJ POLITECHNIKI WROCLAWSKIEJ

$$\int P_{PL}(E_{EXC}, E) dE \propto P_{PLE} \int g(R, E_{EXC}) F(R) dR \quad (6)$$

This kind of experiment we can call two-dimensional photoluminescence excitation spectrum (2D-PL) or Total Photoluminescence Excitation Spectroscopy because in this experiment we have to record whole PL spectrum for each excitation wavelength, integrated it and plotted as a function of the excitation wavelength. This kind of approach let us also to investigate some statistical properties of the system. For example, for QDs with broad size distribution we should observe the redshift in emission peak position when the excitation wavelength is increasing. This effect simple comes from the fact that when the sample is excited by high energy photons whole distribution of QDs in the system is excited giving some particular, averaged emission peak position. However, when the excitation wavelength is reduced close to resonant excitation less and less small QDs is excited and finally only the biggest one QDs are only excited with characteristic emission shifted to the red side of spectrum. This approach allows us to estimate the changes in QDs size distribution under some modified conditions of sample preparation. Example of such approach has been given in the spectra below where emission peak position has been plotted as a function of the excitation wavelength.





ROZWÓJ POTENCJAŁU I OFERTY DYDAKTYCZNEJ POLITECHNIKI WROCLAWSKIEJ

Figure 1. Photoluminescence peak position as a function of excitation wavelength obtained for CdSe/ZnS nanocrystalline powder covered with additional cap layer of TOPO or HDA [²⁴⁷].

This kind of experiment, done at high spectral resolution, when the emission band is probed by the excitation wavelength resonantly, is called Site Selective Spectroscopy and brings many interesting information not only about the energy structure of the emitter but also about its local environment. This technique is especially efficient when applied to lanthanide ions. Some example of using such technique to lanthanides is given in Fig.2.

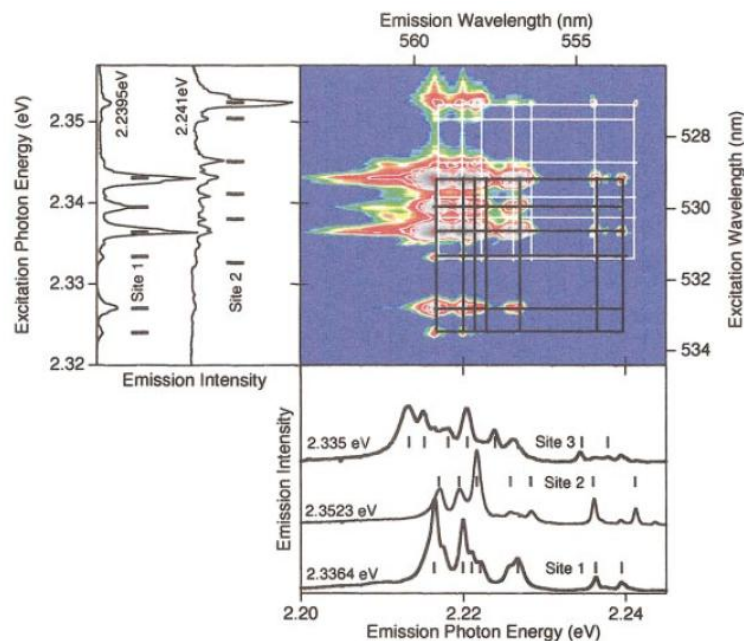


Figure 2. 2D-PLE obtained for Er ions moped into GaN film deposited onto silicon substrate together with cross-sections of green emission from Er placed at different symmetry centers [²⁴⁸].

Interpretation of such experimental data became much more complicated since we deal with the emitter for which we cannot neglect the term describing carriers relaxation $P_{rel}(E_{EXC}; E_{PL})$ even at low temperatures. In this case the ions are excited not directly but in the process when the excitation

²⁴⁷ G. Zatyrb, A. Podhorodecki, J. Misiewicz, K. Nauka, *Optica Applicata* 37, 459 (2007)

²⁴⁸ V. Dierolf i inni, *Journal of Applied Physics* 95, 5464 (2004)

ROZWÓJ POTENCJAŁU I OFERTY DYDAKTYCZNEJ POLITECHNIKI WROCLAWSKIEJ

energy is transferred from the donor to the ion which in this case became an acceptor. Thus, we can only discuss our result in much more complex form taking into account that we record a superposition of two processes. Schematically the difference between these two cases has been shown in Fig. 3 (a). In some cases, however, we can get some more detailed information about the donor and acceptor separately. This is the case when there is possible to detect both, the emission from the acceptor and donor simultaneously. This allows us to measure two excitation spectra simultaneously and in the next step divide the one obtained for acceptor by one obtained for donor. The effect of such procedure has been shown in Fig. 3(b) what is a simple consequence coming from Eq.1 $[P_{\text{trans.}}(E_{\text{EXC}}) \propto P_{\text{PLE}}(E_{\text{EXC}})/P_{\text{abs}}(E_{\text{EXC}})]$.

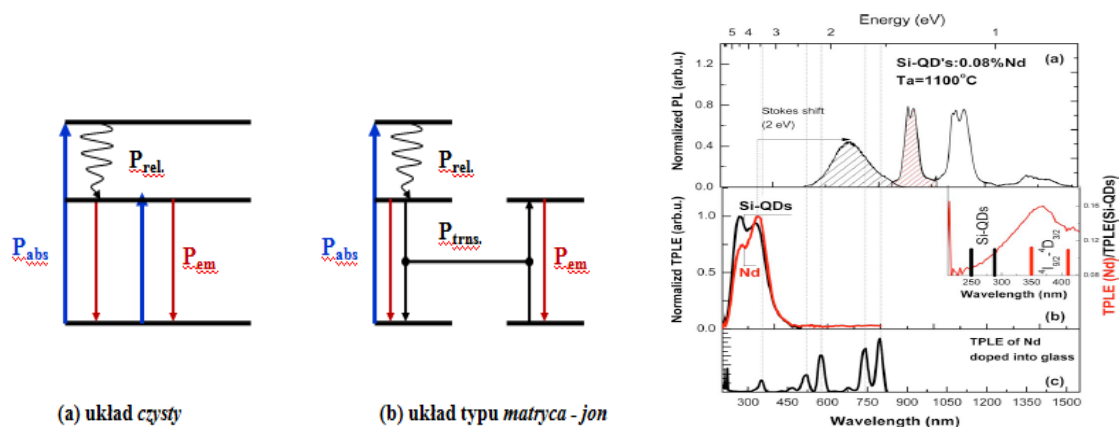


Figure 3. Schematic representation of photoluminescence excitation for the system in which the same system which absorb the light also emit the light as well for the system where these two processes take place in separated objects. Example of experimentally estimated spectral dependence of the energy transfer efficiency based on experimentally obtained excitation spectrum for the donor (here Si-nanocrystals) and for the acceptor/emitter (here Nd^{3+} ions) [249].

²⁴⁹ A.Podhorodecki i inni, Electrochemical Solid State Letters 13, K26 (2010)



ROZWÓJ POTENCJAŁU I OFERTY DYDAKTYCZNEJ POLITECHNIKI WROCŁAWSKIEJ

Obtained in this way information, and especially measured at different temperatures or electric field, allows us to define the energy transfer processes where we can define two main mechanisms: nonradiative dipole-dipole energy transfer (Dexter-Förster) and related with physical charge transfer from donor to acceptor.

7.4 Scanning Probe Microscopy (SPM)

Scanning probe microscopy [²⁵⁰] covers several related technologies for imaging and measuring surfaces on a fine scale, down to the level of molecules and groups of atoms. Instead of using a beam of light or electrons, SPM uses a fine probe that is scanned over a surface (or the surface is scanned under the probe). By applying such a probe, researchers are no longer restrained by the wavelength of light or electrons. The resolution of SPM techniques is very high and allows to resolve even single atoms. What is more, a true 3-D maps of surfaces are now possible to obtain. Scanning Probe Microscopy is a general term, used to describe a growing number of techniques that use a sharp probe to scan over a surface and measure some property of that surface. Some examples are STM (scanning tunneling microscopy), AFM (atomic force microscopy) or SNOM (scanning near-field optical microscope). The basic idea of SPM techniques is shown in the figure below.

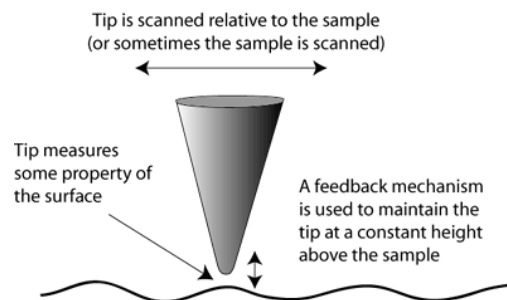


Figure 18. The basic idea common to all SPM techniques.

²⁵⁰ "Scanning Probe Microscopy and Spectroscopy: Methods and Applications", R. Wiesendanger (Cambridge University Press, 1998)



ROZWÓJ POTENCJAŁU I OFERTY DYDAKTYCZNEJ POLITECHNIKI WROCŁAWSKIEJ

In the Fig. 18 a mechanical probe sensor is scanned across an interface. The sensor is extremely sharp tip (3-50 nm radius of curvature). The tip is mounted on a flexible cantilever, allowing the tip to follow the surface profile (up and down relative to the sample surface). When the tip moves in proximity to the investigated object, forces of interaction between the tip and the surface influence the movement of the cantilever. These movements are detected by selective, very sensitive sensors. Various interactions can be studied depending on the mechanics of the probe. The number of techniques is constantly growing, as the tip can be modified in many ways to investigate surface properties.

a) Scanning Tunneling Microscope (STM)

The application of the STM is naturally restricted to conducting or semi-conducting samples. The STM may be applied to samples in very different environments: These microscope works under vacuum conditions as well as in air and, partly with specific modifications, in liquids. The **STM** working principle [²⁵¹,²⁵²] is related to the quantum mechanical tunneling effect: in the framework of quantum mechanics, particles can be described as a superposition of waves with a certain spread in space. If two conducting samples are placed in close proximity to each other, with a small but finite distance between them, electrons from one sample may flow into the other if the distance is of the order of the spread of the electronic wave into space. This is called the tunneling effect because the electrons "tunnel" through the barrier into the adjacent sample. For electrons, the barrier width which may be overcome via a tunneling process is of the order of nm, i.e. of the order of several atomic spacings. The probability of an electron to get through the tunneling barrier decreases exponentially with the barrier width, i.e. the so-called tunneling current (the current of electrons overcoming the tunneling barrier) is an extremely sensitive measure of the distance between two conducting samples. The STM makes use of this sensitivity: A sharp metal needle is brought mechanically into a distance of several nm to a sample that is supposed to be probed. A voltage is applied between the metallic tip and the specimen, typically between a few mV and a few V. While scanning across a certain sample area, the tip collects the electrons tunneling through the barrier. Typical tunneling bias voltages are in the range of 10 to 200 mV and typical tunneling currents used for experiments lie between nA and pA.

²⁵¹ C. F. Quate "Vacuum Tunneling: a new technique for microscopy", *Physics Today* 39, 26 (1986)

²⁵² G. Binnig, H. Rohrer "In touch with atoms", *Reviews of Modern Physics* 71, S324 (1999)



ROZWÓJ POTENCJAŁU I OFERTY DYDAKTYCZNEJ POLITECHNIKI WROCŁAWSKIEJ

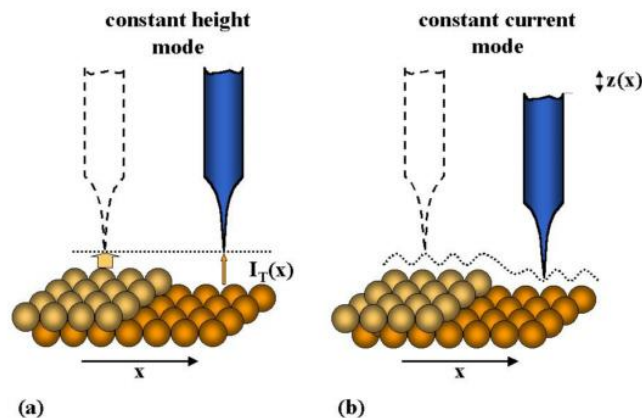


Figure 19. Two modes used for the STM operation: (a) constant height mode and (b) constant current mode (after Forschungszentrum Jülich [²⁵³])

Two types of working modes may be used for the STM: First, the **constant height**-mode, in which the recorded signal is the tunneling current vs. the position of the tip over the sample, and the initial height of the STM tip with respect to the sample surface is kept constant. In the **constant current**-mode, a controller keeps the measured tunneling current constant. In order to do so, the distance between tip and sample must be adjusted to the surface structure and to the local electron density of the probed sample via a feedback loop.

To move the tip up and down from the investigated surface, the STM tip is attached to a piezo-electric element. This is a piece of material with the useful property that it changes its length a little bit, when it is put under an electrical voltage. By adjusting the voltage on the piezo element, the distance between the tip and the surface can be regulated very precisely. The sensitivity of the STM is so large that the small height and electronic corrugation of surface atoms and the electron distribution around them can be detected.

The piezo elements are also used for scanning i.e. to move the tip in the X- and Y- directions, parallel to the surface, recording signal line by line. In this way picture of the examined object is built up. Some of the examples of such a pictures are shown below.

²⁵³ <http://www.fz-juelich.de>



ROZWÓJ POTENCJAŁU I OFERTY DYDAKTYCZNEJ POLITECHNIKI WROCŁAWSKIEJ

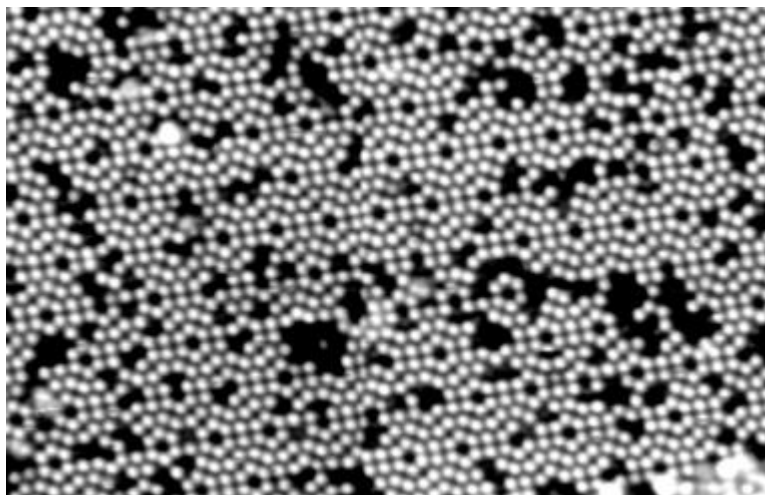


Figure 20. The image shows the silicon (111) surface taken from STM measurement (picture after Forschungszentrum Jülich).

Figure 20 demonstrates the ability of the STM to resolve single atoms: the bright spots on the picture are the silicon atoms. It can be clearly seen the hexagonal structure from cleaving the diamond cubic crystal across the {111} plane. Moreover, also existence of imperfections in the crystal structure may be observed. The following figure was taken in constant-current-mode scan with positive sample voltage.

It should be also mentioned here, that STM can also be used to move single atoms accurately, by pushing or dragging them with the tip at low temperatures. Electrons emitted by the tip can also be used to alter the sample. The ability of STM to serve as a tool for 'rearranging' atoms has made it an important tool in nanosciences.

b) Atomic Force Microscopy (AFM)

The Atomic Force Microscope [²⁵⁴] was developed to overcome a basic drawback with STM - that it can only image conducting or semiconducting surfaces. The AFM, however, has the advantage of imaging almost any type of surface, including polymers, ceramics, composites, glass, and biological samples.

The most important part of the AFM is a flexible cantilever with a atomically sharp tip (typical tip radius is from a few to 10s of nm) attached at one of its ends. If the tip is placed

²⁵⁴ C. R. Blanchard The Chemical Educator 1, 1 (1996)



ROZWÓJ POTENCJAŁU I OFERTY DYDAKTYCZNEJ POLITECHNIKI WROCŁAWSKIEJ

very close to the sample, there is an attractive or repulsive force between the sample surface and the tip. As a result, during sample scanning the cantilever is bent up and down, bringing information about the surface topography. Since all this is going on at a very small scale, we cannot observe the tip directly. Instead, a laser beam is pointed at the tip and is reflected to a sensor. As the tip goes up and down the laser hits different parts of the sensor. With the information the sensor collects, an image of the surface can be recreated.

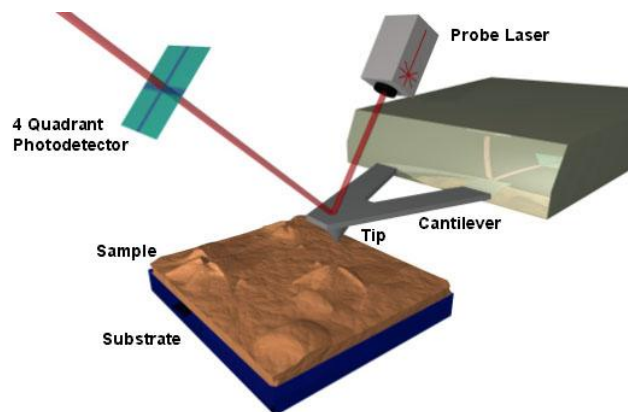


Figure 21. The principles of AFM operations [²⁵⁵].

The AFM may work a few different modes:

- Contact mode. The first and foremost mode of operation, contact mode is widely used. As the tip is raster-scanned across the surface, it is deflected as it moves over the surface corrugation. In constant force mode, the tip is constantly adjusted to maintain a constant deflection, and therefore constant height above the surface. It is this adjustment that is displayed as data. However, the ability to track the surface in this manner is limited by the feedback circuit. Sometimes the tip is allowed to scan without this adjustment, and one measures only the deflection. This is useful for small, high-speed atomic resolution scans, and is known as variable-deflection mode.
- Noncontact mode. This mode belongs to a family of AC modes, which refers to the use of an oscillating cantilever. A stiff cantilever is oscillated in the attractive regime, meaning that the tip is quite close to the sample, but not touching it (hence, “noncontact”). The forces between the tip and sample are quite low, on the order of

²⁵⁵ <http://barrett-group.mcgill.ca/>



ROZWÓJ POTENCJAŁU I OFERTY DYDAKTYCZNEJ POLITECHNIKI WROCŁAWSKIEJ

pN (10^{-12} N). The detection scheme is based on measuring changes to the resonant frequency or amplitude of the cantilever.

- Tapping mode. A stiff cantilever is oscillated closer to the sample than in noncontact mode. Part of the oscillation extends into the repulsive regime, so the tip intermittently touches or “taps” the surface. Very stiff cantilevers are typically used, as tips can get “stuck” in the water contamination layer. The advantage of tapping the surface is improved lateral resolution on soft samples. Lateral forces such as drag, common in contact mode, are virtually eliminated. For poorly adsorbed specimens on a substrate surface the advantage is clearly seen.

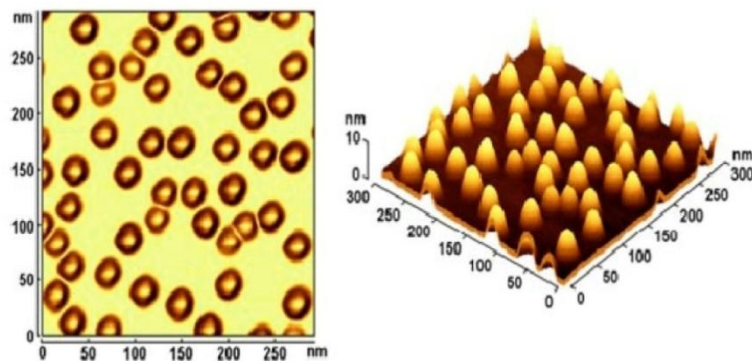


Figure 22. AFM Picture of self-assembled quantum dots of InAs on GaAs(001). Dimensions of the picture is 300x300 nm. Height is 10 nm [²⁵⁶].

Figure 22 shows an example of AFM application. This is an ensemble of *self-assembled quantum dots of InAs on GaAs(001)*. The typical dot size is around 25 nm, and the height is about 7 nm.

c) Scanning near field optical microscopy (SNOM)

The wave-like nature of light causes it to diffract, which limits the spatial resolution of a microscope. Under certain assumptions, the minimum detectable separation of two light scatterers for a given optical system is the Rayleigh Criterion. This limits traditional light-

²⁵⁶ <http://www.centronast.com/>



ROZWÓJ POTENCJAŁU I OFERTY DYDAKTYCZNEJ POLITECHNIKI WROCŁAWSKIEJ

microscopy to a resolution of 200-300 nm, at best, with the exception of cutting edge photolithographic systems whose 100 nm resolution is achieved by using vacuum ultraviolet light. There are other techniques available to extend resolution, but by and large, this is what is possible.

Near-field scanning optical microscopy is a method for imaging beyond the far-field visible diffraction limit with the capability of performing high spatial resolution ($\sim 10\text{-}50$ nm) optical spectroscopy [²⁵⁷]. SNOM overcomes the diffraction limit by confining light via a tiny aperture (typically 10 - 200 nm) which can be raster scanned over a sample surface to construct an image point by point. Light emanating from this aperture rapidly diffracts, but for a small distance (about one aperture diameter) away from the aperture the spatial extent of the light is defined by the aperture. Thus, as long as the distance between the sample surface and the aperture is maintained at a small fraction of the aperture size, the resolution of the image will be determined by the size of the aperture and not the wavelength of light. Optical contrast mechanisms such as absorption, fluorescence, polarization, refractive index, and photoconductivity are all possible with SNOM, making it a completely versatile microscopy technique.

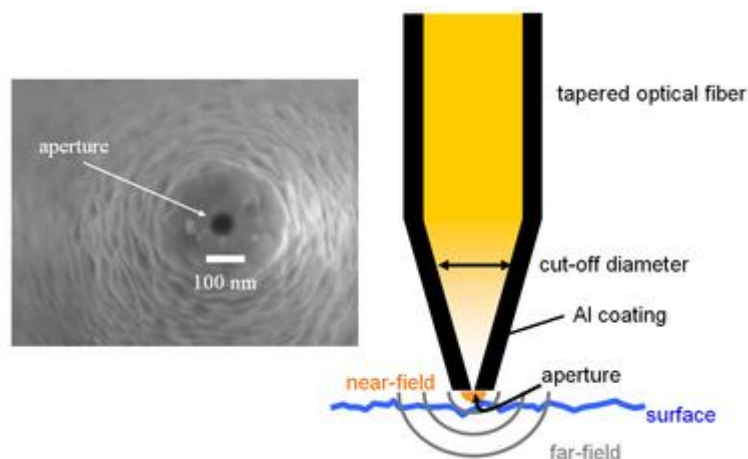


Figure 23. Scheme of a pulled optical fiber with an aluminium coating (the most diffused probe for SNOM systems).

In order to make an SNOM experiment, a point light source must be brought near the surface that will be imaged (within nanometers). The point light source must then be scanned over the

²⁵⁷ B. Hecht, B. Sick, U. P. Wild "Scanning near field optical microscopy with aperture probes: fundamentals and applications", J. Chem. Phys. 112, 7761 (2000)



ROZWÓJ POTENCJAŁU I OFERTY DYDAKTYCZNEJ POLITECHNIKI WROCLAWSKIEJ

surface, without touching it, and the optical signal from the surface must be collected and detected. There are a few different ways to obtain a point light source: One can use pulled or etched optical fibers (tapered optical fibers) that are coated with a metal except for at an aperture at the fiber's tip. The light is coupled into the fiber and is then emitted at the sub-wavelength (50 nm or larger) aperture of the fiber. Or, one can use a standard AFM cantilever with a hole in the center of the pyramidal tip. A laser is focused onto this hole, which is of sub-wavelength dimensions.

The resolution of an SNOM measurement is defined by the size of the point light source used (typically 50-100 nm). The distance between the point light source and the sample surface is usually controlled through a feedback mechanism that is unrelated to the SNOM signal. Currently, most instruments use one of the following two types of feedback: shear force or normal force. In the shear force feedback, or tuning fork feedback, the straight tip is mounted to a tuning fork, which is then oscillated at its resonance frequency. The amplitude of this oscillation is strongly dependent on the tip-surface distance, and it can be effectively used as a feedback signal.

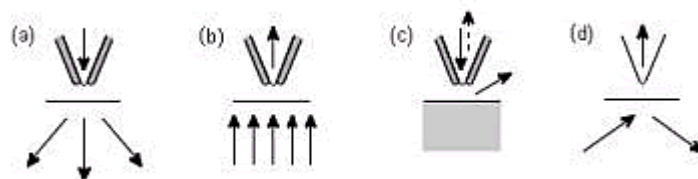


Figure 24. Different modes of SNOM operations (a) illumination, (b) collection, (c) reflection, (d) field enhancement.

Scanning near-field optical microscopy can be performed in many different ways of operation. Most common today is the use of aperture probes for transmission microscopy, either in illumination (a) or in collection (b). However, many samples or substrates are opaque, so that working in reflection is necessary (c). The reflected light can be collected by optics close to the tip, or by the fiber probe itself, in which case often uncoated fiber tips are used. Instead of using a small aperture, a metal tip also may be used (d) to provide a local excitation. If a sharp metal tip is placed in the focus of a laser beam, an effect called local field enhancement will cause the electric field to become roughly 1000 times stronger. This enhancement is localized to the tip, which has a typical diameter of 10 nm. As this tip is scanned over the surface, an image can be formed with a resolution as fine as the tip.



ROZWÓJ POTENCJAŁU I OFERTY DYDAKTYCZNEJ POLITECHNIKI WROCŁAWSKIEJ

(d) Transmission Electron Microscope (TEM)

The transmission electron microscope (TEM) is a scientific instrument that uses electrons instead of light to scrutinize objects at very fine resolutions. They were developed in the 1930s when scientists realized that electrons can be used instead of light to "magnify" objects or specimens under study. TEMs provided a means to go beyond the magnification and resolution limits of light microscopes, allowing for magnification of up to 100,000x and resolutions in the nanometer range.

The transmission electron microscope [²⁵⁸] uses a high energy electron beam transmitted through a very thin sample to image and analyze the microstructure of materials with atomic scale resolution. The electrons are focused with electromagnetic lenses and the image is observed on a fluorescent screen, or recorded on film or digital camera. The electrons are accelerated at several hundred kV, giving wavelengths much smaller than that of light: 200kV electrons have a wavelength of 0.025Å. However, whereas the resolution of the optical microscope is limited by the wavelength of light, that of the electron microscope is limited by aberrations inherent in electromagnetic lenses, to about 1-2 Å. Because even for very thin samples one is looking through many atoms, one does not usually see individual atoms. Rather the high resolution imaging mode of the microscope images the crystal lattice of a material as an interference pattern between the transmitted and diffracted beams. This allows one to observe planar and line defects, grain boundaries, interfaces, etc. with atomic scale resolution. The brightfield/darkfield imaging modes of the microscope, which operate at intermediate magnification, combined with electron diffraction, are also invaluable for giving information about the morphology, crystal phases, and defects in a material. Finally the microscope is equipped with a special imaging lens allowing for the observation of micromagnetic domain structures in a field-free environment.

²⁵⁸ See <http://www.stanford.edu> for more details.



ROZWÓJ POTENCJAŁU I OFERTY DYDAKTYCZNEJ POLITECHNIKI WROCŁAWSKIEJ

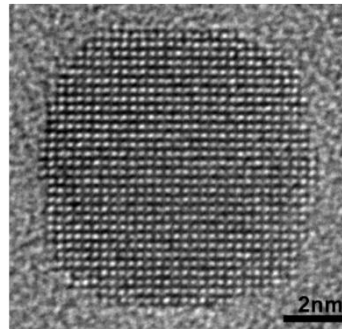


Figure 25. TEM image of PbSe nanocrystal [²⁵⁹]. Lattice fringes are clearly visible.

Sample preparation for TEM generally requires more time and experience than for most other characterization techniques. A TEM specimen must be approximately 1000 Å or less in thickness in the area of interest. The entire specimen must fit into a 3mm diameter cup and be less than about 100 microns in thickness. A thin, disc shaped sample with a hole in the middle, the edges of the hole being thin enough for TEM viewing, is typical. The initial disk is usually formed by cutting and grinding from bulk or thin film/substrate material, and the final thinning done by ion milling. Other specimen preparation possibilities include direct deposition onto a TEM-thin substrate (Si₃N₄, carbon); direct dispersion of powders on such a substrate; grinding and polishing using special devices (t-tool, tripod); chemical etching and electropolishing; lithographic patterning of walls and pillars for cross-section viewing; and focused ion beam (FIB) sectioning for site specific samples.

(e) X-ray Diffraction (XRD)

A crystal lattice is a regular three-dimensional distribution (cubic, rhombic, etc.) of atoms in space. These are arranged so that they form a series of parallel planes separated from one another by a distance d , which varies according to the nature of the material. For any crystal, planes exist in a number of different orientations - each with its own specific d -spacing.

X-ray diffraction is a very important method to characterize the structure of crystalline material. The technique can typically be used for the lattice parameters analysis of single

²⁵⁹ <http://photonics.intec.ugent.be>



ROZWÓJ POTENCJAŁU I OFERTY DYDAKTYCZNEJ POLITECHNIKI WROCŁAWSKIEJ

crystals, or the phase, texture or even stress analysis of polycrystalline materials (like powders). The technique is widely used in research and development applications and its use for production or quality control issues is also growing, benefiting from developments in hardware and software for high throughput capability.

In XRD technique [²⁶⁰], a beam of X-rays incident on a crystalline material undergoes scattering by the electrons associated with the atoms. The scattered X-rays, in turn, undergo interference due to the periodic arrangement of atoms in the crystal and its symmetry. The interference is constructive in certain directions giving rise to a resultant diffracted beam in that direction with enhanced X-ray intensity. The interference is destructive in other directions. The Bragg's equation forms the basis of X-ray diffraction, which determines the conditions of constructive interference of X-ray, i.e. $2d\sin\theta=n\lambda$, where d = the inter-planar spacing, λ denotes the wavelength of incident X-rays, and θ is the angle of diffraction. This Eq. is the basis of most X-ray diffraction analysis, and usually involves fixing one of the parameters and measuring the variation in the second parameter as a function of the third. Moreover, Bragg Eq. provides no indication of the strength of these diffracted beams. In practice total diffraction from a given set of crystal planes occurs over a small angular range about the Bragg angle and outside this range the diffracted intensity drops quickly to zero.

²⁶⁰ http://www.wiley-vch.de/books/sample/3527310525_c01.pdf



ROZWÓJ POTENCJAŁU I OFERTY DYDAKTYCZNEJ POLITECHNIKI WROCLAWSKIEJ

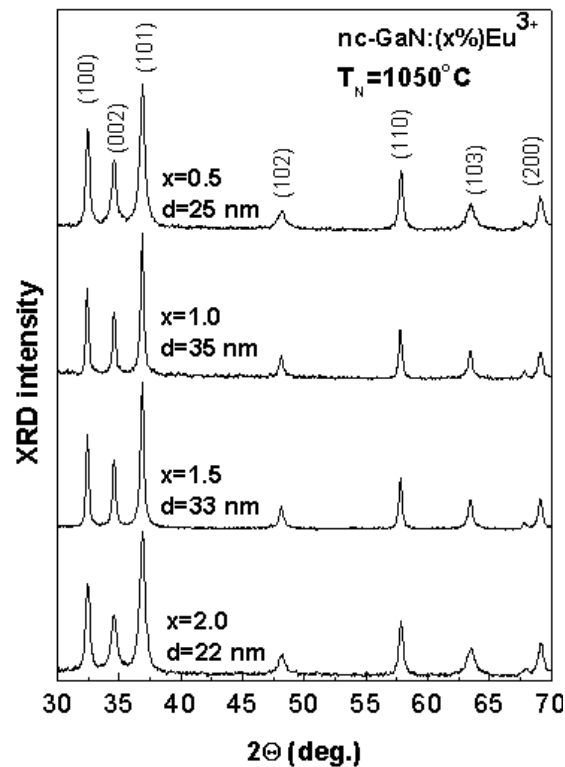


Figure 26. The XRD spectra obtained for GaN nanocrystals with different grain size (25, 35, 33, 22 nm). Diffraction peaks from different lattice planes are clearly visible.

The XRD spectra (see for example Fig. 26) allows i.e. to check crystalline quality of investigated samples. What is more, it is also possible to estimate the nanocrystals size from the broadening of different diffraction peaks. This can be made according to Scherrer formula which in the simplest form have the following form: $D=0.9\lambda/\beta\cos\theta$ (where β is the line broadening at half the maximum in radians, θ is the Bragg angel, λ is the X-ray wavelength and D is the width of the crystal in the direction perpendicular to the particular crystal plane from which other parameters were taken).

Among techniques used for getting structural information about the nanomaterials scanning probe microscopy seems to be most efficient. In this group of techniques we can mention the Scanning Tunneling Microscopy (STM), Scanning Force Microscopy (SFM) like atomic force microscopy (AFM) and Near-field optical spectroscopy (NSOM). The main difference between all these techniques has been given in Fig. 7.1.



ROZWÓJ POTENCJAŁU I OFERTY DYDAKTYCZNEJ POLITECHNIKI WROCLAWSKIEJ

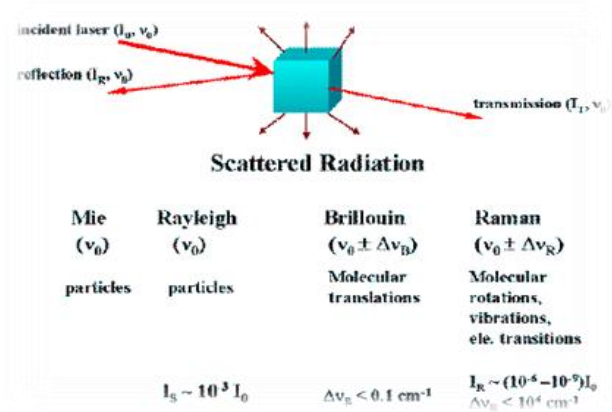
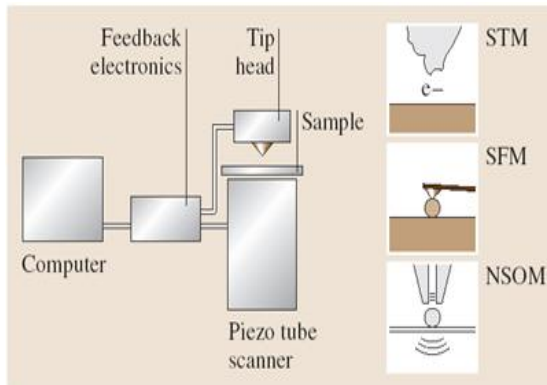


Figure 7.1 Schematically shown experimental techniques used characterization of nanomaterials.

Excellent Good Average Marginal Poor

Projekt współfinansowany ze środków Unii Europejskiej w ramach Europejskiego Funduszu Społecznego



KAPITAŁ LUDZKI
NARODOWA STRATEGIA SPÓJNOŚCI



Politechnika Wrocławska

UNIA EUROPEJSKA
EUROPEJSKI
FUNDUSZ SPOŁECZNY



ROZWÓJ POTENCJAŁU I OFERTY DYDAKTYCZNEJ POLITECHNIKI WROCŁAWSKIEJ